The University of Sheffield

Open Winding Permanent Magnet Synchronous Machine Drives with Particular Reference to Zero Sequence

Hanlin Zhan

A thesis submitted for the degree of Doctor of Philosophy
Department of Electronic and Electrical Engineering
The University of Sheffield
Mappin Street, Sheffield, S1 3JD, UK
May 2017

ABSTRACT

Permanent magnet synchronous machines have drawn much research attention in recent years due to their superiorities on torque density, efficiency, and power factor etc. Meanwhile, the open winding topology can enable the machines to obtain higher DC bus voltage utilization ratio, better fault tolerant capability and higher torque output. Hence, the research on open winding permanent magnet synchronous machines has increased recently. In this thesis, the open winding permanent magnet synchronous machine drives are studied with particular reference to zero sequence.

Firstly, the open winding permanent magnet synchronous machine drives having common DC bus suffer from the zero sequence circulating current issue, which increases the losses and torque ripples. The mechanism analysis of the zero sequence circulating current is therefore presented. The integrated model is established and the influences of the cross coupling voltages in zero sequence and the parasitic effects in inverter nonlinearity are firstly identified. Moreover, two suppression strategies are subsequently proposed, which include the model based and non-model based methods. The non-model based method is constructed on the frequency adaptive proportional resonant controller and has fast dynamic. The non-model based method is based on the extremum seeking algorithm and has better generality for different machines. Secondly, the zero sequence is also utilized to improve the torque performance of the open winding permanent magnet synchronous machine. The zero sequence current injection is adopted to enhance the average torque component of the open winding permanent magnet synchronous machine where the zero sequence back electro-motive force is used. Also, the shifted zero sequence current injection can be used for torque ripple reduction. The proposed torque ripple reduction method reduces the bandwidth requirement of the current controller from 6 times of the fundamental frequency to 3 times of it. Thirdly, the zero sequence characteristics are developed for the sensorless control as well. Two zero sequence back electro-motive force based methods have been proposed, which have higher robustness and non-parametric advantages, respectively. The zero sequence saliency information together with the zero sequence high frequency voltage injection sensorless method is also proposed for the zero and low speed operating region that is not applicable for the back electro-motive force based methods.

Finally, the proposed analyses and methods are all validated via the laboratory open winding permanent magnet synchronous machine drive systems and the 2 dimensional finite element analyses.

ACKNOWLEDGEMENTS

Firstly, I would like to express my sincere thanks to my supervisor, Prof. Z.Q. Zhu. During my Ph.D. study, he offered his best efforts to guide me to the right path to the current progress and the enterprising spirit. Not only the knowledge itself, but also the personality is what I have learnt deeply during these years.

Also, I truly thank my Ph.D. sponsor, Sheffield-Siemens Wind Power Research Centre (S^2WP) very much. I enjoy the time I spent here and I appreciate the great support from S^2WP. Particularly, Dr. Zhan-yuan Wu’s great support for building up the test system should be mentioned.

Meanwhile, I would like to thank all the fellows in the Electrical Machines and Drives Research Group (EMD). The inspiring discussions, the struggle before the accomplishment and the collaborative endeavour are all unforgettable. Mr. John A. Wilkinson’s great help for manufacturing and prototyping should be mentioned.

Finally, I would like to thank my parents. No matter what difficulties I come across, I am strong and confident because of them. They are the people who are always standing behind me and giving me the best they have.

Contents

NOMENCLATURE

B_3	Third harmonic flux density (T)
E_1	Amplitude of the fundamental back EMF (V)
e_a	Phase A back EMF (V)
e_b	Phase B back EMF (V)
e_c	Phase C back EMF (V)
H_6	Amplitude of the inherent sixth torque ripple (Nm)
I_0(s)	Laplace transform of i_0 (A)
I_1	Amplitude of the fundamental phase current (A)
I_3	Amplitude of the injected third harmonic current (A)
i_a	Phase A current (A)
i_b	Phase B current (A)
i_c	Phase C current (A)
i_d	d-axis current (A)
I_d	DC component of d-axis current (A)
I_{d6}	Amplitude of the sixth harmonics in d-axis (A)
i_q	q-axis current (A)
I_q	DC component of q-axis current (A)
I_{q6}	Amplitude of the sixth harmonics in q-axis (A)
i_x	Arbitrary phase current (A)
J	Rotational inertia (kg $\cdot$m^2)
k	Distortion voltage gradient (Ω)
K_i	Resonant coefficient
K_p	Proportional coefficient
K_{PWM}	Amplification factor of inverter
k_{w3}	Winding factor for third harmonic back EMF
LCM	Lowest common multiple
L_d	d-axis inductance (H)
$\mathbf{L_{dq0}}$	Synchronous inductance matrix (H)
L_q	q-axis inductance (H)
$\mathbf{L_s}$	Three phase stator inductance matrix (H)

L_{s0}	DC component of the arbitrary phase self-inductance (H)
L_{s2}	Amplitude of the second harmonic of the self-inductance (H)
M_{s0}	DC component of mutual-inductance between any two phases (H)
M_{s2}	Amplitude of the second harmonic of the mutual inductance (H)
N_P	Pole number
N_S	Slot number
p	Pole pairs
R_s	Phase resistance (Ω)
R_Ω	Resistance coefficient (N s)
T_0	Zero vector time (s)
T_d	Configured dead time (s)
T_e	Electromagnetic torque (Nm)
T_{e-c}	Cogging torque (Nm)
T_f	Period of the fundamental signal (s)
T_i	Turn-on time of vector i (s)
T_j	Turn-on time of vector j (s)
T_l	Load torque (Nm)
t_{off}	Turn-off time of the switching device (s)
t_{on}	Turn-on time of the switching device (s)
T_s	Switching period (s)
U_0(s)	Laplace transform of u_0 (V)
u_d	d-axis voltage (V)
U_{dc}	DC bus voltage (V)
U_{on}	Average conductive voltage drop of the device (V)
u_q	q-axis voltage (V)
y	Slot pitch
γ_6	Phase of the inherent sixth torque ripple (rad)
γ_i	Amplification factor for fundamental current component
δ_d	Phase of the six harmonics in d-axis (rad)
δ_q	Phase of the six harmonics in q-axis (rad)
ΔU	Saturation voltage (V)
Δu_{err-x}	Arbitrary phase distortion voltage (V)
$\Delta\delta_3$	Phase angle of the third harmonic zero sequence current (rad)

θ	Electrical rotor position (rad)
τ	Pole pitch
τ_d	Sampling delay time constant (s)
Ψ_1	Amplitude of the fundamental flux linkage component (Wb)
Ψ_5	Amplitude of the fifth flux linkage component (Wb)
Ψ_7	Amplitude of the seventh flux linkage component (Wb)
$\psi_{d\text{-}pm}$	Coupled PM flux linkage in *d*-axis including harmonics (Wb)
ψ_{f0}	Zero sequence flux-linkage (Wb)
ψ_{pm}	PM flux-linkage (Wb)
$\psi_{q\text{-}pm}$	Coupled PM flux linkage in *q*-axis including harmonics (Wb)
Ω	Rotor speed (rpm)
ω_e	Electrical angular speed (rad/s)
ω_f	Cut-off frequency (rad/s)
ω_m	Mechanical angular speed (rad/s)
ω^N	Normalized angular frequency (p.u.)

CHAPTER 1 GENERAL INTRODUCTION

1.1 Introduction

The permanent magnet synchronous machines (PMSMs) have been widely used in various industrial applications, such as industrial automation [ELR10], electrical vehicles [CHA96], wind power generation [HAQ10], machine tools [LIU12] and household appliances [ZHAO17]. Fig. 1.1 shows the Toyota Prius drive unit including the motor, the generator and the drive. Fig. 1.2 shows the Siemens 3MW wind turbine direct drive permanent magnet (PM) generator. The development of the PMSMs is in company with the PM materials. The rare earth PM materials which have high remanence, high coercivity, high magnetic energy product and linear demagnetization curve [HEN10] enables the PMSM research to enter into a new stage. The PMSMs are therefore extensively investigated and adopted in the aforementioned applications. The advantages of the PMSMs include high efficiency, high torque density, and high power factor [HEN10]. Hence, the drive technology is also very important for these applications. With the development of the power electronics, the inverter based drives are broadly used in different areas. Many advanced control algorithms [BLA72] [BAY72] [FRE96] [ZHO97] [JAH87] [KIM13] [WAL07] [MOR90] [JUN13] are proposed and adopted. New drive topologies [WEL03] with associated advantages also emerge. In this thesis, one of the new promising drive topologies named as open winding (OW) is thoroughly investigated with the particular reference to the zero sequence.

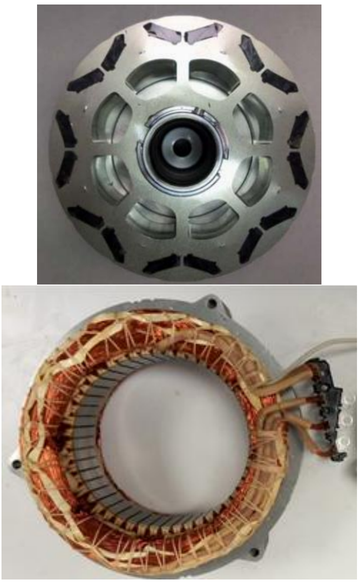

Fig. 1.1 Toyota Prius 2010 PMSM lamination [WEBb].

Fig. 1.2 Siemens 3MW wind turbine direct drive PM generator [WEBc].

1.2 PMSM Topologies and Mathematical Model

1.2.1 PMSM Topologies

As for the PMSMs, the geometry structure can be various. Meanwhile, different PMSM topologies could also have different characteristics specifically suitable for different applications. In general, the PMSMs can be categorised into two types, namely, the surface-mounted PMSM (SM-PMSM) and the interior PMSM (IPMSM) [HEN10]. Fig. 1.3 shows two examples of the PMSM rotor have 2 pole pairs. Fig. 1.3 (a) shows the SM-PMSM and Fig. 1.3 (b) shows the IPMSM. The SM-PMSM is popularly used for the servo system due to its low torque ripple performance and small inductance which is good for fast current control [SLE94]. The IPMSMs are nowadays arising attestations to replace part of the SM-PMSM applications [WEBa]. The IPMSM has saliency which could produce extra reluctance torque via proper control. Meanwhile, the consumption of the PM material of the IPMSM is lower than that of SM-PMSM which is also favourable. Moreover, the winding configuration of the PMSM can be either distributed or concentrated winding. The distributed winding is naturally used and developed from the induction machine for PMSM. Recently, the concentrated winding [ISH06] becomes more attractive due to the shorter end winding, ease of manufacture and potential fault tolerant capability.

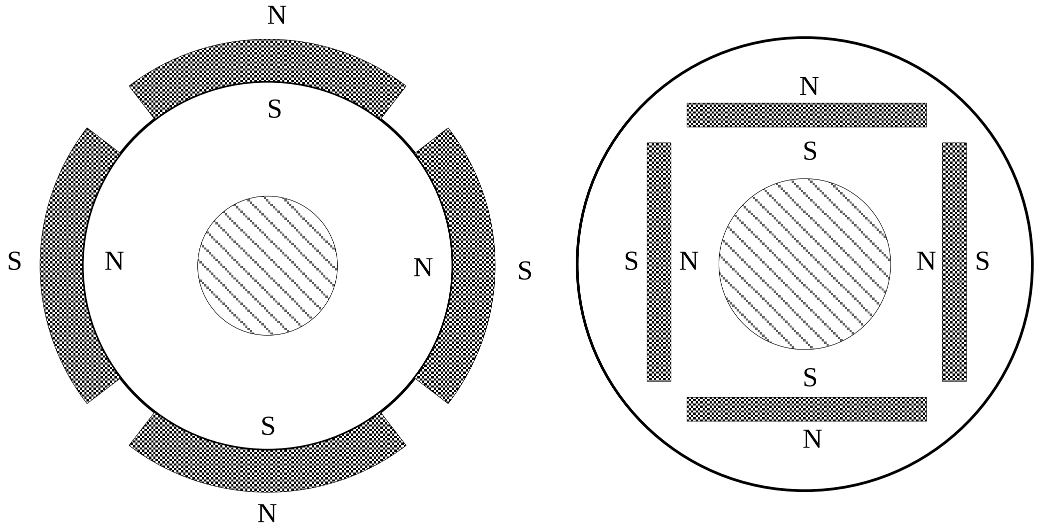

(a) (b)

Fig. 1.3 Two typical PMSM rotor structures. (a) SM-PMSM. (b) IPMSM.

1.2.2 PMSM Mathematical Model

The mathematical models for the SM-PMSM and IPMSM mainly differ on the saliency. Due to the geometrical asymmetry in the equivalent magnetic paths for *d*- and *q*-axes in IPMSM, the *d*- and *q*-axis inductances are different in the IPMSM. The general PMSM mathematical model is usually expressed in the synchronous coordinate as *d*- and *q*-axes. The *d*-axis is aligned with the north pole of the PM. The physical three phase system can be transformed into the synchronous coordinate. The projection is shown in Fig. 1.4.

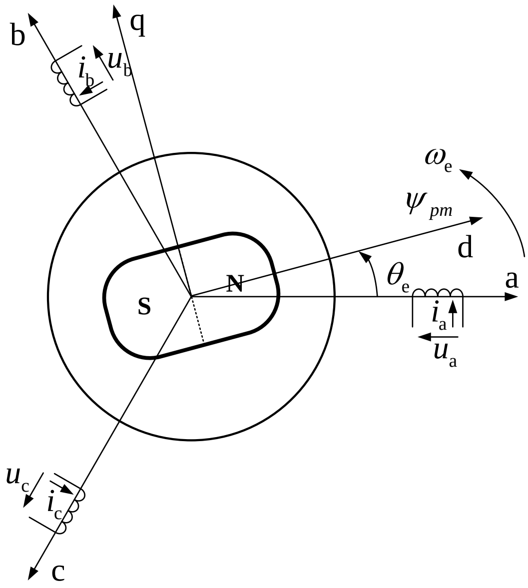

Fig. 1.4 Projection of three phase coordinate to synchronous coordinate.

In general, the voltage equations of PMSM can be expressed as

$$u_q = R_s i_q + \frac{d\psi_q}{dt} + \omega_e \psi_d \tag{1.1}$$

$$u_d = R_s i_d + \frac{d\psi_d}{dt} - \omega_e \psi_q \tag{1.2}$$

where u_d and u_q are *d*- and *q*-axis voltages, respectively, R_s is the phase resistance, i_d and i_q represent the *d*- and *q*-axis currents, respectively, ω_e is the electrical angular speed and

$$\psi_q = L_q i_q \tag{1.3}$$

$$\psi_d = L_d i_d + \psi_{pm} \tag{1.4}$$

where L_d and L_q are d- and q-axis inductances, respectively, and ψ_{pm} is the PM flux-linkage. Usually, L_d is smaller than L_q which is due to the larger magnetic reluctance in d-axis, namely, larger equivalent air gap.

The torque equation can be expressed as

$$T_e = p[\psi_{pm} i_q + (L_d - L_q) i_d i_q] \tag{1.5}$$

where p is the pole pairs. The torque is contributed from the PM torque and the reluctance torque components. If the SM-PMSM has less saturation effect in d-axis, the saliency is negligible and there will be no reluctance torque.

The mechanical motion equation can be represented as

$$T_e = J \frac{d\Omega}{dt} + R_\Omega \Omega + T_l \tag{1.6}$$

where J is the rotational inertia, Ω is the rotor speed, R_Ω is the resistance coefficient and T_l is the load torque.

1.3 Conventional PMSM Drives

1.3.1 General Framework

The conventional PMSM drives consist of pulse width modulation (PWM) strategy, control algorithm and inverter topology. Many PWM strategies [HOL03] [BRO88] have been developed to modulate the output of the inverter, of which, the most popular one is the space vector (SV) PWM (SVPWM) [BRO88] [HOL03]. Meanwhile, the three phase half bridge inverter is commonly used for the medium and low power drives. Fig. 1.5 shows the typical control diagram of the PMSM drives. The current sampling and position sensor are normally required for the closed loop control. The control reference signal can be either speed or torque, which is depending on the application. Meanwhile, the major high performance control algorithms are field oriented control (FOC) [BLA72] [BAY72] and direct torque control (DTC) [FRE96] [ZHO97] which will be introduced in Sections 1.3.3 and 1.3.4, respectively.

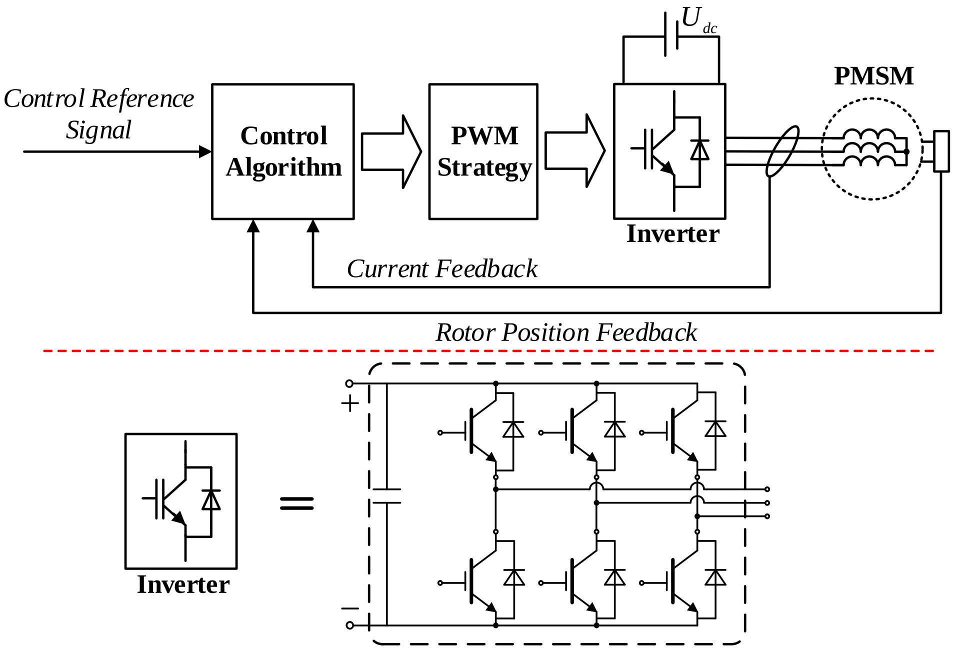

Fig. 1.5 Typical control diagram of the PMSM drives.

1.3.2 Principle of SVPWM

The SVPWM is realized via the combination of the nearest two SVs in the identified sector and two zero vectors. The SV diagram is shown in Fig. 1.6. The zero vectors can be inserted into the vector sequence. When different inserting patterns are adopted, different types of SVPWM are obtained. Consequently, the switching loss and spectrum distribution are different. The common forms include the continues PWM, symmetrical PWM, third harmonic injection PWM and discontinues PWM [ZHO02].

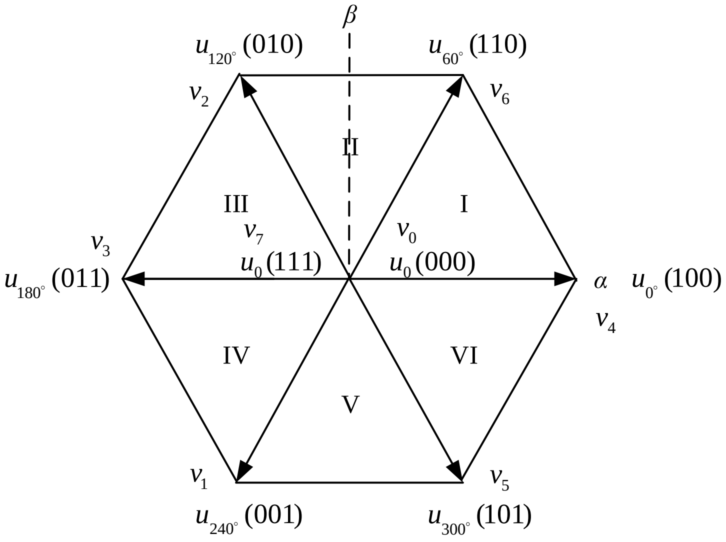

Fig. 1.6 SV diagram.

Meanwhile, the modulation time of the nearest vectors in the selected sector can be calculated as Table 1.1. Hence, the zero vector time can also be determined.

Table 1.1 Calculation of modulation time

Sector	Modulation Time	Sector	Modulation Time
I	$T_6=\frac{T}{2V_{DC}}(\sqrt{3}v_{s\beta ref}-3v_{s\alpha ref})$ $T_2=\frac{T}{2V_{DC}}(\sqrt{3}v_{s\beta ref}+3v_{s\alpha ref})$	II	$T_5=\frac{T}{2V_{DC}}(\sqrt{3}v_{s\beta ref}+3v_{s\alpha ref})$ $T_4=-\frac{\sqrt{3}T}{V_{DC}}v_{s\beta ref}$
III	$T_4=\frac{T}{2V_{DC}}(3v_{s\alpha ref}-\sqrt{3}v_{s\beta ref})$ $T_6=\frac{\sqrt{3}T}{V_{DC}}v_{s\beta ref}$	IV	$T_3=-\frac{\sqrt{3}T}{V_{DC}}v_{s\beta ref}$ $T_1=\frac{T}{2V_{DC}}(3v_{s\alpha ref}-\sqrt{3}v_{s\beta ref})$
V	$T_2=\frac{\sqrt{3}T}{V_{DC}}v_{s\beta ref}$ $T_1=-\frac{T}{2V_{DC}}(\sqrt{3}v_{s\beta ref}+3v_{s\alpha ref})$	VI	$T_1=\frac{T}{2V_{DC}}(\sqrt{3}v_{s\beta ref}+3v_{s\alpha ref})$ $T_5=\frac{T}{2V_{DC}}(3v_{s\alpha ref}-\sqrt{3}v_{s\beta ref})$

1.3.3 Field Oriented Control (FOC) [BLA72] [BAY72]

Fig. 1.7 shows the classical FOC system for PMSM. In the diagram, the SVPWM is adopted due to its higher DC bus utilization ratio. The voltage reference signals are generated from two proportional integral (PI) current controllers. The $i_d^*=0$ control is applied which results in no reluctance torque and the *q*-axis current reference signal is directly proportional to the generated torque. The *q*-axis current reference is from the speed PI controller. The current feedback signals can be transformed into the *d*- and *q*-axes and then after the low pass filter (LPF) to be used for feedback. The speed feedback is the differential of the position signal. If necessary, the LPF can also be used for this signal. The FOC enables a linearized control for PMSM.

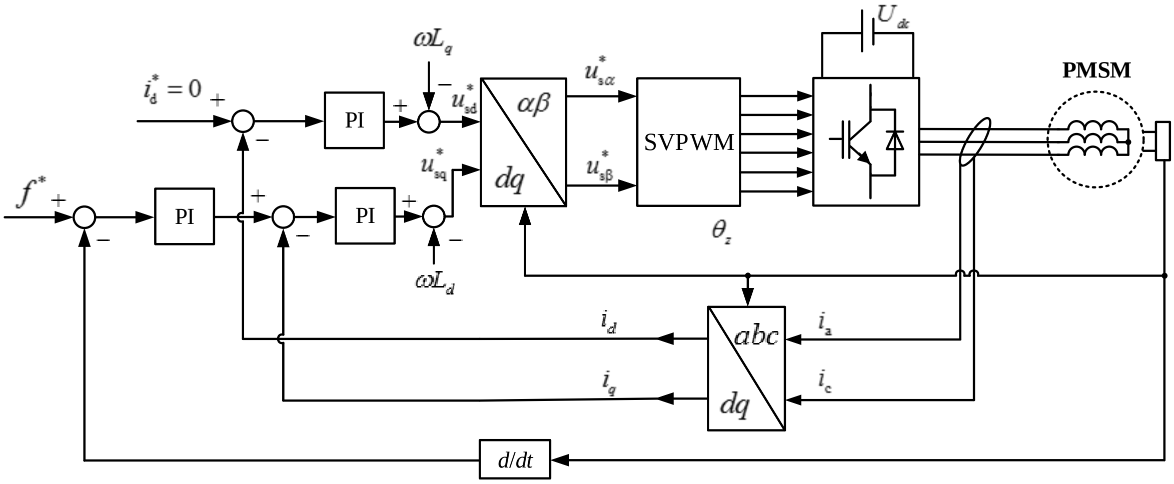

Fig 1.7 Diagram of FOC.

1.3.4 Direct Torque Control (DTC) [FRE96] [ZHO97] [TAK86] [DEP88]

A classical DTC PMSM drives diagram is shown in Fig. 1.8. Two hysteresis comparators are adopted to control the deviations of the stator flux-linkage and torque components. The stator flux-linkage is not only decided by the PM flux-linkage but also the armature reaction flux-linkage as

$$|\psi_s| = \sqrt{\psi_d^2 + \psi_q^2} = \sqrt{\left(\psi_{pm} + L_d i_d\right)^2 + \left(L_q i_q\right)^2} \,. \tag{1.7}$$

The amplitude of the stator flux-linkage might not be constant if the optimized torque control is applied, such as MTPA, which is relevant to the i_d and i_q.

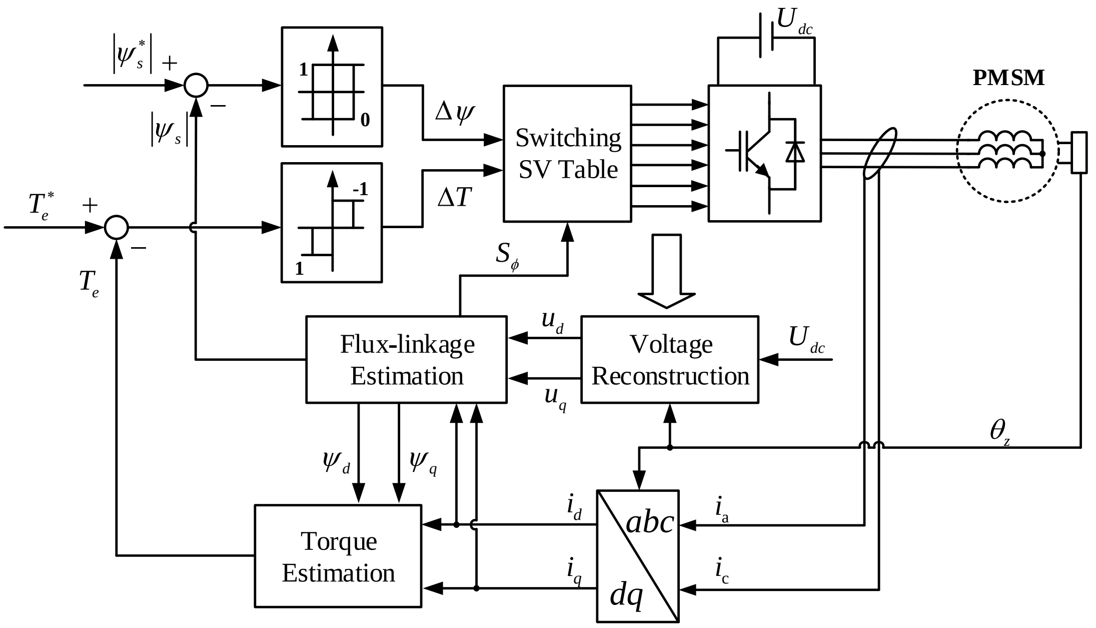

Fig. 1.8 Diagram of DTC [ZHO97].

1.3.5 Other Control Algorithms

Based on the classical control algorithms including FOC and DTC, several kinds of other control algorithms with specific features have also been broadly investigated, which have also formed independent research branches. The major control algorithms include flux-weakening control [JAH87] [MOR90] [SON96], maximum torque per ampere (MTPA) control [KIM13] [JUN13] and sensorless control [CHE03] [COR98] [YOO11]. Meanwhile, the parameter identification algorithm [WAN14], fault tolerant control [WAL07] and modern control theory employments, such as artificial neural network [RAH98], predictive control [PRE13], particle swarm optimization [LIU13], fuzzy control [LI09], etc, are also studied widely.

The flux-weakening control consists of the feedforward [MOR90] and feedback methods [SON96]. Figs. 1.9 (a) and (b) show the feedforward and feedback methods, respectively. The feedforward method is of fast dynamic performance but requires the machine parameters. Additionally, the nonlinear effect such as the saturation and temperature variation cannot be included in the conventional feedforward method. The feedback method has better generality but slower dynamic when compared to the feedforward method. Therefore, to overcome the drawbacks of the feedforward or feedback method, the improved methods are still under development.

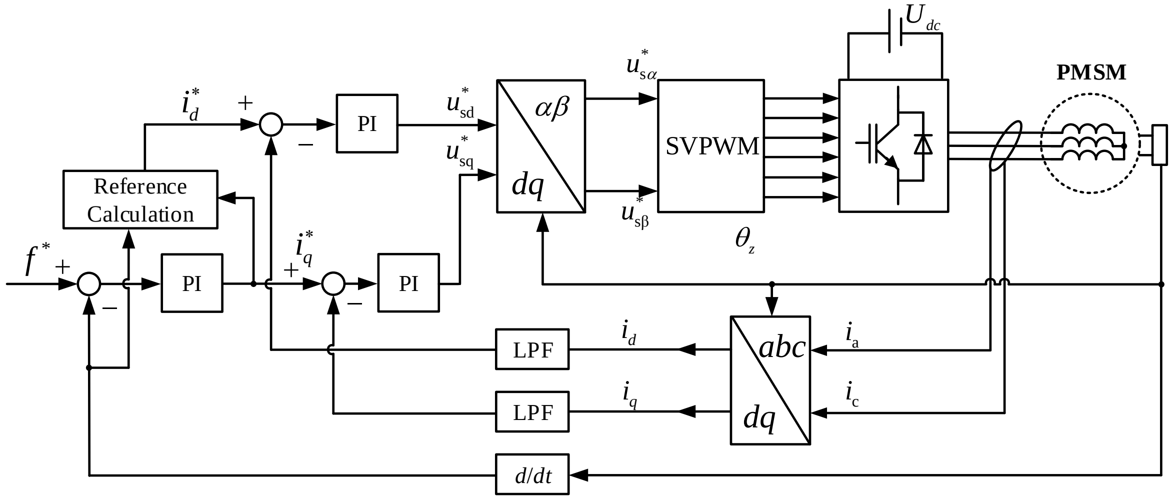

(a)

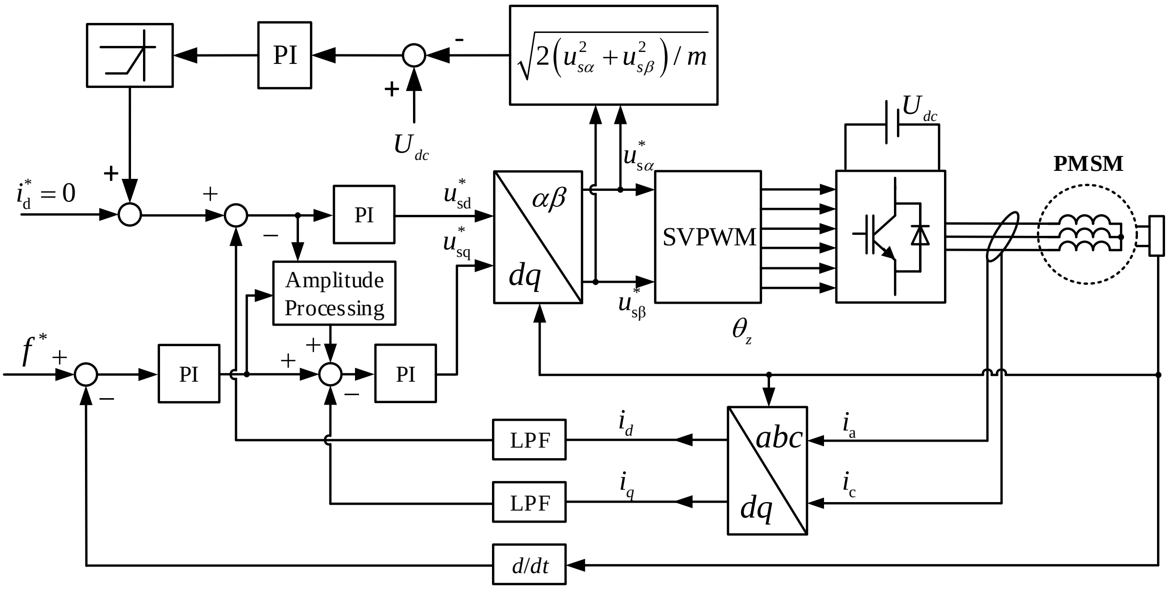

(b)

Fig. 1.9 Diagrams of flux-weakening control. (a) Feedforward method. (b) Feedback method.

The MTPA control is researched to maximize the torque with lowest copper loss. The MTPA control includes the feedforward [JUN13] and adaptive methods [KIM13]. The feedforward method is similar to the feedforward method for flux-weakening control. The machine parameters are necessary to be used for calculating the proper *d*-axis current reference signal. The look-up-table (LUT) or regression function can be used to implement the feedforward method. Fig. 1.10 (a) shows a feedforward method for MTPA control [JUN13]. On the other hand, the adaptive MTPA method is essentially perturbation based method. The searching algorithms are usually adopted in the adaptive MTPA control. Fig. 1.10 (b) shows a high frequency current injection based MTPA control whose mathematical theory is based on extremum seeking [KIM13]. The adaptive MTPA method is insensitive to the machine parameter variation while the perturbation signal is contained in the currents which could result in torque ripple and additional loss.

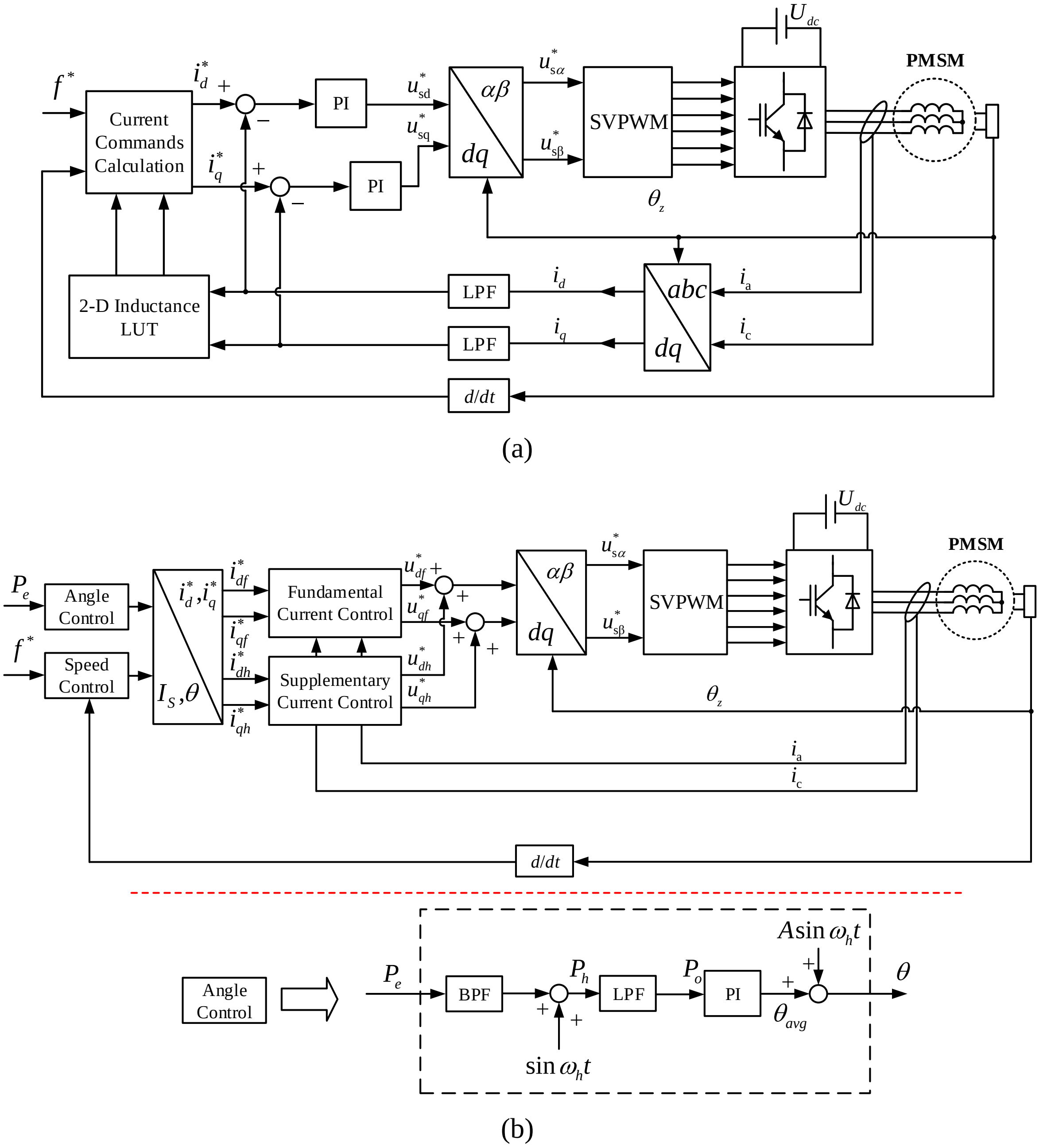

Fig. 1.10 Diagrams of MTPA control. (a) Feedforward method. (b) Adaptive method.

The sensorless control is another popular research essential. To eliminate the position sensor which is expensive, many methods have been proposed. In theory, the rotor position information can be contained in the back electro motive force (EMF) [CHE03] [CHI09] or the saliency related machine parameters [COR98] [YOO11]. The back EMF based methods are usually developed based on the flux-linkage model or the back EMF model. The saliency related parameters for the PMSM include the synchronous inductance and high frequency resistance. The most common methods are based on the inductance saliency. While the eddy current reflected high frequency resistance which also contains rotor saliency can also be used. Fig. 1.11 (a) shows the back EMF based sensorless method using sliding mode observer for IPMSM [CHE03]. Fig. 1.11 (b) shows the high frequency square wave injection based sensorless method relying on inductance saliency [YOO11].

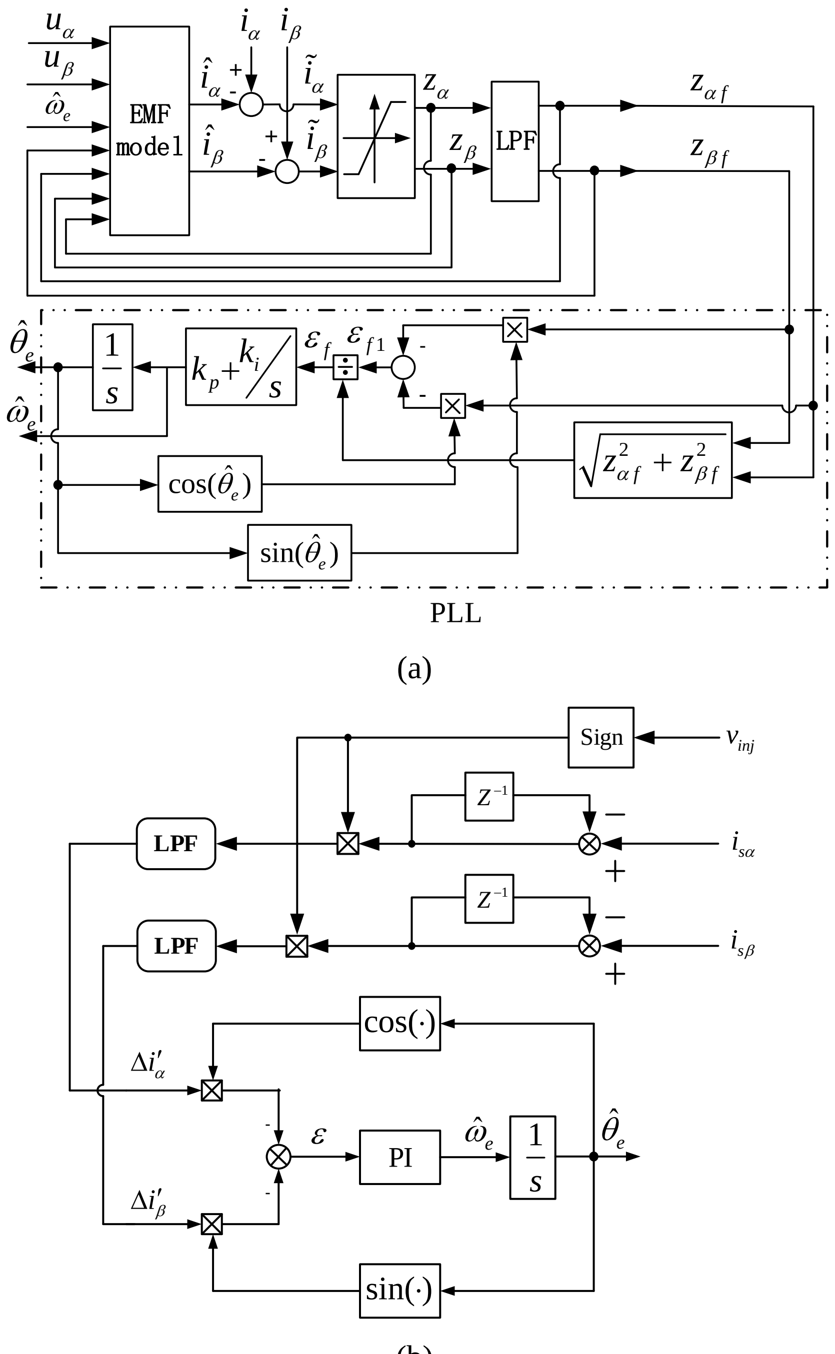

(a)

(b)

Fig. 1.11 Diagrams of two typical sensorless methods. (a) Sliding mode observer based method. (b) High frequency square wave injection based method.

1.4 Open-winding (OW)-PMSM Drives

1.4.1 OW-PMSM

The OW-PMSM drives [ZHA17] are investigated and improved in this thesis. The OW-PMSM is simply defined as Fig. 1.12. No matter for the Y-connected or delta-connected PMSM, the three phase windings of the PMSM can be disconnected and placed as three independent phase windings as shown in Fig. 1.12, which is driven by H-bridge for each phase. Compared to the Y-connected or delta-connected PMSM topology, the number of the driven terminals increases from 3 to 6, namely, multi-terminal machine. As for the OW-PMSM, the dual-inverter drives are utilized, which is essentially equivalent to the H-bridge driven topology. However, the concept is different since the control strategy can be easily implemented based on dual-inverter structure. Meanwhile, more flexible controllability can be expected. Due to the independence of the phase winding, better fault tolerant capability can also be obtained. Moreover, the zero sequence is essentially controllable for the OW-PMSM, as a result, more stable torque performance can be achieved under fault mode. Since the DC bus utilization ratio of the OW-PMSM is much higher, the capability of the power delivery for OW-PMSM is higher as well. Moreover, according to the investigation in this thesis, the OW-PMSM also has specific superiority on sensorless control. However, the increase of the switching device number and the induced circulating phenomenon are also inevitable. Hence, the advantages and disadvantages of the OW-PMSM can be summarised as Table 1.2.

Table 1.2 Advantages & disadvantages of OW-PMSM

Advantages	**Disadvantages**
➢ Higher DC bus utilization ratio ➢ Wider torque-speed curve covered region ➢ Fault tolerant capability ➢ Higher power/torque delivery ➢ Superiority on sensorless control ➢ Allow to use lower DC bus voltage	➢ Increase of switching device number ➢ Zero sequence circulating current

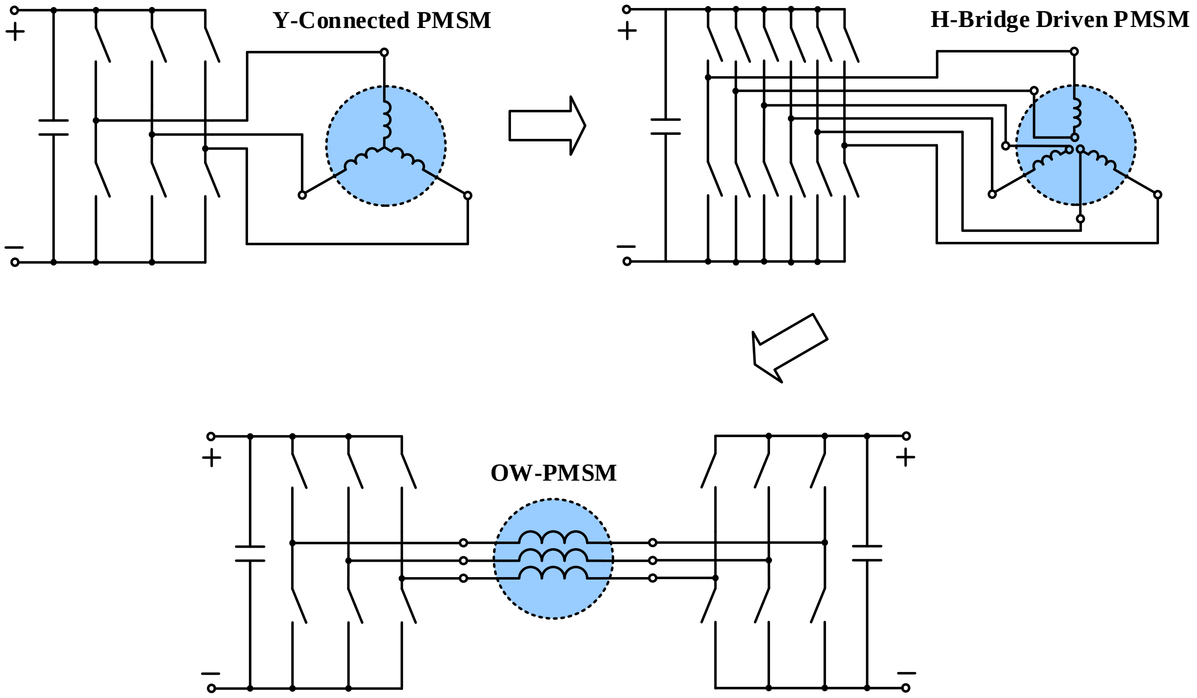

Fig. 1.12 Evolution of OW-PMSM topology.

1.4.2 Topologies of OW-PMSM drives

The most common drive topology for OW-PMSM is the common DC bus one which is shown in Fig. 1.13 [ZHA17]. Two voltage source inverters (VSIs) are connected to the six terminals of the OW-PMSM. The DC bus for these two inverters is the same one, which makes the drive topology equivalent to three H-bridge-driven structure for each phase winding. In this topology, the equivalent zero sequence is no longer open circuit. The third harmonic back EMF contained in the OW-PMSM and the zero sequence modulated voltage from the inverter will consequently induce circulating current, which should be avoided. However, the zero sequence current is useful for the stable torque maintaining for the fault tolerant control, which also requires this characteristic. Since each phase of the OW-PMSM is driven by an H-bridge, any phase current waveform shapes can be generated independently, which is different from the conventional single inverter driven structure.

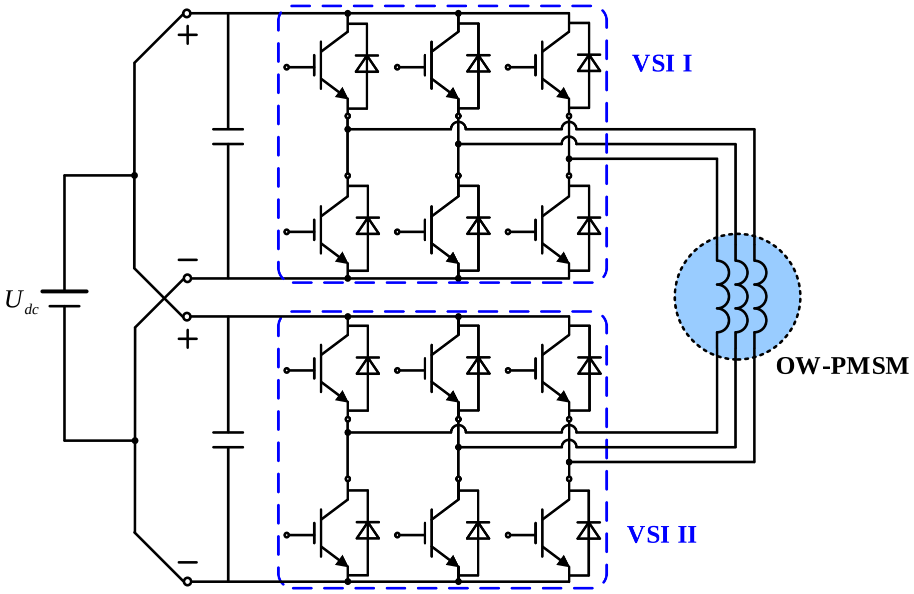

Fig. 1.13 OW-PMSM drive with common DC bus.

Another drive topology for OW-PMSM is the isolated DC bus one that is shown in Fig. 1.14 [KWA07]. The dual inverter drive is supplied by two isolated DC sources and hence the zero sequence is open circuit. The zero sequence circulating current can be consequently avoided. Meanwhile, the multi-level characteristic can be obtained as well. By adopting isolated DC sources with different voltages (1:2), the multi-level phase voltage characteristic is obtained in [SHI01]. The current commutation of the isolated DC bus type is different from the common DC bus one. Compared to the common DC bus one, the isolated DC bus supplies increase the system complexity, cost and size. However, the DC bus utilization ratio is higher and the zero sequence circulating current does not exist.

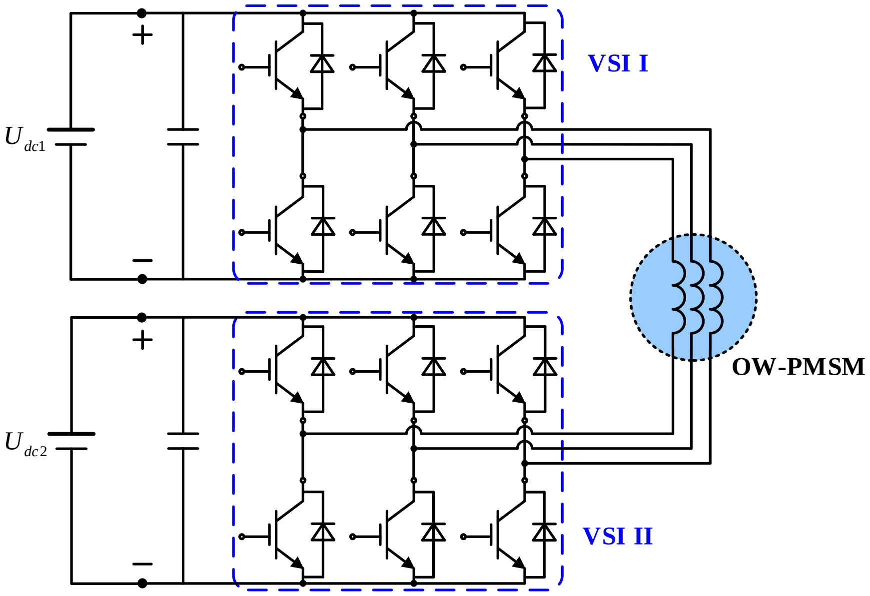

Fig. 1.14 OW-PMSM drive with isolated DC bus.

Fig. 1.15 shows the OW-PMSM drive with floating capacitor and single DC supply [KIM04]. This topology equivalently forms open circuit for zero sequence. Hence, the zero sequence circulating current is avoided as well. Meanwhile, the DC voltage of the floating capacitor can be controlled to the suitable and optimal value as necessary to achieve multi-level modulation on phase winding. The other isolated DC supply is not required but similar benefits are still obtained. The power volume of the inverter in capacitor side can be less than the DC side since the power is not delivered via this inverter in capacitor side. However, no active power can be provided from the capacitor side, which should be noticed.

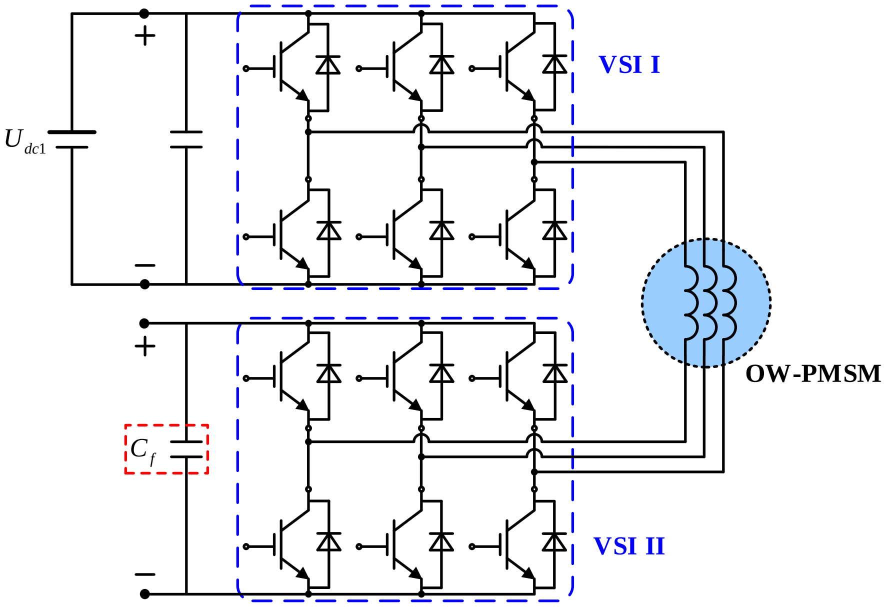

Fig. 1.15 OW-PMSM drive with floating capacitor and one DC supply.

Fig. 1.16 shows a dual three level OW-PMSM drive topology that has been used for OW induction machine drives [KAN06]. Since the common DC bus is adopted, the zero sequence circulating current should be tackled for this topology. Meanwhile, the middle point of the DC bus capacitors is connected, the DC bus capacitor voltage balancing scheme needs to be investigated as well. Similarly, a simplified dual five level OW drive is studied in [MON07] together with common mode voltage elimination. However, it should be noticed that the power rating of the lower inverter is not reduced for this topology. From the perspective of hardware cost, it is not as good as the topologies having reduced power rating capability.

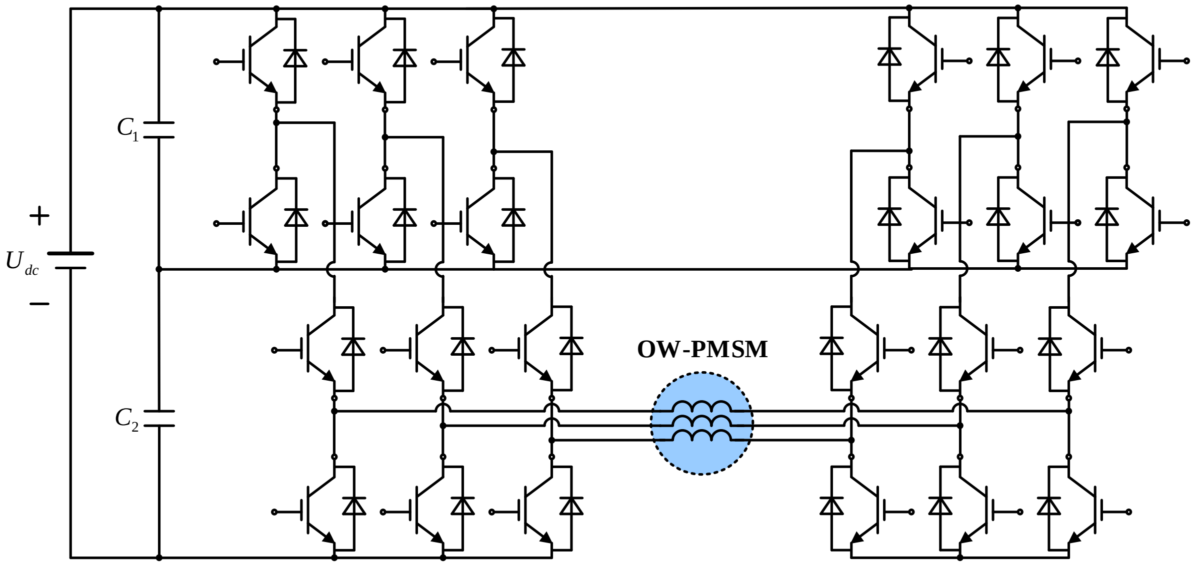

Fig. 1.16 Dual three level OW-PMSM drive.

Fig. 1.17 shows an OW drive topology with 4 sets of auxiliary bidirectional switches [SOM04]. This topology is proposed to replace the isolated DC bus one and still possess higher DC bus utilization ratio as the isolated DC bus one. When compared to the three level topology, the additional bulky DC capacitor can be consequently avoided. The zero sequence circulating current can be suppressed as well.

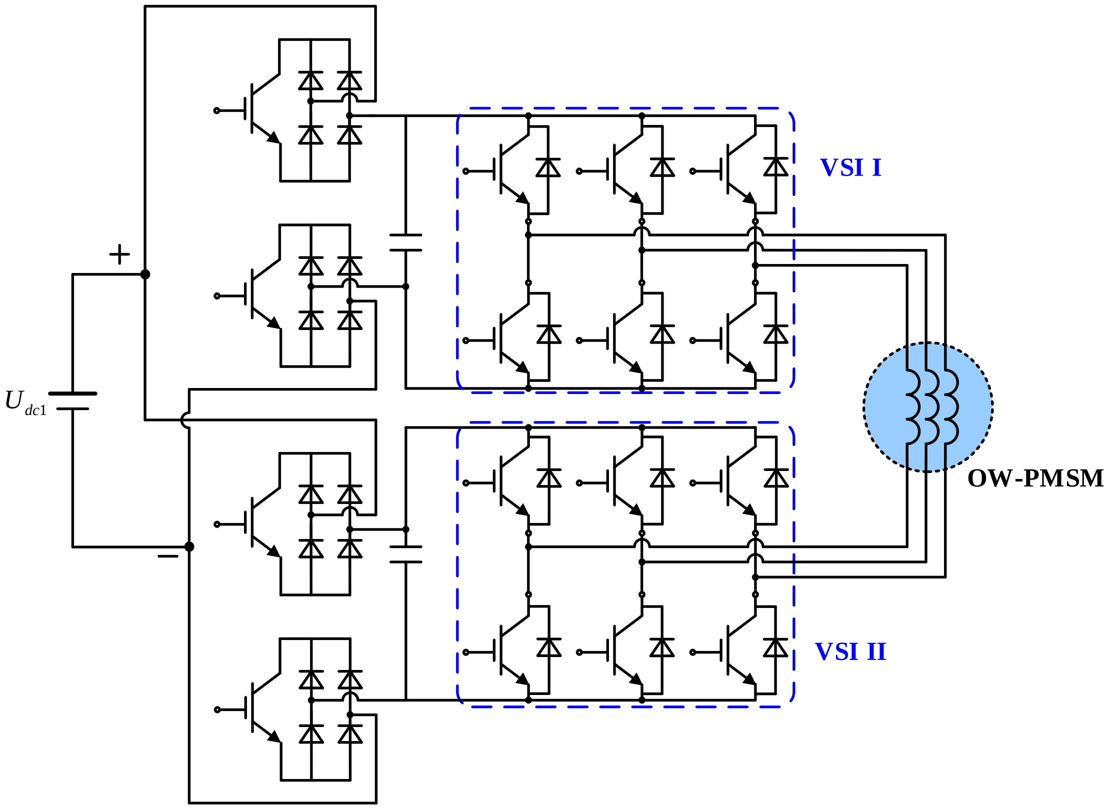

Fig. 1.17 OW-PMSM drive with auxiliary bidirectional switches.

In addition to the fully controlled OW-PMSM drives, Fig. 1.18 shows a half-controlled OW-PMSM converter for wind power generation [NIA14]. From the motor drive perspective, this topology is not capable. However, from the generator aspect, this topology is feasible. Different from the full diode rectifier based converter, this topology provides additional controllable degree of freedom which shows advance in power factor correction [ZHO16]. It is a trade-off between the conventional fully controlled topology and the diode rectifier based topology. The inverter side can be a fraction of the rated power, which performs as the compensation system by connecting to capacitor as the energy storage. Generally, this topology can be a cost effective solution for specific application [PAN12]. Besides, another topology shown in Fig. 1.19 has also been proposed in [YAN10] where the lower bridge switch is the fully controlled one and the upper is the diode. Similarly, the voltages and currents are partially controlled in this topology.

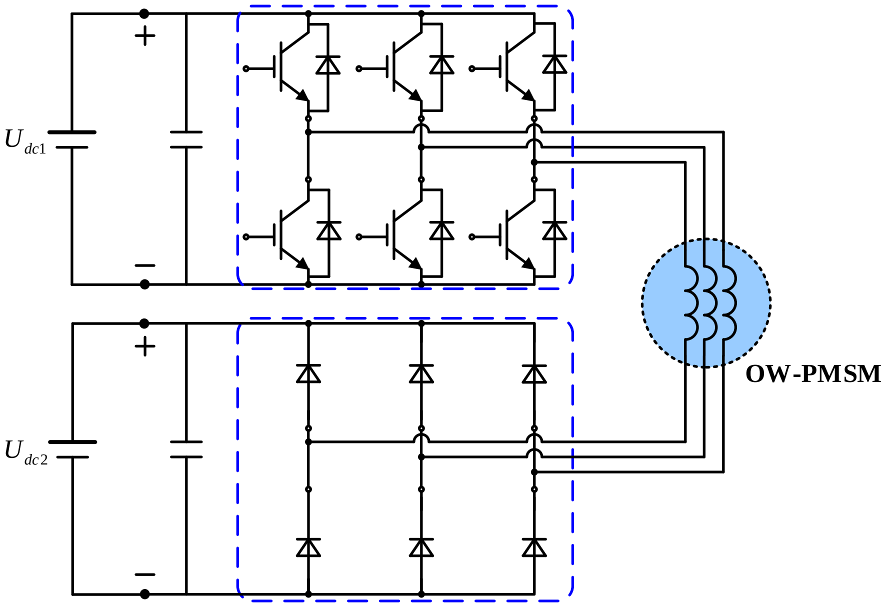

Fig. 1.18 Half-controlled OW-PMSM converter I.

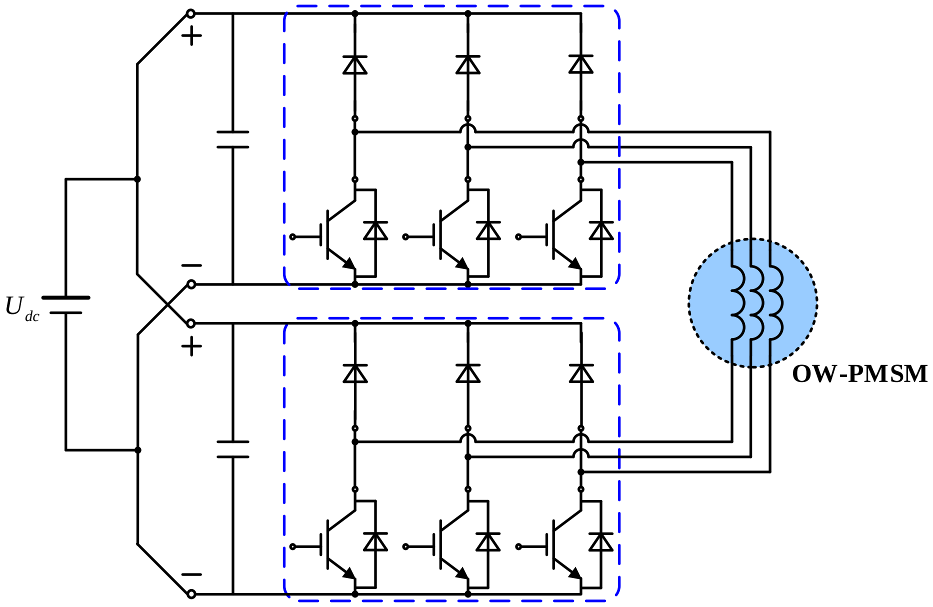

Fig. 1.19 Half-controlled OW-PMSM converter II.

1.4.3 Summary of Current Research

The first OW drive was proposed in [JAH80] by following the concept of modular machine. Each phase of the modular machine is driven by an H-bridge structure, which is equivalent to the common DC bus topology supplying multi-phase machine. After that, the OW drives have been extensively researched for applications such as EV [WEL03] and wind power generation [NIA14]. Meanwhile, the research perspectives as follow have been thoroughly investigated.

- Improved PWM schemes.
- Circulating current suppression.
- Fault tolerant control.

Since the OW drives provide more SV combinations when compared to the conventional single inverter drive, more PWM schemes can be developed by selecting different combinations. The improved PWM schemes for OW drives can effectively improve the total harmonic distortion of the output voltage or reduce the necessary switching frequency to reach the same performance. Furthermore, for the OW drives containing zero sequence path and allowing circulating current, the common mode voltage elimination techniques are also compulsory to reduce the circulating current from the inverter side. Usually, the OW induction machine contains much less third harmonic, therefore, the common mode voltage eliminated PWM strategies are qualified for the associated drives where the zero sequence disturbances are mainly from the inverter side [SOM13].

However, for the OW-PMSM drives, not only the inverter side, but also the machine side introduces zero sequence disturbances. Hence, several techniques have been proposed to tackle this issue. The PI controller [ZHA17a] or proportional resonant (PR) controller [ZHA17] are mostly adopted to suppress the zero sequence current. The integrated disturbances analysis is carried out in [ZHA17], namely, the Chapter 2 of this thesis.

Beyond constructing the framework of the control system, the potential fault tolerant control of the OW drives is studied as well. The earliest OW drive proposed in literature is originally for the fault tolerant control purpose [JAH80]. The fault tolerant control capability is therefore compared to other topologies in [WEL04]. Also, the OW-PMSM under short or open circuit faults have been investigated in [SHA10]. Due to the redundant switching devices in OW drives, the nature of the fault tolerant capability of the OW drives is better than the conventional single three phase machine drives.

In general, the current researches for OW-PMSM drives have only been partly achieved. Except for the aforementioned three topics, other research topics are still under development. Hence, more efforts should be put in. In this chapter (Section 1.1 to Section 1.4), the overview of techniques are introduced from conventional single inverter drives to OW-PMSM drives. The detailed and chapter-related techniques will be presented in the introduction part of the following each chapter.

1.5 Research Scope and Contribution of Thesis

1.5.1 Research Scope

In this thesis, the OW-PMSM drives with particular reference to zero sequence is carried out. The research scope of the thesis is shown in Fig. 1.20. The basic control framework is the FOC. Firstly, as the constituent part of the FOC, the PWM strategies are investigated and used in Chapter 3 to Chapter 8. The phase shift based SVPWM is used in Chapter 6 for zero sequence current based sensorless method. In the other chapters, the zero sequence steerable (ZSS)-SVPWM is proposed and used. The MTPA, flux-weakening and parameter identification for OW-PMSM have not been investigated in this thesis. Chapter 2 and Chapter 3 are for the zero sequence circulating current analysis and suppression strategies, respectively. The torque improvement methods utilizing zero sequence back EMF are proposed and discussed in Chapter 4 and Chapter 5. Chapter 4 discusses the average torque enhancement technique and Chapter 5 presents the torque ripple reduction technique. Three sensorless methods relying on zero sequence are proposed in Chapter 6 to Chapter 8. The zero sequence current based sensorless method and the non-parametric sensorless method both based zero sequence back EMF are presented in Chapter 6 and Chapter 7, respectively. The zero sequence saliency based high frequency injection sensorless method are proposed in Chapter 8. The zero sequence back EMF based methods are for high speed operation and the zero sequence saliency based method is for zero and low speed operation. Finally, the general conclusion is drawn in Chapter 9. The whole thesis is around the exploitation of zero sequence in the OW-PMSM drives.

Meanwhile, Fig. 1.21 shows the diagram of the research decision making. From the perspective of zero sequence path, the common DC bus topology is different from the conventional PMSM drives. Therefore, it is considered to be further exploited. The drawback of this topology leads to circulating current issue to be addressed. Hence, Chapter 2 and Chapter 3 are on this topic. On the other hand, the associated benefits of the zero sequence circuit are explored in Chapter 4 to Chapter 8, which include the sub-topics on torque improvement and sensorless control.

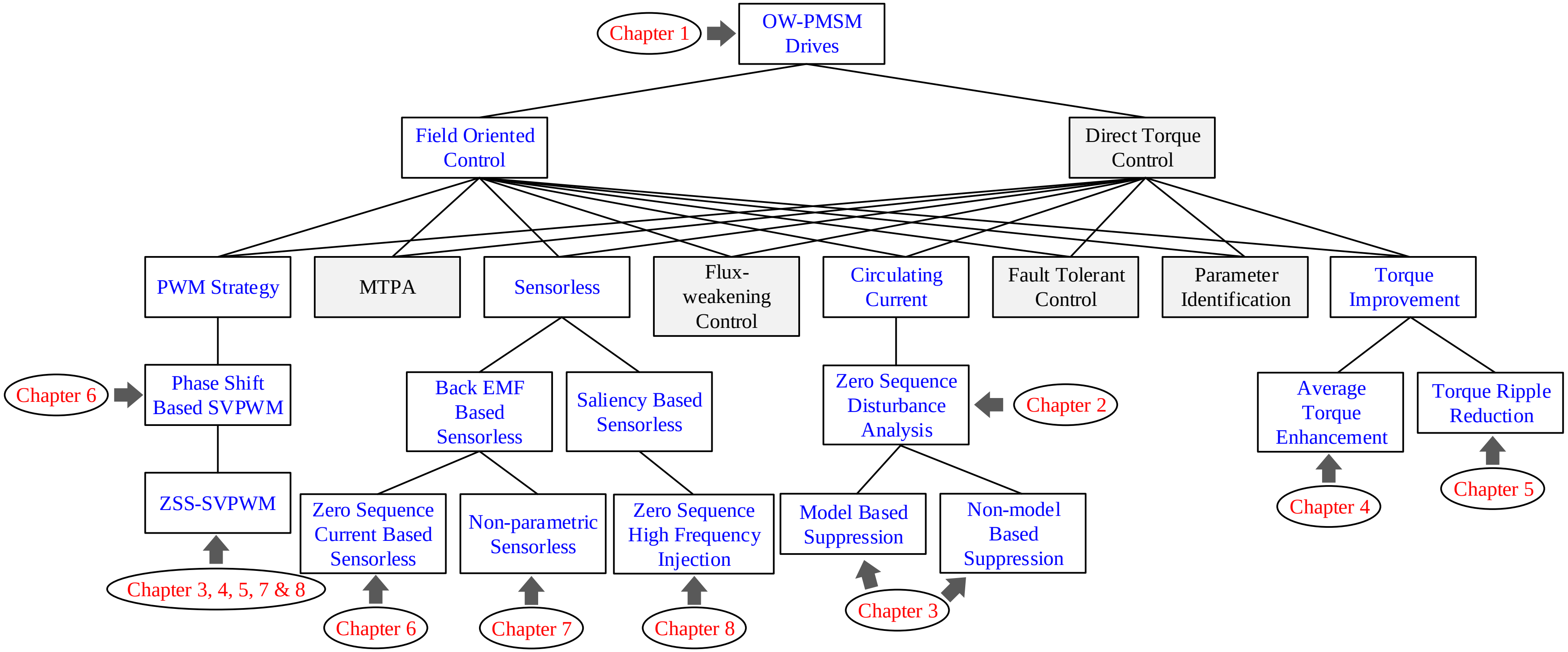

Fig. 1.20 Research scope of the thesis.

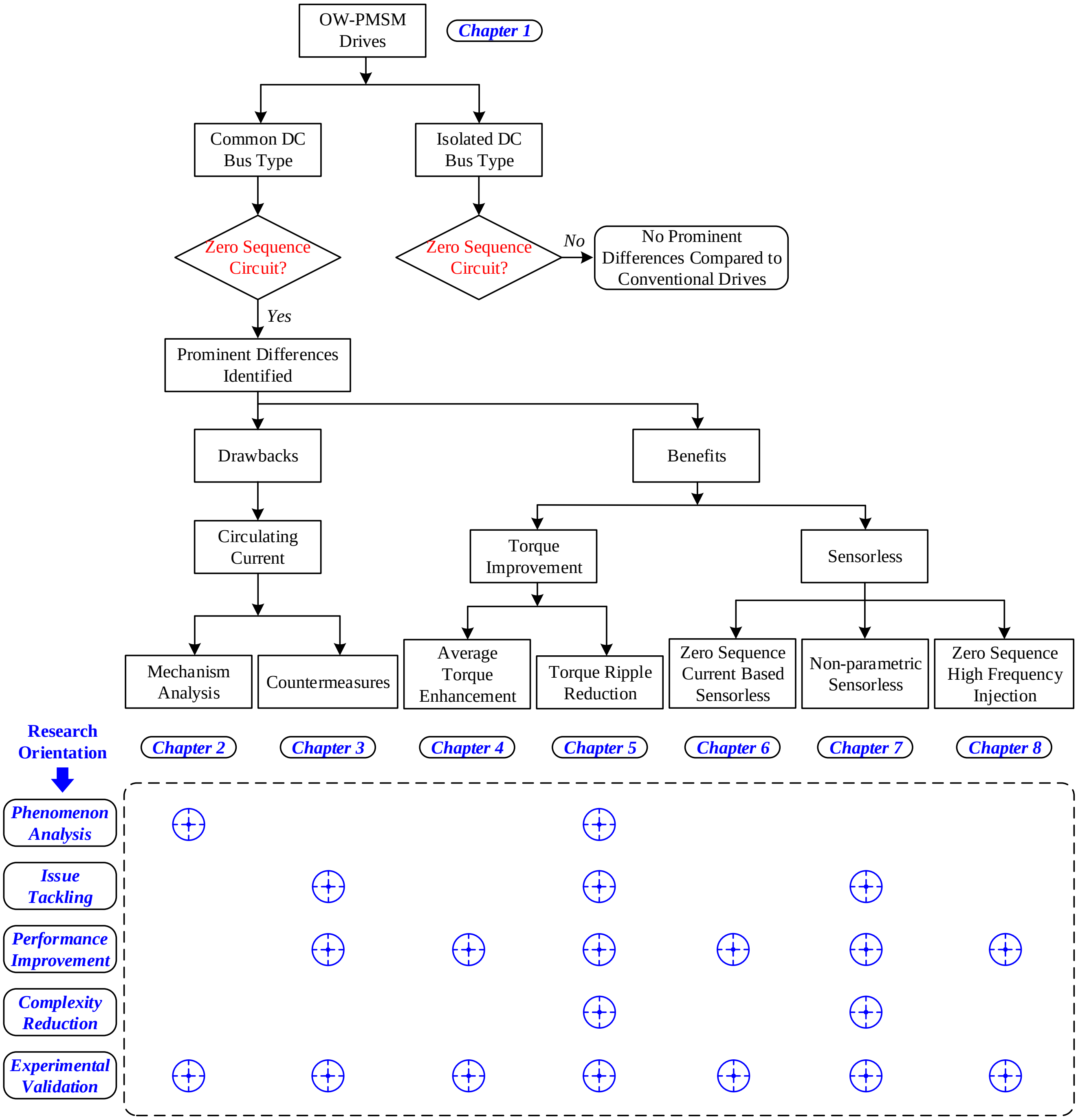

Fig. 1.21 Diagram of research decision-making.

1.5.2 Contributions of Thesis

The key contributions for each chapter are as follows:

Chapter 2: The integrated mechanism analysis of zero sequence circulating current is put forward where zero sequence cross coupling voltages and parasitic effects of inverter nonlinearity are firstly identified.

Chapter 3: Two countermeasures for suppressing zero sequence circulating current are proposed. One is model based method having fast dynamic and the other one is non-model based method having better generality.

Chapter 4: An average torque enhancement technique by utilising zero sequence current shaping is proposed.

Chapter 5: A torque ripple reduction technique with reduced bandwidth requirement on current controller by injecting zero sequence current is proposed.

Chapter 6: A zero sequence circulating current based sensorless method is proposed.

Chapter 7: A non-parametric zero sequence based sensorless method is proposed, which is also capable of circulating current suppression.

Chapter 8: A novel zero sequence high frequency voltage injection based sensorless method is proposed, which is suitable for zero and low speed operation.

CHAPTER 2 ANALYSIS OF ZERO SEQUENCE CIRCULATING CURRENT AND DISTURBANCES

The zero sequence circulating current is normally found in OW-PMSM with common DC bus. It is necessary to firstly investigate its formation mechanism in order to develop the associated suppression techniques. The zero sequence disturbances, including zero sequence back EMF, cross coupling voltages, zero sequence modulation voltage and inverter nonlinearity, are identified and studied in this chapter.

This chapter was published in ECCE 2016 and IEEE Transaction on Industry Applications.

2.1 Introduction

Open winding (OW) machine drives are recently investigated and developed for electrical vehicle (EV) propulsion, wind power generation and industrial motor drives [WEL03] [SHI08] [WAN13] [NIA15] owing to high DC bus utilization and potential fault tolerant capability. Meanwhile, the permanent magnet synchronous machines (PMSMs) are also widely used in various industrial applications due to high efficiency, torque density and power factor [ELR14] [ZHU11]. Specifically, the OW-PMSM inheriting the synthesis of OW topology and PMSM is attracting more and more research attentions [WEL03] [SHI08] [WAN13] [NIA15] [ZHO15].

In general, the OW drive topologies can be divided into two types, viz., OW drive with common DC bus and isolated DC bus. The common DC bus one essentially requiring no isolation transformer can reduce the system volume, weight and cost. But the zero sequence path existing in the OW drive with common DC bus enables additional zero sequence current to circulate within the system including the OW drive and machine. The zero sequence circulating current will consequently cause unwanted power losses, torque ripple and system instability [NIA15] [ZHO15]. Hence, it is necessary to investigate the origins of the zero sequence circulating current and seek solutions to suppress it.

At present, zero sequence back EMF is regarded as the major disturbance source of OW-PMSM drives in the majority of the relevant research papers [NIA15] [ZHO15] [AN17] [HWA14]. Meanwhile, zero sequence circulating current due to inverter nonlinearity [SMO13] and PWM modulated voltage [OLE05] are also investigated independently, which could also be applied to OW-induction machine (IM) (OW-IM). However, according to current research, the possible origins of the circulating current are not fully identified in literature. Meanwhile, the accurate mathematical model and thorough mechanism explanation are not presented as well. In [SAN13], a simple sinusoidal feedforward strategy is adopted to suppress the zero sequence circulating current. This strategy might not be able to tolerate the variation of operating condition. In [ZHO15], a zero vector redistribution method is proposed to control the zero sequence current and only the zero sequence back EMF is regarded as the major disturbance source. As for OW-IM, the authors in [SOM13] investigate the influence of inverter nonlinearity that could also cause zero sequence circulating current. However, due to the parasitic effects of the switching device, it is not revealed in literature that the inverter nonlinearities will no longer induce zero sequence circulating current within small current range, as will be presented in this paper. Meanwhile, the PWM strategy modulated zero sequence voltage is studied in [OLE05] and the phase shift based method is proposed for the cancellation. Besides, in [SOM02], the authors propose an OW topology with 4 additional auxiliary bidirectional switches enabling a switched neutral point structure to suppress the third harmonic currents and reach a higher DC bus utilization. A PI controller is used in [AN17] to suppress the zero sequence circulating current. The static error of PI controller for alternating signal still exists. With regard to five-phase OW drives, an SVPWM scheme with common mode voltage elimination ability for single DC supply is proposed and two of the possible switching sequences are chosen for further investigation [BOD14]. Moreover, in [HWA14], a zero sequence current estimator auxiliary vector control method to compensate zero sequence EMF is proposed based on sinusoidal PWM strategy.

In this chapter, the integrated formation mechanism and mathematical model for zero sequence circulating current are studied. The main contribution is proposing thorough mathematical model of equivalent zero sequence circuit by including the influences of zero sequence back EMF, cross coupling voltages in zero sequence, inverter nonlinearity and PWM modulated zero sequence voltage. Of which, the influence of zero sequence voltages due to the parasitic effects of switching devices and the cross coupling voltages in zero sequence are also investigated for the first time in this chapter. A deeper understanding of the zero sequence circulating current in OW-PMSM drive with common DC bus is therefore obtained. This chapter is organized as follows: In Sections 2.2 and 2.3, the zero sequence disturbances from machine and inverter side are investigated, respectively. In Section 2.4, the synthetic disturbance model is summarized. Finally, the experimental validation is presented in Section 2.5.

2.2 Zero Sequence Disturbances from Machine Side

2.2.1 Zero Sequence back EMF

Third harmonic back EMF is usually observed in the phase back EMF of PMSM except for those with specific winding configurations or structure designs. The saturation and third harmonic shaping of permanent magnet can increase the third harmonic flux density [SHE06] [WAN14a] [ZHA16a]. Also, if the coil pitch factor of third harmonic is zero, the third harmonic would not emerge in the observed phase back EMF. However, this special winding configuration also decreases the winding factor of fundamental component. Hence, the torque density will consequently decrease. The coil pitch factor varies when different winding configurations are applied. The condition is derived as follow:

The coil pitch factor of the υ *th* harmonic in the AC machine can be expressed as

$$k_{w\upsilon} = \sin(\upsilon \frac{y\pi}{2\tau}) \tag{2.1}$$

where y represents the slot pitch and τ is the pole pitch. The pole pitch satisfies

$$\tau = \frac{N_S}{N_P} \tag{2.2}$$

where N_S is the slot number and N_P is the pole number.

Let $k_{w3} = 0$, namely, zero third harmonic winding factor, it will satisfy

$$\upsilon \frac{y\pi}{2\tau} = k\pi,\ k = 1, 2, 3.... \tag{2.3}$$

Meanwhile, for a reasonable design and the maximum fundamental component,

$$0 < y < \tau . \tag{2.4}$$

The zero winding factor of the υ *th* harmonic will satisfy

$$y = (\frac{\upsilon - 1}{\upsilon})\tau . \tag{2.5}$$

Due to zero angle shift between phases, third harmonic back EMF in the phase demonstrates as zero sequence back EMF. The magnetization type, magnet shaping and teeth saturation

[SHE06] [WAN14a] [ZHA16a] can all impose influence on the third harmonic flux density distribution inducing zero sequence back EMF. The winding factor of the third harmonic exhibits damping effect for the third harmonic back EMF in the phase. Although third harmonic back EMF has no influence on the conventional Y-connected single three phase machine system, it behaves as a voltage source in the equivalent zero sequence circuit of the OW-PMSM. Fig. 2.1 shows the phase back EMF waveform and the spectrum analysis of a 3kW OW-PMSM with 96/slot-32/pole combination at 10rpm. It can be seen that the third harmonic component is dominant in the phase back EMF.

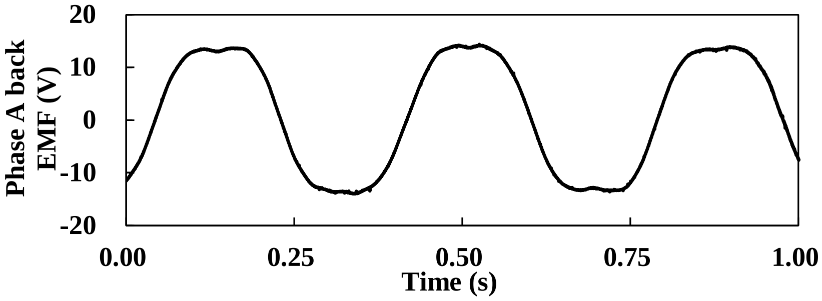

(a)

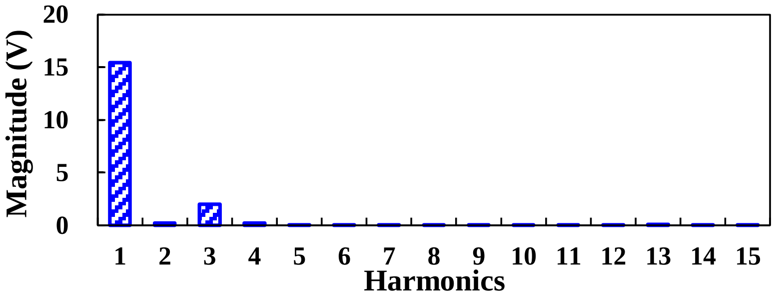

(b)

Fig. 2.1 Measured phase back EMF waveform and spectrum analysis of the 96/slot-32/pole OW-PMSM. (a) Waveform. (b) Spectrum.

2.2.2 Cross Coupling Voltages in Zero Sequence

Zero sequence signals are usually decoupled from *dq*-axis under the assumption of ideal synchronous machine. In the assumption, the amplitudes of the second harmonics of the phase self-inductance L_{S2} and the mutual-inductance M_{S2} should satisfy $L_{S2}= M_{S2}$ which is also called as the condition of ideal synchronous machine. The relationships between the second harmonics and the phase self and mutual inductances are

$$L_{aa} = L_{s0} - L_{s2}\cos 2\theta \tag{2.6}$$

$$M_{ab} = -M_{s0} - M_{s2}\cos 2(\theta + \frac{2\pi}{3}) \tag{2.7}$$

$$M_{ac} = -M_{s0} - M_{s2}\cos 2(\theta - \frac{2\pi}{3})\,. \tag{2.8}$$

Both L_{S2} and M_{S2} contribute to the saliency of the synchronous machine. However, this condition is not always satisfied when different winding configurations of the PMSMs are applied. The typical application is the fault tolerant PMSM [GUO15] adopting concentrated winding configuration. The low mutual inductance is required for these machines to achieve magnetic isolation capacity. The influence from the winding configuration imposing on inductance is analyzed in [PRI15]. Meanwhile, this discrepancy consequently leads to the coupling between zero sequence and *dq* axes. The coupling inductance component can be defined as $L_{\Delta}=(L_{S2}-M_{S2})/2$. Typically, Fig. 2.2 shows the phase self- and mutual-inductances of the 12/slot-10/pole OW-PMSM with double layer concentrated winding and the 96/slot-32/pole OW-PMSM with single layer winding distribution by using 2 dimensional (2D) finite element (FE). The inductances are calculated according to the method proposed in [QI09]. It can be seen that the coupling inductance of the 12/slot-10/pole OW-PMSM is much more obvious than that of the 96/slot-32/pole OW-PMSM.

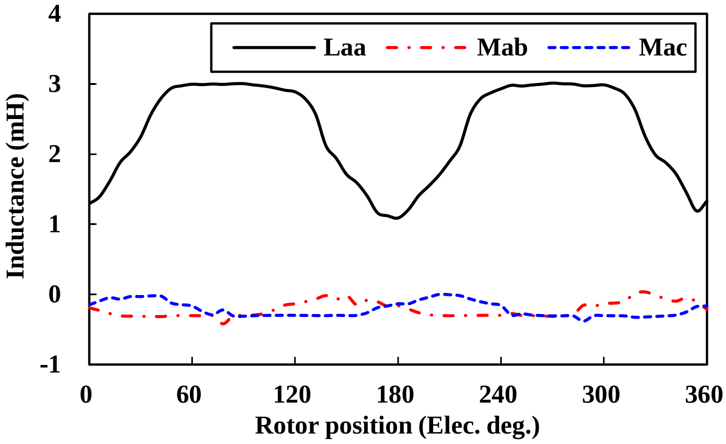

(a)

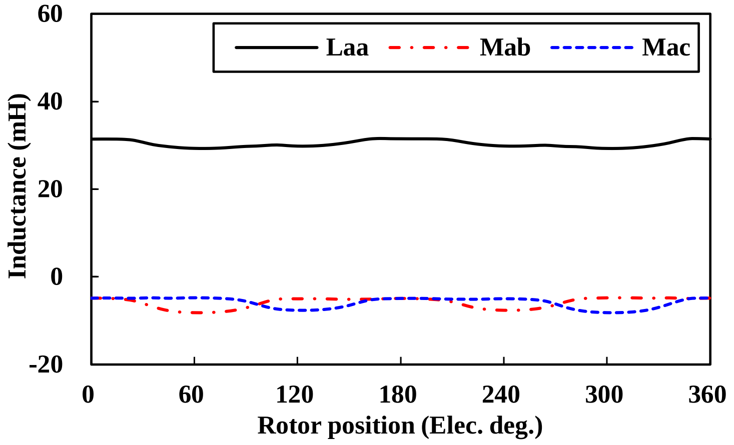

(b)

Fig. 2.2 Phase self- and mutual-inductances curves of the OW-PMSMs calculated by 2D-FE. (a) 12/slot-10/pole OW-PMSM with double layer concentrated winding. (b) 96/slot-32/pole OW-PMSM with single layer overlapping winding.

Meanwhile, the difference of the coupling inductance of the two OW-PMSMs can be understood via the phase A armature winding current flux-linkage distributions those are shown in Fig. 2.3. In Fig. 2.3 (a), only phase A is excited by 5A current component and the majority of the flux-linkage is self-closed. A small quantity of flux-linkage is closed via phase B, which represents the mutual inductance characteristic. In Fig. 2.3 (b), more flux-linkage generated by phase A is closed via phase B due to the overlapping coils. The winding distribution affects the coupling inductance of the OW-PMSM. The overlapping winding distribution usually leads to a smaller coupling inductance characteristic for the OW-PMSM.

If the condition of $L_{S2}=M_{S2}$ is not satisfied, the inductance matrix transformed into $dq0$ coordinate has cross coupling terms between dq axes and zero sequence, namely, L_{Δ}. Hence, the d- and q-axis currents will consequently impose coupled voltage components into zero sequence and induce corresponding zero sequence circulating current. Therefore, it is necessary to take the influence of these cross coupling components in zero sequence into consideration for a comprehensive circulating current modelling. When $L_{S2}\neq M_{S2}$, the coupled inductance terms between zero sequence and dq axes can be expressed as

$$L_{d0}=\frac{L_{0d}}{2}=L_{\Delta}\cos 3\theta \tag{2.9}$$

$$L_{q0}=\frac{L_{0q}}{2}=-L_{\Delta}\sin 3\theta \tag{2.10}$$

where $\omega t=\theta$.

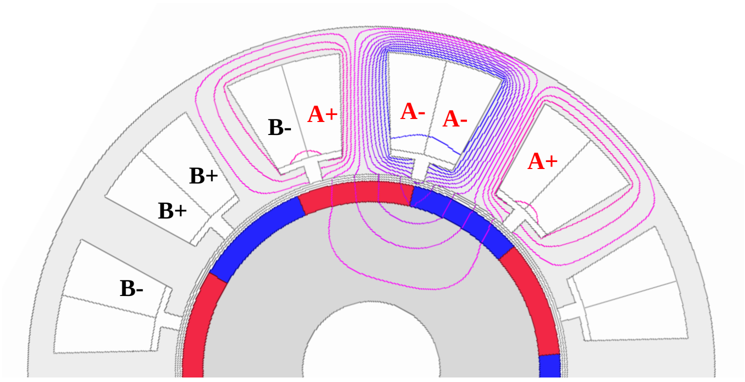

(a)

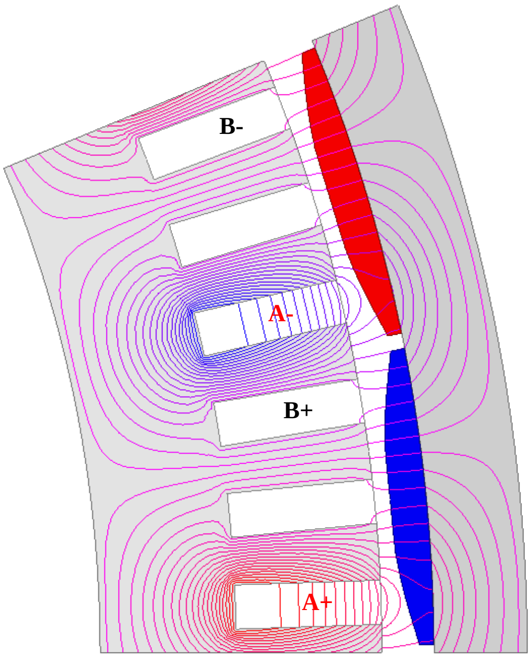

(b)

Fig. 2.3 Phase A armature winding current flux-linkage distribution of the OW-PMSMs. (a) 12/slot-10/pole OW-PMSM. (b) 96/slot-32/pole OW-PMSM.

The complete derivation is presented as follows:

The three phase stator inductance matrix $\mathbf{L_s}$ is

$$\mathbf{L_s}=\begin{bmatrix} L_{aa} & M_{ab} & M_{ac} \\ M_{ba} & L_{bb} & M_{bc} \\ M_{ca} & M_{cb} & L_{cc} \end{bmatrix}$$
$$=\begin{bmatrix} L_{s0}-L_{s2}\cos 2\theta & -M_{s0}-M_{s2}\cos 2(\theta+\frac{2\pi}{3}) & -M_{s0}-M_{s2}\cos 2(\theta-\frac{2\pi}{3}) \\ -M_{s0}-M_{s2}\cos 2(\theta+\frac{2\pi}{3}) & L_{s0}-L_{s2}\cos 2(\theta-\frac{2\pi}{3}) & -M_{s0}-M_{s2}\cos 2\theta \\ -M_{s0}-M_{s2}\cos 2(\theta-\frac{2\pi}{3}) & -M_{s0}-M_{s2}\cos 2\theta & L_{s0}-L_{s2}\cos 2(\theta+\frac{2\pi}{3}) \end{bmatrix}.$$

(2.11)

The synchronous inductance matrix $\mathbf{L_{dq0}}$ is

$$\mathbf{L_{dq0}}=\mathbf{C^{-1}L_sC}=\begin{bmatrix} L_d & L_{qd} & L_{0d} \\ L_{dq} & L_q & L_{0q} \\ L_{d0} & L_{q0} & L_0 \end{bmatrix} \qquad (2.12)$$
$$=\begin{bmatrix} L_d & 0 & 2L_\Delta \cos 3\theta \\ 0 & L_q & -2L_\Delta \sin 3\theta \\ L_\Delta \cos 3\theta & -L_\Delta \sin 3\theta & L_0 \end{bmatrix}$$

where $\mathbf{C}$ satisfies

$$\mathbf{C}=\begin{bmatrix} \cos\theta & -\sin\theta & 1 \\ \cos(\theta-\frac{2\pi}{3}) & -\sin(\theta-\frac{2\pi}{3}) & 1 \\ \cos(\theta+\frac{2\pi}{3}) & -\sin(\theta+\frac{2\pi}{3}) & 1 \end{bmatrix}. \qquad (2.13)$$

Also

$$L_d=L_{s0}+M_{s0}-\frac{1}{2}L_{s2}-M_{s2} \qquad (2.14)$$

$$L_q=L_{s0}+M_{s0}+\frac{1}{2}L_{s2}+M_{s2} \qquad (2.15)$$

$$L_\Delta=\frac{1}{2}(L_{s2}-M_{s2})\,. \qquad (2.16)$$

Hence, the corresponding induced voltages due to *dq*-axis currents imposed on zero sequence are

$$u_{0-id} = \frac{d\psi_{d0}}{dt} = \frac{d(i_d L_{d0})}{dt} = -3\omega i_d L_{\Delta} \sin 3\omega t \tag{2.17}$$

$$u_{0-iq} = \frac{d\psi_{q0}}{dt} = \frac{d(i_q L_{q0})}{dt} = -3\omega i_q L_{\Delta} \cos 3\omega t\,. \tag{2.18}$$

Meanwhile, it can be seen that these voltage disturbances can be regarded as current controlled voltage sources (CSVSs) based on *dq*-axis currents.

Fig. 2.4 shows the 2D-FE results of the zero sequence induced voltages of a 12/slot-10/pole fractional OW-PMSM with non-overlapping winding configuration (L_{Δ}>0) with and without 4A *q*-axis current. It can be seen that the zero sequence induced voltage is shifted and distorted at on-load condition due to the cross coupling voltage components from *dq* axes. The variation of the zero sequence third harmonic induced voltage accounts for 31.7% for the 12/slot-10/pole OW-PMSM, which is due to the cross coupling voltages and cannot be neglected. Fig. 2.5 shows the 2D FE results of the zero sequence induced voltages of a 96/slot-32/pole OW-PMSM with overlapping winding configuration (L_{Δ}≈0) with and without 5A *q*-axis current. It can be found that *q*-axis current imposes much less influence on the zero sequence induced voltage of the overlapping winding OW-PMSM.

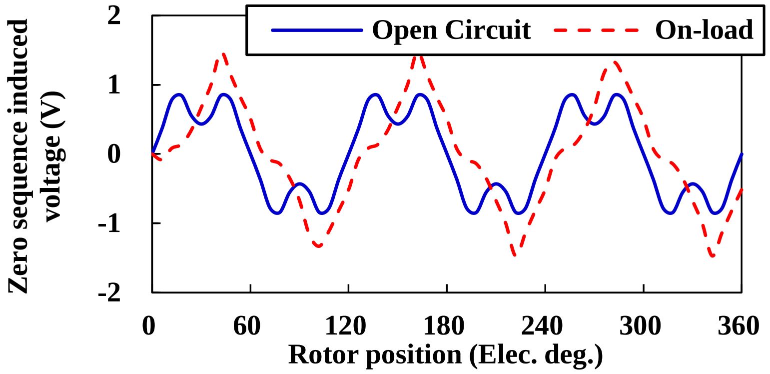

Fig. 2.4 Zero sequence induced voltage of the 12/slot-10/pole OW-PMSM at open circuit and on-load conditions (150rpm).

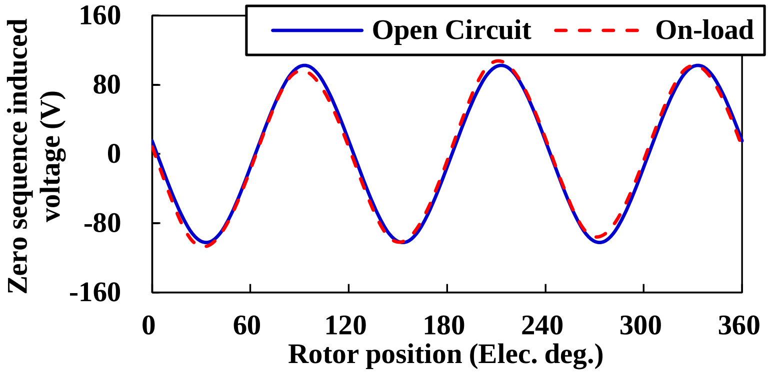

Fig. 2.5 Zero sequence induced voltage of the 96/slot-32/pole OW-PMSM at open circuit and on-load conditions (170rpm).

2.3 Zero Sequence Disturbances from Inverter Side

2.3.1 Equivalent Zero Sequence Modulation Voltage

In conventional space vector pulse width modulation (SVPWM) strategy, the equivalent zero sequence modulation signal is quasi-triangle wave, which induces no zero sequence current due to the open circuit characteristic of the equivalent zero sequence circuit. However, for the OW-PMSM with common DC bus, the existence of zero sequence circuit enables the equivalent zero sequence modulated voltage to induce corresponding circulating current. Hence, the phase shift based SVPWM [OLE05] is used to eliminate the relevant part of zero sequence disturbance voltage. The PWM strategy induced zero sequence disturbance voltage can be effectively eliminated via phase shift based SVPWM. However, the other zero sequence disturbance voltage sources are not eliminated effectively. Figs. 2.6 and 2.7 show the synthetic and separate modulation signals for each inverter with 120 °and 180 °shift when 40Hz and 0.5 p.u. reference is given. The 120 ° shift method shows no modulated zero sequence voltage as expected. Meanwhile, the 180 shift method shows typical quasi-triangle waveform in zero sequence.

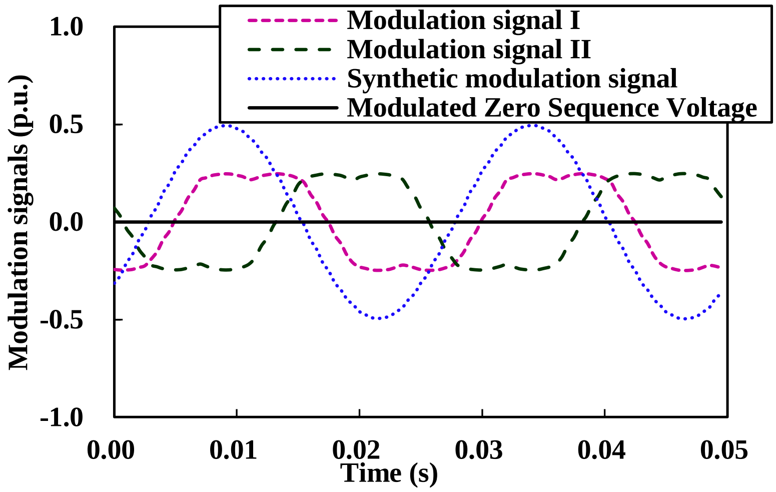

Fig. 2.6 Synthetic and separate modulation signals for each inverter with 120 °shift (40Hz, 0.5 p.u.).

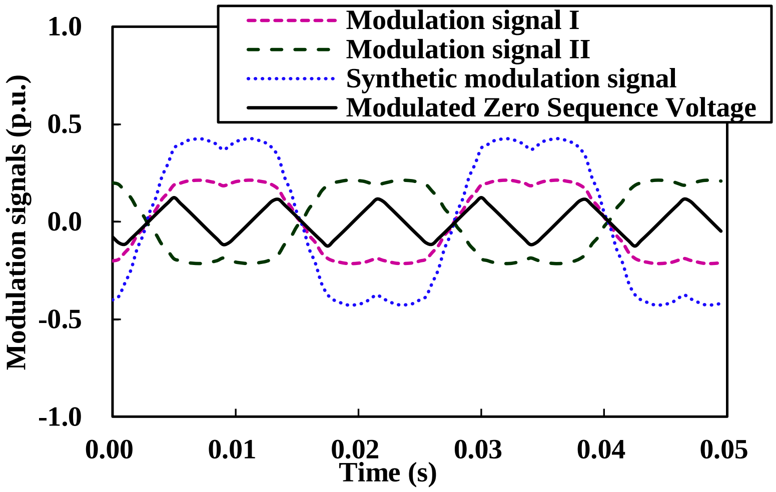

Fig. 2.7 Synthetic and separate modulation signals for each inverter with 180 °shift (40Hz, 0.5 p.u.).

2.3.2 Inverter Nonlinearity

The inverter nonlinearity characteristic of the OW-PMSM drive with common DC bus is different from conventional single three phase machine drives since the inherently contained 3rd, 9th … components in phase distortion voltage induced by inverter nonlinearity can only float the neutral point voltage of the Y connected single three phase machine. Whereas, those zero sequence components due to inverter nonlinearity will be superimposed on the equivalent zero sequence modulation voltage discussed in Section 2.3.1, as part of the zero sequence voltage disturbance from inverter side.

The inverter nonlinearity for OW drive is simply modelled via sign function in [SOM13] and the equivalent zero sequence disturbance voltage is approximately regarded as alternating square wave, in which the third harmonic is dominant. However, the precise model of inverter nonlinearity requires the description for parasitic effects during small current range, namely, near to zero current [GON10] [WAN14]. The inverter nonlinear distortion voltage at small current range exhibits resistive effect instead of saturation voltage drop since the parasitic capacitances. The influence of the corresponding effects on OW drives has not been reported yet. The modelling is established as follows.

Firstly, the phase distortion voltage error can be modelled as a nonlinear function [GON10] depending on phase current, viz.,

$$\Delta u_{err-x} = f(i_x) = 2\Delta U\left(\frac{1}{1+e^{-ki_x}} - \frac{1}{2}\right) \tag{2.19}$$

where $\Delta u_{err\text{-}x}$ represents arbitrary phase distortion voltage, i_x represents arbitrary phase current, k and ΔU are the distortion voltage model parameters describing the nonlinearity. Higher parasitic capacitance usually leads to lower k. The longer configured dead time and higher DC bus result in larger ΔU. The differential of (2.19) relative to phase current is usually defined as high frequency (HF) equivalent resistance [WAN14]. Fig. 2.8 shows the phase voltage error and HF equivalent resistance curves for arbitrary phase.

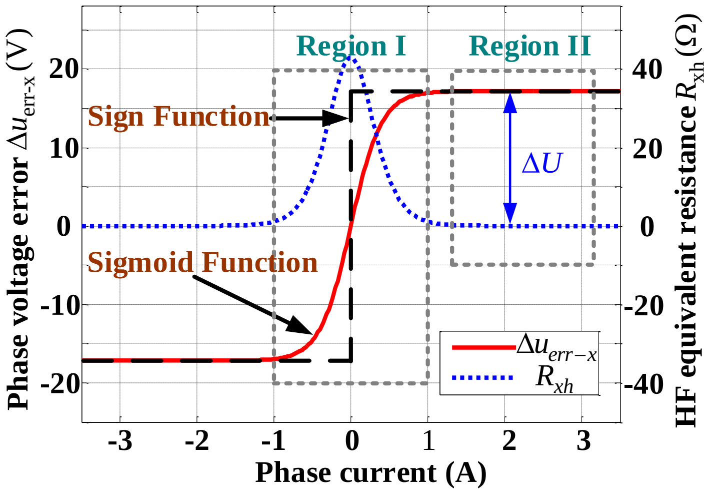

Fig. 2.8 Phase voltage error and HF equivalent resistance ($U_{dc} = 540\text{V}$, the dead time is 3.0μs) [WAN14].

The sigmoid type function provides more detail information than the conventional sign function to describe the small current signal characteristics in region I, which is shown in Fig. 2.8. Within region I, the inverter nonlinearity demonstrates resistive characteristics due to the parasitic effects of the switching device, instead of saturation voltage distortion. Hence, the inverter nonlinearity represents equivalent three phase resistance network in series with the machine for small current signals and almost no zero sequence disturbance voltage will be introduced under this condition. However, the zero sequence disturbance voltage becomes dominant when the phase current escapes from the small current region I.

The synthetic distortion voltage is

$$\begin{bmatrix} u_{d-dt} \\ u_{q-dt} \\ u_{0-dt} \end{bmatrix} = \frac{2}{3} \begin{bmatrix} \cos\theta & \cos(\theta - \frac{2\pi}{3}) & \cos(\theta + \frac{2\pi}{3}) \\ -\sin\theta & -\sin(\theta - \frac{2\pi}{3}) & -\sin(\theta + \frac{2\pi}{3}) \\ \frac{1}{2} & \frac{1}{2} & \frac{1}{2} \end{bmatrix} \begin{bmatrix} f(i_a) \\ f(i_b) \\ f(i_c) \end{bmatrix} \tag{2.20}$$

Specifically, the zero sequence disturbance voltage is

$$u_{0-dt} = \frac{f(i_a) + f(i_b) + f(i_c)}{3} \tag{2.21}$$

Fig. 2.9 shows the zero sequence distortion voltage and three phase distortion voltages when the three phase current amplitudes are 3A and 0.25A. It can be seen that the zero sequence distortion voltage demonstrates as third quasi-square wave when the phase current is beyond region I and the zero sequence distortion voltage is not dominant when the phase current is within region I. The model will be validated via experiment in Section 2.5 on three phase reactor load with phase shift SVPWM strategy to avoid influence from other zero sequence disturbance sources.

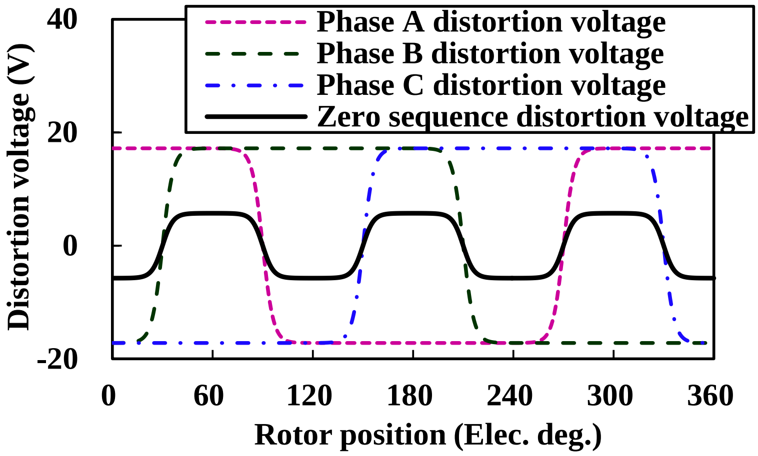

(a)

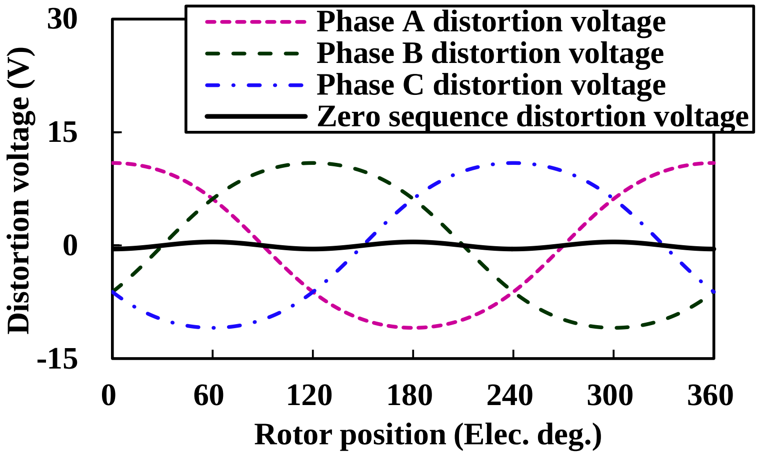

(b)

Fig. 2.9 Three phase and synthetic zero sequence distortion voltages beyond and within linear region. (a) Distortion voltages beyond linear region. (b) Distortion voltages within linear region.

2.4 Synthetic Disturbance Model

According to the analysis in Section II and III, the zero sequence disturbance could contain 4 possible disturbance sources. The zero sequence back EMF and cross coupling voltages in zero sequence exist in the machine side. The equivalent zero sequence modulation voltage and inverter nonlinearity are from inverter side. Of which, the zero sequence disturbance voltages from inverter nonlinearity and cross coupling in zero sequence perform as CCVSs.

Fig. 2.10 shows the synthetic disturbance model, namely, the equivalent zero sequence circuit considering all possible disturbance voltage sources where $g(i_a,i_b,i_c)=[f(i_a)+f(i_b)+f(i_c)]/3$, $g_d(i_d)=-6\omega i_d L_\Delta \sin 3\omega t$ and $g_q(i_q)=6\omega i_q L_\Delta \cos 3\omega t$ describing the characteristics of the CCVSs. u_0 represents the modulated zero sequence voltage depending on the modulation strategy and whether it is steerable or not. e_0 is the zero sequence back EMF which is mainly the third harmonic component. Hence, the synthetic zero sequence differential equation can be expressed as

$$\begin{aligned} u_0 &= u_{0-dt} + u_{0-id} + u_{0-iq} + e_0 + R_s i_0 + L_0 \frac{di_0}{dt} \\ &= \frac{f(i_a) + f(i_b) + f(i_c)}{3} - 6\omega i_d L_\Delta \sin 3\omega t + 6\omega i_q L_\Delta \cos 3\omega t + 3\omega \psi_{f0} \sin 3\omega t + R_s i_0 + L_0 \frac{di_0}{dt} \end{aligned} \tag{2.22}$$

where ψ_{f0} represents the zero sequence flux linkage.

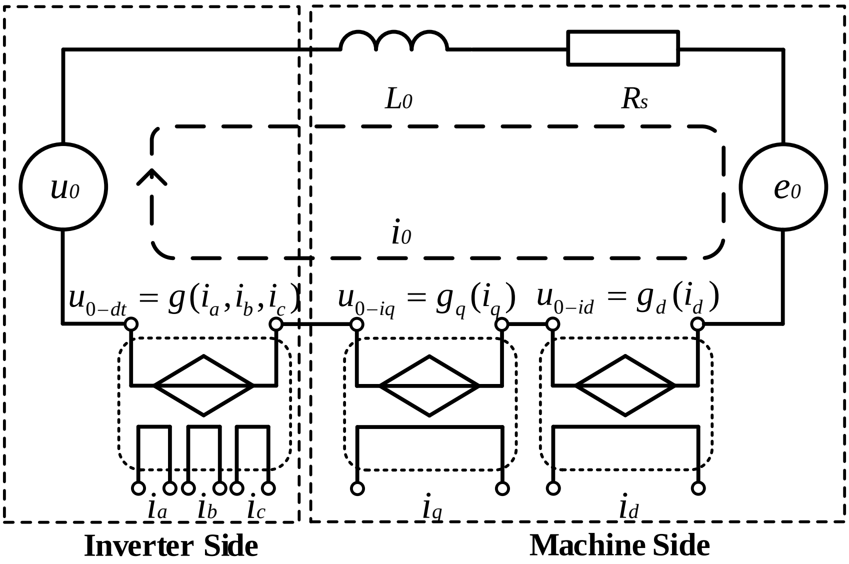

Fig. 2.10 Equivalent zero sequence circuit.

2.5 Experimental Validation

The experiment platform including the 12/slot-10/pole OW-PMSM, OW connected three phase reactor and 96/slot-32/pole OW-PMSM is shown in Fig. 2.11. The specifications of the two OW-PMSMs are shown in Table 2.1. The 12/slot-10/pole OW-PMSM is used to validate the cross coupling voltages in zero sequence with zero sequence voltage measurable structure, which is shown in Fig. 2.12 (a). The OW connected three phase reactor shown in Fig. 2.12 (b) is used to verify the inverter nonlinearity effect. The suppression strategy is validated on a 3kW 96/slot-32/pole OW-PMSM platform based on dSPACE, which is shown in Fig. 2.11 (c). The switching frequency as well as the system interrupt frequency is 5kHz. The switching dead-time is set as 2μs.

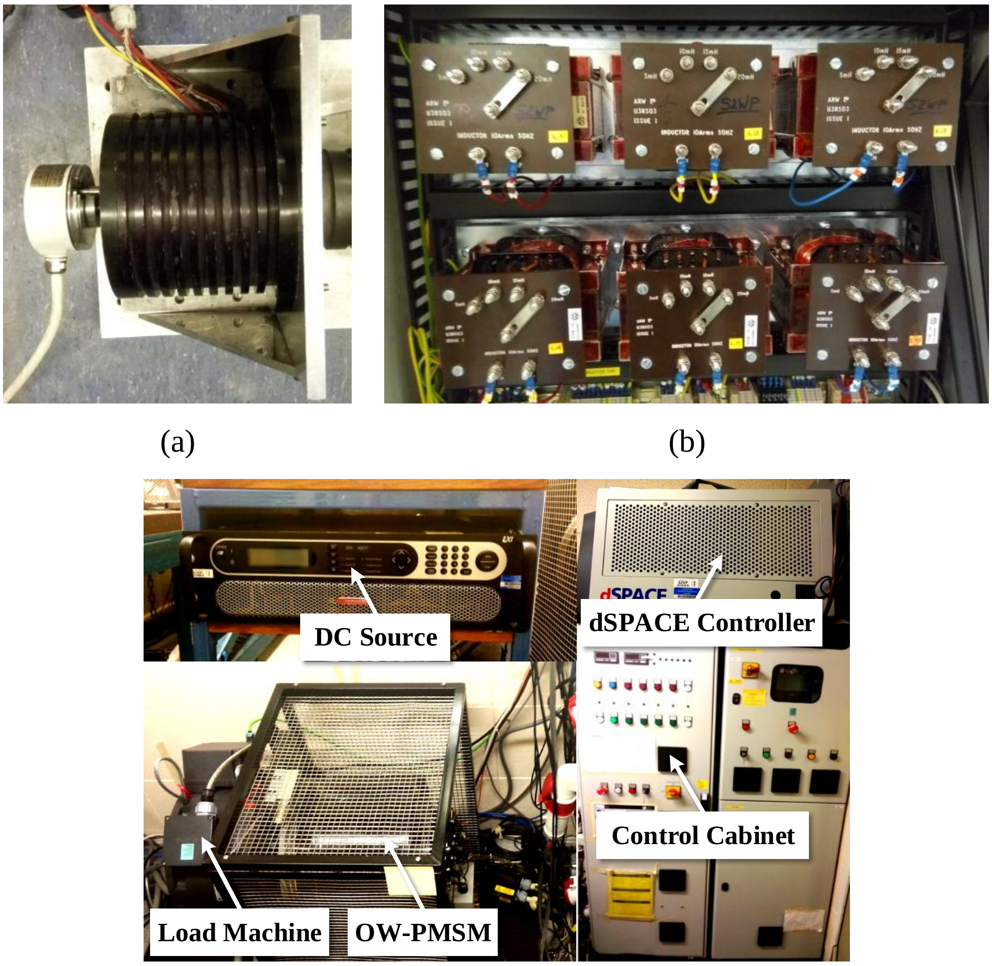

(a) (b)

(c)

Fig. 2.11 Experiment platform pictures. (a) 12/slot-10/pole OW-PMSM. (b) OW connected three phase reactor. (c) 96/slot-32/pole OW-PMSM drives.

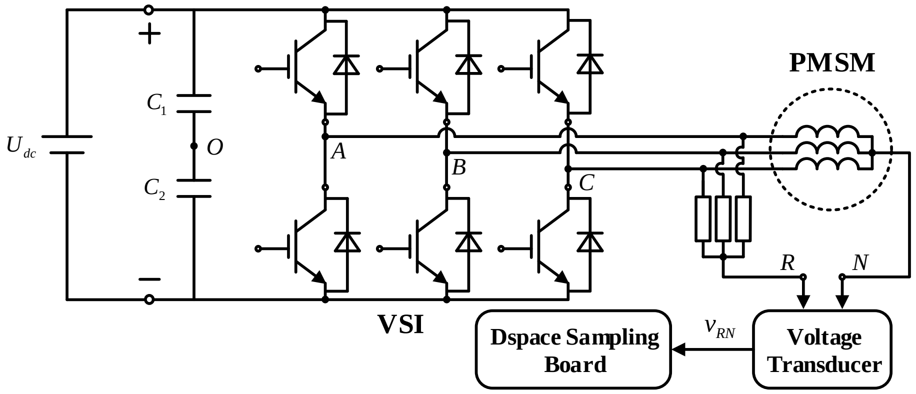

(a)

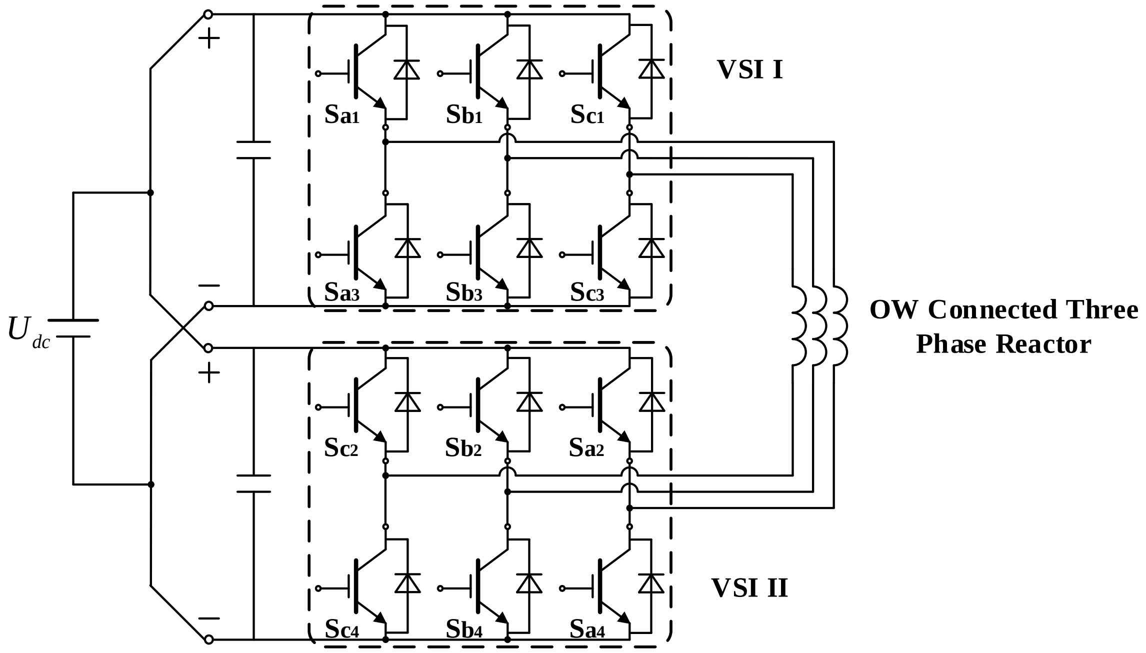

(b)

Fig. 2.12 System configuration of the induced zero sequence voltage measurable PMSM drive and test configuration of the OW connected three phase reactors. (a) Induced zero sequence voltage measurable PMSM drive. (b) Test configuration of the OW connected three phase reactors.

Table 2.1 Specification of Two prototype OW-PMSMs

Parameter	OW-PMSM I	OW-PMSMS II
Pole number	10	32
Slot number	12	96
Stack length	50 mm	110 mm
Airgap length	1 mm	2 mm
Slot opening	2 mm	5.58 mm
Stator bore radius	28.5 mm	N/A
Stator outer radius	N/A	195.2 mm
Magnet thickness	3 mm	4.5 mm
Magnet remanence	1.2 T	1.2 T
Magnet conductivity	$6.67\times10^{5}\ (\Omega\text{m})^{-1}$	$6.67\times10^{5}\ (\Omega\text{m})^{-1}$
Series turns per phase	132	832
Tooth tip width	12.92 mm	7.19 mm
Pole-pitch	17.91 mm	37.62 mm
Rated torque	3.85Nm	95Nm

Rated current	7A	2.83A
Rated speed	400rpm	80rpm
Rated frequency	33.33Hz	21.33Hz

As for the machine side, Fig. 2.1 has shown the measured phase back EMF and spectrum analysis. Hence, the zero sequence back EMF has been experimentally validated. Meanwhile, Fig. 2.12 (a) shows the zero sequence induced voltage measurable PMSM drive which is used to investigate the zero sequence voltage induced by armature winding currents, namely, the cross coupling voltages in zero sequence. The conventional single VSI topology has the open circuit characteristic of the equivalent zero sequence circuit. Hence, the measured voltage is just the synthesis of zero sequence back EMF and the cross coupling voltages in zero sequence from the machine side. Fig. 2.13 shows the measured voltage and electrical position signal at open circuit and on-load (i_q=3.62A) conditions, respectively. The distortion phenomena is in according with the analysis model and FE result which is shown in Fig. 2.4. The variation trend of the third harmonic voltages for the FE and measured results are identical, which are 31.7% and 26.5%, respectively.

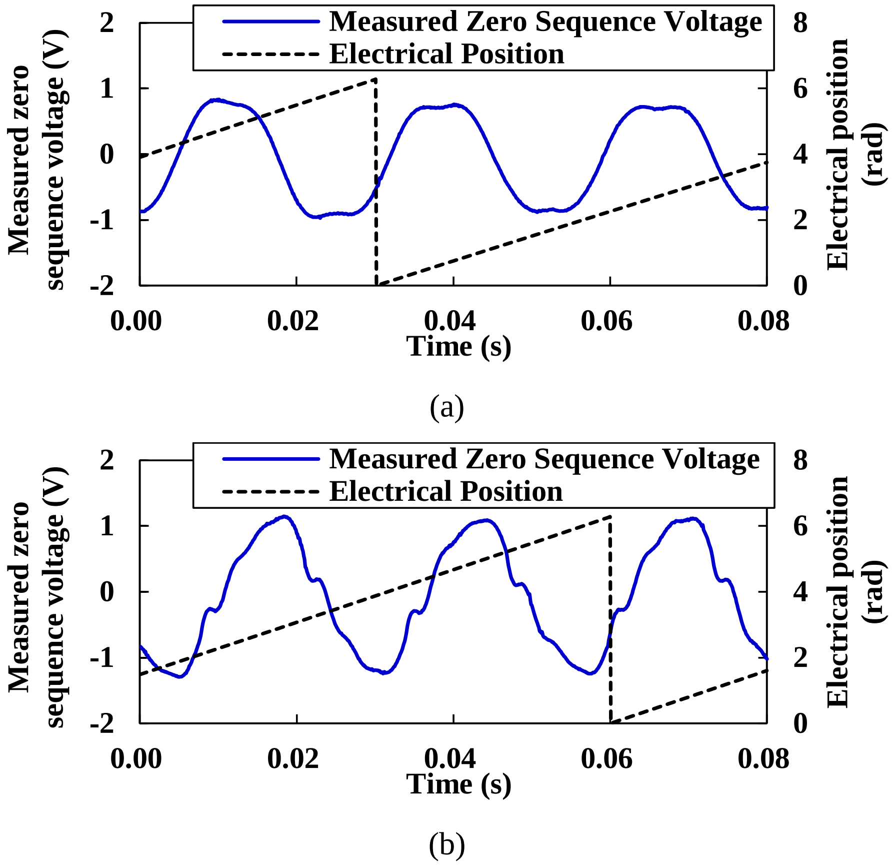

Fig. 2.13 Measured zero sequence voltages and electrical position signals at open circuit and on-load conditions. (a) i_q=0. (b) i_q=3.62A.

With regard to the inverter side, Fig. 2.14 shows the zero sequence and phase A current waveforms of the OW connected three phase reactor under small and large current conditions when 120 ° shift SVPWM method is applied. Before the saturation point of the reactor, the zero sequence back EMF, the modulated zero sequence voltage and the cross coupling voltages in zero sequence can be neglected. Only the inverter nonlinearity exerts an effect on the equivalent zero sequence circuit. When the phase current is in the linear region, the phase current is sinusoidal and no distinct zero sequence current emerges, which can be seen in Fig. 2.14 (a). However, the third harmonic zero sequence current emerges when the phase current is beyond linear region which is shown in Fig. 2.14 (b). The experiment results confirm the analysis model for inverter nonlinearity considering parasitic effects.

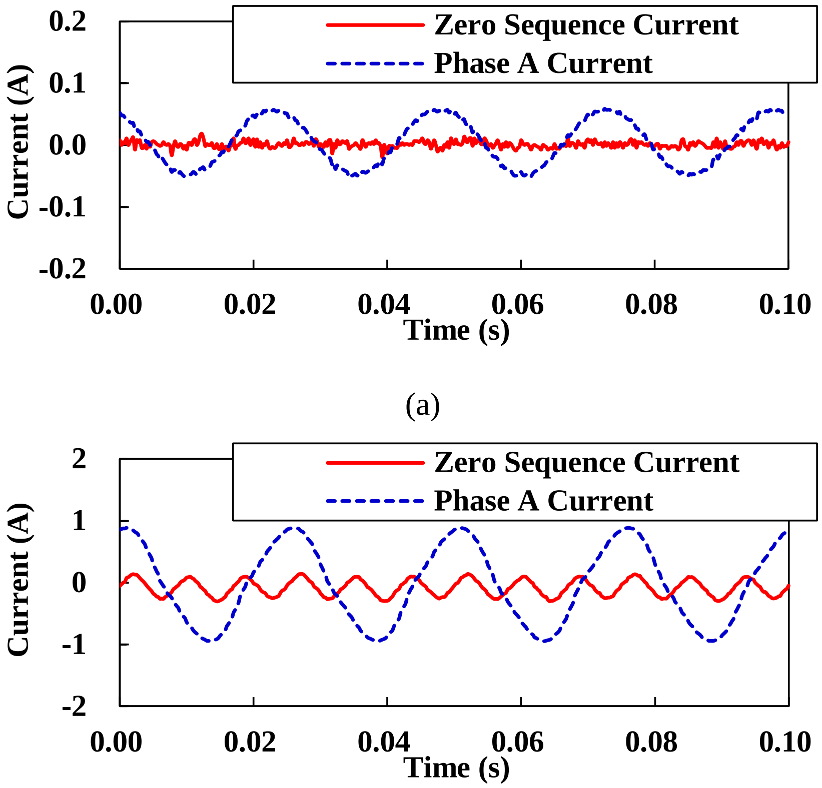

(a)

(b)

Fig. 2.14 Zero sequence and phase A currents of the OW connected three phase reactor under small and large current conditions. (a) Small current. (b) Large current.

Moreover, Figs. 2.15 and 2.16 show the phase currents and spectrum analysis of the OW connected three phase reactor at small current condition (eliminate the influence of inverter nonlinearity [23]) when different shift angles are applied. The fundamental reference voltage is given in the low level to maintain the phase current within the small current region deliberately. Under this condition, the zero sequence back EMF, cross coupling voltages in zero sequence and inverter nonlinearity can be neglected. Hence, as confirmed by this experiment results, the 120° shift modulation method having quasi triangular zero sequence voltages fully counteracted can exhibit lowest zero sequence current. As for the conventional SVPWM, the third harmonic voltage accounts for 16.7% of the fundamental voltage, which is dominant and hard to be neglected.

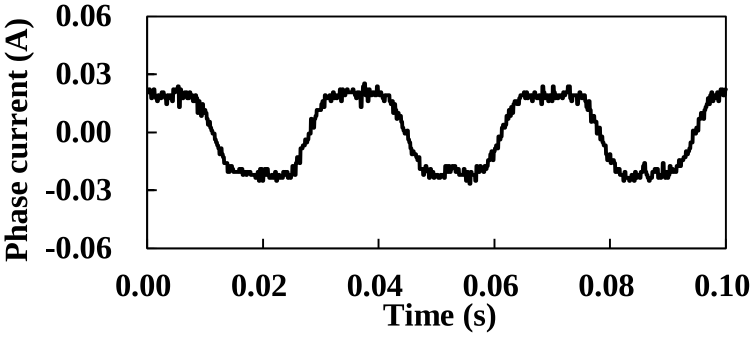

(a)

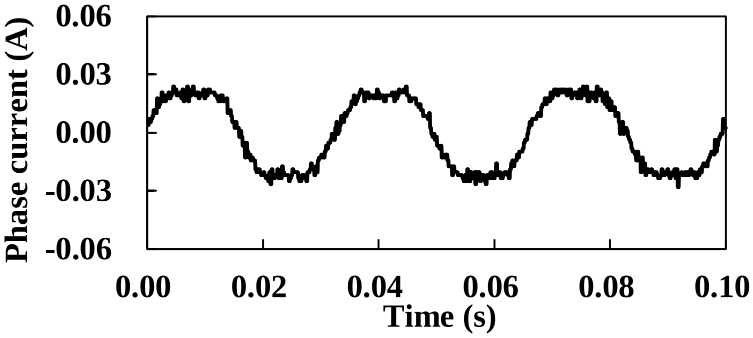

(b)

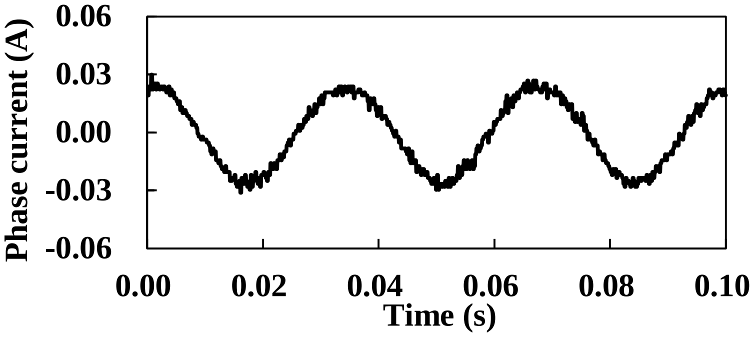

(c)

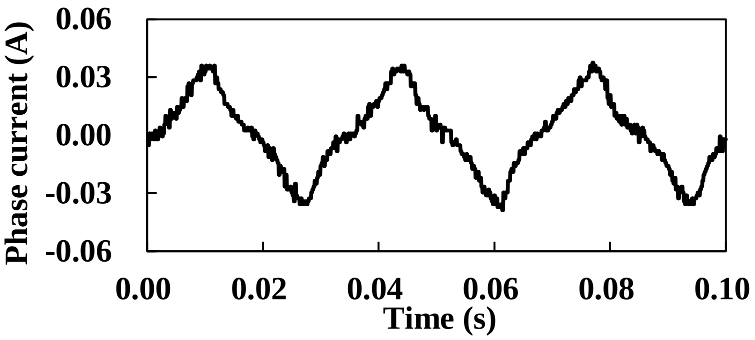

(d)

Fig. 2.15 Phase current waveforms of the OW connected three phase reactor with different phase shift modulation. (a) 180 °shifted. (b) 150 °shifted. (c) 120 °shifted. (d) 90 °shifted.

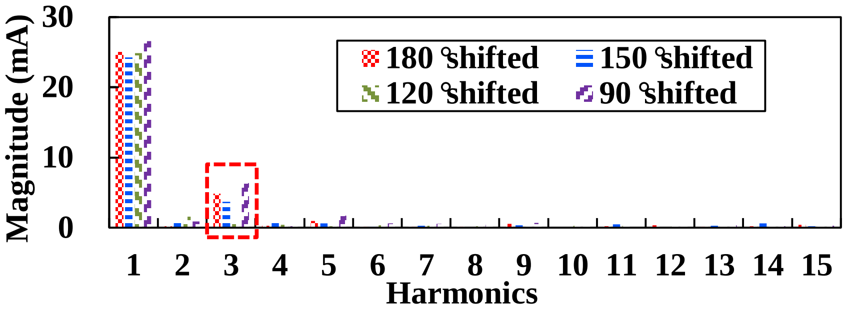

Fig. 2.16 Spectrum analysis of the OW connected three phase reactor with different phase shift modulation.

2.6 Conclusion

This chapter has proposed a systematic analysis model for the zero sequence circulating current of the OW-PMSM drive with common DC bus. It is found that the zero sequence back EMF, the cross coupling voltages in zero sequence, from the machine side, PWM strategy modulated zero sequence voltage and inverter nonlinearity, from the inverter side, all contribute to the formation of zero sequence voltage disturbance. The influence of the cross coupling voltages in zero sequence mainly depend on the winding configurations. The inverter nonlinearity exhibits resistive characteristic in small current condition because of the parasitic effects of the switching device, which induces almost no zero sequence disturbance voltage. But it is dominant when the phase currents are beyond the small current region. Experiment results have confirmed the analysis.

CHAPTER 3 ZERO SEQUENCE CIRCULATING CURRENT SUPPRESSION STRATEGIES

Based on the analysis of zero sequence disturbances in chapter 2, the suppression strategies can be developed. Therefore, in this chapter, two suppression strategies are proposed and validated. The first one is a zero sequence model based method and the second one is a non-model based method.
This chapter was published in IEMDC 2017 and IEEE Transactions on Industry Applications.

3.1 Introduction

Permanent magnet synchronous machine (PMSM) is becoming popular nowadays due to its high torque and efficiency performances. It is commonly used in many automatic applications such as servo system, electric vehicle, wind power generation and home appliance [LIU12] [CHA96] [HAQ10] [ZHAO17]. Meanwhile, the open winding (OW)-PMSM (OW-PMSM) as a specific type of PMSMs is also arising the attentions [JAH80]-[ZHO15]. The OW-PMSM drive system can provide higher DC bus voltage utilization ratio, which can consequently reduce the requirement of the withstand voltage for the switching devices or deliver more power [WEL04]. Also, it is capable of fault tolerant operation and flexible and independent current control characteristics [JAH80] [WEL04] [SAN13].

The OW-PMSM drive can be generally classified as the common DC bus and isolated DC bus types. The isolated DC bus one requires dual isolated DC sources. It can provide higher DC bus utilization ratio when compared to the single three phase PMSM drive system. While the common DC bus one only requires single DC source which can decrease the size of the drive. However, the common DC bus one naturally contains the zero sequence path which could produce the associated zero sequence circulating current [SOM13]. As identified in [ZHA17], the disturbance sources for zero sequence current include the zero sequence back EMF, cross-coupling voltages, zero sequence modulated voltage and the inverter nonlinearity. The additional zero sequence current can distort the phase currents, increase the system losses and possibly introduce torque ripples. In order to tackle this issue, several approaches have been proposed [SOM02]-[ZHO15].

The additional switching device or the common mode voltage filter might be chosen to suppress the zero sequence current. The four additional auxiliary bidirectional switches are used in [SOM02] and [SOM04] to modulate the equivalent neutral point voltage and suppress the circulating current with a higher DC bus utilization ratio. The bypass circuit constructed with resistance and capacitances having low impedance is proposed in [KAL14] to avoid the circulating current flow into the OW machine. As for the neutral point connected power converter system which also has the equivalent zero sequence path as the OW-PMSM with common DC bus, the integrated AC choke can be used for reducing the circulating current [ZHU12]. The additional switching devices or passive choke can be effective to suppress the circulating current while the increase of the system cost as well as the volume is also inevitable.

Despite of the zero sequence back EMF, cross coupling voltages and inverter nonlinearity, the improved PWM strategies for OW machines have the capability of eliminating or reducing the modulated zero sequence voltage from the inverter side and can further reduce the zero sequence current. The associated techniques are commonly used for OW-induction machine (IM) (OW-IM) since it has negligible zero sequence back EMF. The decoupled space-vector-based PWM strategy for OW-IM is proposed in [SOM08] by forcing the zero sequence voltage to zero for each inverter. An improved SVPWM strategy capable of common mode voltage (CMV) elimination is presented in [BOD14] and two switching sequences are further investigated. Also, a phase shift based PWM strategy for OW-IM is reported in [SOM02a] and [OLE05] which is still suitable for OW-IM.

Moreover, the zero sequence controller is also another approach for suppressing zero sequence circulating current. The proportional integral (PI) controller is fundamentally used for this purpose [AN16], [ZHAN17a]. Since the zero sequence disturbance is AC signal, the PI controller cannot ensure zero static error. Hence, the PI controller combined with zero sequence back EMF feedforward is also used [HWA14], [SAN14]. However, the precise zero sequence back EMF information is necessary for the feedforward solutions, which is not quite favourable. Therefore, the proportional resonant (PR) [ZHAN17] or quasi PR controller [ZHO15] is adopted to achieve the zero static error for the suppression of zero sequence circulating current. While the current approaches are effective to suppress the zero sequence circulating current, the parameter design of the zero sequence controller is still based on the parameters of the equivalent zero sequence circuit, which includes the zero sequence inductance, phase resistance and/or zero sequence back EMF. Namely, the suppression strategies are model based method.

In this chapter, a frequency adaptive proportional resonant (FA-PR) controller is firstly proposed and investigated, based on the zero sequence controller framework. Together with applying the phase shift based SVPWM method, the proposed model based method can obtain better higher order harmonic current suppression capability. Then, in order to overcome the drawbacks in the model based method, in this chapter, a non-model based suppression method is also proposed by using the extremum seeking (ES) algorithm together with the adjustable SVPWM strategy for OW-PMSM. The proposed method can achieve the optimal shift angle for the adjustable SVPWM automatically via the small perturbation searching scheme. The integrated PWM strategy becomes adaptive SVPWM strategy for suppressing the zero sequence circulating current. No parameters of the equivalent zero sequence circuit are required. Hence, the second proposed method is more general for different OW-PMSMs having various equivalent zero sequence parameters. This chapter is organized as follows: In Section 3.2, the FA-PR controller based method is presented with experimental validation. In Section 3.3, the proposed adaptive SVPWM strategy is also presented with experimental validation. The conclusion is drawn in Section 3.4.

3.2 Frequency Adaptive Proportional Resonant (FA-PR) Controller Based Suppression Strategy

3.2.1 Principle of FA-PR Controller Based Suppression Strategy

On the basis of Chapter 2, it can be seen that only u_0 is steerable and the other 3 sources might vary within the whole operation range of the OW-PMSM. The alternating zero sequence circulating current is mainly induced by the third harmonic disturbance whose frequency, phase and amplitude are motor operation frequency and armature winding current dependent. Hence, the corresponding suppression strategy shown in Fig. 3.1 is proposed to attenuate the zero sequence circulating current.

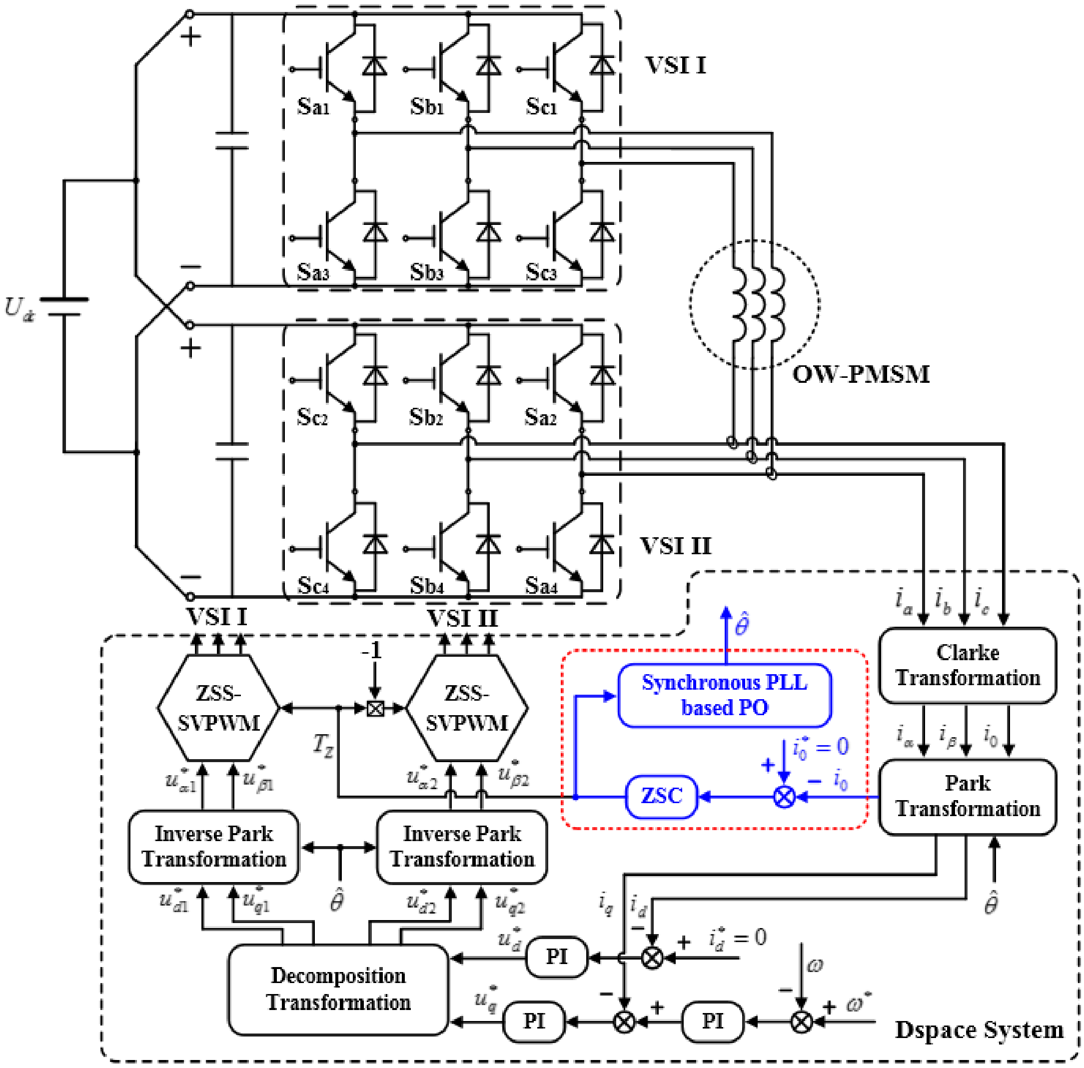

Fig. 3.1 Suppression strategy of the OW-PMSM for zero sequence circulating current attenuation using FA-PR controller.

Of which, the zero sequence steerable space vector pulse width modulation (ZSS-SVPWM) is developed to provide a controllable zero sequence component. The flow chart of the ZSS-SVPWM strategy is shown in Fig. 3.2. The zero sequence component is no longer essentially generated by the SVPWM but superimposed by the zero sequence controller output. Hence, the over modulation process should be redesigned by considering the influence from the additional zero sequence component, which is also shown in Fig. 3.2.

The zero vector time can be reconstructed as

$$T_0 = T_s - T_X - T_Y - T_z. \tag{3.1}$$

where T_0 is the zero vector time, T_s is the switching period, T_X and T_Y are the fractions of the total T_s. Meanwhile, the output of the zero sequence voltage is linear with the zero vector time so the controller can be easily used.

If the over modulation is reached, the T_X, T_Y and T_Z can be scaled down as

$$\gamma = T_s / (T_X + T_Y + T_Z) \tag{3.2}$$

$$T_X' = \gamma T_X ; T_Y' = \gamma T_Y ; T_Z' = \gamma T_Z . \tag{3.3}$$

where T_X', T_Y' and T_Z' are the scaled fractions of the total T_s and the scaled zero sequence control signal duration time, respectively. The other parts of the ZSS-SVPWM are identical to the conventional SVPWM.

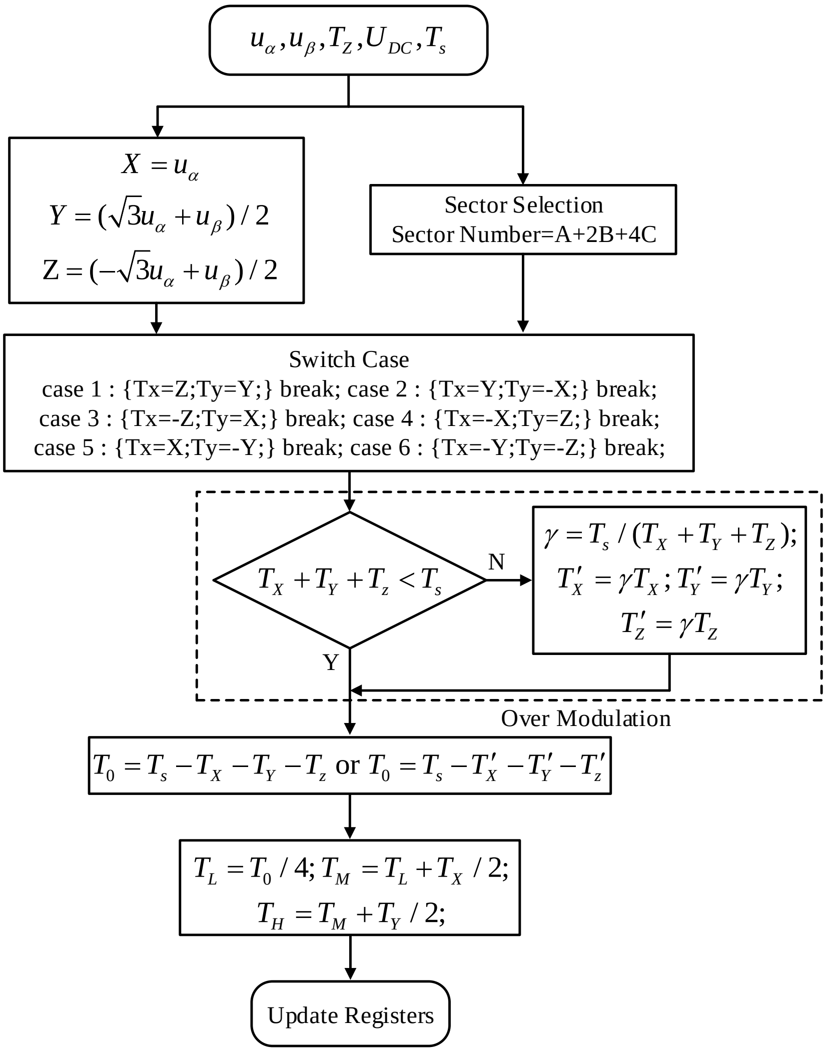

Fig. 3.2 Flow chart of the ZSS-SVPWM strategy.

In addition, the quasi-triangle wave generated by the SVPWM is also one the of the zero sequence disturbance sources, and therefore, the relevant disturbance burden will be imposed on the zero sequence controller. In order to reduce the controller burden, the phase shift based method is combined to eliminate the disturbance due to modulation strategy, which is achieved by decomposition transformation, viz.,

$$\begin{bmatrix} u_{d1} \\ u_{q1} \\ u_{d2} \\ u_{q2} \end{bmatrix} = \frac{1}{2} \cdot \begin{bmatrix} 1 & \tan(\pi/6) \\ -\tan(\pi/6) & 1 \\ -1 & \tan(\pi/6) \\ -\tan(\pi/6) & -1 \end{bmatrix} \cdot \begin{bmatrix} u_d \\ u_q \end{bmatrix}. \tag{3.4}$$

The actual d- and q-axis voltage reference signals can be decomposed into two sub-coordinates, d_1q_1 and d_2q_2, which are synchronized with the dq-coordinate but having π/6 and 5π/6 shifted angle versus the dq-coordinate. Meanwhile, these two sub-coordinates are $2\pi/3$ shifted from each other. The relationship is shown in Fig. 3.3.

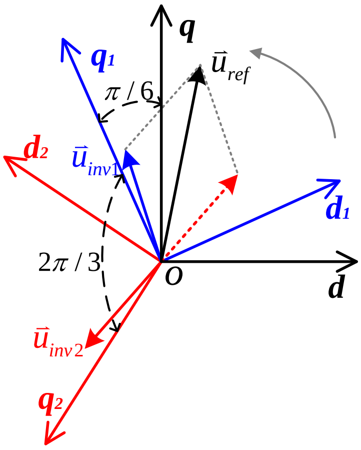

Fig. 3.3 Synthetic voltage vector of the two sets of the inverters.

The quasi-triangle waves in zero sequence generated by both SVPWM modules can be consequently counteracted due to the phase shift. The phase shift is achieved by reconstructing the voltage references signal instead of modifying the SVPWM modules.

Since the operation frequency of the OW-PMSM varies according to conditions, the frequency of the zero circulating current will also change with it. The zero sequence current controller should be adaptive to the frequency variation. Hence, the FA-PR controller is adopted, which is shown in Fig. 3.4.

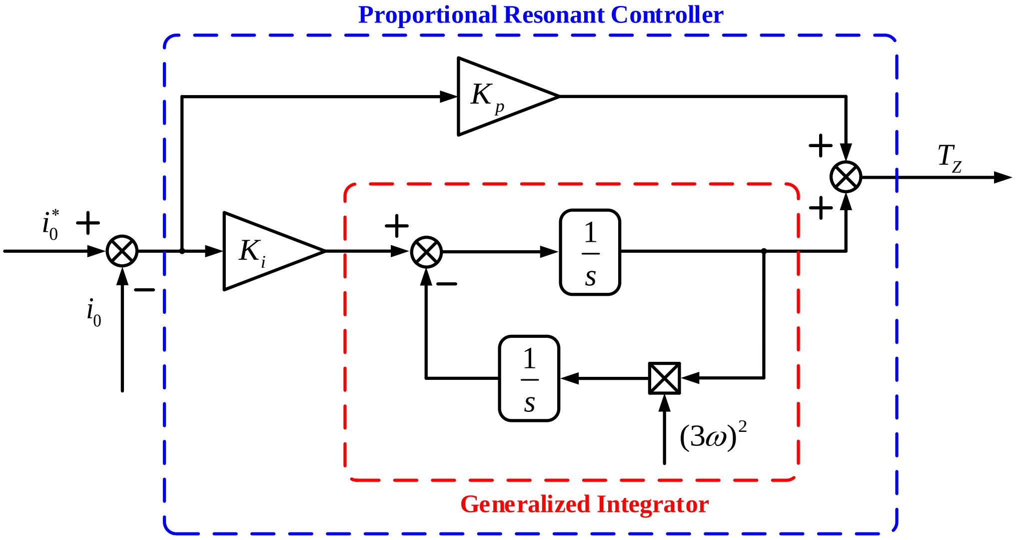

Fig. 3.4 Block diagram of the FA-PR controller.

The transfer function of the FA-PR is

$$C(s) = K_p + \frac{K_i s}{s^2 + (3\omega)^2} \tag{3.5}$$

where K_p is the proportional coefficient, K_i is the resonant coefficient and 3ω is the resonant frequency.

When compared to conventional PI controller, the integrator is replaced by the generalized integrator. The input speed feedback is used to determine the resonant frequency of the FA-PR controller. As shown in Fig. 3.5, the FA-PR controller has highest gain at the selected resonant frequency, viz., 3ω. Hence, the third harmonic disturbance can be responded by the FA-PR controller. The static error of PI controller for alternating signal can be avoided when the FA-PR controller is used. Meanwhile, this controller can also adapt to variable speed condition.

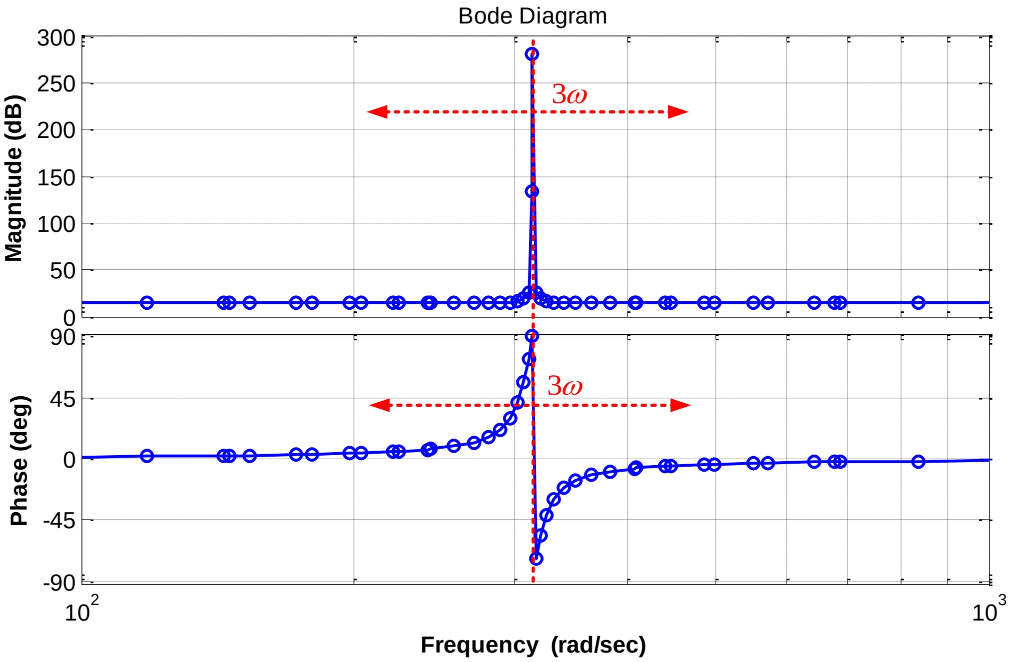

Fig. 3.5 Bode diagram of the FA-PR controller.

Meanwhile, for the conventional SVPWM without shifting or reference signal reconstructing, the equivalent zero sequence voltage spectrum is shown in Fig. 3.6. Even with the FA-PR controller, the higher order harmonics including ninth, fifteenth…cannot be eliminated accordingly. Hence, the shifting based ZSS-SVPWM can further reduce the influence from these voltage components when compared to the conventional methods.

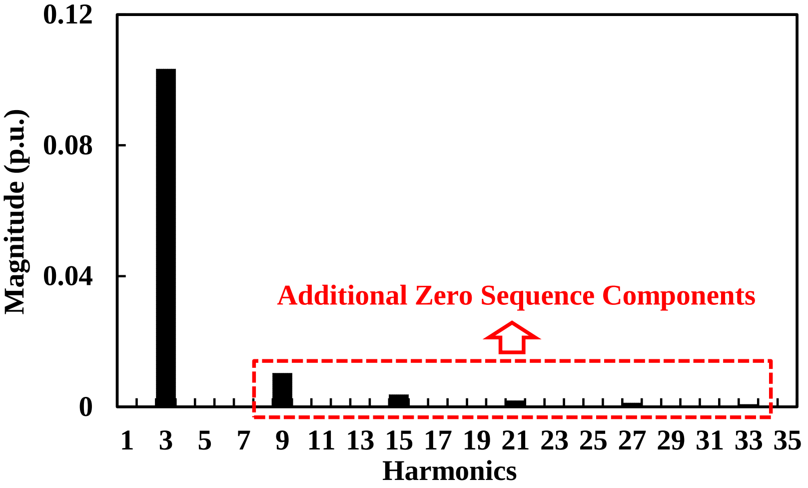

Fig. 3.6 Spectrum analysis of the zero sequence modulated voltage for 180 °shifted SVPWM.

3.2.2 Experimental Validation of FA-PR Controller Based Suppression Strategy

In order to validate the effectiveness of the suppression strategy, Fig. 3.7 (a) shows the phase A and zero sequence currents when controller is enabled at 5s. Figs. 3.7 (b) and (c) are the corresponding zoomed regions A and B in Fig. 3.7 (a). It can be seen that the zero sequence circulating current induced by multi sources is suppressed.

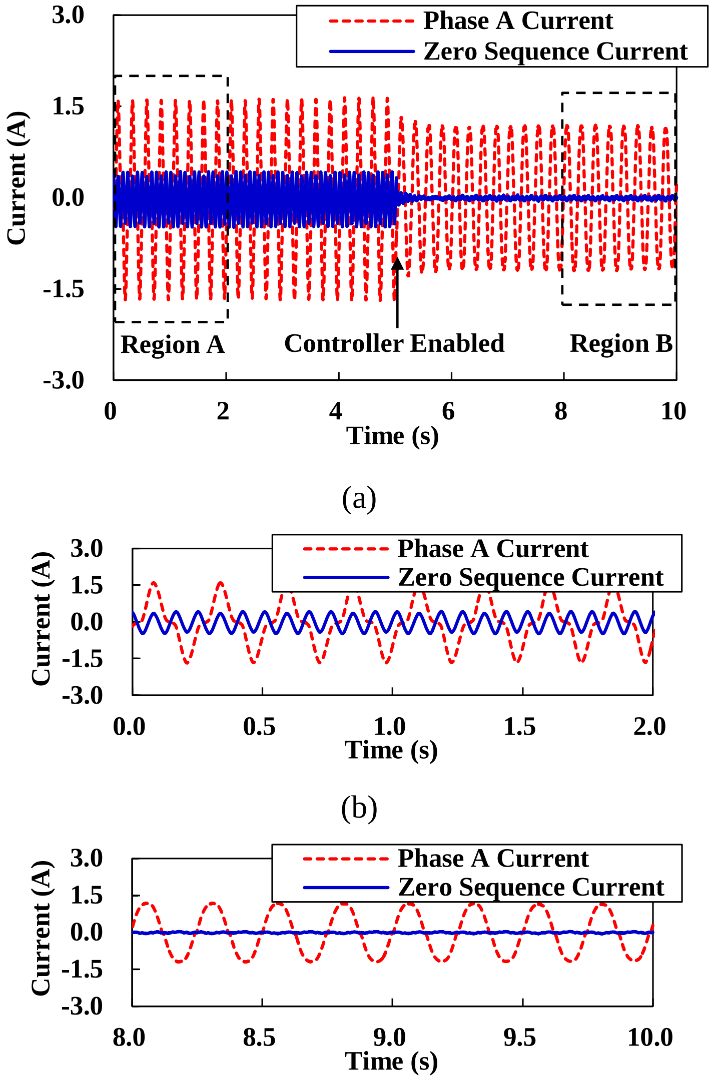

(a)

(b)

(c)

Fig. 3.7 Experiment results of the zero sequence circulating current suppression strategy. (a) Transient phase A and zero sequence current waveforms before and after controller enabled. (b) Before controller enabled. (c) After controller enabled.

To verify the effects on higher order harmonics elimination, the suppression performance comparison is shown in Fig. 3.8 with and without the phase shifted method. It can be seen that before the shift enabled, even with FA-PR controller, the ninth and the higher order harmonics cannot be suppressed, as shown in Fig. 3.8 (b). It can be found in Fig. 3.8 (c) that the ripple in the zero sequence circulating current is much lower. For these two scenarios, the parameters for the FA-PR controller are the same.

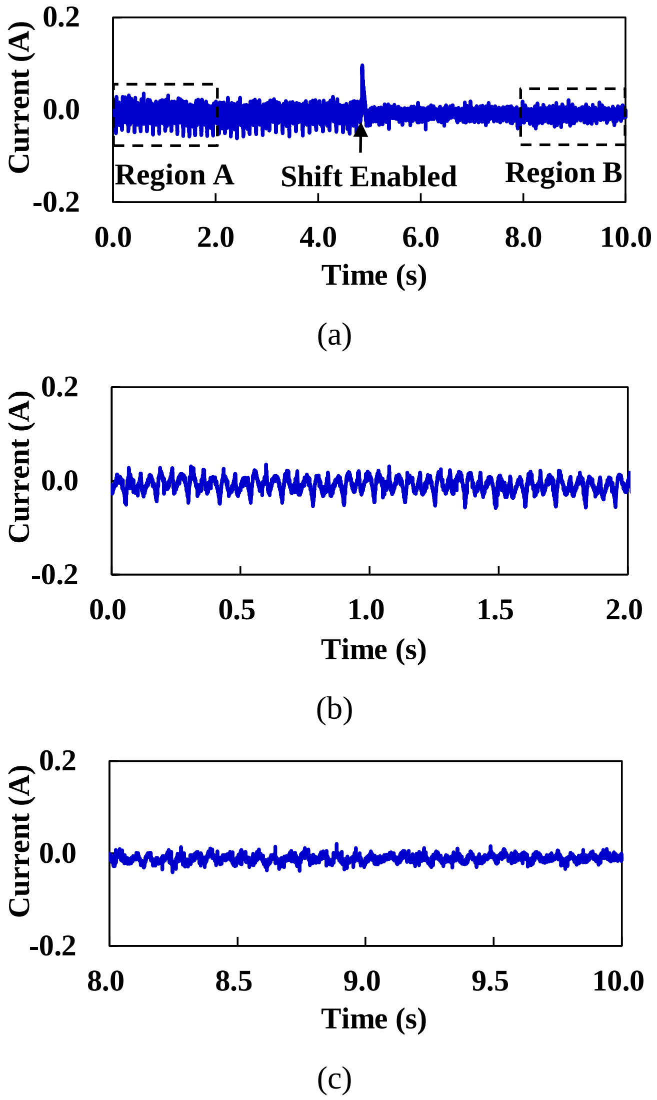

(a)

(b)

(c)

Fig. 3.8 Suppression performances with and without the phase shift method. (a) Before and after shift enabled. (b) Before shift enabled. (c) After shift enabled.

Figs. 3.9 and 3.10 show the transient step speed and step load tests, respectively. The low frequency envelope curve occurring in the phase, *d*- and *q*-axis currents are due to the mechanical eccentricity which is operating frequency dependent. It can be seen that the ripples in the zero sequence currents slightly increase after the step speed and step load conditions. The suppression effect is still guaranteed.

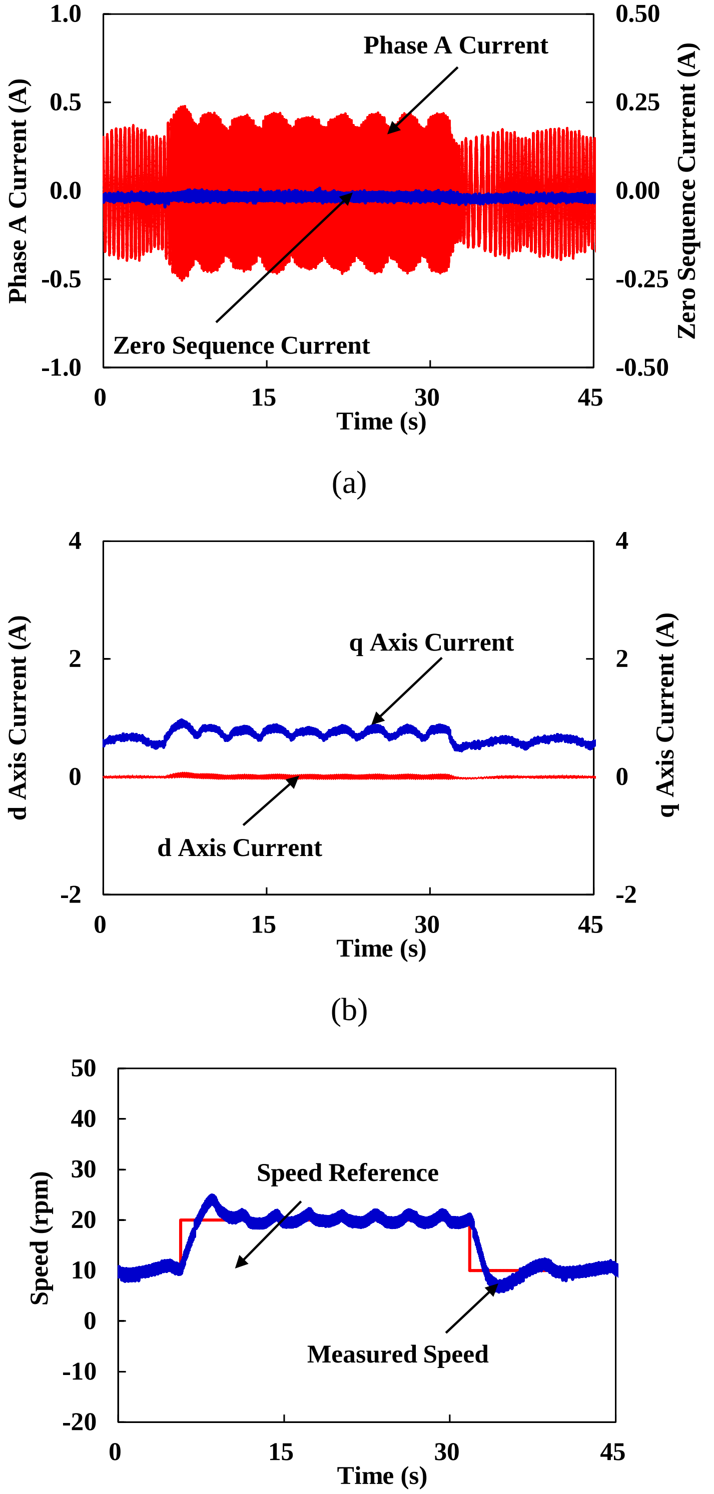

(a)

(b)

(c)

Fig. 3.9 Transient step speed performance. (a) Phase A current and zero sequence current. (b) *d*- and *q*-axis currents. (c) Speed reference and the measured speed.

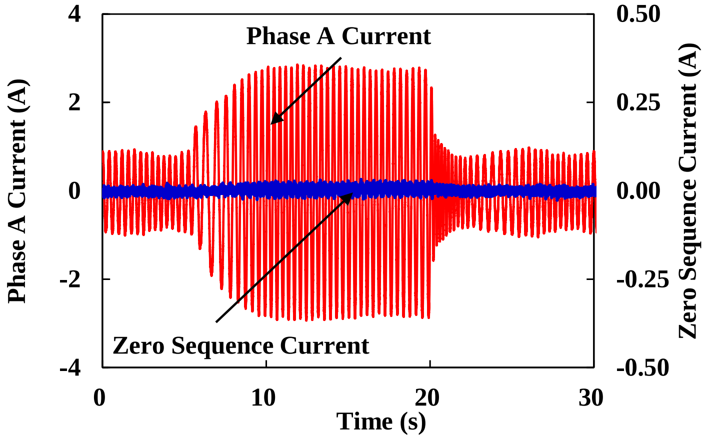

(a)

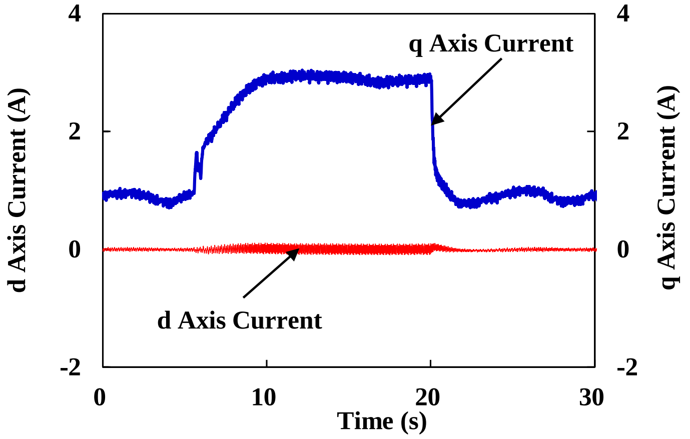

(b)

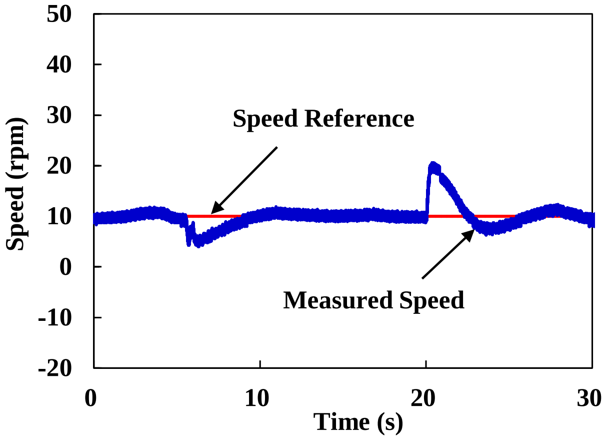

(c)

Fig. 3.10 Transient step load performance. (a) Phase A current and zero sequence current. (b) *d*- and *q*-axis currents. (c) Speed reference and the measured speed.

3.3 Adaptive SVPWM Strategy Based Suppression Strategy

3.3.1 Shiftable Zero Sequence Voltage

The most commonly used SVPWM strategy is the symmetrical PWM (SYPWM) equally distributing zero sequence vector time to turn-on time T_0 and T_7 of the two different zero vector, viz.

$$T_0 = T_7 = \frac{1}{2}(T_s - T_i - T_j) \tag{3.6}$$

where T_s is the switching period, T_i and T_j (i, j=1, 2, … , 6) are the turn-on times of the two selected nearest active vectors used to construct the reference vector.

As for OW topology, the conventional SVPWM is realized as shown in Fig. 3.11 and the two independent SVPWM modules are identical to the conventional single three-phase SVPWM module. However, the zero sequence modulated voltage in this method is uncontrollable and modulated inherently, which will impose the influence on zero sequence current. Generalized expressions of the zero sequence modulated voltages $v_{0\text{-}k}$ (k = 1 or 2) for the two sets of VSIs are listed in Table 3.1. T_{nk} (n = 0, 1, … , 7) is the turn-on time for each vector V_{nk} where V_{0k} and V_{7k} are zero vectors. According to either reference vector for the two SVPWM modules, the synthetic zero sequence voltage $v_{0\text{-}m} = v_{0\text{-}1} - v_{0\text{-}2}$ is determined.

TABLE 3.1 COMPARISON OF MAXIMUM OUTPUT PHASE VOLTAGE

Sector I $(0 \le \varphi_k \le \frac{\pi}{3})$	Sector II $(\frac{\pi}{3} \le \varphi_k \le \frac{2\pi}{3})$
$v_{0-k} = (-\frac{T_{0k}}{T_s} - \frac{1}{3}\frac{T_{1k}}{T_s} + \frac{1}{3}\frac{T_{2k}}{T_s} + \frac{T_{7k}}{T_s})$ $T_{1k} = \frac{\sqrt{3}}{2} mT_s \cos(\varphi_k + \frac{\pi}{6})$ $T_{2k} = \frac{\sqrt{3}}{2} mT_s \cos(\varphi_k + \frac{3\pi}{2})$	$v_{0-k} = (-\frac{T_{0k}}{T_s} + \frac{1}{3}\frac{T_{2k}}{T_s} - \frac{1}{3}\frac{T_{3k}}{T_s} + \frac{T_{7k}}{T_s})$ $T_{2k} = \frac{\sqrt{3}}{2} mT_s \cos(\varphi_k + \frac{11\pi}{6})$ $T_{3k} = \frac{\sqrt{3}}{2} mT_s \cos(\varphi_k + \frac{7\pi}{6})$
Sector III $(\frac{2\pi}{3} \le \varphi_k \le \pi)$	Sector IV $(\pi \le \varphi_k \le \frac{4\pi}{3})$
$v_{0-k} = (-\frac{T_{0k}}{T_s} - \frac{1}{3}\frac{T_{3k}}{T_s} + \frac{1}{3}\frac{T_{4k}}{T_s} + \frac{T_{7k}}{T_s})$ $T_{3k} = \frac{\sqrt{3}}{2} mT_s \cos(\varphi_k + \frac{3\pi}{2})$ $T_{4k} = \frac{\sqrt{3}}{2} mT_s \cos(\varphi_k + \frac{5\pi}{6})$	$v_{0-k} = (-\frac{T_{0k}}{T_s} + \frac{1}{3}\frac{T_{4k}}{T_s} - \frac{1}{3}\frac{T_{5k}}{T_s} + \frac{T_{7k}}{T_s})$ $T_{4k} = \frac{\sqrt{3}}{2} mT_s \cos(\varphi_k + \frac{7\pi}{6})$ $T_{5k} = \frac{\sqrt{3}}{2} mT_s \cos(\varphi_k + \frac{\pi}{2})$

Sector V $(\frac{4\pi}{3} \le \varphi_k \le \frac{5\pi}{3})$	Sector VI $(\frac{5\pi}{3} \le \varphi_k \le 2\pi)$
$v_{0-k} = (-\frac{T_{0k}}{T_s} - \frac{1}{3}\frac{T_{5k}}{T_s} + \frac{1}{3}\frac{T_{6k}}{T_s} + \frac{T_{7k}}{T_s})$ $T_{5k} = \frac{\sqrt{3}}{2} m T_s \cos(\varphi_k + \frac{5\pi}{6})$ $T_{6k} = \frac{\sqrt{3}}{2} m T_s \cos(\varphi_k + \frac{\pi}{6})$	$v_{0-k} = (-\frac{T_{0k}}{T_s} - \frac{1}{3}\frac{T_{6k}}{T_s} + \frac{1}{3}\frac{T_{1k}}{T_s} + \frac{T_{7k}}{T_s})$ $T_{6k} = \frac{\sqrt{3}}{2} m T_s \cos(\varphi_k + \frac{\pi}{2})$ $T_{1k} = \frac{\sqrt{3}}{2} m T_s \cos(\varphi_k + \frac{11\pi}{6})$

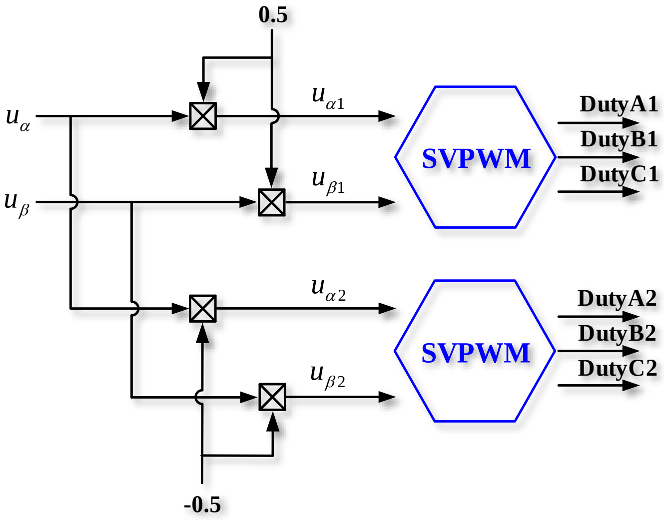

Fig. 3.11 Conventional SVPWM for OW drives.

Similar to (3.6), the zero vector times T_{0k} and T_{7k} of the four zero vectors for the two VSIs are equal, and hence, as indicated in Table 3.1, the zero vector time components cancel out each other and have no influence on the construction of zero sequence voltages $v_{0\text{-}k}$. Only the selected active vectors contribute to zero sequence voltages for either set of VSI. It also can be revealed that the analytical expressions for the zero sequence voltage of either set of VSI are both piecewise functions with cosinoidal expression in each range of the six sectors. The zero sequence modulated voltage waveform is the well-known quasi-triangle modulation wave, which is also equivalent to the mid-value line of the up and down envelopes of the three phase voltage reference signals. When the conventional method shown in Fig. 3.11 is adopted, the voltage references for two SVPWM modules are anti-phase, and hence, the two zero sequence quasi-triangle waves are anti-phase too. In this manner, the modulated zero sequence disturbance voltage is twice of either set of the VSI. However, the zero sequence modulated voltage can actually be produced actively instead of being modulated inherently. But it will consequently require the improvement of the conventional SVPWM for OW-

PMSM. The proposed adjustable SVPWM is aiming to achieve this, which will be presented in Section 3.3.3.

3.3.2 Adjustable SVPWM Strategy

The PWM strategies adopted in the most of inverter drive systems are fixed, which means that the degree of freedom is limited. Meanwhile, for OW drive system, the conventional PWM strategies are not able to satisfy the corresponding requirements due to the existence of additional zero sequence disturbance current as explained in Chapter 2. With regard to the conventional solutions, eliminating the PWM-induced third harmonic voltage is firstly done by modifying SVPWM strategy, such as the phase-shift-based method [OLE05]. Meanwhile, the frequency-adaptive zero sequence current controller can also be implemented to compensate back EMF-induced third harmonic voltage [ZHA17]. Different from these solutions modifying the SVPWM module or using extra frequency-adaptive zero sequence controller, in this section, a generalized and adjustable SVPWM strategy is proposed and investigated without adding FA zero sequence current controller to have zero sequence current suppression capability. Moreover, the proposed adjustable SVPWM strategy only reconstructs the voltage references of the individual SVPWM modules and no modification needs to be implemented on the original SVPWM module usually used in single inverter drive system. Hence, it is convenient to apply the proposed method to OW drive system by utilizing the original SVPWM module of single inverter drive. It is also found in this paper that the proposed adjustable SVPWM strategy can be equivalent to several PWM strategies for OW system, such as the conventional OW-SVPWM, the phase-shift-based SVPWM and OW-SPWM. Based on the framework, the phase-shift-based SVPWM is revealed to be essentially equivalent to H-bridge SPWM. The proposed adjustable SVPWM strategy can possess better current waveform and higher DC bus utilization capability for OW-PMSM and it can also degenerate to conventional methods.

In the conventional SVPWM strategy for OW topology, the shifted phase angle of the phase voltage reference between inverter I and inverter II is 180 degrees. Consequently, the modulated third harmonic phase voltage is also enhanced as twice of the single inverter one. In order to avoid this issue, 120 degrees phase shift method [OLE05] is adopted. However, both of the phase-shift-based SVPWM and SPWM possess the same modulation index. Moreover, the phase-shift-based SVPWM method contains no modulated third harmonic voltage in the phase winding anymore which is the same as SPWM.

However, the phase-shift-based method decreases the DC bus voltage utilization ratio. The less shifted angle is, the higher DC bus voltage utilization will be obtained. If the load machine is an OW-PMSM containing a third harmonic back EMF and other zero sequence disturbance voltages, it is necessary to generate an equivalent modulated third harmonic voltage to compensate them. Assuming the phase shift angle between inverter I and inverter II is γ, the phase A voltage can be expressed as

$$\begin{aligned} v_a &= v_{a1} - v_{a2} \\ &= V_1 \sin(\omega t - \gamma/2) + V_3 \sin(3\omega t - 3\gamma/2) - V_1 \sin(\omega t + \gamma/2) - V_3 \sin(3\omega t + 3\gamma/2) \\ &= -2V_1 \sin(\gamma/2)\cos\omega t - 2V_3 \sin(3\gamma/2)\cos 3\omega t \end{aligned} \tag{3.7}$$

It can be found that the shifted angle will not change the phase of the synthetic phase voltage for the reference voltage. But the amplitudes of the fundamental and third order components vary with the shifted angle. For conventional OW-SVPWM method, γ=180 degrees. It becomes 120 degrees when the phase-shift-based SVPWM method is adopted. In this manner, the amplitude of the third order component is zero which explains the effect of third harmonic current elimination. However, as discussed in Section II, the phase-shift-based SVPWM method (equivalent to SPWM) still cannot address the third order back EMF issue which induces the phase current distortion. No matter the conventional SVPWM or the phase-shift-based SVPWM strategies, both are not suitable for the PMSM containing third harmonic back EMF.

In fact, the modulated third harmonic voltage does not need to be eliminated completely. If there is still part of residual modulated third harmonic, with the OW-PMSM containing a third harmonic back EMF, the modulated third order harmonic can be utilized to compensate the third harmonic back EMF. Because it is not possible to force the existing tested PMSM to contain no third harmonic back EMF, modulating the corresponding voltage to counteract it is a possible way. More importantly, with less shifted angle constructing part of modulated third harmonic voltage between the two sets of inverters, the higher DC bus utilization can be obtained. The possible improved DC bus utilization ratio will be discussed later in this section. In the meantime, the distortion in phase current induced by the third back EMF harmonic can also be reduced when compared to the phase-shift-based SVPWM method.

Thus, a variable modulated third harmonic phase voltage is necessary and can be obtained by varying the shift angle between two sets of the inverters. The optimal shifted angle should also be obtained. Fig. 3.12 demonstrates the synthetic voltage vector of the two sets of the inverters. In order to unify the definition, the relevant shift angle δ is defined, which is the angle between the voltage vector of set I and the reversed voltage vector of set II. δ =60 degrees is equivalent to the γ=120 degrees shift method, viz. $\delta=\pi-\gamma$.

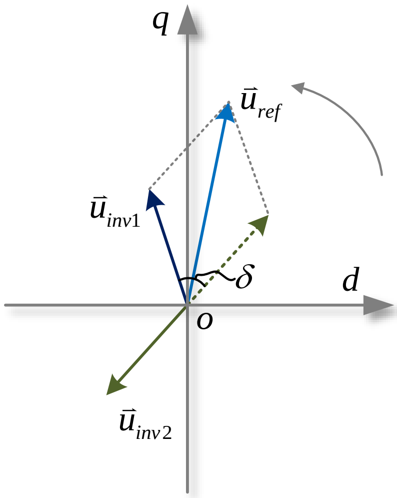

Fig. 3.12 Synthetic voltage vector of the two sets of the inverters.

Therefore, if δ is adjusted, the theoretical variations of fundamental and third order harmonic components are shown in Fig. 3.13. The third harmonic voltage will be reversed after the 60 degrees point. It is obvious that the fundamental component decreases with the increase of δ. Hence, the variation of the relevant angle introduces a scaling factor for the output voltage capability of the PWM strategy, viz.

$$\zeta_1 = \cos(\delta / 2) \tag{3.8}$$

Meanwhile, the scaling factor for third harmonic voltage is

$$\zeta_3 = \left|\cos(3\delta / 2)\right| \tag{3.9}$$

Furthermore, the maximum output phase voltage in linear modulation region is adopted to evaluate the maximum output voltage capability of different PWM strategies and different topologies. The comparison is listed in Table II. When δ =60 degrees, the proposed method degenerates to OW-SPWM and becomes OW-SVPWM if δ =0 degree.

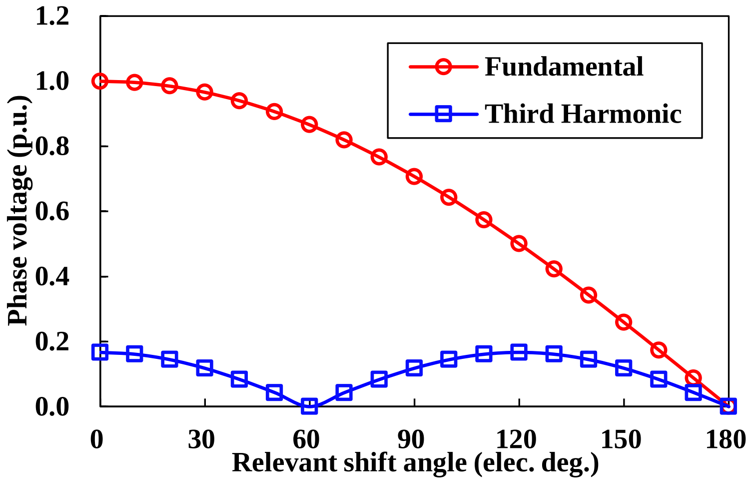

Fig. 3.13 Theoretical fundamental and third harmonic voltage components with different relevant shift angle.

TABLE 3.2 COMPARISON OF MAXIMUM OUTPUT PHASE VOLTAGE

	OW-SPWM	OW-SVPWM	Proposed method	single inverter SPWM	single inverter SVPWM
Maximum output phase voltage	V_{dc}	$2V_{dc}/\sqrt{3}$	$2V_{dc}\cos(\delta/2)/\sqrt{3}$	$V_{dc}/2$	$V_{dc}/\sqrt{3}$
Equivalent relevant shift angle	$\delta=60^{\circ}$	$\delta=0^{\circ}$	δ	$\delta=128.6^{\circ}$	$\delta=120^{\circ}$

In general, if δ is within [0, 60°], the output voltage capability is still higher than that of SPWM with OW topology. The third harmonic voltage will also vary within this region. If the PWM induced voltage can be used to counteract the third harmonic back EMF in the OW-PMSM with δ in [0, 60º], that can be an optimal operation point with minimum zero sequence current disturbance and relative higher DC bus voltage utilization.

Therefore, the proposed adjustable SVPWM strategy is shown in Fig. 3.14.

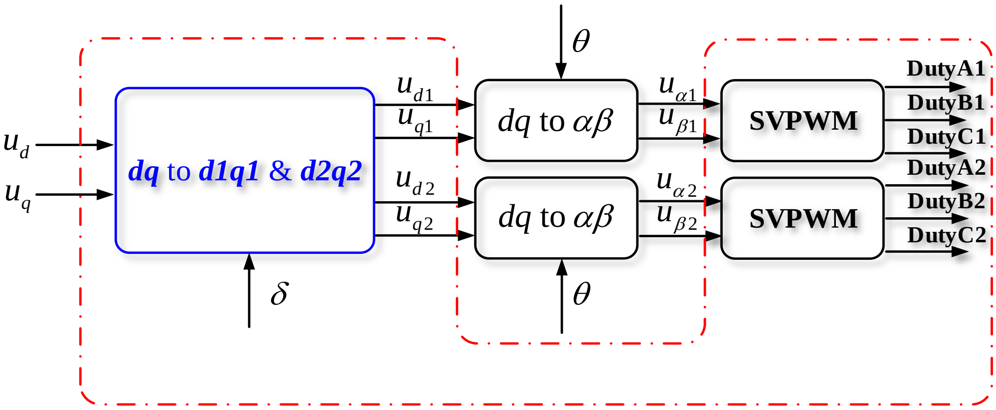

Fig. 3.14 Proposed generalized and adjustable SVPWM for OW topology.

The coordinate transformation for *dq* to *d1q1* & *d2q2* is:

$$\begin{bmatrix} u_{d1} \\ u_{q1} \\ u_{d2} \\ u_{q2} \end{bmatrix} = \frac{1}{2} \cdot \begin{bmatrix} 1 & \tan(\delta/2) \\ -\tan(\delta/2) & 1 \\ -1 & \tan(\delta/2) \\ -\tan(\delta/2) & -1 \end{bmatrix} \cdot \begin{bmatrix} u_d \\ u_q \end{bmatrix} \tag{3.10}$$

3.3.3 Adaptive SVPWM

Although it is possible to construct a lookup table for the relevant shift angle through the self-commissioning, the process is complicated and time consuming. For different OW-PMSMs containing different percentage of zero sequence disturbances, the self-commissioning should be re-implemented. Hence, it is expected and necessary to have the adaptive countermeasure to achieve the online optimal relevant shift angle searching. According to the framework, the searching variable is one dimensional. Therefore, the extremum seeking (ES) method [ARI03] is adopted for this scenario. Fig. 3.15 shows the overall system diagram of the OW-PMSM drive system with adaptive circulating current suppression. However, it is also possible that the zero sequence circulating current cannot be fully suppressed even with the well-adjusted phase angle. That is because the amplitude of the combined zero sequence voltage produced by the inverter varies together with the phase angle.

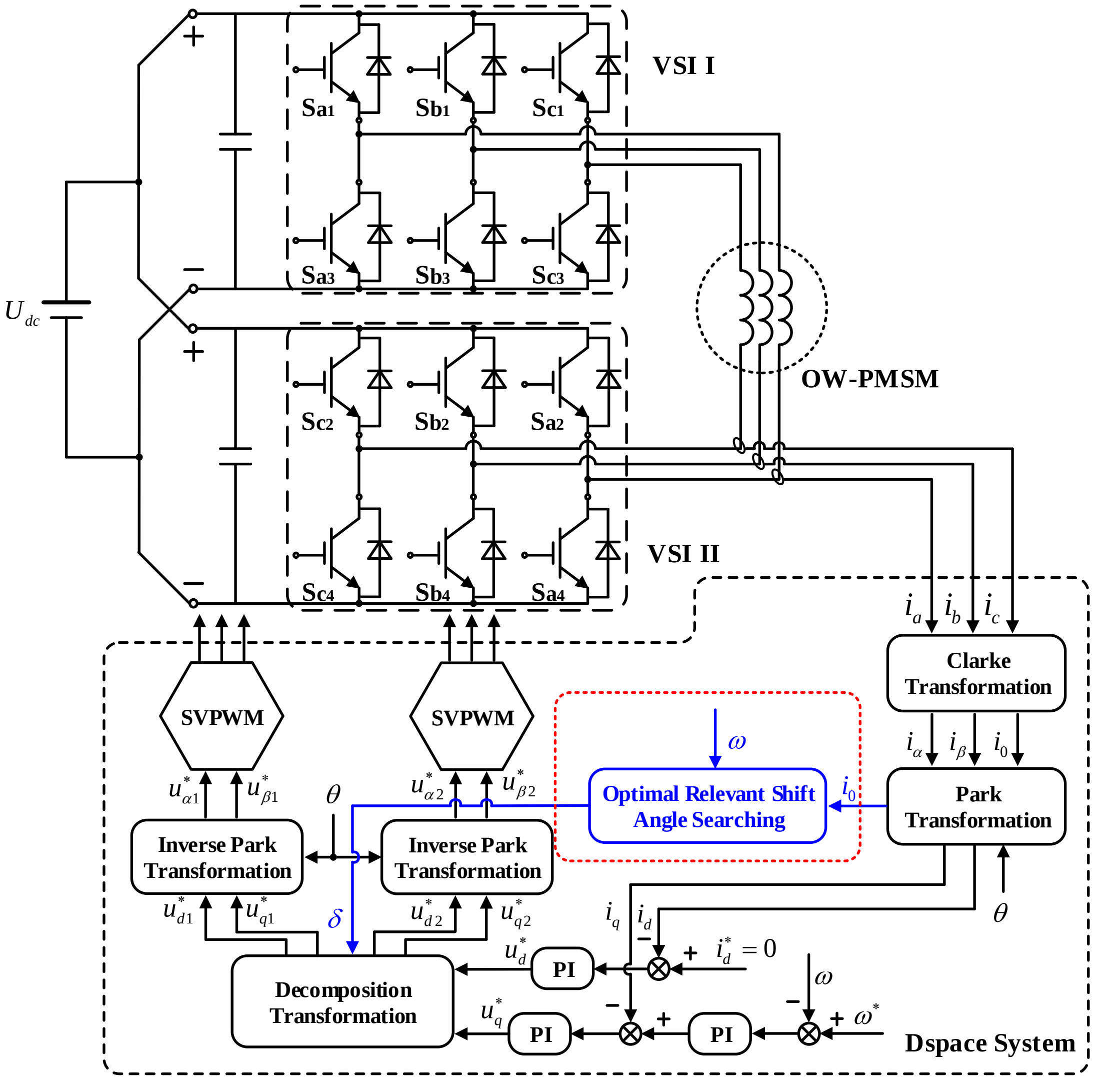

Fig. 3.15 OW-PMSM drive system with adaptive circulating current suppression.

The ES method is essentially a non-model based optimal value searching method with small perturbation injection. This method can automatically find the desirable local minimum or maximum point upon the specific cost function. However, it is necessary to provide information indicating the system performance under parameter variation for the ES searching. The absolute average component of the circulating current can be used. In order to extract the average component, the VW-MAF is consequently adopted. The VW-MAF is a type of finite impulse response (FIR) filter with VW. The differential equation of the VW-MAF can be written as

$$J[n] = \frac{1}{M(\omega)} \sum_{i=0}^{M(\omega)-1} \left| i_0[n+i] \right| \tag{3.11}$$

where

$$M(\omega)=\left\lfloor \frac{2\pi}{3\omega T_s} \right\rfloor \tag{3.12}$$

the symbol $\lfloor\cdot\rfloor$ means to round down, i_0 is the zero sequence current, T_s is the sampling period and ω represents the electrical angular speed. The sampling signals are shown in Fig. 3.16.

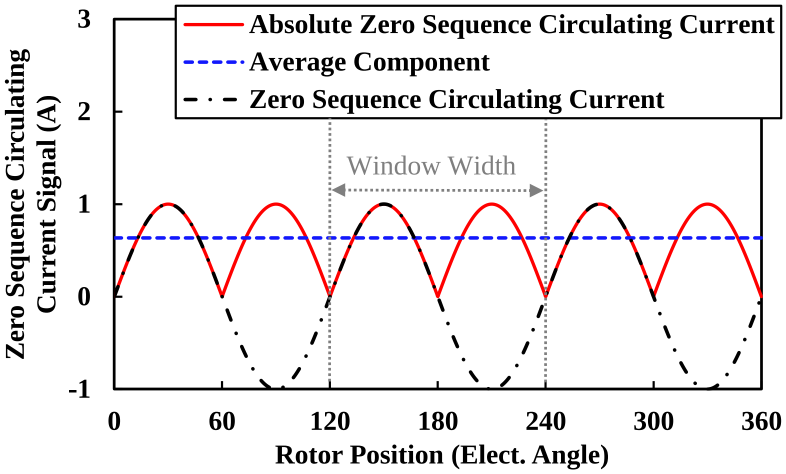

Fig. 3.16 Sampling signals.

The frequency response of the VW-MAF is

$$H(e^{j\omega^N})=\frac{1}{M(\omega)}\cdot\frac{\sin(M(\omega)\omega^N/2)}{\sin(\omega^N/2)}e^{-j(M-1)\omega^N/2} \tag{3.13}$$

where ω^N is the normalized angular frequency.

The amplitude response can be consequently expressed as

$$|H(e^{j\omega^N})|=|\frac{1}{M(\omega)}\cdot\frac{\sin(M(\omega)\omega^N/2)}{\sin(\omega^N/2)}|. \tag{3.14}$$

Typically, if the sampling frequency is 5kHz and the fundamental operation frequency is 60Hz, the window width M=27. The associated amplitude response can be shown in Fig. 3.17. According to the shown amplitude response of the VW-MAF, the zero gain points occur at $2\pi k/M(\omega)$ where k=1, 2, 3…, namely, $3k\omega/f_s$ where f_s is the sampling frequency.

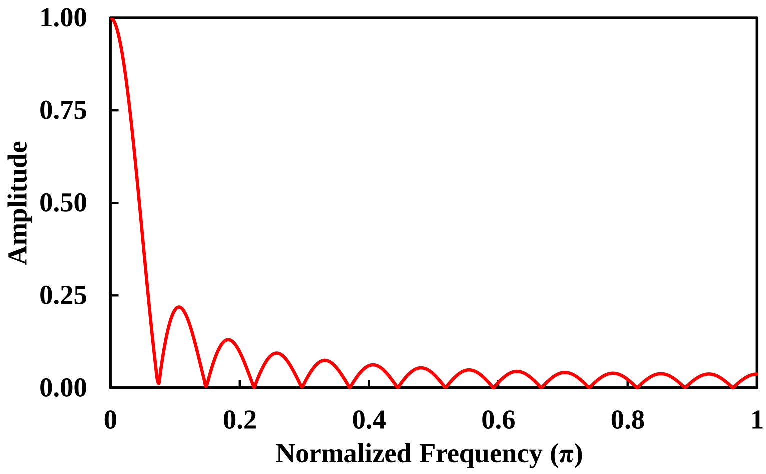

Fig. 3.17 Normalized amplitude response of the VW-MAF.

Meanwhile, the absolute zero sequence circulating current shown in Fig. 3.16 can be expressed as

$$|i_0| = I_0 |\sin(3\omega t)|. \tag{3.15}$$

Hence, (3.15) can be expressed in Fourier series as

$$i_0 = \frac{a_0}{2} + \sum_{n=1}^{\infty} (a_n \cos n\omega t + b_n \sin n\omega t) \tag{3.16}$$

where $n = 1, 2, \cdots$ and

$$a_n = \begin{cases} \dfrac{-4I_0}{\pi(\dfrac{n^2}{9} - 1)}, n = 6k, k = 1, 2, 3... \\ 0, otherwise \end{cases} \tag{3.17}$$

$$a_0 = \frac{4I_0}{\pi} \quad (3.18) \qquad\qquad b_n = 0. \quad (3.19)$$

Therefore, the spectrum analysis of the quantified condition with I_0=1A can be shown as Fig. 3.18. The effective components appear at $6k\omega/f_s$ which are locating at the zero gain points ($3k\omega/f_s$) of the VW-MAF. The finally passed component is only the DC component of the absolute signal of the zero sequence circulating current. The higher order components are eliminated adaptively. However, it should be also noticed that the window width $M(\omega)$ is integer in the implementation which is due to the digitization. The zero gain points can slightly deviate from the high order components of the absolute signal of the zero sequence circulating current. Minor higher order components could pass damply. The wider the window is, the smaller the quantization error will be, while the lower dynamic of the adaptive searching method will occur. The ES searching is executed every period of the window width. The window width is selected as the lowest value to maximize the dynamic.

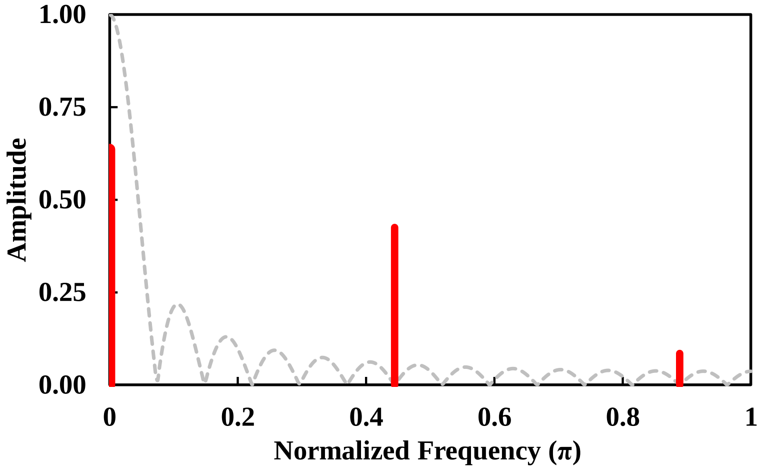

Fig. 3.18 Spectrum analysis of the absolute signal of the zero sequence circulating current.

The ES is an effective real time optimization control algorithm which is independent of the target model. Meanwhile, this algorithm is easy to be implemented as digitized form and different from the flow chart based searching algorithm. The ES algorithm is shown in Fig. 3.19.

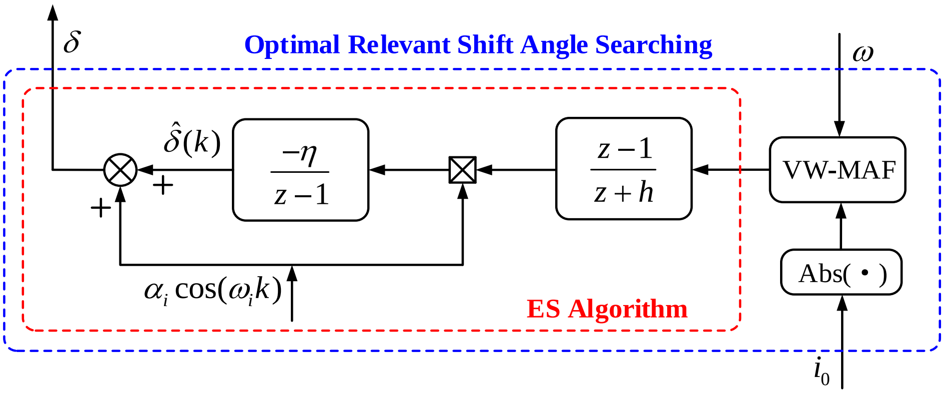

Fig. 3.19 ES algorithm based optimal relevant angle searching method.

In Fig. 3.19, the $(z-1)/(z+h)$ performs as high pass filter, $-\eta/(z-1)$ performs as integrator, η is adjustable step length, $\delta(k)$ is the optimal parameter to be found, $\hat{\delta}(k)$ is the estimation of $\delta(k)$, $J[\delta(k)]$ is the objective function, $\alpha_i\cos(\omega_i k)$ is the perturbation signal, α_i is the amplitude and ω_i is the frequency.

The signals are processed as follows:

$$\xi(k) = -h\xi(k-1) + J[\delta(k-1)] \tag{3.20}$$

$$\hat{\delta}(k+1) = -\eta\alpha_i \cos(\omega_i k)\{J[\delta(k)] - (1+h)\xi(k)\} + \hat{\delta}(k) \tag{3.21}$$

$$\delta(k+1) = \hat{\delta}(k+1) + \alpha_i \cos[\omega_i (k+1)]\,. \tag{3.22}$$

The target of the ES algorithm is to minimize $J[\delta(k)]$ by adjusting $\delta(k)$. The gradient information is obtained by injecting the perturbation signal. The optimal point is searched along the direction of negative gradient. Assume f^* is the extreme point of the objective function and δ^* is the associated parameter to be searched. The objective function can be generally expressed in quadric form as

$$J[\delta(k)] = f^* + \frac{1}{2} f''(\delta - \delta^*)^2 \tag{3.23}$$

where f'' is the second derivative of J upon δ. Let $\tilde{\delta} = \delta^* - \hat{\delta}$ and expand $J(\delta)$ at around the extreme point as

$$J \approx (f^* + \frac{\alpha_i^2 f''}{4}) + \frac{\alpha_i^2 f''}{4}\cos 2\omega_i k - \alpha_i f'' \cos(\omega_i k)\tilde{\delta} \tag{3.24}$$

where the second order term $\frac{1}{2} f''\tilde{\delta}^2$ is neglected.

After the high pass filter, the DC component is filtered and the residual signal is

$$\frac{z-1}{z-h}[J] \approx \frac{\alpha_i^2 f''}{4}\cos 2\omega_i k - \alpha_i f'' \cos(\omega_i k)\tilde{\delta}\,. \tag{3.25}$$

Multiply (3.25) by $\alpha_i \cos\omega_i k$ as

$$\alpha_i \cos(\omega_i k)\frac{z-1}{z-h}[J] \approx -\frac{\alpha_i^2 f''}{2}\tilde{\delta} \tag{3.26}$$

where the high frequency terms $\cos(\omega_i k)$, $\cos(2\omega_i k)$, $\cos(3\omega_i k)$ …are neglected due to following integrator.

Hence, take (3.26) as the input of the integrator, the attenuation of the estimation error can be obtained as

$$\tilde{\delta}(k+1) = (1 - \frac{\eta \alpha_i^2 f''}{2})\tilde{\delta}(k) . \tag{3.27}$$

It can be clearly found that if $1 - \eta \alpha_i^2 f'' / 2 \subseteq (-1,1)$ by selecting η and α_i properly, the estimation error $\tilde{\delta}(k)$ will decay to zero exponentially, namely, $\hat{\delta}(k)$ can approach the extreme point δ^* exponentially.

3.3.4 Experimental Validation of Adaptive SVPWM

The proposed method is implemented on the dSPACE control system. The switching frequency is chosen as 5kHz and the dead-time is set as 2μs. The sampling frequency is the same as the switching frequency, as well as the interrupt frequency. The specification of the OW-PMSM is shown in Table 3.3. The experimental platform is shown in Fig. 3.20.

TABLE 3.3 SPECIFICATION OF THE OW-PMSM

Parameter	Value
Pole pairs	16
Resistance (Ω)	3.76
Rated RMS current (A)	2.83
Rated speed (rpm)	80
No-load PM flux linkage (Wb)	0.9
Encoder resolution	4096
Rated frequency (Hz)	45.33
d-axis inductance (mH)	17
q-axis inductance (mH)	17
DC bus voltage (V)	200

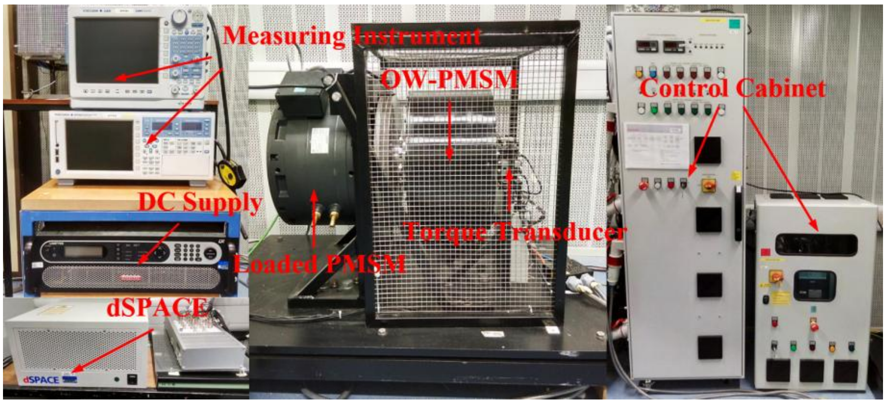

Fig. 3.20 Experiment platform.

Fig. 3.21 shows the self-commissioning procedure of the relevant shift angle δ which varies from 0 to 90 degrees. The optimal relevant shift angle appears at around 40 degrees. Meanwhile, Fig. 3.22 to Fig. 3.24 show the operation waveforms with three typical relevant shift angles. Fig. 3.22 shows the 0 degree shift, namely, the conventional SVPWM for OW-PMSM. Fig. 3.23 shows the 60 degree shift condition which is the conventional phase shift based SVPWM for OW machine. Fig. 3.24 shows the 40 degree shift condition which is the optimal operation point obtained via the self-commissioning, which is to be searched adaptively by using the proposed method.

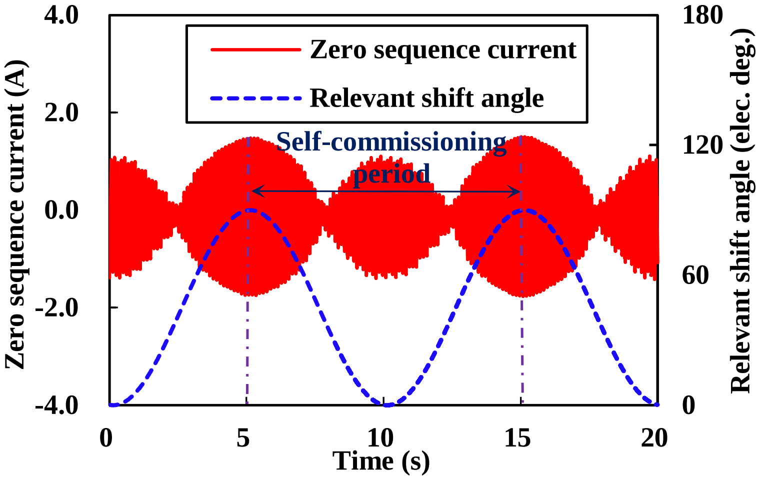

(a)

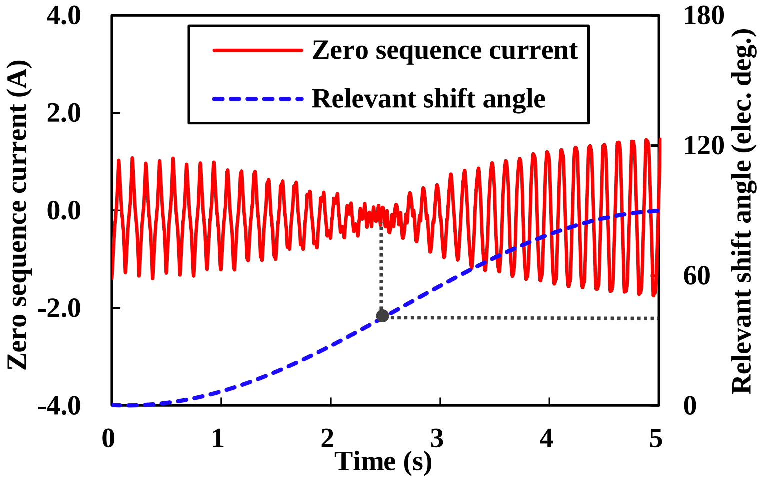

(b)

Fig. 3.21 Self-commissioning procedure waveforms of the relevant shift angle. (a) Zero sequence current and relevant shift angle waveforms of the OW-PMSM in the self-commissioning period. (b) Magnification of the optimal zero sequence current point.

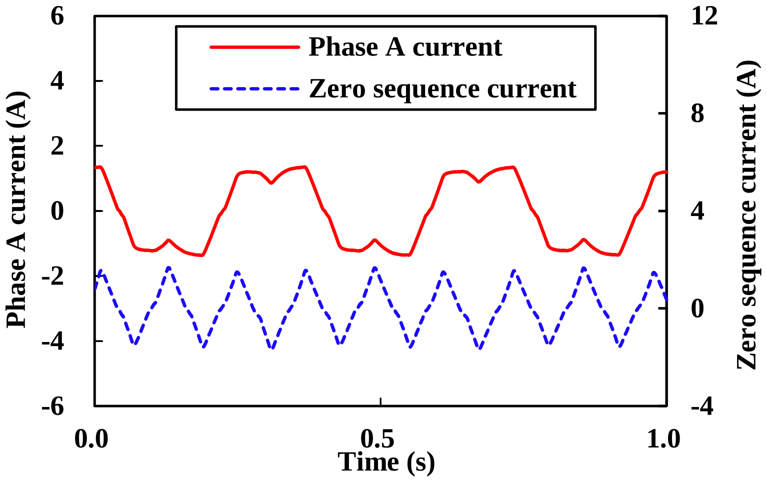

(a)

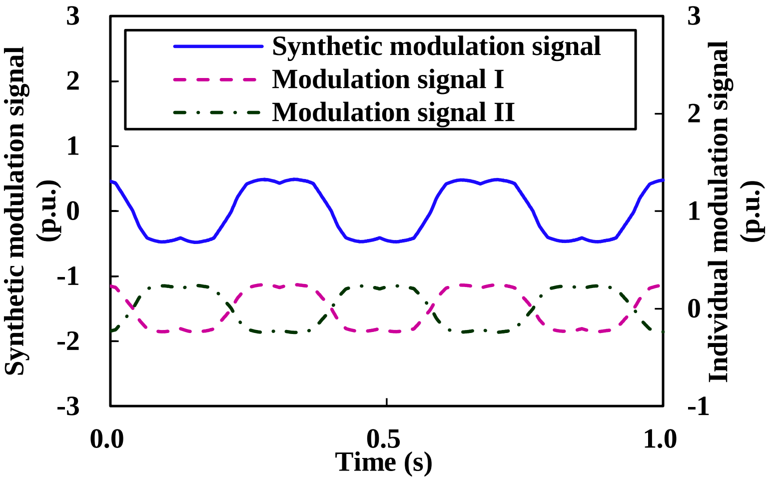

(b)

Fig. 3.22 Operation waveforms of the OW-PMSM with 0 degree shift. (a) Phase A current and zero sequence current. (b) Modulation signals.

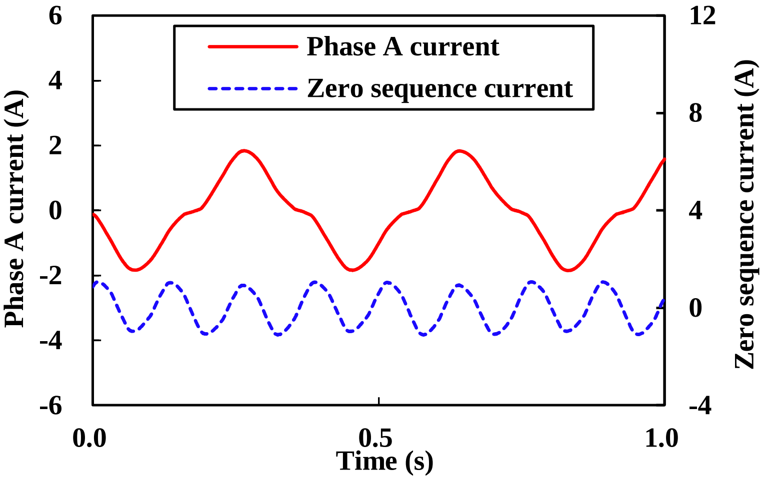

(a)

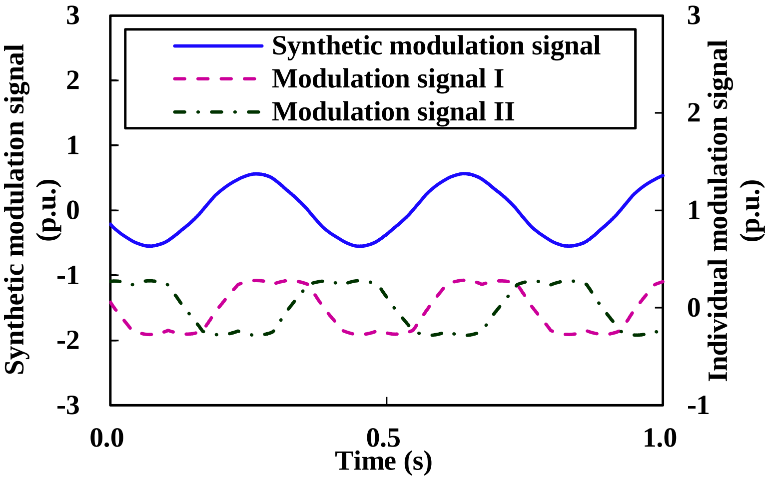

(b)

Fig. 3.23 Operation waveforms of the OW-PMSM with 60 degrees shift. (a) Phase A current and zero sequence current. (b) Modulation signals.

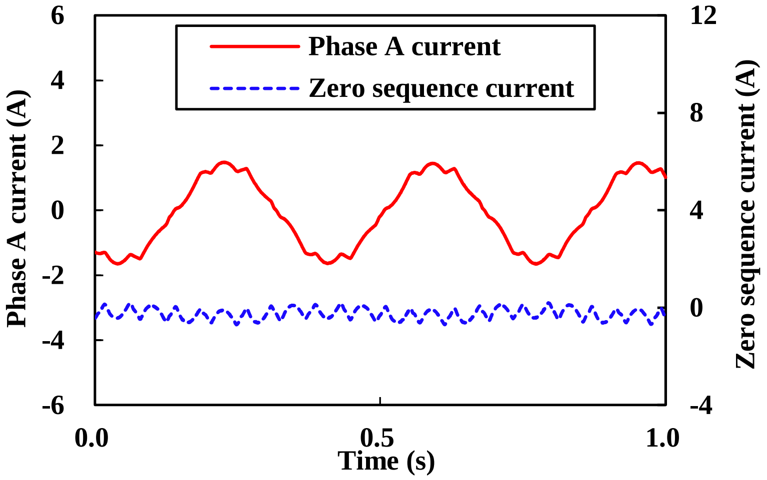

(a)

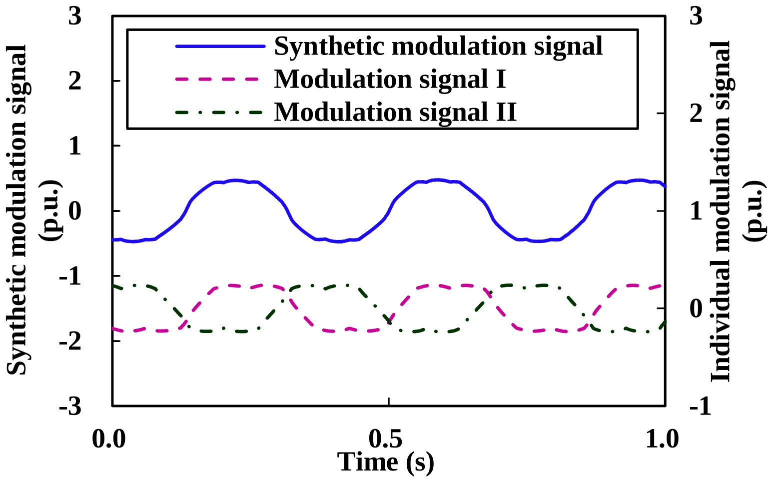

(b)

Fig. 3.24 Operation waveforms of the OW-PMSM with 40 degrees shift. (a) Phase A current and zero sequence current. (b) Modulation signals.

The performance of the proposed adaptive optimal relevant shift angle searching method is presented in Fig. 3.25 to Fig. 3.27 with the OW-PMSM operating at 10rpm. From Fig. 3.25 to Fig. 3.27, the amplitudes of the perturbation signals are set as 3, 5 and 7, respectively. The associated zero sequence circulating current waveforms are shown in Figs. 3.25(a), 3.26(a) and 3.27(a), respectively. The output signals of the objective function are shown in Figs. 3.25(b), 3.26(b) and 3.27(b), respectively. Also, the real-time searching relevant shift angles are shown in Figs. 3.25(c), 3.26(c) and 3.27(c), respectively. It can be seen from the performance results that the optimal relevant shift angle for the condition is around 40 degrees which is accordance with the self-commissioning results. Meanwhile, the higher the amplitude of the perturbation signal is set, the faster the convergence will be. However, the steady fluctuation could be higher as well. The parameter selection is a trade-off between convergence ratio and steady fluctuation.

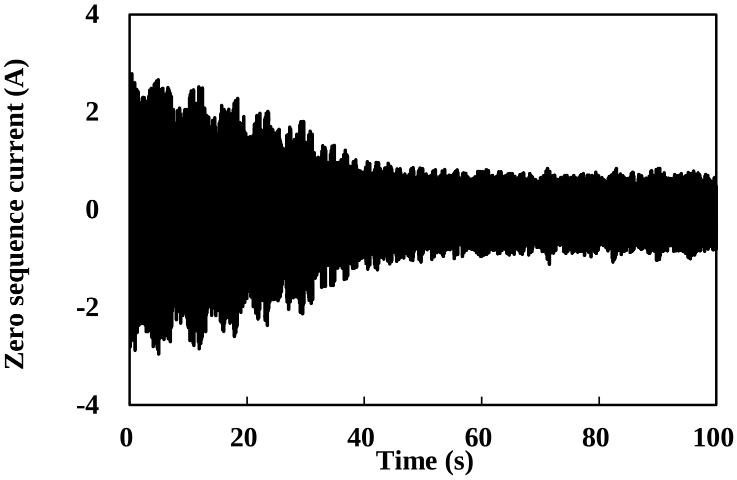

(a)

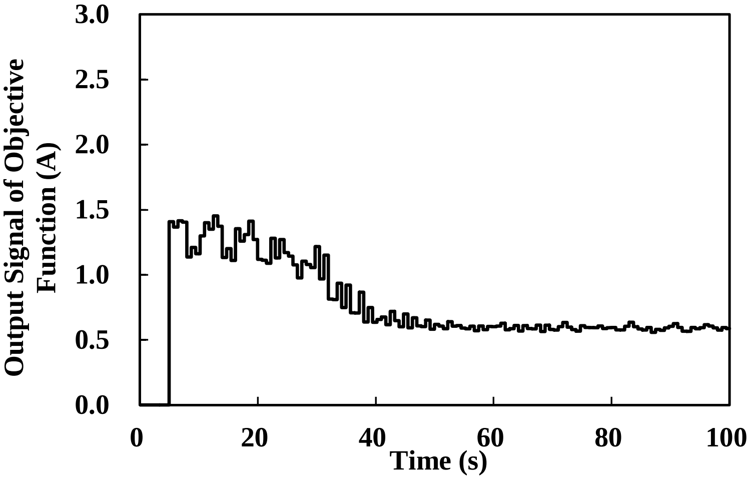

(b)

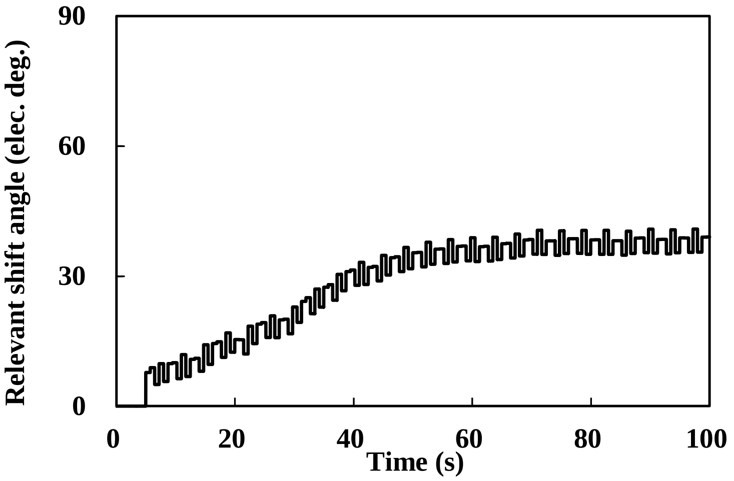

(c)

Fig. 3.25 Performance of the proposed adaptive optimal relevant shift angle searching method (α_i=3, ω_i=0.8π, η=10, h=0.4). (a) Zero sequence circulating current. (b) Output signal of the objective function. (c) Relevant shift angle.

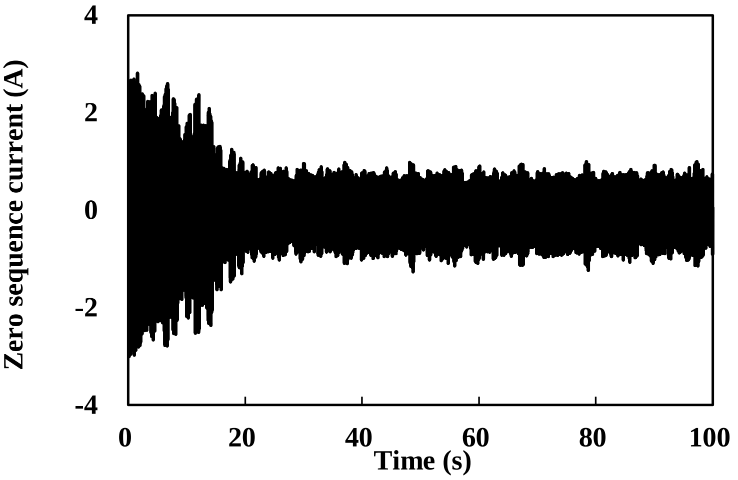

(a)

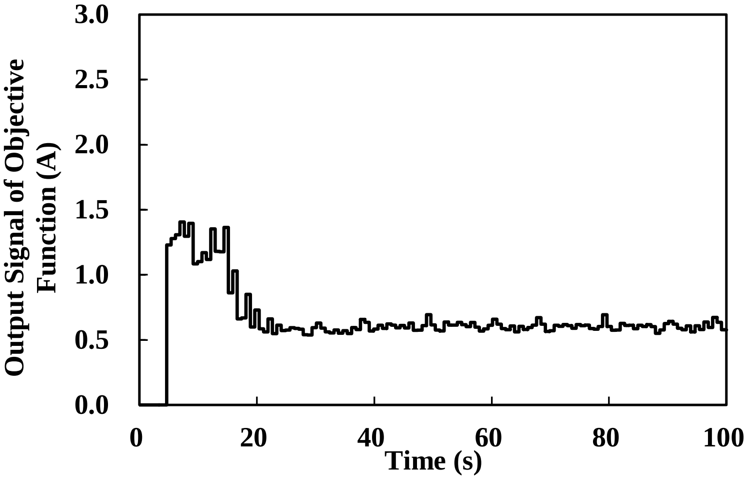

(b)

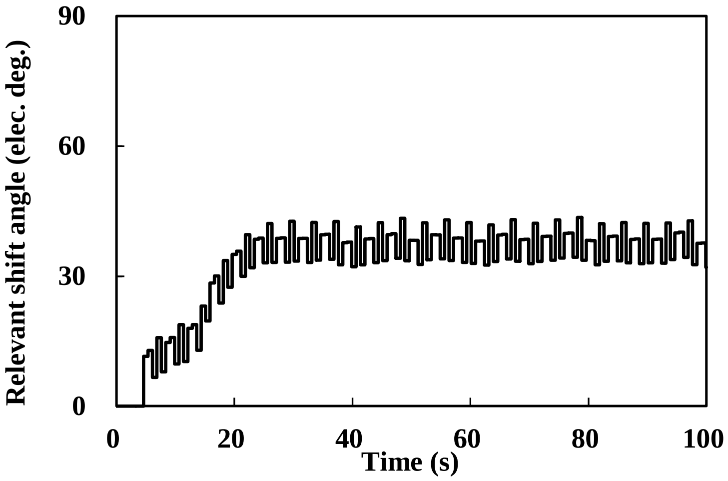

(c)

Fig. 3.26 Performance of the proposed adaptive optimal relevant shift angle searching method (α_i=5, ω_i=0.8π, η=10, h=0.4). (a) Zero sequence circulating current. (b) Output signal of the objective function. (c) Relevant shift angle.

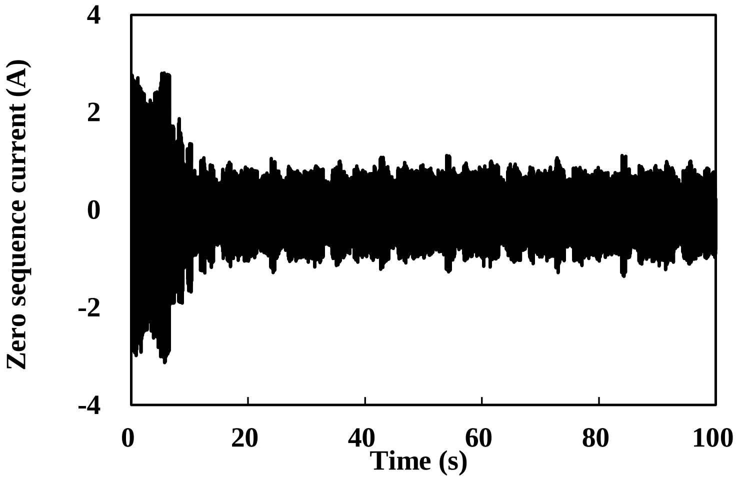

(a)

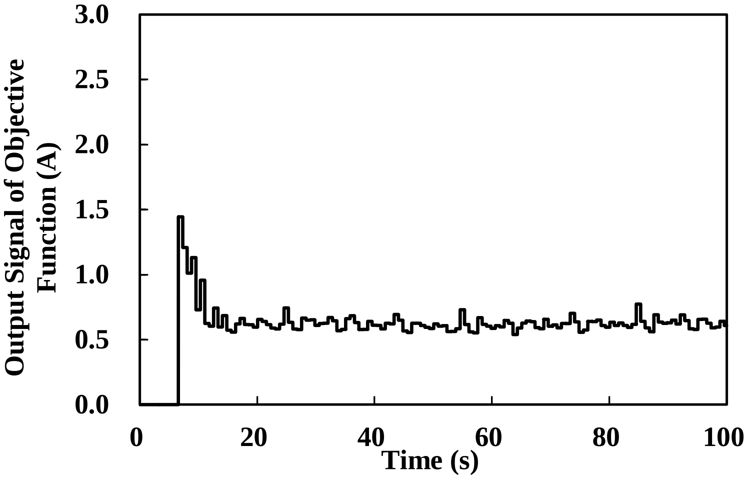

(b)

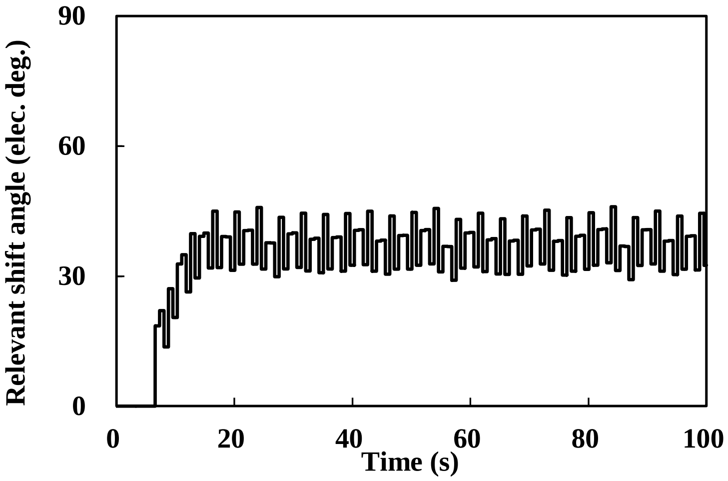

(c)

Fig. 3.27 Performance of the proposed adaptive optimal relevant shift angle searching method (α_i=7, ω_i=0.8π, η=10, h=0.4). (a) Zero sequence circulating current. (b) Output signal of the objective function. (c) Relevant shift angle.

3.4 Conclusion

In this chapter, two zero sequence circulating current suppression strategies have been proposed. The first one is zero sequence model based method using FA-PR controller and the second one is the non-model based method utilizing ES algorithm. The first method has better dynamic performance while requires equivalent zero sequence parameters to design the control parameters. The second method has better generality for different OW machines but slower dynamic performance.

CHAPTER 4 AVERAGE TORQUE ENHANCEMENT BY ZERO SEQUENCE CURRENT INJECTION

Except for the zero sequence circulating current suppression, the zero sequence path existing in OW-PMSM can also be used for system performance improvement. In this chapter, an average torque enhancement technique by using zero sequence current injection is presented.

This chapter has been submitted to IEEE Transactions on Power Electronics.

4.1 Introduction

Open-winding (OW) permanent magnet synchronous machine (PMSM) (OW-PMSM) is becoming an attractive solution to industrial applications, such as electric vehicle [WEL03] and wind power generator [NIA15], due to its capabilities of higher DC bus utilization ratio [WEL03], fault tolerance [JAH80], non-parametric sensorless drive [ZHA16] and potential torque enhancement which will be introduced in this paper. However, it also leads to the increase of the quantity of switching device, which requires the design tradeoff between the system performance and the cost. Specifically, for the torque enhancement techniques, several solutions have been proposed either from the machine design or control side, or both.

The essence of these techniques is to exploit the harmonics in the machine design and drive. One purpose is to shape the flux density or current waveform, and hence, the fundamental component can be boosted, which shares the same principle of the space vector pulse width modulation (SVPWM) with high DC bus utilization [BRO88]. Namely, the equivalent third harmonic injection is used for this purpose. The other objective is to utilize the harmonics themselves to generate additional torque components. In this case, the harmonics in the EMF and current are necessary.

From the machine design side, the optimal shaping of the permanent magnet with third harmonic injection is firstly presented in [LI03], of which the numerical conclusion is investigated and drawn. The analytical derivation is then proposed in [WAN14a] with the conclusion that the optimal third harmonic amplitude is 1/6 of the fundamental component. Afterwards, the similar techniques are extended to five-phase surface mounted PMSM [WAN14b] and three-phase interior PMSM [WAN14a]. Merely from the design perspective, namely, assuming that the PMSMs are supplied with sinusoidal current waveforms, the improved average torque is only contributed by the increased fundamental component in the flux density. However, the harmonic components are not exploited to generate higher average torque. Hence, many approaches [PAR05] [DUR14] [LYR02] [SER15] [WAN15] [WAN12] are proposed to utilize the harmonics from the control side and to further improve the average torque performance.

In [PAR05], a five-phase PMSM drive by using sinusoidal plus third harmonic currents is presented. The five-phase machine contains a third harmonic path which allows the third harmonic in the phase back EMF can interact with the third harmonic phase current to produce torque. The third harmonic current injection is also extended to five phase induction machine drive in [DUR14]. Only proportional regulator is used to control the third harmonic currents, in which, the static error and insufficient performance are inevitable. Meanwhile, in [LYR02], the third harmonic current injection is also applied in six-phase induction machine to enhance the torque performance. The reconstructed zero sequence path, namely, the connection between the neutral point of the six-phase machine and the midpoint of the DC bus capacitors, is necessary. As for the single three phase machine, the third harmonic current injection is also adopted but still requires the connection between the neutral point of the machine and the midpoint of the DC bus capacitors [SER15]. Meanwhile, the ideal square wave currents for brushless DC machine are infeasible due to the lack of zero sequence. The third harmonic in the square wave is actually cannot be produced and utilized. Similarly, in [WAN15], the third harmonic injection is adopted for a dual three-phase PMSM with reconstructed zero sequence path. Assisted by the phase shift between two sets of three-phase windings, the torque ripple is also minimized. In addition, the harmonic current injection is also used in the dual rotor multi-phase PMSM [WAN12]. In [KHA12], the comparative study of harmonic injection for different multi-phase machines is presented. In general, the equivalent series resistance (ESR) of the DC bus electrolytic capacitors will increase with the decrease of the operation frequency. The reconstructed zero sequence path will introduce the third harmonic current to the DC bus electrolytic capacitors, and hence it might increase the losses and temperature of these electrolytic capacitors which are the vulnerable part of the inverter. The lifetime of the inverter will also decrease.

In this chapter, a torque enhancement strategy for OW-PMSM using zero sequence current shaping technique is proposed. Based on current research attempts, the torque enhancement strategy has not been investigated on the OW-PMSM drive. Meanwhile, by means of the naturally existing zero sequence path in OW-PMSM drive with common DC bus, it is not necessary to reconstruct the specific path for the third harmonic current, which is similar to the five-phase machine. The negative effects on the DC bus electrolytic capacitors can be avoided. Meanwhile, different from the employment of conventional proportional regulator, the frequency adaptive (FA) proportional resonant (PR) (FA-PR) controller is adopted to achieve more desirable harmonic current control performance. Together with the detailed analysis of the principle and optimal current shaping, the systematic implementation is also presented. This chapter is organized as follows: In Section 4.2, the OW-PMSM drive system configuration is introduced. In Section 4.3, the principle of torque enhancement including analytical optimal shaping is presented. In Section 4.4, the implementation of zero sequence current control is presented. Finally, the finite element (FE) and experimental validations are given in Section 4.5.

4.2 OW-PMSM Drive System Configuration

4.2.1 OW-PMSM Model

Due to the existence of zero sequence path, OW-PMSM drive with a common DC bus is different from the conventional single three phase driven PMSM. The zero sequence equation needs to be considered in the system modelling and the corresponding influence will also be reflected. Conventionally, the third harmonic back EMF component in the phase back EMF is not eliminated on purpose since it only exhibits in zero sequence which is open circuit. Moreover, the third harmonic flux linkage inducing third harmonic back EMF is also used to increase the fundamental component within the same flux density amplitude constraint for the sake of avoiding saturation [WAN14a]. Hence, the third harmonic back EMF is usually observed in most of the PMSMs or OW-PMSMs. The OW-PMSM model considering zero sequence equation is expressed as

$$\mathbf{u} = \begin{bmatrix} R_s & -\omega L_q & 0 \\ \omega L_d & R_s & 0 \\ 0 & 0 & R_s \end{bmatrix} \cdot \mathbf{i} + \begin{bmatrix} L_d & 0 & 0 \\ 0 & L_q & 0 \\ 0 & 0 & L_0 \end{bmatrix} \cdot \dot{\mathbf{i}} + \begin{bmatrix} 0 \\ \omega \psi_f \\ 3\omega \psi_{f0} \sin 3\theta \end{bmatrix} \tag{4.1}$$

where $\mathbf{u}=[u_d, u_q, u_0]^T$, $\mathbf{i}=[i_d, i_q, i_0]^T$, u_d is the d-axis voltage, u_q is the q-axis voltage, u_0 is the zero sequence voltage, i_d is the d-axis current, i_q is the q-axis current, i_0 is the zero sequence current, R_s is the winding resistance, L_d is the d-axis inductance, L_q is the q-axis inductance, L_0 is the zero sequence inductance, ω represents the electrical angular speed, “ · ” denotes the differential operator, ψ_f is the fundamental flux-linkage, ψ_{f0} is the zero sequence flux linkage (the third harmonic flux linkage) and θ is the electrical rotor position.

Hence, the equivalent zero sequence circuit of the OW-PMSM is shown in Fig. 4.1.

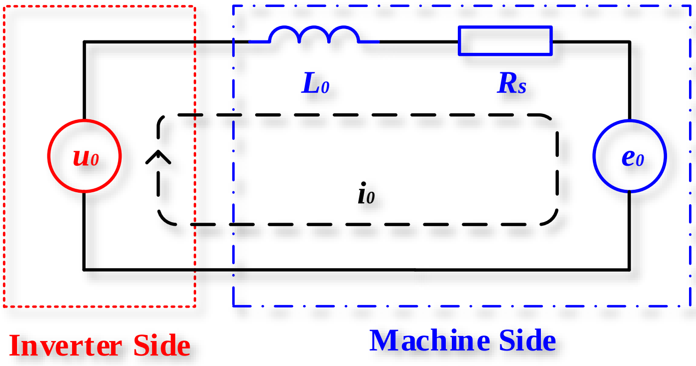

Fig. 4.1 Equivalent zero sequence circuit of the OW-PMSM.

The zero sequence voltage u_0 from inverter side is generated from the specific PWM strategy. The zero sequence inductance is described as

$$L_0 = L_{s0} - 2M_{s0} \tag{4.2}$$

where L_{s0} represents the DC component of the arbitrary phase self-inductance and M_{s0} represents the DC component of mutual-inductance between any two phases.

The winding phase resistance is equivalent to zero sequence resistance. The zero sequence back EMF is expressed as

$$e_0 = 3\omega\psi_{f0}\sin 3\theta\,. \tag{4.3}$$

The zero sequence equivalent equation is

$$u_0 = (L_{s0} - 2M_{s0})\frac{di_0}{dt} + i_0 R_s + 3\omega\psi_{f0}\sin 3\theta\,. \tag{4.4}$$

4.2.2 OW-PMSM Drive System Configuration

In order to increase the torque capability of the OW-PMSM drive system, the third harmonic current injection technique is proposed in this paper. The proposed control system diagram and the drive topology are both shown in Fig. 4.2. Two voltage source inverters (VSIs) are used to drive the OW-PMSM. Common DC bus structure is adopted to enable zero sequence path. Zero sequence steerable (ZSS)-SVPWM (ZSS-SVPWM) together with decomposition transformation eliminating higher order voltage harmonics induced by SVPWM is used as well [4]. The zero sequence current is controlled by FA-PR controller. The zero sequence third harmonic current reference is generated from the harmonic current reference generator (HCRG). The working principle and details will be elaborated in the following sections.

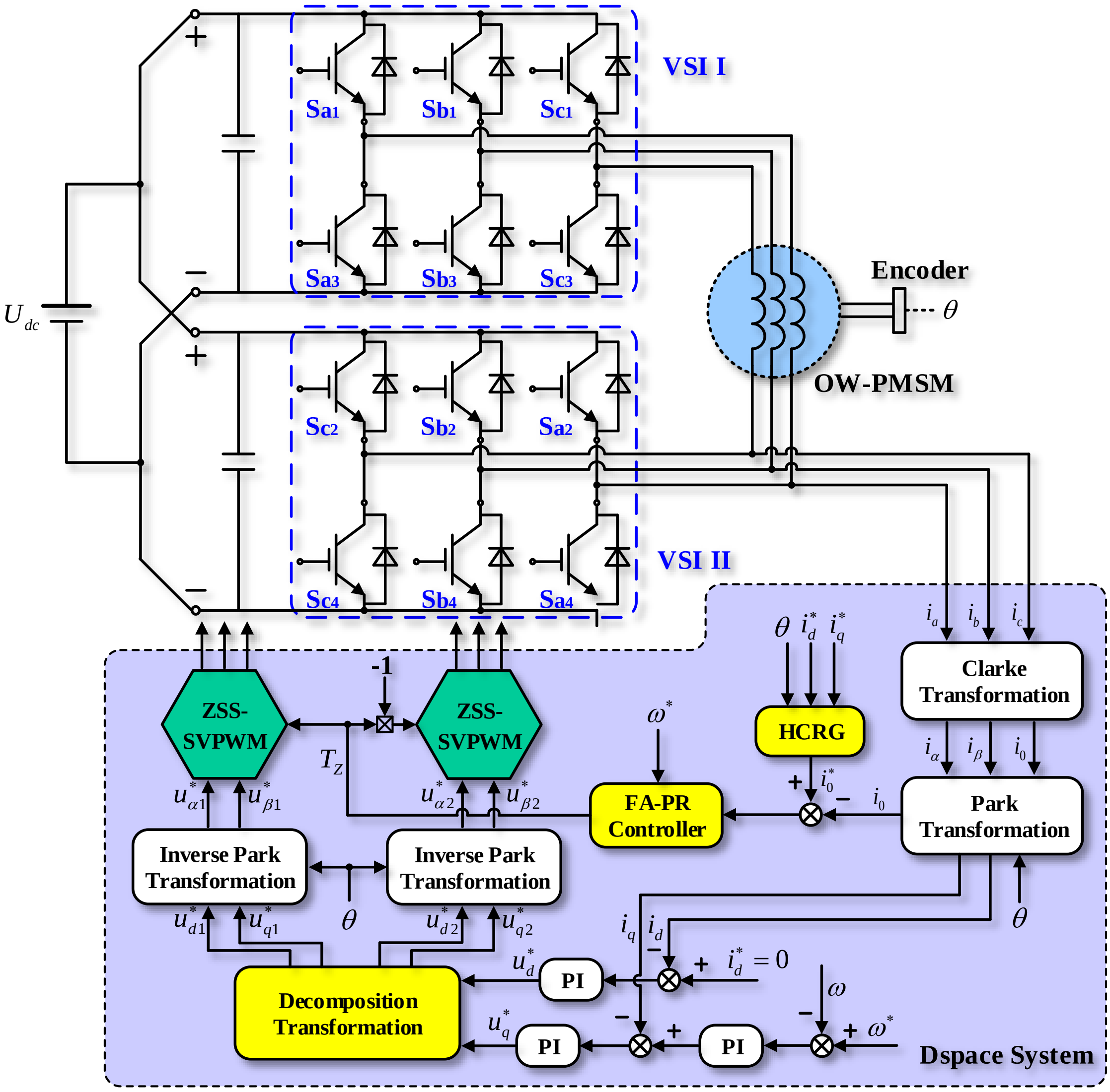

Fig. 4.2 OW-PMSM torque enhancement drive system diagram.

4.3 Principle of Torque Enhancement Technique

The third harmonic shaping techneque enables the fundamental component become higher within the same amplitude constraint. Therefore, it is possible to obtain a higher fundamental current component under the same current constraint by injecting the third harmonic current into the phase current. Meanwhile, the third harmonic current component and the third harmonic back EMF can interact to produce additional average torque component.

The torque capability of the OW-PMSM is described via power dividing mechanical speed, viz.

$$T_e = \frac{e_a i_a + e_b i_b + e_c i_c}{\omega_m} \tag{4.5}$$

where T_e is the electromagnetic torque, e_a, e_b and e_c represent three phase back EMFs, i_a, i_b and i_c represent three phase currents and ω_m is the mechanical angular speed.

The possible combinations include: sinusoidal back EMF + sinusoidal phase current, shaped back EMF + sinusoidal phase current, sinusoidal back EMF + shaped phase current and shaped back EMF + shaped phase current. The copprsonding combinations demonstrate different operations.

4.3.1 Sinusoidal Back EMF + Sinusoidal Phase Current

When the operating condition is sinusoidal back EMF + sinusoidal phase current, the three phase back EMFs are

$$\begin{gathered} e_a = E_1 \sin \omega t \\ e_b = E_1 \sin(\omega t + 2\pi / 3) \\ e_c = E_1 \sin(\omega t - 2\pi / 3) \end{gathered} \tag{4.6}$$

where E_1 is the amplitude of the fundamental back EMF, ω is the electrical angular speed.

Meanwhile, the three phase sinusoidal currents are

$$\begin{gathered} i_a = I_1 \sin \omega t \\ i_b = I_1 \sin(\omega t + 2\pi / 3) \\ i_c = I_1 \sin(\omega t - 2\pi / 3) \end{gathered} \tag{4.7}$$

where I_1 is the amplitude of the fundamental phase current.

According to (4.5), the electromagnetic torque is

$$T_{eA} = \frac{e_a i_a + e_b i_b + e_c i_c}{\omega_m} = \frac{3 E_1 I_1}{2\omega_m} \ . \tag{4.8}$$

This operating conditon is usually used for the most of the PMSM models by assuming the ideal sinusoidal phase currents and back EMFs.

4.3.2 Shaped Back EMF + Sinusoidal Phase Current

If the magnets are shaped with optimal amplitude of the third harmonic, the fundamental flux density becomes higher. Hence, the fundamental phase back EMF also becomes higher. Assume the amplification factor of the fundamental back EMF is γ_e, the amplitude of the fundamental back EMF is

$$E_{1(+3\mathrm{rd})} = \gamma_e E_1 . \tag{4.9}$$

And also, γ_e satifies

$$\gamma_e = \gamma_e(B_3) \tag{4.10}$$

where γ_e is relevant to the amplitude of the third harmonic flux density B_3. The maximum value of γ_e has been analytically deduced in [WAN14a].

As for the third harmonic back EMF, the amplitude satisfies

$$E_3 \propto \omega k_{w3} B_3 \tag{4.11}$$

where k_{w3} is the winding factor for third harmonic back EMF.

Therefore, the three phase back EMFs are

$$\begin{aligned} e_a &= E_{1(+3\mathrm{rd})} \sin \omega t + E_3 \sin 3\omega t \\ e_b &= E_{1(+3\mathrm{rd})} \sin(\omega t + 2\pi/3) + E_3 \sin 3\omega t \\ e_c &= E_{1(+3\mathrm{rd})} \sin(\omega t - 2\pi/3) + E_3 \sin 3\omega t \end{aligned} \tag{4.12}$$

According to (4.1), the electromagnetic torque is

$$T_{eB} = \frac{e_a i_a + e_b i_b + e_c i_c}{\omega_m} = \frac{3E_{1(+3rd)} I_1}{2\omega_m} = \frac{3\gamma_e E_1 I_1}{2\omega_m} . \tag{4.13}$$

The third harmonic back EMFs have no contibution to the output torque component itselft and they are the only consequence of the third harmonic flux linkage. The improved torque is due to the increase of the fundamental back EMFs. This operating condition is usually the single three phase PMSM with Y connection. The zero sequence path in this drive is open circuit.

4.3.3 Sinusoidal Back EMF + Shaped Phase Current

Sinusodial back EMF + shaped phase current can be another possible combination, such as the PMSMs having sinusodial back EMFs and driven with third harmonic current injected in zero sequence. OW topology and connecting the middle point of DC bus capacitors to the neutral point of the machine can be feasible solutions. However, the low frequency harmonic current will induce the additional loss and increase of the tempreature of the capacitors which should be avoided. Hence, OW topology is preferable for zero sequence current injection implementation.

Under the same maximum current constraint with the third harmonic current injection, the fundamental current component will increase to

$$I_{1(+3rd)} = \gamma_i (I_3) I_1 \tag{4.14}$$

where γ_i is the amplification factor for fundamental current component, which depends on the amplitude of the injected third harmonic current I_3.

Hence, the three phase currents are

$$\begin{aligned} i_a &= I_{1(+3rd)} \sin \omega t + I_3 \sin 3\omega t \\ i_b &= I_{1(+3\mathrm{rd})} \sin(\omega t + 2\pi / 3) + I_3 \sin 3\omega t \\ i_c &= I_{1(+3\mathrm{rd})} \sin(\omega t - 2\pi / 3) + I_3 \sin 3\omega t \,. \end{aligned} \tag{4.15}$$

The three phase back EMFs are the same as (4.6). On the basis of (4.5), the electromagnetic torque is

$$T_{eC} = \frac{e_a i_a + e_b i_b + e_c i_c}{\omega_m} = \frac{3E_1 I_{1(+3rd)}}{2\omega_m} = \frac{3\gamma_i E_1 I_1}{2\omega_m} \,. \tag{4.16}$$

Similarly, only the fundamental component contributes to the increase of the torque capability for this condition.

4.3.4 Shaped Back EMF + Shaped Phase Current

Shaped back EMF + shaped phase current condition takes advantage of both conditions in Section 4.3.2 and Section 4.3.3, which means that both fundamental components of back EMF and phase current increase. Moreover, the third harmonic back EMF and the third harmonic current can interact to generate additional average torque componet and further enhance the torque capability.

The three phase back EMFs (4.12) in Section 4.3.2 and three phase currents (4.15) in Section 4.3.3 are combined. The electromagnetic torque can be expressed as

$$T_{eD} = \frac{e_a i_a + e_b i_b + e_c i_c}{\omega_m} = \left(\frac{3\gamma_e \gamma_i E_1 I_1}{2\omega_m} + \frac{3E_3 I_3}{2\omega_m}\right) - \frac{3E_3 I_3}{2\omega_m}\cos 6\omega t \tag{4.17}$$

where the term $\frac{3k_{w1}\gamma_e \gamma_i E_1 I_1}{2\omega_m} + \frac{3E_3 I_3}{2\omega_m}$ is DC component showing the average torque capability and the term $\frac{3E_3 I_3}{2\omega_m}\cos 6\omega \mathrm{t}$ is AC component showing the torque ripple characteristic.

In this paper, the prototype OW-PMSM has surface mounted and shaped magnets, the third harmonic back EMFs naturally exist. Together with the shaped phase current, this operating condition is the proposed strategy. It is also possible to utilize higher order back EMF harmonics by injecting the associated higher order current harmonics. However, the contribution from these harmonics will be very limited even with optimal design. Meanwhile, they are usually not in the same pattern for different PMSMs. Hence, the higher order harmonics are not discussed in this paper.

4.3.5 Optimal Injected Third Harmonic Current Amplitude

Since the driven PMSMs might contain different percentages of third harmonic back EMF component when different machine designs are applied, it is necessary to determine the optimal injected third harmonic current amplitude which is related to the percentage of third harmonic back EMF.

Assume phase A current as

$$i_a(t) = I_{1(+3\mathrm{rd})}\sin\omega t + I_3 \sin 3\omega t\,. \tag{4.18}$$

Define the third harmonic current percentage as

$$\rho = \frac{I_3}{I_{1(+3\mathrm{rd})}}\,. \tag{4.19}$$

Hence, phase A current can be represented as

$$i_a(t) = I_{1(+3\mathrm{rd})} \sin \omega t + \rho I_{1(+3\mathrm{rd})} \sin 3\omega t\,. \tag{4.20}$$

The extreme points of (4.20) can be obtained by letting

$$\frac{di_a(t)}{dt} = 0\,. \tag{4.21}$$

Consequently, the maximum values can be obtained as

$$I_{a-\max}(\rho) = \begin{cases} (1-\rho) I_{1(+3\mathrm{rd})},\, 0 < \rho \le \dfrac{1}{9} \\ 8 I_{1(+3\mathrm{rd})} \rho (\dfrac{1+3\rho}{12\rho})^{\frac{3}{2}},\, \rho > \dfrac{1}{9} \end{cases}. \tag{4.22}$$

When the constant amplitude constraint is applied, the maximum value should satisfy

$$I_{a-\max}(\rho) = I_1\,. \tag{4.23}$$

Meanwhile, the electromagnetic torque with shaped back EMF and shaped phase current can be expressed as

$$T_{eD} = \frac{3}{2\omega_m}(E_{1(+3rd)} I_{1(+3rd)} + E_3 I_3) = \frac{3}{2\omega_m}(E_{1(+3rd)} I_{1(+3rd)} + E_3 I_{1(+3rd)} \rho)\,. \tag{4.24}$$

When $0 < \rho \le \frac{1}{9}$, T_{eD} is monotonous increasing function upon ρ, the maximum torque occurs at $\rho = \frac{1}{9}$, which is

$$T_{eD1-\max} = \frac{3}{16\omega_m}(9E_{1(+3rd)} I_1 + E_3 I_1)\,. \tag{4.25}$$

When $\rho > \frac{1}{9}$, T_{eD} can be represented as

$$T_{eD}(\rho) = \frac{3}{2\omega_m}(E_{1(+3rd)} + E_3\rho)\frac{I_1}{8\rho}(\frac{1+3\rho}{12\rho})^{-\frac{3}{2}}\,. \tag{4.26}$$

The extreme point of T_{eD} should meet

$$\frac{dT_{eD}}{d\rho} = 0\,. \tag{4.27}$$

Namely, the optimal injected third harmonic current percentage for $\rho > \frac{1}{9}$ can be consequently obtained as

$$\rho = \frac{1}{6 - 3\frac{E_3}{E_{1(+3rd)}}}. \tag{4.28}$$

Since $\rho = \frac{1}{9}$ still does not reach the fundamental maximum value, (4.25) is obviously not the global maximum torque value, and hence, the maximum torque component should globally meet (4.28). When the third harmonic back EMF component is zero, namely, E_3=0, the optimal $\rho = \frac{1}{6}$ which enables a maximum fundamental component in the phase current. The measured phase back EMF waveform and the associated spectrum analysis of the tested OW-PMSM are shown in Figs. 4.3 (a) and (b). The relationship between percentage of third harmonic back EMF and the optimal third harmonic current is shown in Fig. 4.3 (c). The optimal operating point for the tested OW-PMSM is circled in Fig. 4.3 (c).

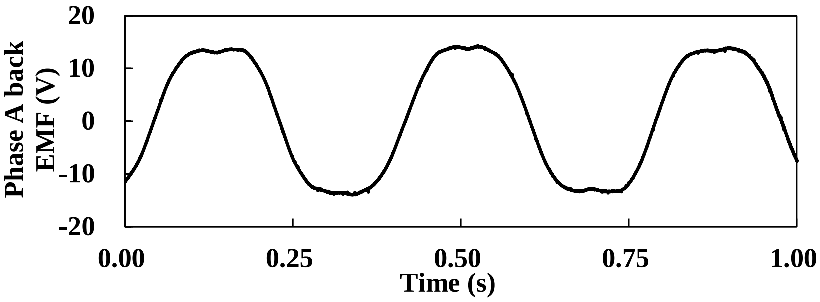

(a)

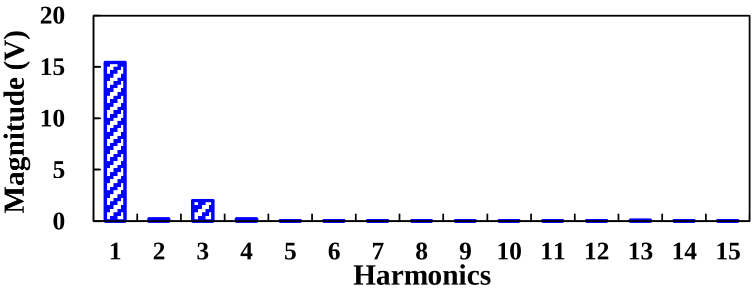

(b)

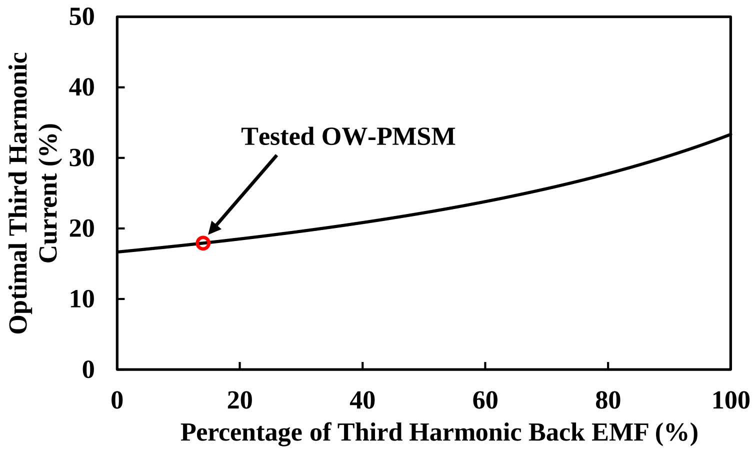

(c)

Fig. 4.3 Measured phase back EMF waveform, the associated spectrum analysis and the optimal third harmonic current curve against the percentage of third harmonic back EMF. (a) Phase back EMF. (b) Spectrum analysis. (c) The relationship.

Fig. 4.4 shows the average torque and torque ripple planes regarding to different third harmonic current and back EMF components. The operating points A, B C and D represent the conditions discussed in Sections 4.3.1 to 4.3.4. If concurrent design of the PMSM and controller can be achieved, the operating point D is the optimal point. However, most of the PMSMs in applications are designed independently and the percentage of third harmonic back EMF is not fixed. Meanwhile, the third harmonic current component can be adjusted freely. The optimal injected third harmonic current component should follow (4.28) to maximize the average torque. Nonetheless, it can be also observed from Fig. 4.3 (b) that the torque ripple introduced by third harmonic reaction will be increased together with average torque.

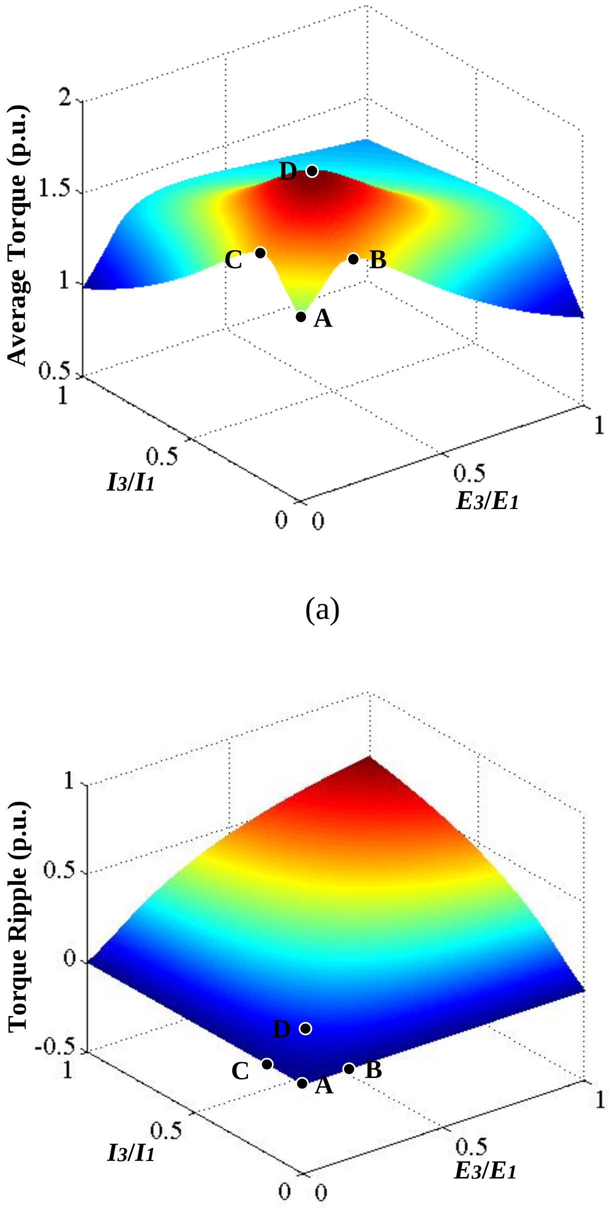

(a)

(b)

Fig. 4.4 Torque performance with different combinations of third harmonic back EMF and current components. (a) Average torque. (b) Torque ripple.

4.4 Implementation of Zero Sequence Current Control

In order to implement a controllable zero sequence loop, it is necessary to revise the SVPWM module to enable a steerable zero sequence component and a controller specifically for alternating component. Hence, the OW-PMSM drive will contain three current loops including *d*-, *q*-axes and zero sequence current loops.

4.4.1 Harmonic Current Reference Generator (HCRG)

The HCRG is used for generating appropriate zero sequence current reference signal and enabling torque enhancement or circulating current suppression effect. Namely, dual operating mode is possible for the OW-PMSM drive if losses or torque ripples are concerned. The sinusoidal current waveforms produce less copper loss and torque ripple [ZHA16a]. However, since the OW drive with common DC bus allows zero sequence circulating current, several suppression strategies with zero sequence controllers [AN16] [ZHO15] [ZHA16] are adopted. In the framework of the zero sequence current control, the zero sequence current suppression and the third harmonic current injection can be either achieved via appropriate reference signals without revising the control framework.

When the sinusoidal current mode is required, the reference signal is simply represented as

$$i_0^* = 0 . \tag{4.29}$$

In the torque enhancement mode, the reference signal is

$$i_0^* = \rho i_q^* \sin 3\theta \tag{4.30}$$

where ρ is decided by (4.28) and i_q^* is the q-axis current reference signal.

It can be seen that once the percentage of third harmonic back EMF contained in the phase back EMF is obtained, ρ is fixed for one specific OW-PMSM. Meanwhile, (4.30) is for field oriented control with $i_d^* = 0$. If nonzero i_d is applied, such as the flux weakening or maximum torque per ampere control, it requires further optimization.

4.4.2 Zero Sequence Controller

The same FA-PR controller and ZSS-SVPWM presented in Chapter 3, Section 3.2.1 are also utilized in this chapter for the purpose of deliberate zero sequence current injection.

4.5 Finite Element (FE) and Experimental Validations

4.5.1 FE Validation

The proposed torque enhancement can be firstly validated via 2 dimensional FE analysis. Fig. 4.5 shows the FE analysis results with and without shaped phase currents. The fundamental amplitude of the sinusoidal case is 2A and the amplitude of the injected third harmonic current is 0.412A which accounts for 17.83% of the fundamental component, namely, 2.31A. Fig. 4.5 (a) shows the corresponding phase A current waveform. The fundamental current component can be increased by injecting a third harmonic component and the total phase current waveform is saddle-shaped. The associated spectrum analysis is also shown in Fig. 4.5 (b).

Fig. 4.5 (c) shows the torque waveforms of the OW-PMSM with sinusoidal and shaped currents. The average torque of the shaped case is higher than that of the sinusoidal one. Fig. 4.5 (d) shows the spectrum analysis of the torque waveforms shown in Fig. 4.5 (c). It can be seen that the average torque of the sinusoidal one is 45.81Nm and that of the shaped one is 53.88Nm. The increased percentage is 17.62%. Meanwhile, according to (4.8) and (4.17), the theoretical improved average torque can be 18.06%. However, the calculation is based on a linear model which might not perfectly describe the nonlinear performance.

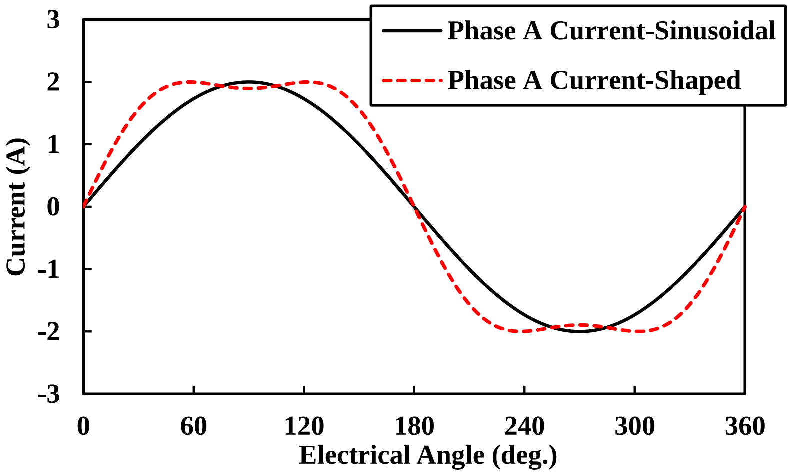

(a)

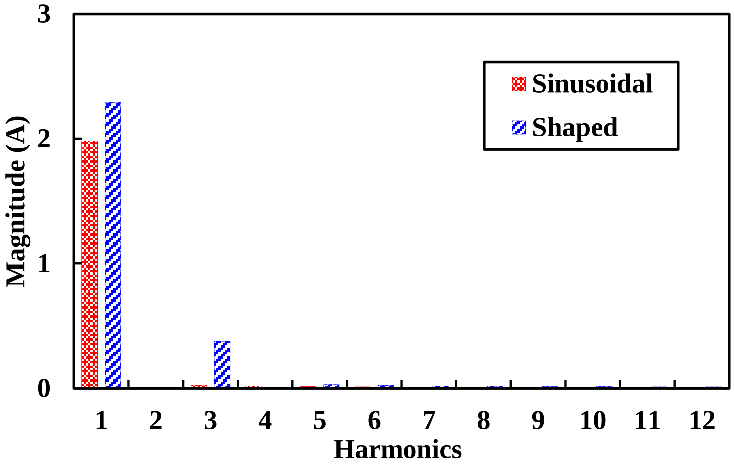

(b)

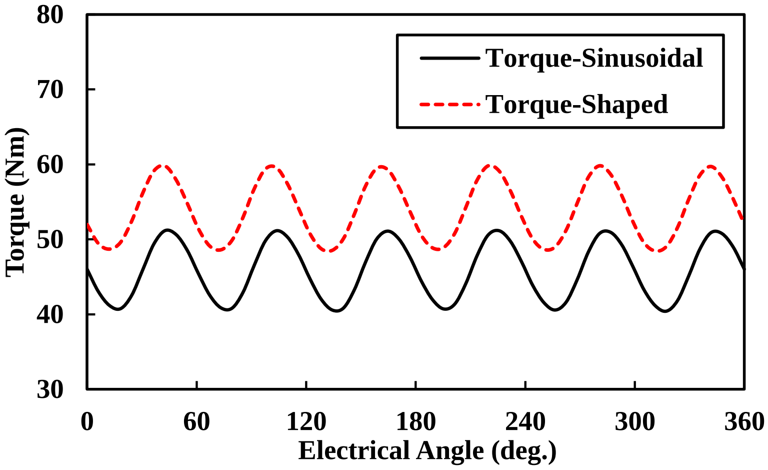

(c)

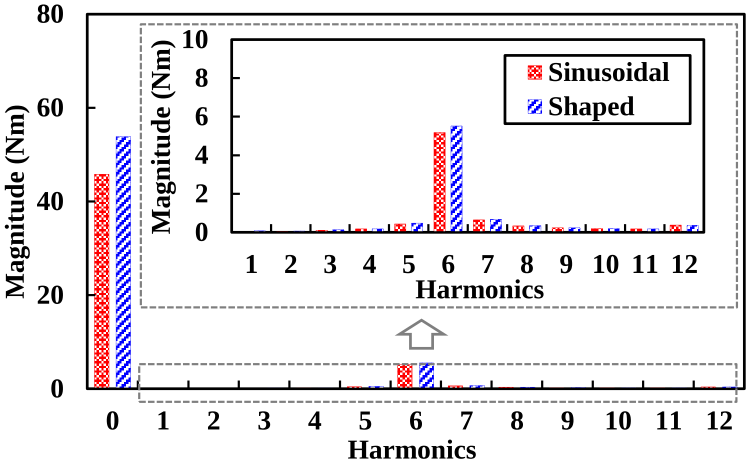

(d)

Fig. 4.5 FE analysis results with and without shaped phase currents. (a) Shaped and sinusoidal phase A current waveforms. (b) Spectrum analysis of the sinusoidal and shaped phase current waveforms. (c) Torque waveforms with and without shaped currents. (d) Spectrum analysis of the torque waveforms with and without shaped phase currents.

4.5.2 Experimental Validation

The proposed method is also experimentally validated on the prototype OW-PMSM drive system. The algorithm is implemented on the dSPACE system. Table I shows the specification of the prototype OW-PMSM. The switching frequency is 5kHz and the dead time is set to 2μs. Fig. 4.6 shows the experiment platform. The load is supplied by a three phase PMSM operating at generator mode with adjustable resistance load. The load can be adjusted via changing the load resistance.

TABLE I SPECIFICATION OF THE TESTED OW-PMSM

Parameter	Value
Pole pairs	16
Resistance (Ω)	3.76
Rated RMS current (A)	2.83
Rated speed (rpm)	170
Encoder resolution	4096
Rated frequency (Hz)	45.33
d-axis inductance (mH)	17
q-axis inductance (mH)	17

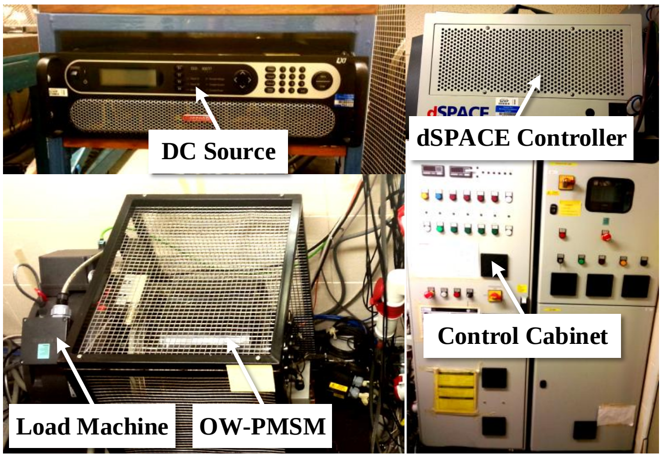

Fig. 4.6 Experiment platform.

Fig. 4.7 shows the measured phase A current and torque waveforms with sinusoidal phase current excitation. However, due to the inverter nonlinearity, slight zero current clamping effect is still observed. The fifth and seventh current harmonics can also be seen in the associated spectrum analysis in Fig. 4.9 (a). Fig. 4.8 shows the measured phase A current and the torque waveform with shaped phase current excitation. According to (4.28) and the percentage of the measured third harmonic back EMF, the optimal percentage of the third harmonic current is 17.83% which is consistent with the condition of the FE analysis in Section 4.5.1. Fig. 4.9 (b) shows the spectrum analysis of the measured torque waveforms with sinusoidal and shaped phase currents. It can be seen that the measured average torque is 45.24Nm for the sinusoidal phase current excitation and 53.16Nm for the shaped phase current excitation. The experimental increased percentage is 17.52%. The experiment confirms the effectiveness of the proposed method.

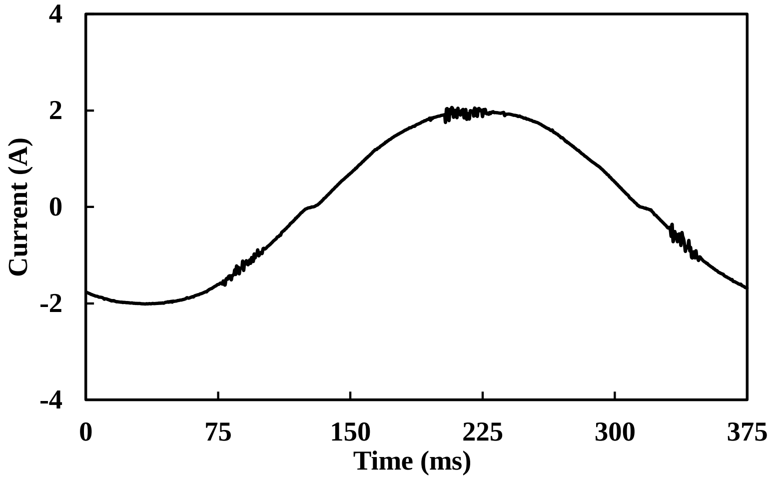

(a)

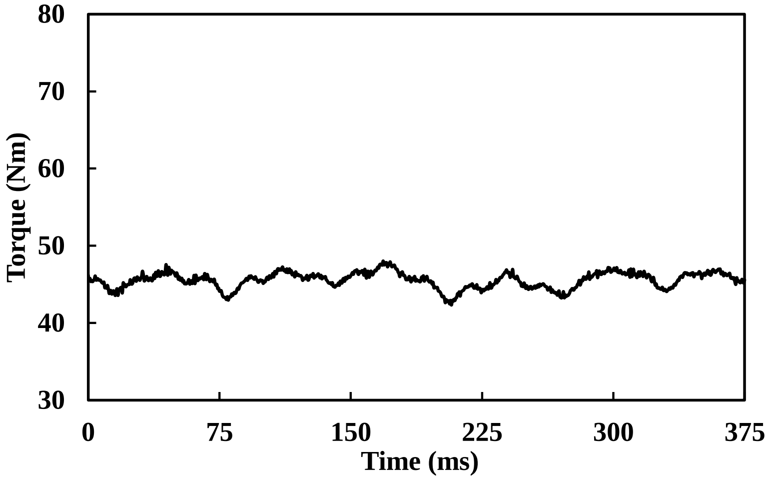

(b)

Fig. 4.7 Measured waveforms under sinusoidal phase current. (a) Phase A current. (b) Measured torque waveform (15rpm).

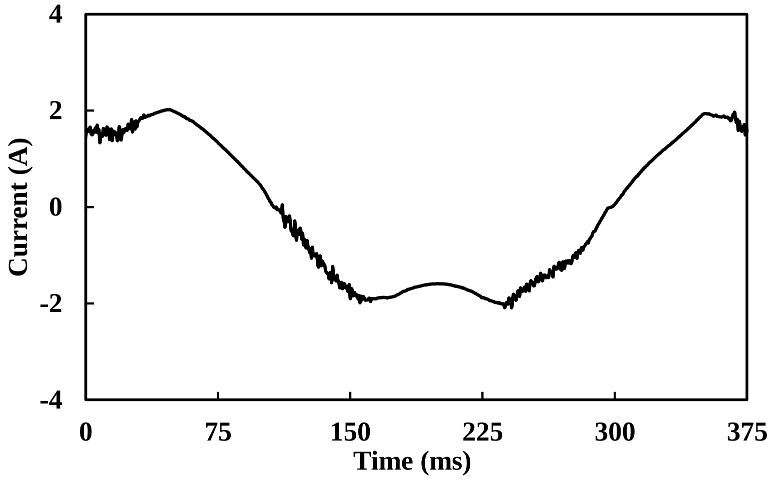

(a)

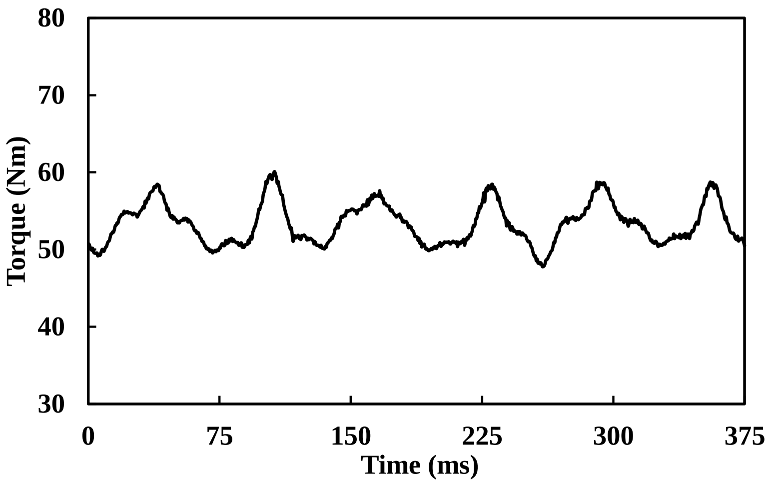

(b)

Fig. 4.8 Measured waveforms under shaped phase current. (a) Phase A current. (b) Measured torque waveform (15rpm).

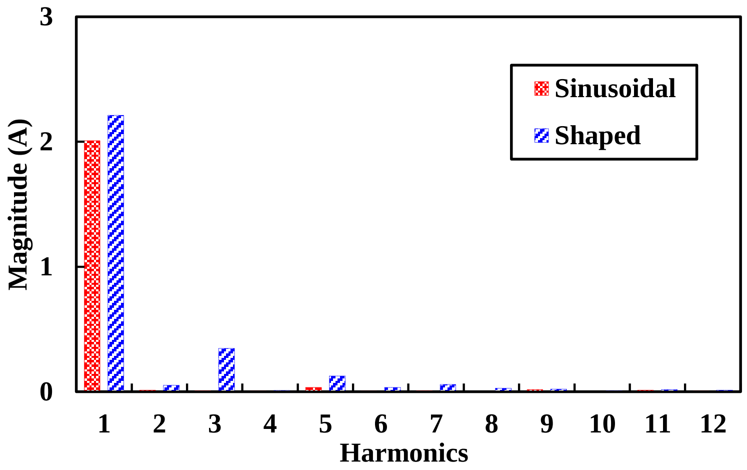

(a)

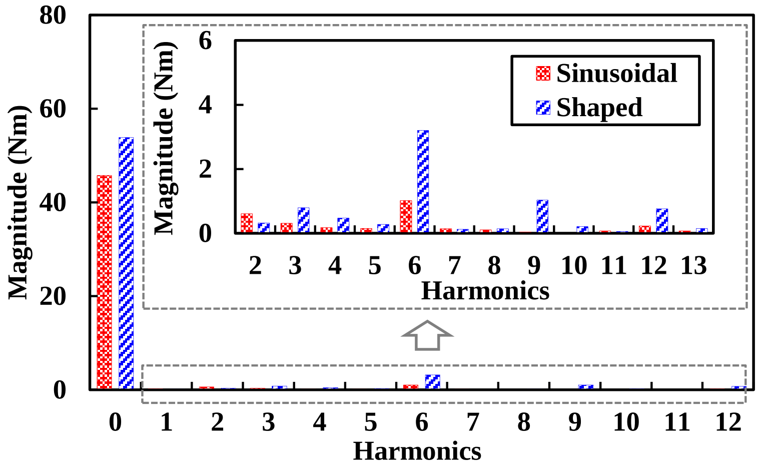

(b)

Fig. 4.9 Associated spectrum analysis. (a) Spectrum analysis of the sinusoidal and shaped phase currents. (b) Spectrum analysis of the measured torque waveforms with sinusoidal and shaped phase currents.

4.6 Conclusion

A torque enhancement method for OW-PMSM by using zero sequence current shaping has been proposed in this chapter. Meanwhile, the principle of the torque enhancement has been explained including the derivation of the theoretical percentage of the optimal third harmonic current component. The systematic implementation of the strategy together with the implementation details has also been presented. Finally, the FE and experimental results have validated the effectiveness of the proposed method. As for the prototype OW-PMSM, it has been proved that the theoretical increased average torque is 18.06%, which is verified via FE and experiment, being 17.62% and 17.52%, respectively.

CHAPTER 5 INHERENT TORQUE RIPPLE MITIGATION WITH REDUCED BANDWIDTH REQUIREMENT

The zero sequence current injection is used for torque enhancement in Chapter 4.The zero sequence current can also be used to minimize the torque ripple via its interaction with zero sequence back EMF and subsequently to reduce the bandwidth requirement for the current controller.

This chapter has been submitted to IEEE Transactions on Industrial Electronics.

5.1 Introduction

Permanent magnet synchronous machine has been widely used for wind power generation, electrical vehicle, industrial automation, etc. The requirements on the system performance progressively increase, in which, the torque ripple is always expected to be suppressed to low level to reduce the system noise and vibration. Hence, many methods have been proposed to achieve this target. In general, the methods can be categorized into two approaches including the machine design and control perspectives [JAH96].

From the machine design aspect, the rotor or stator skewing is commonly used for reducing the cogging torque of the PMSM [ISL09] [CHU13] [ZHU09]. Meanwhile, the back electro-motive force (EMF) harmonics causing pulsating torque ripples can be mitigated by using short pitch winding [HEN94], distributed winding [HEN94], permanent magnet shaping [SCU14] [JAN11], fractional slot [WU15], etc. However, for the ease of manufacture and the reduction of cost, these techniques from machine design perspective may not be feasible to be applied. Hence, the approaches [REN15] [PAR12] [CHO96] [JIA10] [ZHE16] [PET00] [SPR98] [MAT05] [MOR16] [SIA16] from the control side have also been proposed.

Firstly, the imperfect outputs of the inverter based drive can be compensated. In [REN15], the modified switching table based direct torque control is proposed, which is capable of inherently eliminating the harmonic voltages produced by the conventional vector combination. The harmonic currents and torque ripple can be consequently reduced. On the other side, the inverter nonlinearity inducing harmonic currents can also be compensated by feedforward or adaptive methods [PAR12] [CHO96]. In [PAR12], an adaptive dead time compensation method is proposed to eliminate the associated distorted output voltages. The quality of the phase currents has been improved. In addition to the perfection of the output voltages, the active current harmonics are also utilized to further optimize the torque performance of the PMSM drives. In [JIA10], the active harmonic current is deliberately injected in q-axis to produce compensatory torque ripple to mitigate the synthetic torque ripple. Meanwhile, by considering the open winding (OW) PMSM, in [ZHE16], the 5th and 7th phase current harmonics are actively utilized to achieve the same target, which is equivalent to 6th current harmonic injection in q-axis. Based on the same essence, the adaptive attempt has also been carried out. In [PET00], the adaptive controller based algorithm is proposed to achieve torque ripple minimization by 27dB experimentally.

Meanwhile, another popular approach also arises recently is the high dynamic/bandwidth controller based strategy [SPR98] [MAT05] [MOR16] [SIA16]. The ripple in the speed feedback induced by the torque ripple can consequently cause the response of the speed controller and the generation of the current reference harmonic, or applying the feedforward signal, the current controller regulates the corresponding reference harmonics to compensate the torque ripple. Usually, this principle requires high dynamic/bandwidth of the controller and the conventional PI controller has the limit. In [SPR98], a deadbeat current controller having high bandwidth is used to mitigate the torque ripple. The repetitive current controller [MAT05] is also adopted together with the periodic q-axis current reference to reduce the torque ripple of the PMSM drive. Moreover, the model predictive torque control strategy is put forward in [MOR16] to enable the torque ripple compensation in variable speed PMSM drive, in which, the feedforward signal is applied in the torque loop. As for the torque ripple reduction of predictive control with parameter mismatch, an improved method is proposed in [SIA16] to reduce the uncertainty and improve the prediction accurateness.

Although the methods proposed so far vary a lot, the essence is still based on generating harmonic currents in q-axis to compensate the existing torque ripple. The fundamental back EMF interacting with the harmonic current produces the demanded torque component. In this chapter, the zero sequence alternating current which does not modulate with the fundamental back EMF is utilized instead. The modulation with the zero sequence back EMF that produces higher order alternating torque component becomes the compensation countermeasure. The brought benefit is that the frequency of injected current harmonic consequently reduces. Hence, the bandwidth burden imposed on the current controller decreases. Typically, to suppress the 6th torque ripple, the injected current harmonic decreases from the 6th to the 3rd. The proposed method is particularly suitable for the high power drives with low switching frequency and the high speed drives that naturally have limited current controllability. This chapter is organized as follows: In Section 5.2, the torque analysis is introduced. In Section 5.3, the conventional torque ripple mitigation strategy is briefly presented. In Section 5.4, the principle of the proposed method is described. The systematic implementation is shown in Section 5.5. The finite element (FE) and experimental validations are shown in Section 5.6.

5.2 Torque Ripple Analysis

The torque ripple analysis of the PMSM/OW-PMSM drive system is presented in this section. In general, the torque ripple could be induced by non-ideal effects from both the machine and control sides. From the machine side, the inherent cogging torque and harmonic back EMFs could both contribute to the torque ripple. From the control side, the non-ideal current control due to the inverter nonlinearity could produce distorted current including the 5th, 7th, 11th and 13th harmonics currents. Therefore, they will also induce corresponding torque ripples. Usually, the 6th torque ripple is the lowest order and most dominant component, which will be explained in the following analysis in this section.

5.2.1 Cogging Torque

One of the prominent causes of the torque ripple is due to the cogging torque in the PMSMs. The number of cogging torque ripple within one mechanical cycle satisfies [ZHU09]

$$N_L = \mathrm{LCM}(N_S, N_P) \tag{5.1}$$

where N_S is the number of slots of the PMSM, N_P is the number of poles of the PMSM and LCM represents the lowest common multiple.

Hence, the number of times of the cogging torque within one electrical cycle is

$$N_C = \frac{2N_L}{N_P}. \tag{5.2}$$

Specifically, the investigated and tested PMSM with OW topology is 96 slot/32 pole and hence the number of times of the cogging torque can be obtained, viz., 6, according to (5.1) and (5.2). Fig. 5.1 shows the 2 dimensional (2D) finite element (FE) predicted cogging torque waveform and the corresponding spectrum analysis of the investigated OW-PMSM. It can be seen that the sixth harmonic torque component is the most dominant one, which is in accordance with the analytical result.

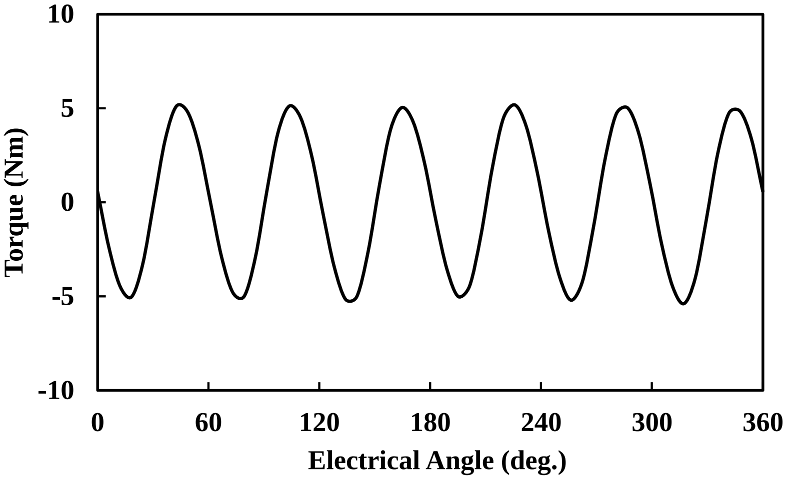

(a)

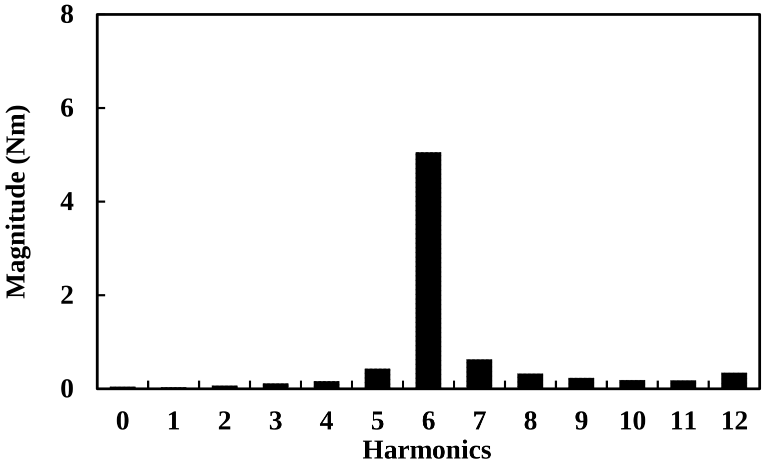

(b)

Fig. 5.1 2D FE cogging torque waveform and the spectrum analysis of the investigated OW-PMSM at open circuit. (a) Cogging torque waveform. (b) Spectrum analysis.

5.2.2 PM Flux Linkage Harmonic

Due to the non-sinusoidal air gap PM flux density distribution at open circuit, the 5th, 7th, 11th and 13th back EMF harmonics in the phase are frequently observed in the PMSMs. In which, the 5th and 7th harmonic back EMFs are the majority. The 11th and 13th can be neglected. These back EMF harmonics are from the PM flux linkage harmonics. Skewing, specific winding configuration and magnet shaping can be used to mitigate them. The negative effect of the 5th and 7th back EMF harmonics is the deterioration of control performance including larger estimation error in sensorless drives [WAN14d] and the induced torque ripple.

In order to analyze the torque ripple induced by them, the three phase PM flux linkage variation of the OW-PMSM can be represented as

$$\psi_a = \Psi_1 \cos(\omega t) + \Psi_5 \cos(5\omega t + \theta_5) + \Psi_7 \cos(7\omega t + \theta_7) \tag{5.3}$$

$$\psi_b = \Psi_1 \cos(\omega t - 2\pi/3) + \Psi_5 \cos(5\omega t + 2\pi/3 + \theta_5) + \Psi_7 \cos(7\omega t - 2\pi/3 + \theta_7) \tag{5.4}$$

$$\psi_c = \Psi_1 \cos(\omega t + 2\pi/3) + \Psi_5 \cos(5\omega t - 2\pi/3 + \theta_5) + \Psi_7 \cos(7\omega t + 2\pi/3 + \theta_7) \tag{5.5}$$

where Ψ_1, Ψ_5 and Ψ_7 are the amplitudes of the fundamental, fifth and seventh flux linkage components.

Transform (5.3)-(5.5) into *dq* axes as

$$\psi_{d-pm} = \Psi_1 + \Psi_5 \cos(6\omega t + \theta_5) + \Psi_7 \cos(6\omega t + \theta_7) \tag{5.6}$$

$$\psi_{q-pm} = -\Psi_5 \sin(6\omega t + \theta_5) + \Psi_7 \sin(6\omega t + \theta_7)\,. \tag{5.7}$$

Meanwhile, the electromagnetic torque of the OW-PMSM can be expressed as

$$T_e = \frac{3}{2} p(\psi_d i_q - \psi_q i_d) \tag{5.8}$$

where p is the number of pole pairs, i_d is the *d*-axis current, i_q is the *q*-axis current and

$$\psi_d = \psi_{d-pm} + L_d i_d \tag{5.9}$$

$$\psi_q = \psi_{q-pm} + L_q i_q \tag{5.10}$$

where L_d represents the *d*-axis inductance, L_q represents the *q*-axis inductance, $\psi_{d\text{-}pm}$ is the coupled PM flux linkage in *d*-axis including harmonics and $\psi_{q\text{-}pm}$ is the coupled PM flux linkage in *q*-axis including harmonics as well. The PM flux linkage is not coupled with *q* axis for ideal PMSM model. But when the harmonics are considered, the *q* axis flux linkage also contains PM flux linkage harmonics.

Hence, substitute (5.9) and (5.10) into (5.8)

$$T_e = \frac{3}{2} p\{\psi_1 i_q + (L_d - L_q) i_d i_q + \sqrt{i_d^2 + i_q^2}[\psi_5 \sin(6\omega t + \theta_5 + \gamma) - \psi_7 \sin(6\omega t + \theta_7 + \gamma)]\} \tag{5.11}$$

where $\gamma = \arctan(i_q / i_d)$.

Further, the alternating torque component is

$$T_{e-f} = \frac{3}{2} p \sqrt{i_d^2 + i_q^2} [\psi_5 \sin(6\omega t + \theta_5 + \gamma) - \psi_7 \sin(6\omega t + \theta_7 + \gamma)] . \tag{5.12}$$

It can be seen that the torque ripple is the 6th harmonic and related to the armature current, amplitudes and phases of the 5th and 7th PM flux linkages. Assume the armature currents are constant, the 6th torque ripple is from the modulation between the fundamental armature currents and the 5th and 7th back EMF harmonics. As it should be, the armature currents might contain harmonics that could also induce torque ripple, which will be analyzed in Section II (C).

Define $\Delta\psi = \psi_5 - \psi_7$ and $\Delta\theta = \theta_5 - \theta_7$. Meanwhile, normalize $\sqrt{\psi_5^2 + \psi_7^2} = 1$, $\sqrt{i_d^2 + i_q^2} = 1$ and *p*=1, the torque ripple induced by PM flux linkage can be shown in Fig. 5.2.

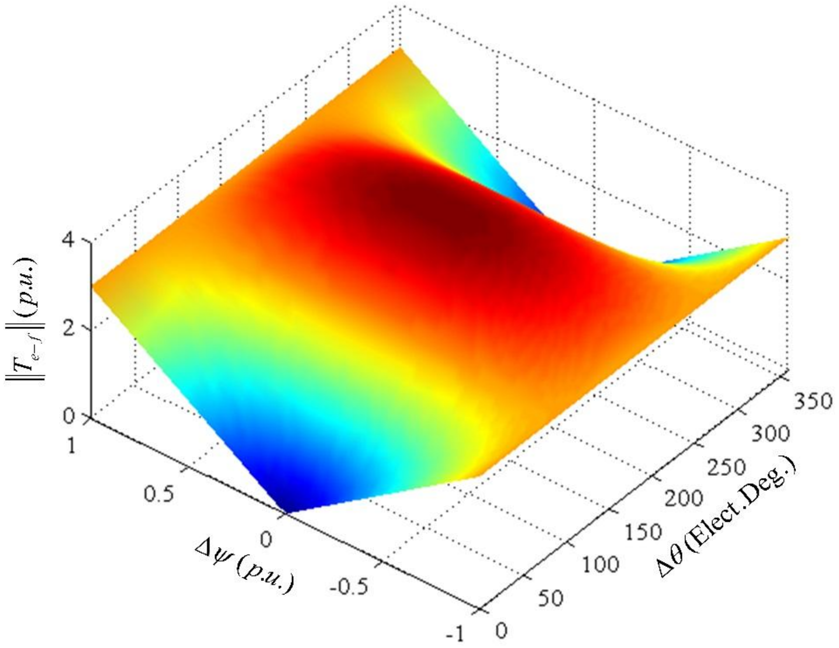

Fig. 5.2 Magnitude of torque ripple induced by PM flux linkage.

5.2.3 Inverter Nonlinearity

In order to avoid the shoot-through state of the half bridge, the dead time should be inserted. The inserted dead time consequently induces the distortion of the output voltage from the inverter, which is different from the reference signals. Not only are the drop of the fundamental component, but also the associated voltage harmonics produced through this effect, which is the inverter nonlinearity. In addition, the equivalent dead time considering both the set dead time and the inverter nonlinearities can be calculated as follows

$$T_{cn} = T_d + t_{on} - t_{off} + \frac{U_{on}}{U_{dc}} T_s \tag{5.13}$$

where T_d is the configured dead time by the DSP registers, t_{on} and t_{off} are the turn-on time and turn-off time of the switching device, respectively, U_{on} is the average conductive voltage drop of the device, U_{dc} is the DC bus voltage and T_s is the PWM period. Hence, ΔU_{err} indicating the arbitrary phase voltage error can be calculated from

$$\Delta U_{err} = \frac{T_{cn}}{T_s} U_{dc}\,. \tag{5.14}$$

Meanwhile, according to the current commutation analysis [CHO96] in the inverter, the distortion voltages of the inverter can be represented as the functions of the three phase currents:

$$\begin{bmatrix} u_{err-A} & u_{err-B} & u_{err-C} \end{bmatrix}^T = \begin{bmatrix} sign(i_a) & sign(i_b) & sign(i_c) \end{bmatrix}^T . \tag{5.15}$$

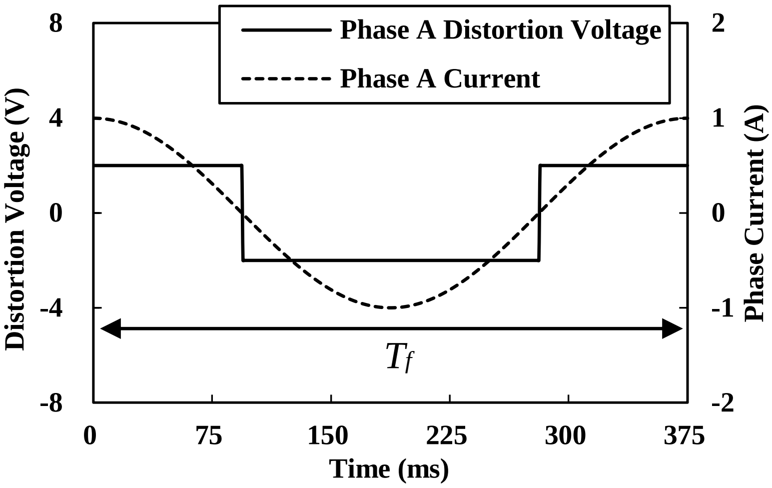

Fig. 5.3 Phase A current and distortion voltage waveforms.

Take phase A as an example, the periodic function of the distortion voltage within on period can be expressed as

$$u_{err-A}(t) = \begin{cases} \Delta U_{err}, -\dfrac{T_f}{2} \le t < -\dfrac{T_f}{4} \\ -\Delta U_{err}, -\dfrac{T_f}{4} \le t < \dfrac{T_f}{4} \\ \Delta U_{err}, \dfrac{T_f}{4} \le t < \dfrac{T_f}{2} \end{cases} \tag{5.16}$$

where t is the time and T_f is the period of the fundamental signal.

The Fourier series of (5.16) can be obtained as

$$u_{err-A}(t)=\sum_{n=1}^{\infty}a_n\cos(\frac{2n\pi t}{T_f}) \tag{5.17}$$

where

$$a_n=\begin{cases}0, n=2k \\ \dfrac{(-1)^k 4\Delta U_{err}}{n\pi}, n=2k-1\end{cases} k=1,2,3.... \tag{5.18}$$

The amplitude and phase spectrum analysis for three phase distortion voltages with ΔU_{err}=2V are shown in Fig. 5.4. Since the third, ninth, fifteenth…harmonics are in the zero sequence which can be suppressed by the zero sequence controller [ZHA16a], the fifth and seventh harmonics are the dominant interferences. The fifth harmonic is negative sequence and the seventh is positive sequence. Consequently, modulated by the rotor position, the fifth and seventh harmonics will result in sixth harmonic in the synchronous frame. The associated current ripples will be induced.

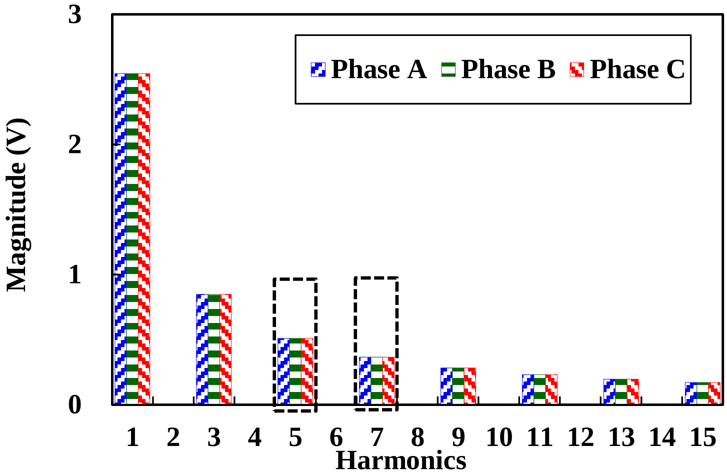

(a)

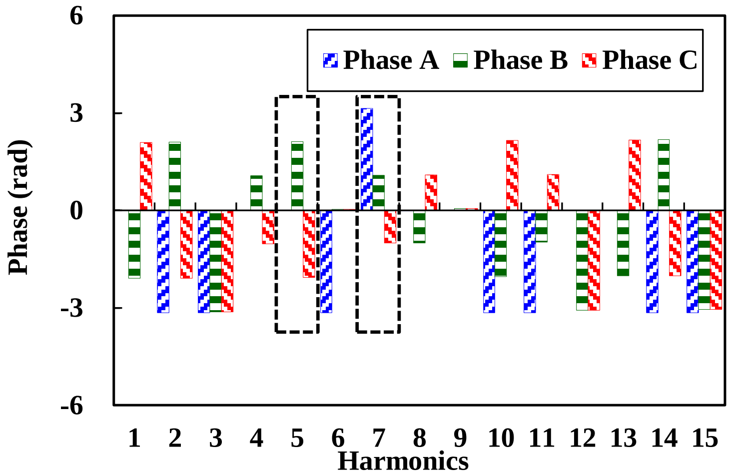

(b)

Fig. 5.4 Amplitude and phase spectrum analysis for three phase distortion voltages. (a) Amplitude spectrum. (b) Phase spectrum.

Assume the sixth current harmonics in *d*- and *q*-axes can be represented as

$$i_d = I_d + I_{d6} \sin(6\omega t + \delta_d) \tag{5.19}$$

$$i_q = I_q + I_{q6} \sin(6\omega t + \delta_q) \tag{5.20}$$

where I_d and I_q are the DC components, I_{d6} and I_{q6} are the amplitudes of the sixth harmonics in *d*- and *q*-axes, and δ_d and δ_q are the phases of the six harmonics in *d*- and *q*-axes.

Substitute (5.19) and (5.20) into (5.8) and the torque ripple generated by the interaction between the fundamental flux linkage and the sixth harmonic currents can be obtained as

$$T_{e-i} = \frac{3}{2} p \sqrt{H_1^2 + H_2^2 + 2H_1 H_2 \cos(\delta_d - \delta_q)} \sin(6\omega t + \delta_6) \tag{5.21}$$

where

$$H_1 = \Psi_1 I_{q6} + (L_d - L_q) I_d I_{q6} \tag{5.22}$$

$$H_2 = (L_d - L_q) I_q I_{d6} . \tag{5.23}$$

Due to the relative small proportion, the resulting higher order torque ripple harmonics including the interactions between the sixth current harmonics and the flux linkage harmonics and the twelfth reluctant torque ripple produced by the sixth current harmonics in *d*- and *q*-axes are neglected.

5.2.4 Total Torque Ripple

The total torque ripple is the superposition of cogging torque, flux linkage harmonics induced torque ripple and the inverter nonlinearity induced torque ripple. The expression can be summarized as

$$T_{e-r} = T_{e-c} + T_{e-f} + T_{e-i} \tag{5.24}$$

where $T_{e\text{-}c}$ represents the cogging torque. Hence, according to the analysis, the primary torque ripple can be the sixth harmonic for many PMSMs.

5.3 Conventional Torque Ripple Mitigation Strategy

In the conventional torque ripple mitigation strategies, the high dynamic of the controller in *q*-axis is required. This is due to the reversal current reference harmonic is usually generated reversely to compensated the torque ripple. In order to perfectly track the current reference signal, the controller should be capable of high bandwidth. Fig. 5.5 shows the typical framework usually adopted in the conventional methods. In Fig. 5.5, the FSG represents the feedforward signal generator and the HBC represents the high bandwidth controller. In different methods, the FSG could exist or not. If the FSG does not exist, it requires high bandwidth on the speed controller and the torque ripple which is reflected on the speed ripple can be consequently suppressed. If the FSG is used, which could be named in different ways, the synthetic *q*-axis current reference is sent to HBC and the desired current control can be achieved. The FSG could be adaptive, model based or even lookup table based. No matter what kinds of FSG implementations are adopted, the requirement on the HBC for the high frequency current, such as sixth times harmonic current, is the same.

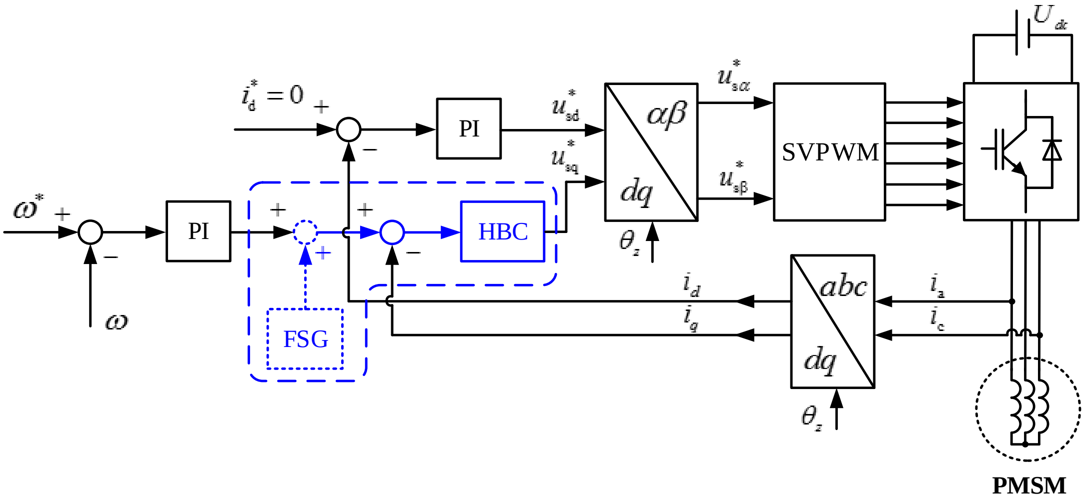

Fig. 5.5 Typical framework of conventional torque ripple mitigation strategies.

5.4 Principle of Proposed Torque Ripple Mitigation Strategy

In the conventional mitigation strategies, the reversal high frequency is generated and will interact with the fundamental back EMF component of the PMSM to create compensating torque component. The generated high frequency current should be in the same frequency as the torque ripple. However, for the drive system with low switching frequency (high power system) or operating in the high speed, the high frequency current control performance is limited which is due to the decrease of the PWM periods within one fundamental operating period of the machine. Hence, it will degrade the torque ripple mitigation performance for the conventional method. In the proposed method, the sixth harmonic current is no longer generated to interact with the fundamental back EMF component. But the third harmonic back EMF in the zero sequence is utilized. With the aid of the existing zero sequence path in the OW-PMSM drive system, the zero sequence current which is the third harmonic is injected to modulated with the zero sequence back EMF. Therefore, the expecting sixth torque ripple can be generated to compensate the existing torque ripple in the drive system.

However, it should also be noticed that the proposed method requires the existence of the third harmonic zero sequence back EMF in the phase back EMF. In general, the third harmonic is not eliminated on purpose in the machine design since it only emerges in the zero sequence. For the conventional single three phase drive system with Y connection, the equivalent zero sequence path is open circuit, and hence, it will not induce issues for the PMSM performance. Meanwhile, the third harmonic back EMF can also be designed by shaping the PMs for the average torque enhancement of the PMSM. The saturation in the teeth could also increase the third harmonic back EMF component. The third harmonic zero sequence back EMF is commonly observed in the PMSMs [SHE06].

The three phase back EMFs of the OW-PMSM can be expressed as

$$\begin{aligned} e_a &= E_1 \sin \omega t + E_3 \sin 3\omega t \\ e_b &= E_1 \sin(\omega t + 2\pi/3) + E_3 \sin 3\omega t \\ e_c &= E_1 \sin(\omega t - 2\pi/3) + E_3 \sin 3\omega t \end{aligned} \tag{5.25}$$

where E_1 and E_3 are the amplitudes of the fundamental and third harmonic back EMFs.

Meanwhile, the three phase current with third harmonic zero sequence current injection can be represented as

$$i_a = I_1 \sin \omega t + I_3 \sin(3\omega t + \Delta\delta_3)$$

$$i_b = I_1 \sin(\omega t + 2\pi/3) + I_3 \sin(3\omega t + \Delta\delta_3) \tag{5.26}$$

$$i_c = I_1 \sin(\omega t - 2\pi/3) + I_3 \sin(3\omega t + \Delta\delta_3)$$

where I_1 and I_3 are the amplitudes of the fundamental and third harmonic currents and $\Delta\delta_3$ is the phase angle of the third harmonic zero sequence current.

The produced torque can be consequently expressed as

$$T_e = \frac{i_a e_a + i_b e_b + i_c e_c}{\omega_m} = \frac{3(E_1 I_1 + E_3 I_3 \cos \Delta\delta_3)}{2\omega_m} - \underbrace{\frac{3}{2} E_3 I_3 \cos(6\omega t + \Delta\delta_3)}_{\text{Active Sixth Torque Harmonic}}. \tag{5.27}$$

It can be found that the active sixth torque harmonic component is $\frac{3}{2} E_3 I_3 \cos(6\omega t + \Delta\delta_3)$. The associated amplitude and phase of the active sixth torque harmonic are controllable by simply varying the injected zero sequence current including its amplitude and phase angle.

Meanwhile, according to the analysis in Section III, the amplitude and phase of the inherent sixth torque ripple of the OW-PMSM can vary for different OW-PMSMs. Hence, the generalized expression of the inherent sixth torque ripple of the OW-PMSM can be further written as

$$T_{e-r} = H_6 \cos(6\omega t + \gamma_6) \tag{5.28}$$

where H_6 and γ_6 are the amplitude and phase of the inherent sixth torque ripple of the OW-PMSM.

Hence, the optimal operating point, namely, the lowest synthetic torque ripple point satisfies

$$T_{e-r} = -\frac{3}{2} E_3 I_3 \cos(6\omega t + \Delta\delta_3). \tag{5.29}$$

And then, the criterion is

$$\begin{cases} I_3 = -\dfrac{2H_6}{3E_3} \\ \Delta\delta_3 = \gamma_6 \end{cases}. \tag{5.30}$$

Once the criterion is reached, the relevant inherent torque ripple can be consequently suppressed. The required zero sequence third harmonic current should be regualated properly.

5.5 Systematic Implementation

5.5.1 System Configuration

According to the analysis in the Section IV (A), the systematic implementation is constructed as Fig. 5.6. The OW-PMSM adopts common DC bus to form the zero sequence path. Meanwhile, the CCRG in Fig. 5.6 represents the compensation current reference generator, the FA-PR controller represents the frequency adaptive-proportional resonant controller and ZSS-SVPWM means zero sequence steerable-SVPWM. The key point of the implementation is construction of the zero sequence control loop which includes the CCRG, FA-PR controller and the ZSS-SVPWM. The CCRG is responsible for generating proper compensation current reference to ensure the torque ripple mitigation effect. An adaptive AC signal capable controller should be used to track the alternating third harmonic reference. The conventional SVPWM should be revised to provide controllable zero sequence component, namely, the redistribution of the zero vectors.

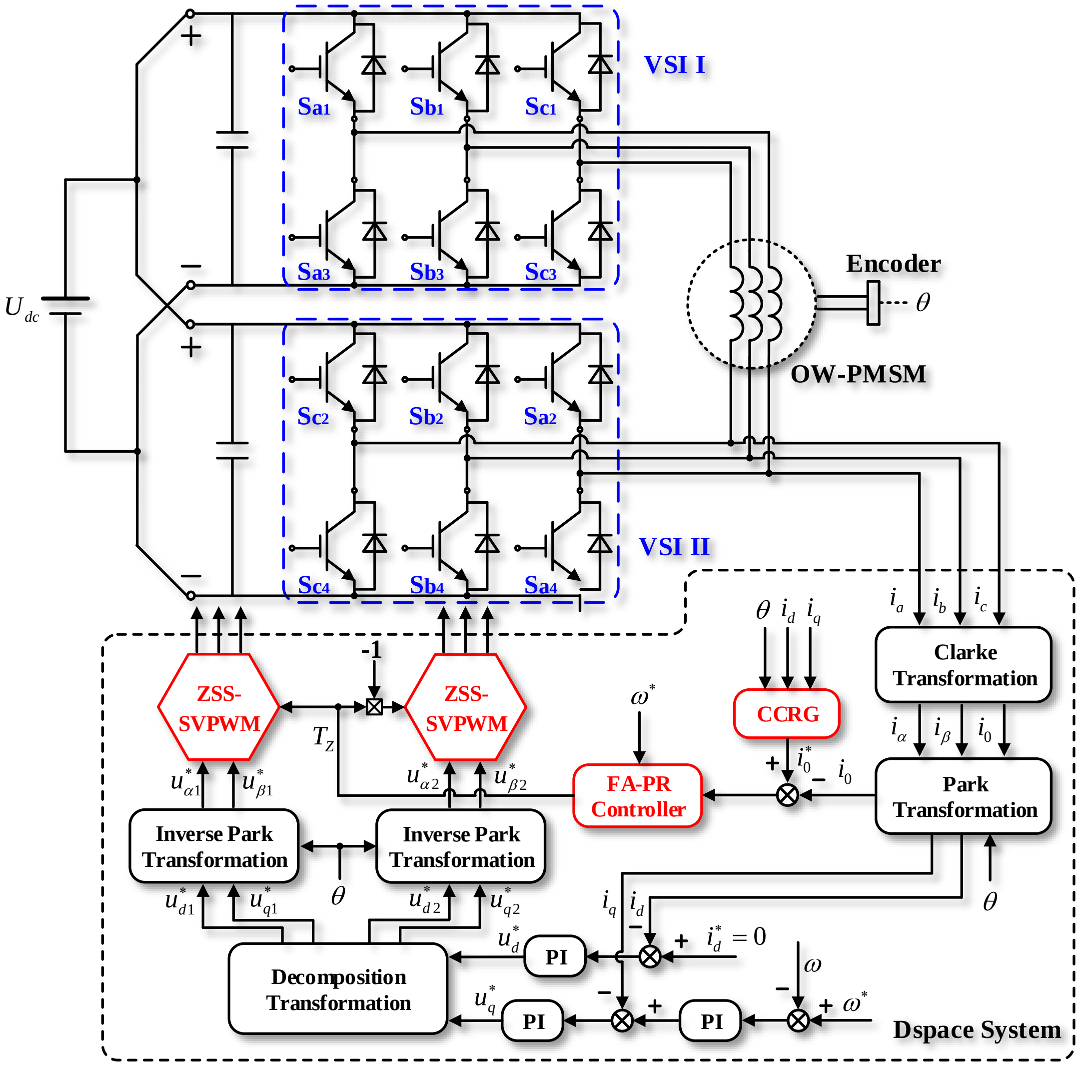

Fig. 5.6 Systematic implementation of the proposed torque ripple mitigation strategy.

5.5.2 CCRG

It should be noticed that the CCRG can be either adaptive or off-line data based. Several torque mitigation strategies have been proposed in the adaptive way by using the torque transducer or speed ripple information to minimize the torque ripple. From this aspect, the CCRG can be achieved in the similar way. However, the adaptive implementation might be lack of fast dynamic and increase the complexity of the algorithm. At the primary verification stage of the proposed method, the off-line data based CCRG is used. Together with the torque transducer, the optimal suppression point can be achieved at each loaded points. The reference signal can be generated as

$$i_0^* = I_3(i_d, i_q)\sin[3\theta + \Delta\delta_3(i_d, i_q)]\,. \tag{5.31}$$

Since the i_d=0 is often used, the reference signal can be further simplified as

$$i_0^* = I_3(i_q)\sin[3\theta + \Delta\delta_3(i_q)] \,. \tag{5.32}$$

5.5.3 Zero Sequence Current Control

In order to control the reference AC signal, the PR controller is utilized. Meanwhile, the frequency feedback is also used to enable the adaptive capability of the PR controller. The centre frequency used in the generalized integrator is from the operation frequency feedback. Hence, the zero sequence current controller can regulate the corresponding third harmonic in various operation frequency. The block diagram of the FA-PR controller is shown in Fig. 3.4.

Meanwhile, the transfer function of the FA-PR controller can be expressed as

$$C(s) = K_p + \frac{K_i s}{s^2 + \omega_0^2} \tag{5.33}$$

where K_p is the proportional coefficient and K_i is the resonant coefficient.

The block diagram of the zero sequence regulating loop can be plotted as Fig. 5.7. The center frequency feedback can be obtained from the position sensor, such as encoder or resolver. The inverter is regarded as a zero order hold with K_{PWM} as the amplification coefficient and τ_s as the time constant. The feedforward component represents the zero sequence back EMF. R_s is the winding resistance. L_{s0} is the average inductance of the self-inductance. M_{s0} is the average inductance of the mutual-inductance. L_{s0}-$2M_{s0}$ represents the zero sequence inductance. τ_d is the time constant of the sampling.

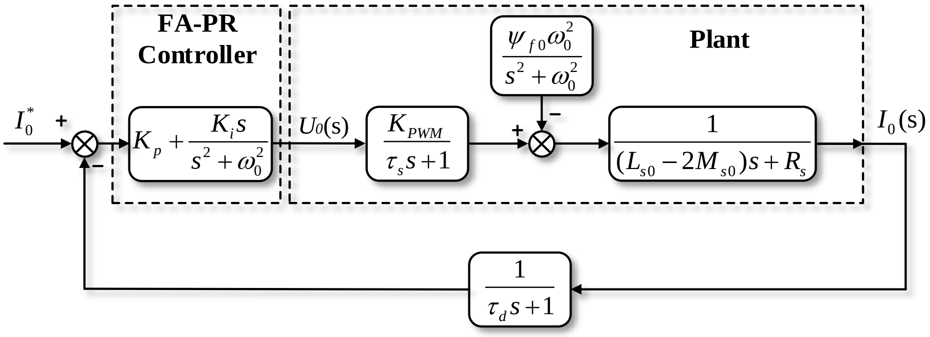

Fig. 5.7 Block diagram of the zero sequence regulating loop.

5.6 FE and Experimental Validation

5.6.1 FE Validation

The FE validation of the proposed torque mitigation strategy is carried out by varying the amplitude and phase of the injected zero sequence third harmonic current to observe the ripples of the final torque waveforms. The prototype OW-PMSM is 96 slots/32 poles. Fig. 5.8 shows the torque ripple plane under different amplitudes and phases of the injected third harmonic currents, which is quantified into percentage of the rated torque. It can be seen that the conventional excitation, namely, the sinusoidal current excitation (0A, 0 elect. deg.) produces much higher torque ripple than the optimal operating point (1A, 90 elect. deg.) shown in Fig. 5.8, which is also the global optimal point. The torque ripple can be minimized to 1.6% when compared to the normal operation with 11.2% torque ripple. Hence, the torque ripple mitigation effect is clearly obtained by the proposed method.

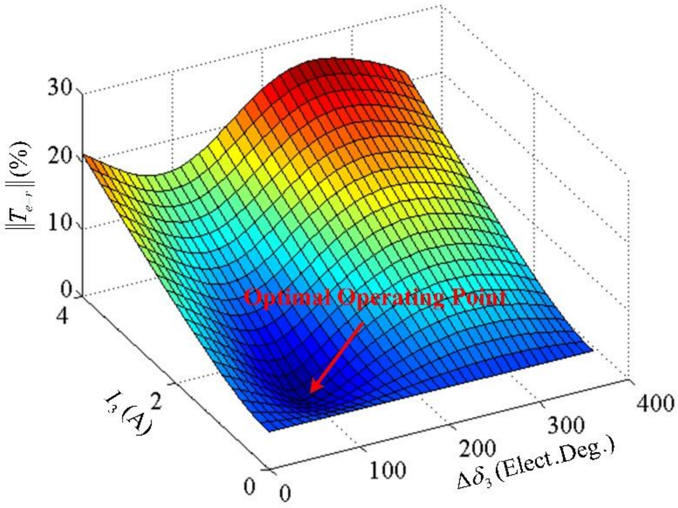

Fig. 5.8 Quantified torque ripple plane under different amplitudes and phases of the injected third harmonic currents.

Meanwhile, in order to observe the effects in detail, the operating waveforms of the typical operating points are shown in Fig. 5.9. Fig. 5.9 (a) shows the phase A current waveforms under sinusoidal current excitation and the optimal injection conditions. The amplitude and phase of the injected zero sequence third harmonic current are 1A and 90 elect. deg., respectively. Fig. 5.9 (b) shows the associated spectrum analysis. Fig. 5.9 (c) shows the associated instantaneous torque waveforms within one electrical period. The torque ripple mitigation can be visually observed. Further to that, the spectrum analysis of the torque waveforms shown in Fig. 5.9 (b) is shown in Fig. 5.9 (d). As the expectation, the sixth torque ripple reduces to the negligible level when compared to the conventional excitation.

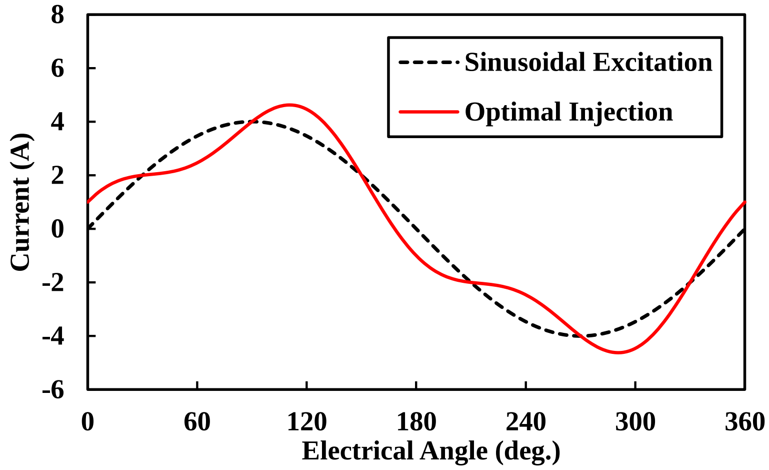

(a)

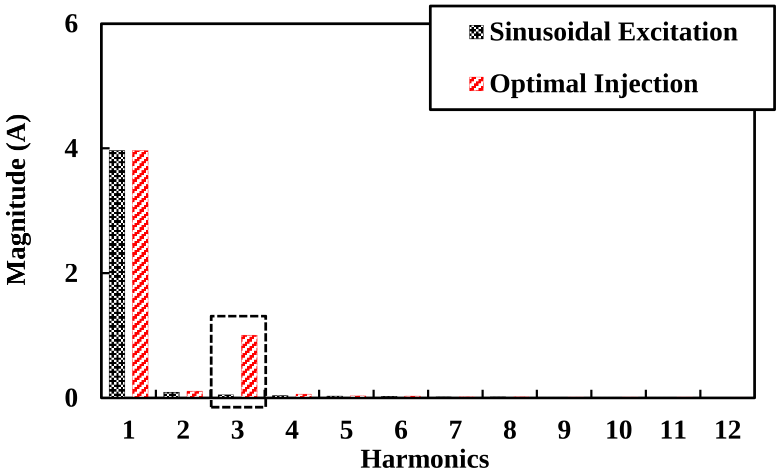

(b)

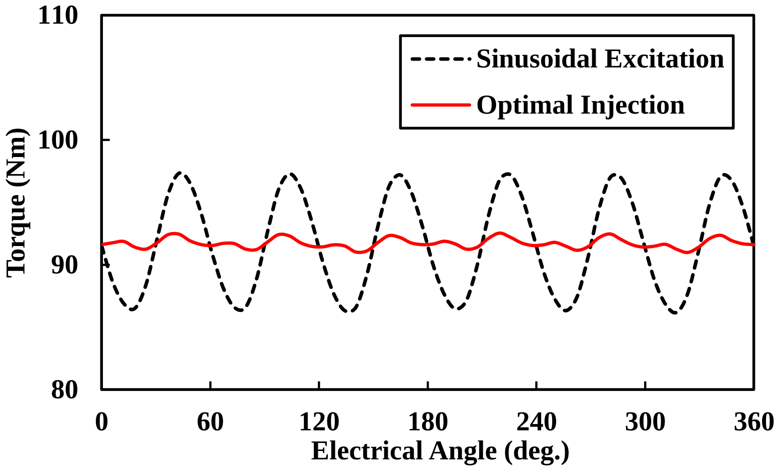

(c)

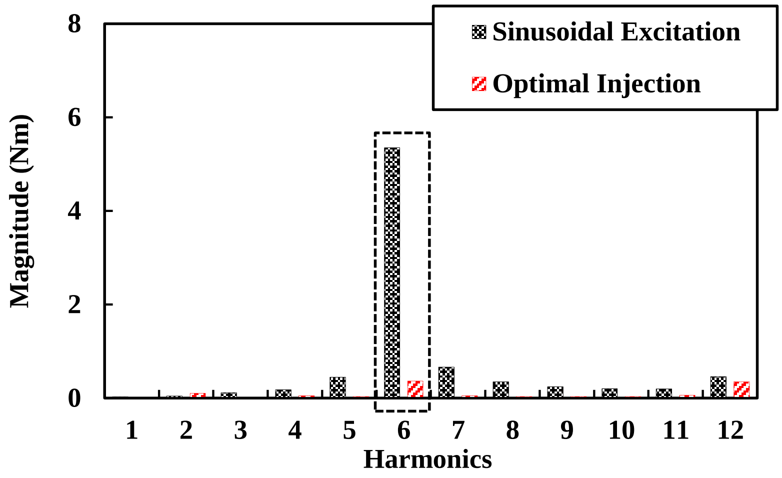

(d)

Fig. 5.9 Operating waveforms at the rated operating points. (a) Phase A current waveforms. (b) Phase A current spectrum analysis. (c) Instantaneous torque waveforms. (c) Instantaneous torque spectrum analysis.

5.6.2 Experimental Validation

The proposed torque ripple mitigation strategy was validated on the prototype OW-PMSM drive controlled by the dSPACE system. The switching frequency is 5kHz and the dead-time is set to 2μs. The specification of the OW-PMSM is listed in Table 5.1. The experiment platform is shown in Fig. 4.6.

TABLE 5.1 SPECIFICATION OF PROTOTYPE OW-PMSM

Parameter	Value
Pole pairs	16
Resistance (Ω)	3.76
Rated current (A)	2.82
Rated speed (rpm)	80
Encoder resolution	4096
d-axis inductance (mH)	17
q-axis inductance (mH)	17

Fig. 5.10 shows the measured operating waveforms of the typical operating points including the conventional sinusoidal excitation and the optimal zero sequence current injection. Fig. 5.10 (a) shows the phase A current waveforms, in which, the amplitude and phase of the third harmonic current are 0.48A and 100 elect. deg., respectively. Fig. 5.10 (b) shows the

associated spectrum analysis. Fig. 5.10 (c) shows the measured instantaneous torque waveforms. Fig. 5.10 (d) shows the associated spectrum analysis. It can be seen that the dominant sixth torque ripple has been suppressed to a low level. When compared to the FE results in Fig. 5.9, the measured instantaneous torque waveforms contain lower order harmonics. It can be from the mechanical asymmetry of the installation. Meanwhile, although the sixth harmonic is still the most dominant one, the associated magnitude decreases. This can be induced by the inverter nonlinearity related phase current distortion and the counteraction from the torque ripple of the loaded PMSM, which are not included into the FE analysis. Furthermore, the speed PI controller itself has the certain effect of suppressing torque ripple. Specifically, in Fig. 5.10 (d), the discussed dominant sixth torque ripple harmonic has been suppressed as expected.

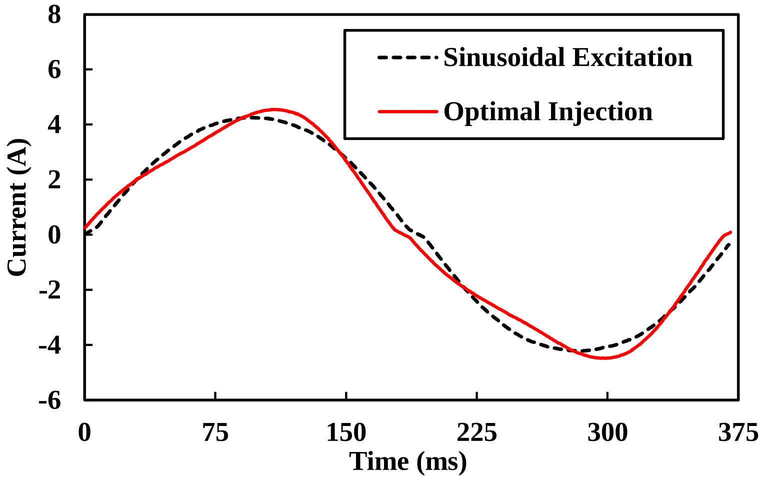

(a)

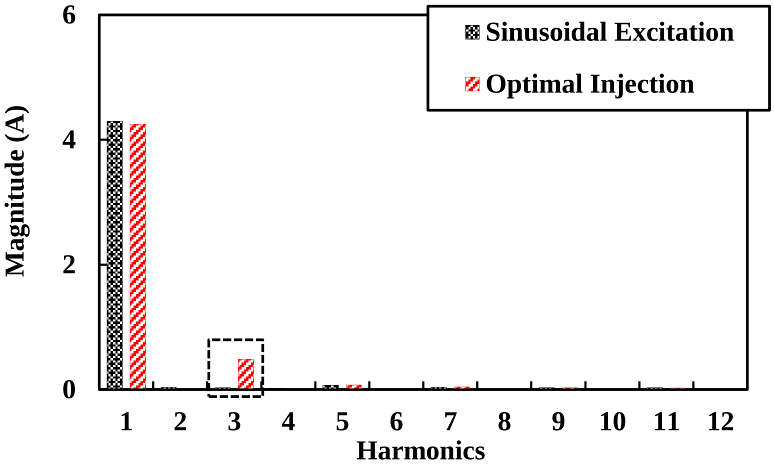

(b)

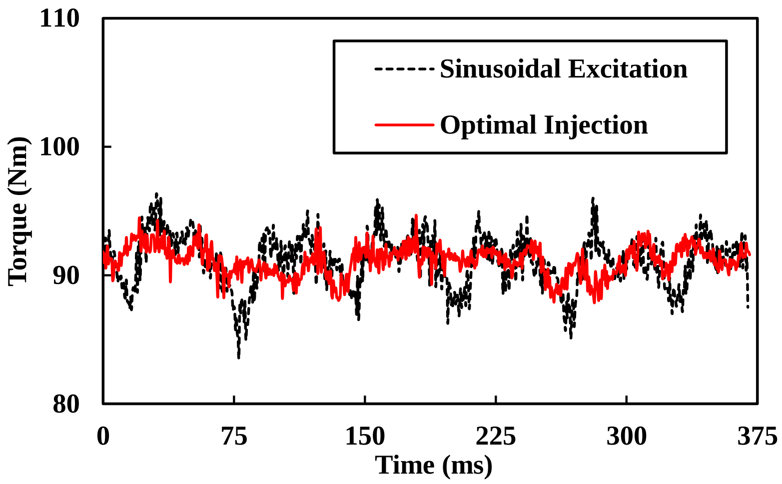

(c)

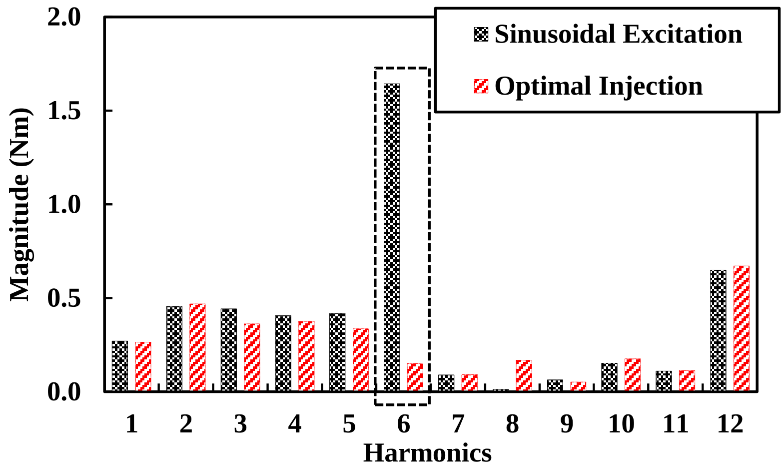

(d)

Fig. 5.10 Measured operating waveforms at the rated operating points. (a) Phase A current waveforms. (b) Phase A current spectrum analysis. (b) Instantaneous torque waveforms. (c) Instantaneous torque spectrum analysis.

5.7 Conclusion

A novel torque ripple mitigation strategy based on zero sequence current injection has been proposed in this chapter. The torque ripple mechanism has been analyzed. Meanwhile, the principle and systematic implementation of the proposed method also have been introduced. The proposed method is capable of reducing the bandwidth requirement on the current controller from six times of the maximum fundamental frequency to three times of that. Since the compensation torque is produced in zero sequence which is decoupled from the *d*- and *q*-axes, the robustness has also been obtained. Both the FE analysis and the experiment have validated the effectiveness of the proposed method.

CHAPTER 6 ZERO SEQUENCE CURRENT BASED SENSORLESS METHOD

The exploitation of the zero sequence can also be extended to the sensorless control. The zero sequence current induced by the zero sequence back EMF contains the rotor position information. Therefore, a novel zero sequence current based sensorless method is presented in this chapter.

This chapter was published in IEEE Transactions on Industrial Electronics.

6.1 Introduction

Open-winding (OW) machine topology [JAH80] [PRA15] [ZHO15] has been investigated in recent years with regard to fault tolerant control and flux-weakening performance [NGU17] [WEL04] [SAN13] due to the favorable distinctions including the redundancy of switching devices and the flexible control freedom. OW-permanent magnet synchronous machine (OW-PMSM) as one of the OW machines, which combines the advantages of PMSM and OW machine topology, has drawn much attention by researchers. Meanwhile, sensorless control (also called self-sensing control [COR98]) enabling the elimination of mechanical position sensor for closed loop drive system becomes attractive for industrial applications since it helps to reduce the cost, improve system robustness and minimize drive system volume.

In general, sensorless methods can fall into four categories consisting of high frequency (HF) signal injection based methods [JAN95] [BIA08] [LIU14] [STA06] [LIN03], PWM carrier signal based methods [NOG03] [LEI11] [GAO09], zero sequence based methods [LEI11], [SHE04] [TSO15] [CAR05] and back electro-motive force (EMF) based methods [CHE03] [WAN14d] [MOR02]. HF signal injection methods include different injection patterns and the typical ways are rotating [JAN95], pulsating [BIA08], stationary axis [LIU14] and zero sequence injection [STA06] with sinusoidal or square waves [YOO11]. PWM carrier signal based method can be regarded as one kind of special HF signal injection methods due to the same essence of disturbance effects. Both HF signal injection and carrier signal based methods require saliency of the machine including inductance saliency or eddy current induced resistance saliency [YAN12] [YAN12b].

Zero sequence based methods include third harmonic back EMF or current based methods and zero sequence reflected saliency based methods. Hence, third harmonic back EMF or current signals are sometimes necessary for these methods [SHE04], [LIU14]. Moreover, a zero sequence voltage measurement unit including a voltage transducer together with three phase resistance network is usually required in the third harmonic back EMF based methods. These methods provide a non-disturbance way to obtain the rotor position information without requiring any machine parameters which are usually necessary in fundamental back EMF based methods, though fundamental back EMF based methods are also non-disturbance ones.

In [LEI11], the zero sequence carrier signal generated by space vector PWM is used to modulate the position information. Hence, high dynamic performance can be achieved since the signal does not interact with the current controller and then no filters need to be used in the control loop. In [STA06], zero sequence voltage vector is applied to the induction machine (IM) to obtain periodic perturbation and position information from the current differential. [SHE04] proposes a sensorless method for brushless DC (BLDC) machine by using third harmonic component and the flux-weakening control cooperating with was also demonstrated. This method is improved in [SHE06] by introducing phase locked loop (PLL) technique. It is further improved in [LIU14] by using enhanced rotor position estimator in software for PMSM with continues position output. An adaptable sensorless commutation method for BLDC machine utilizing zero sequence voltage is proposed in [TSO15]. A non-integrating Rogowski Coil is used in [CAR05] to extract the zero sequence current derivative to track the flux position of the IM. Meanwhile, [BRI06] analyzes carrier-signal voltage injection zero sequence current based sensorless control, especially for rotor position estimation, in delta connected three phase ac machines. [GAR07] studies and compares the negative and zero sequence carrier signal based sensorless methods in terms of accuracy, bandwidth and stability. A low frequency signal demodulation based sensorless method employing zero sequence voltage component is proposed in [CON06] to estimate the air-gap flux position.

Sensorless control method utilizing the identity of the OW-PMSM may bring additional benefits when compared to the conventional methods directly transplanted to OW-PMSM drives. Hence, a novel sensorless control strategy based on OW-PMSM will be proposed in this chapter. The contribution is that the proposed method no longer needs voltage transducer and three phase resistance network which are necessary in conventional third harmonic based methods in the single inverter controlled PMSM. Moreover, the torque ripple analysis, losses comparison and zero sequence parameter sensitivity analysis are also carried out and confirmed by 2-dimensional finite element analysis (2D FEA). Meanwhile, due to the essence of decouple (zero sequence relative to *d-q* axis), the proposed method is less affected by the fundamental signals. Therefore, the proposed method has robust estimation characteristic. Due to the essence of back EMF, the proposed method is appropriate for the applications including wind power generation and motor drives operating above certain speed, which provide enough signal intensity of back EMF. The standstill and low speed operations are not feasible. This chapter is organized as follows: In Section 6.2, the system configuration and OW-PMSM model considering zero sequence is introduced. In Section 6.3, the phase shift based SVPWM is presented. In Section 6.4, the principle of the proposed method is described. The torque ripple analysis, losses comparison and zero sequence parameter sensitivity analysis are shown in Section 6.5. The experimental validation with high system inertia (2.5 kg m^2) is suitably tested in Section 6.6.

6.2 Configuration and Modelling of Common DC Bus Based OW-PMSM Drive System

6.2.1 Configuration of OW-PMSM Drive System

Fig. 1.13 shows the OW-PMSM drive system with common DC bus. The dual voltage source inverter (VSI) drive is connected to the six terminals of the OW-PMSM. Meanwhile, each phase of the OW-PMSM can be regarded as controlled by an H-bridge structure which is more flexible than the conventional single inverter type. Also, this topology contains zero sequence path when compared to the isolated DC bus one, which enables the flow of zero sequence current.

6.2.2 Equations of OW-PMSM Model Considering Zero Sequence

The OW-PMSM model is similar to the conventional single inverter controlled PMSM with Y-connection. However, for OW-PMSM with common DC bus, the zero sequence equation which is usually ignored in a single inverter system needs to be included due to the existence of zero sequence path. The zero sequence back EMF is commonly induced by third harmonic flux-linkage at each phase winding resulting in third harmonic back EMF. The existence of the third harmonic is firstly determined by the machine design, as discussed in [SHE06]. The third harmonic flux-linkage is obtained through B_3k_{w3} where B_3 is the magnitude of the third harmonic component of the airgap flux density and k_{w3} is the winding factor for third harmonic. B_3 can be determined via the field distribution and the saturation. k_{w3} is the product of the coil pitch factor, the distribution factor and the skew factor. Hence, any one of the factors approaching zero can lead to low or even no third harmonic back EMF. However, the third harmonic may not be eliminated on purpose in order to increase the fundamental airgap flux density and the back EMF, and hence, the torque density of PMSMs [ZHO14], and thus, it can be found in many PMSMs.

Fig. 2.1 shows the measured phase back EMF waveform and the corresponding harmonic spectrum of the tested OW-PMSM at 10 rpm. It can be seen that the third harmonic component accounts for 13% of the fundamental one.

Hence, the OW-PMSM model considering zero sequence equation can be described as (4.1). Conventional model-based sensorless methods utilize the *d-q* axis or α-β axis equivalent model equations to construct the observer and extract the rotor position information signal that is contained in the back EMFs. Zero sequence equation is usually ignored because the zero sequence path is open circuit. In OW-PMSM with common DC bus, the zero sequence path exists and needs to be considered. Meanwhile, as revealed in (4.1), the equivalent zero sequence circuit is shown in Fig. 4.1.

The zero sequence voltage u_0 from inverter side is generated from PWM, and specifically, for conventional space vector PWM (SVPWM), the produced u_0 is quasi-triangle wave which will be analyzed in Section 6.3. From the machine side, the zero sequence inductance is expressed as

$$L_0 = L_{s0} - 2M_{s0} \tag{6.1}$$

where L_{s0} represents the average inductance of the arbitrary phase self-inductance and M_{s0} represents the average inductance of mutual-inductance between any two phases.

The winding phase resistance is equivalent to zero sequence resistance. The zero sequence back EMF is expressed as

$$e_0 = 3\omega\psi_{f0}\sin 3\theta\,. \tag{6.2}$$

Hence, the zero sequence equivalent equation is

$$u_0 = (L_{s0} - 2M_{s0})\frac{di_0}{dt} + i_0 R_s + 3\omega\psi_{f0}\sin 3\theta\,. \tag{6.3}$$

It can be found that the rotor position information θ is inherently contained in the zero sequence back EMF e_0. According to equation (6.4), the rotor positon can be extracted.

6.3 Phase Shift Based SVPWM for OW-PMSM

In OW-PMSM drive system, the conventional SVPWM strategy is not suitable for the operation because the existing zero sequence path allows the voltage disturbance in zero-axis to induce the disturbance current. The disturbance voltage includes the low frequency common mode voltage (CMV) produced by SVPWM and also the back EMF harmonics such as 3rd 9th 15th …components sharing the same phase angle in three phase back EMFs. There are high frequency CMV produced by SVPWM. However, due to low pass filter characteristic of the equivalent zero sequence circuit, high frequency components have little influence. On the other hand, under specific occasion, *e.g.* low switching frequency and low zero sequence inductance, the high frequency components need to be considered. Hence, in order to eliminate the interference from the SVPWM, a phase shift based SVPWM is introduced and adopted for the whole control system in this section, which is shown in Fig. 6.1.

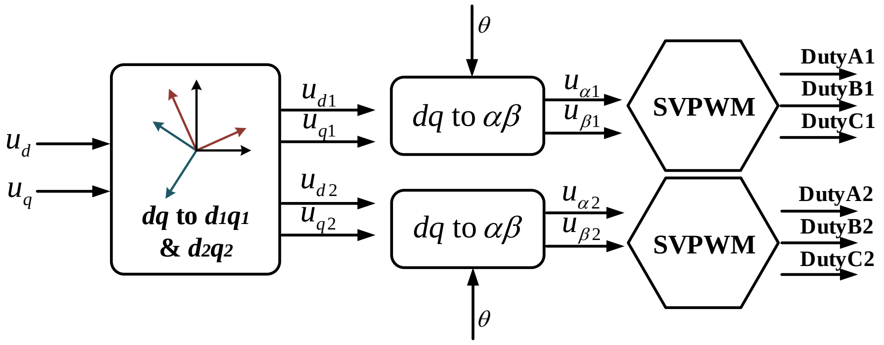

Fig. 6.1 Phase-shift-based SVPWM for OW-PMSM.

As what has been known that the conventional SVPWM strategy contains quasi-triangle waves in modulation signals in three phases to improve the DC bus voltage utilization [ZHO02]. It imposes almost no influence on single inverter drive system, but will induce current in OW configuration with common DC bus. The basic countermeasure is to shift the voltage reference signals for two sets of the inverters and obtain a counteraction between zero sequence voltages of the two modules [OLE05]. The actual *d*- and *q*-axis voltage reference signals can be decomposed into two sub-coordinates, d_1q_1 and d_2q_2, which are synchronized with the *dq*-coordinate but have π/6 and 5π/6 shifted angles to the *dq*-coordinate, respectively, as shown in Fig. 6.2.

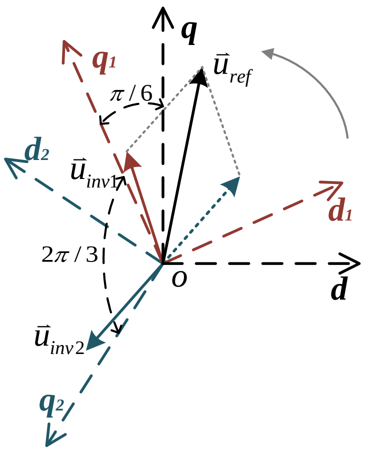

Fig. 6.2 Synthetic voltage vector of the two sets of the inverters.

Meanwhile, the decomposition transformation can be deduced as

$$\begin{bmatrix} u_{d1} \\ u_{q1} \\ u_{d2} \\ u_{q2} \end{bmatrix} = \frac{1}{2} \cdot \begin{bmatrix} 1 & \tan\frac{\pi}{6} \\ -\tan\frac{\pi}{6} & 1 \\ -1 & \tan\frac{\pi}{6} \\ -\tan\frac{\pi}{6} & -1 \end{bmatrix} \cdot \begin{bmatrix} u_d \\ u_q \end{bmatrix}. \tag{6.4}$$

This phase shift based SVPWM achieves the phase shifting by reconstructing the reference signals for each SVPWM module. In [OLE05], the phase shifting is obtained by modifying the SVPWM algorithm inherently. Therefore, for the proposed method, the conventional SVPWM can be directly utilized without any modification. Because the SVPWM algorithm is usually packaged as a sub-function for coding in embedded control system, the proposed structure of the phase shifted based SVPWM saves time for the implementation and debugging. Moreover, the zero sequence voltage output from the inverter side is eliminated and the equivalent zero sequence circuit can be simplified as u_0=0, which is necessary for the proposed sensorless method and will be explained with more details in Section 6.4 to avoid disturbance from inverter side. Fig. 2.6 shows the phase modulation signals and the synthetic reference signal implemented in dSPACE control system for the two inverters. The amplitude of the synthetic reference signal is 0.5 p.u. and the frequency is 40 Hz. Within one carrier period, vector 0 and vector 7 are still equally distributed for each set of the inverter.

6.4 Principle of Proposed Sensorless Method

6.4.1 Proposed Sensorless Method

Voltage transducer is necessary in the conventional third harmonic back EMF based sensorless method, but is not required in the proposed sensorless method. Usually, the rotor position information is inherently contained in the zero sequence back EMF, *e.g.* the third harmonic back EMF. Once the third harmonic back EMF is observed or measured, the rotor position can be extracted.

Conventional methods are usually based on the terminal voltage measurement of the equivalent zero sequence circuit shown in Fig. 6.3 and simplified as equivalent zero sequence circuit in Fig. 6.4. The three phase resistance network, which is equivalent to R_{net} in Fig. 6.4, extends a measurement terminal *R*. Additionally, the neural point *N* of the PMSM is also necessary. Because the equivalent zero sequence circuit in Fig. 6.4 is an open circuit, the measured voltage between *R* and *N* is the zero sequence back EMF e_0 which is then utilized to estimate the position signal.

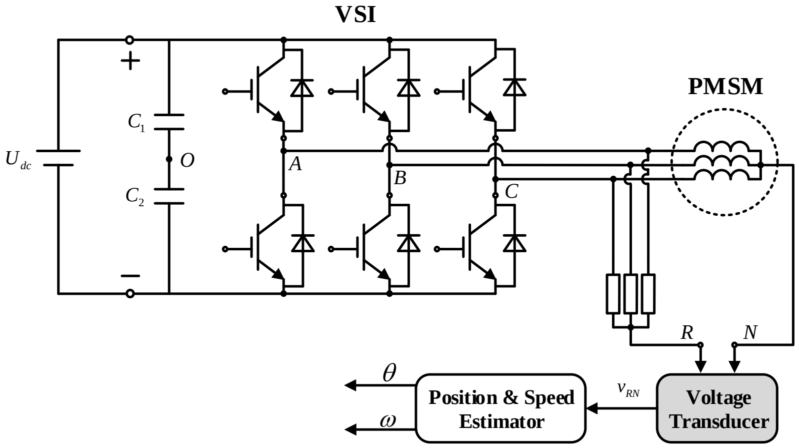

Fig. 6.3 Conventional third harmonic back EMF based sensorless method.

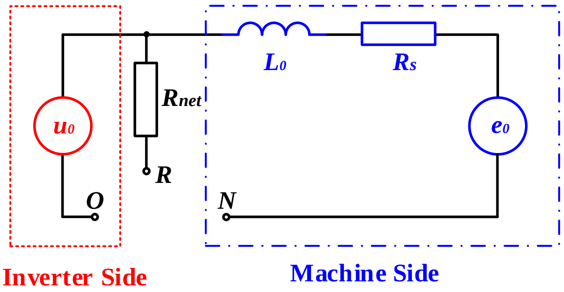

Fig. 6.4 Simplified equivalent zero sequence circuit of the conventional third harmonic EMF based sensorless methd.

The method proposed in this paper utilizes the common DC bus based OW topology which has been shown in Fig. 4.1 and enables an interconnected zero sequence circuit without the necessity of the three phase resistance network for terminal extension, namely, the terminals N and O in Fig. 6.4 are connected to each other inherently. If the phase shift based SVPWM introduced in Section 6.3 is adopted, the inverter side only shows the short circuit characteristic (u_0=0 V) and the machine side keeps the same. The equivalent zero sequence circuit can be simplified as Fig. 6.5. Hence, the third harmonic back EMF e_0 induces corresponding zero sequence current which in turn can be used to reconstruct the third harmonic back EMF and finally used for the position estimation. Thus, the voltage transducer is no longer needed. However, the compromise is the introduction of the zero sequence current. Therefore, the corresponding influence including losses and torque ripple will be investigated and compared in Section 6.5. In addition, the equivalent zero sequence circuit is independent to the d-q axis equivalent circuits, which is axis based decoupling. Hence, the robustness of the estimation can be higher than that of the d-q axis or fundamental signals based methods.

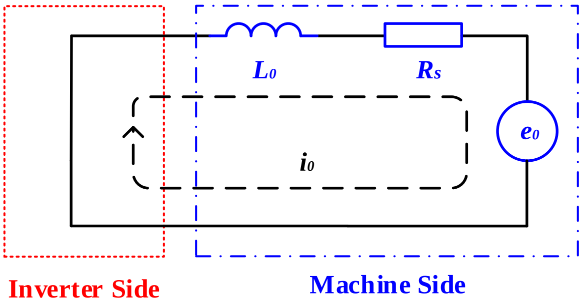

Fig. 6.5 Simplified equivalent zero sequence circuit of the OW-PMSM by using phase-shift-based SVPWM algorithm.

According to Fig. 6.5, the zero sequence equation is written as

$$0 = L_0 \frac{di_0}{dt} + i_0 R_s + 3\omega\psi_{f0} \sin 3\theta \,. \tag{6.5}$$

Meanwhile, in equation (6.6), i_0 can be obtained via

$$i_0 = \frac{i_a + i_b + i_c}{3} \tag{6.6}$$

where i_a, i_b and i_c are phase A, phase B and phase C currents, respectively.

According to this principle, the zero sequence model based sensorless strategy is proposed and shown in Fig. 6.6. The synchronous PLL based quadrature signal generator (QSG) in Fig. 6.6 is used to generate the equivalent zero sequence current signals which satisfy

$$\begin{cases} i'_{\alpha 0} = i_0 \\ i'_{\beta 0} = \dfrac{di_0}{dt} \end{cases} . \tag{6.7}$$

Meanwhile, the outputs of the synchronous PLL based QSG are used to reconstruct the zero sequence back EMF $\hat{e}_0$ according to (6.6). The estimated $\hat{e}_0$ then serves as the input signal of the synchronous PLL based position observer (PO) to estimate the rotor position signal.

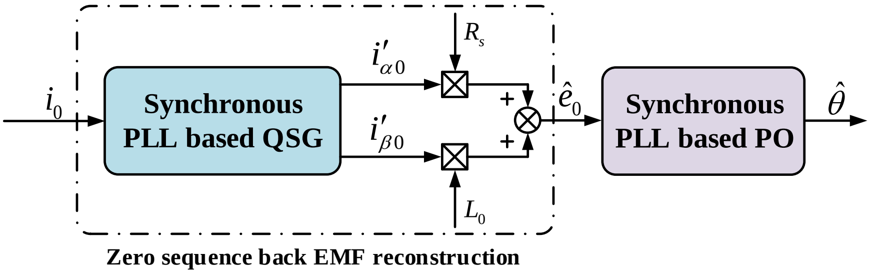

Fig. 6.6 Proposed sensorless strategy.

6.4.2 Analysis of the Synchronous PLL Based QSG and PO

In (6.6), the first term $L_0 \frac{di_0}{dt}$ in the right side of the equation requires the differential information of i_0. In the implementation, if it is directly discretized as

$$L_0 \frac{di_0}{dt} = L_0 \frac{i_0[n] - i_0[n-1]}{\Delta T} \tag{6.8}$$

it would not be a good choice since the pure digital differentiator suffers from the noise amplification and phase error [XIN15], where $i_0[n]$ and $i_0[n\text{-}1]$ are the discretized sampled zero sequence current values, n represents the time index and ΔT is the interruption interval of the control system. Hence, the synchronous PLL based QSG is used to achieve this target with better performance. The structure of the QSG is shown in Fig. 6.7.

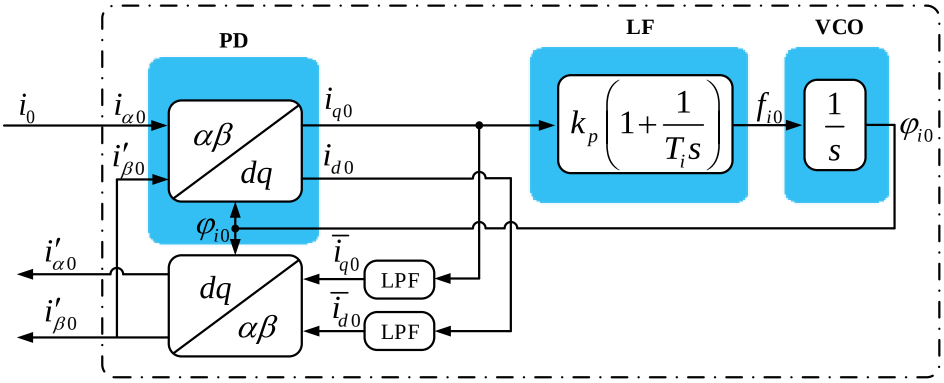

Fig. 6.7 Synchronous PLL based QSG.

The transfer function of the low pass filters (LPFs) in Fig. 6.7 on the synchronous reference coordinate are both first order and expressed as

$$H(\mathrm{s})=\frac{\bar{I}_{d0}(\mathrm{s})}{I_{d0}(\mathrm{s})}=\frac{\bar{I}_{q0}(\mathrm{s})}{I_{q0}(\mathrm{s})}=\frac{\omega_f}{s+\omega_f} \tag{6.9}$$

where ω_f is the cut-off frequency.

Meanwhile, when they are transformed into *dq*-axis, the transfer functions are

$$D(\mathrm{s})=\frac{I'_{\alpha 0}(\mathrm{s})}{I_{\alpha 0}(\mathrm{s})}=\frac{k\omega_0 s}{s^2+k\omega_0 s+\omega_0^2} \tag{6.10}$$

$$Q(\mathrm{s})=\frac{I'_{\beta 0}(\mathrm{s})}{I_{\alpha 0}(\mathrm{s})}=\frac{k\omega_0^2}{s^2+k\omega_0 s+\omega_0^2} \tag{6.11}$$

where $k=\omega_f/\omega_0$. The bode diagrams of *D*(s) and *Q*(s) are shown in Fig. 6.8. It can be seen that *Q*(s) shows 0 dB gain at the cut-off frequency point that is ω_0 and the phase angle is shifted 90 degree. It is equivalent to digital differentiator for sinusoidal signal at ω_0. Hence, the input signal $i_{\alpha 0}$ is shifted but maintains the same amplitude of the input signal as an orthogonal signal $i'_{\beta 0}$. *D*(s) acts as a band-pass filter (BPF) for the selected centre frequency ω_0 to bring the benefit of filtering out harmonics and DC bias interference in $i_{\alpha 0}$.

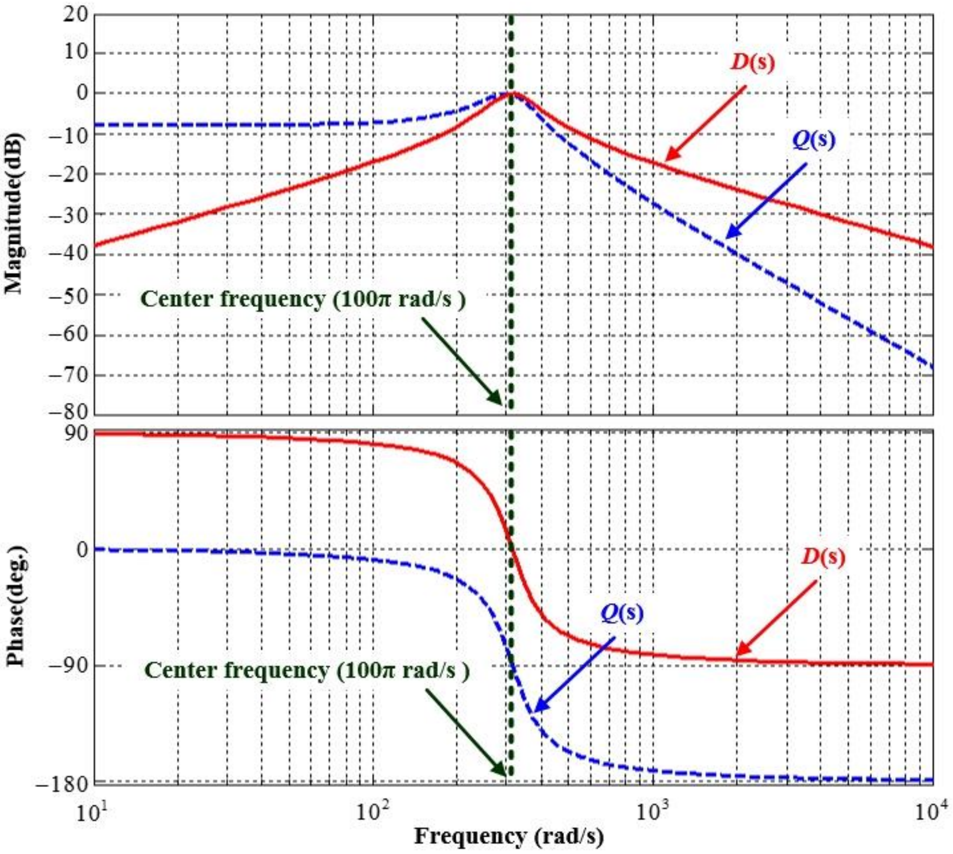

Fig. 6.8 Bode diagram of D(s) and Q(s) (k=0.4, ω_0=100π rad/s).

The transfer function describing the relationship between $i'_{\alpha 0}$ and $i'_{\beta 0}$ is expressed as

$$G(\mathrm{s}) = \frac{I'_{\alpha 0}(\mathrm{s})}{I'_{\beta 0}(\mathrm{s})} = \frac{s}{\omega_0}. \tag{6.12}$$

The dual output signals from the dq to $\alpha\beta$ transformation can be transformed into time-domain differential equation as (6.14) and hence the two signals are orthogonal if they are both sinusoidal.

$$i'_{\alpha 0} = \frac{1}{\omega_0}\frac{di'_{\beta 0}}{dt} \tag{6.13}$$

Similarly, the synchronous PLL based PO is shown in Fig. 6.9, whereby, the difference is that a frequency multiplication index h is introduced to make the estimated position signal match the third harmonic back EMF. In the inner loop of the PO, the phase angle signal θ_{i0} is triple the observed rotor position angle $\hat{\theta}$. The input signal is the reconstructed zero sequence back EMF which is usually measured via voltage transducer together with three phase resistance network in conventional third harmonic EMF based sensorless method. The PO and QSG almost maintain the identical structure which brings the convenience of modularization programming and simpler implementation. The detail characteristics of the synchronous PLL based PO are not elaborated in detail again since it shares the same basic structure with the QSG other than the frequency multiplication index.

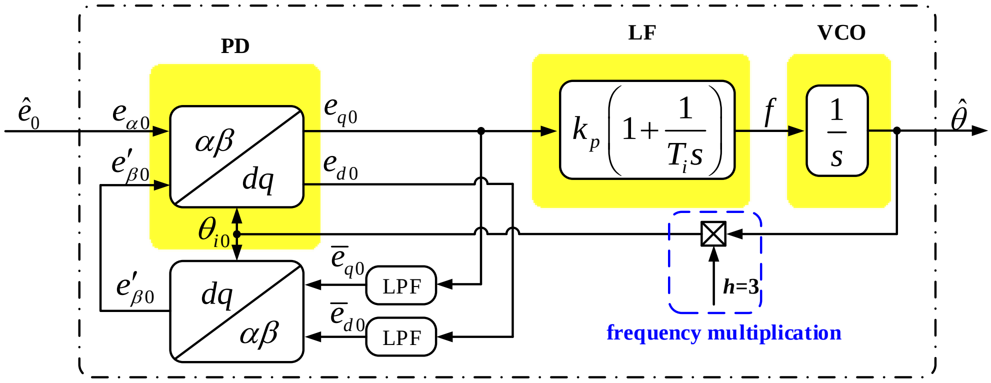

Fig. 6.9 Synchronous PLL based PO.

6.5 Torque Characteristics, Losses and Parameter Sensitivity Analysis of Proposed Method

The proposed sensorless method is based on the zero sequence current excited by the zero sequence back EMF. Therefore, the influence of the proposed method on the machine performance needs to be investigated, which includes the torque ripple and power loss, as will be presented in this section. The analyzed results are carried out by 2D FEA. Meanwhile, the parameter sensitivity analysis for the proposed method is also carried out in this section.

6.5.1 Torque Ripple Characteristics

The torque ripple characteristics of the proposed method and the no injection one are presented in Fig. 6.10. The third harmonic current is 0.6 A which is superimposed on the rated current. The speed is 170 rpm. Meanwhile, the quantified comparison results are shown in Table 6.1. The proposed method induces 4.47% torque ripple which is close to that of the no injection one.

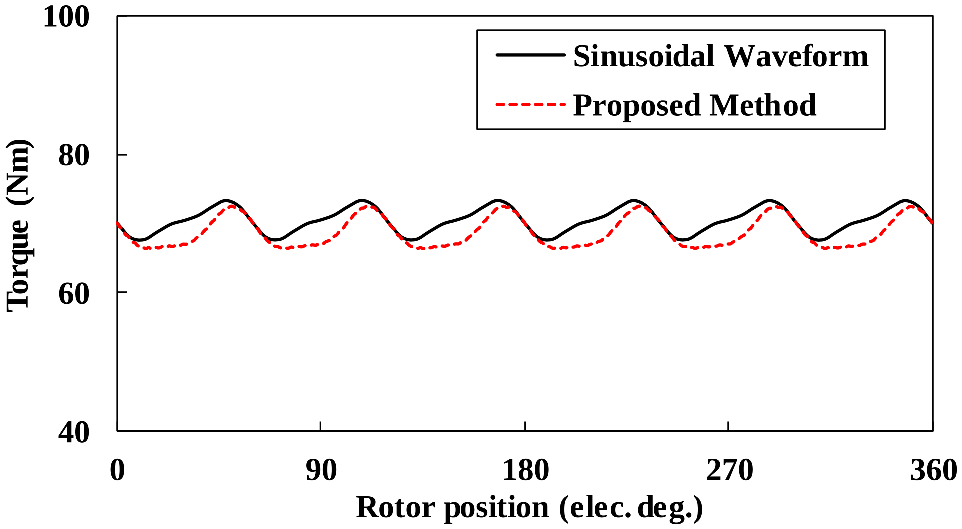

Fig. 6.10 Torque characteristics of the proposed method and the original sinusoidal one.

TABLE 6.1 TORQUE CHARACTERISTICS OF THE PROPOSED METHOD AND NO INJECTION CONDITION

	Average torque (Nm)	Maximum torque (Nm)	Minimum torque (Nm)	Torque ripple (Nm)	Percentage of ripple
No injection	70.38	73.28	67.61	2.83	4.02%
Proposed method	68.67	72.45	66.32	3.07	4.47%

The synthetic torque ripple contains two parts. The first one is the torque ripple introduced by third harmonic current. The other is the torque ripple inherently contained in the OW-PMSM.

The torque ripple introduced by the third harmonic current against rotor position is obtained as

$$T_6 = \frac{3E_0 I_0}{2\omega_m}\sin(6\omega t + \frac{\pi}{2} - \gamma) \tag{6.14}$$

where E_0 is the amplitude of zero sequence back EMF, I_0 is the amplitude of zero sequence current, $\omega t=\theta$ when zero initial position is assumed and γ=arctan($3\omega L_0/R_s$). The derivation of (6.15) is given in the appendix. The amplitude and phase angle of the torque ripple introduced by third harmonic current simultaneously varies with the speed variation since the equivalent impedance of the zero sequence circuit varies at different operation speed.

Meanwhile, the inherent torque ripple of the OW-PMSM also exists, which is mainly composed of the 6th and 12th harmonics. Fig. 6.11 shows the spectrum analysis of the torque waveform of the OW-PMSM with no additional current injection. The 6th harmonic is more dominant than the 12th harmonic.

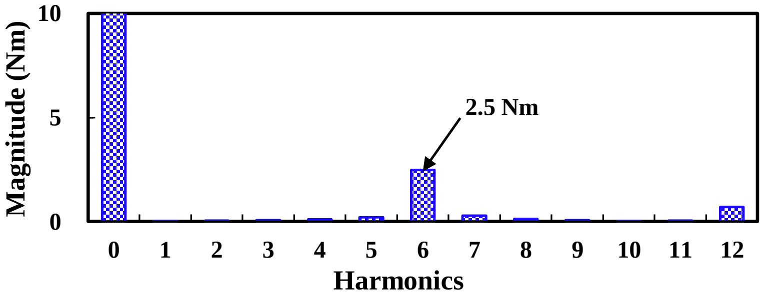

(a)

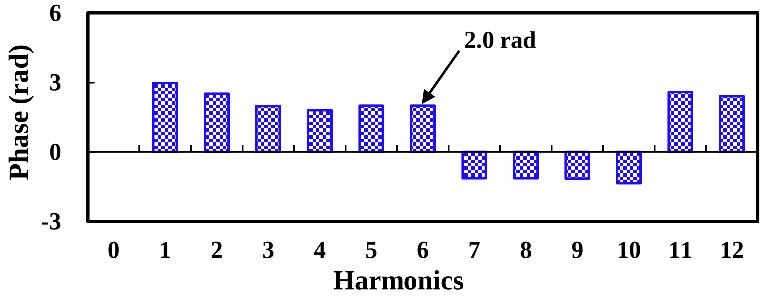

(b)

Fig. 6.11 Spectrum analysis of inherent torque ripple of OW-PMSM. (a) Magnitude analysis. (b) Phase analysis.

Only the 6th harmonic is considered, then the inherent torque ripple of the OW-PMSM is expressed as

$$T_m = H_6 \sin(6\omega t - \gamma_6) \tag{6.15}$$

where H_6 and γ_6 are the amplitude and phase angle of the 6th torque ripple harmonic.

Hence, the torque ripple characteristics against speed can be shown in Fig. 6.12. The torque ripple induced by the third harmonic current increases with the speed and increases slowly after 80 rpm. The inherent torque ripple of this OW-PMSM is regarded constant. However, it should be noted that the inherent torque ripple characteristic could change for different machine designs. The synthetic torque ripple reaches the lowest point at around 23 rpm and then increases with the speed. The trough is formed due to the cancellation between the torque ripple introduced by the third harmonic current and the inherent torque ripple having around π phase difference, which is shown in Fig. 6.13. The synthetic torque ripple would not increase linearly with the speed since the increase of the equivalent zero sequence impedance suppresses the amplitude of the zero sequence current.

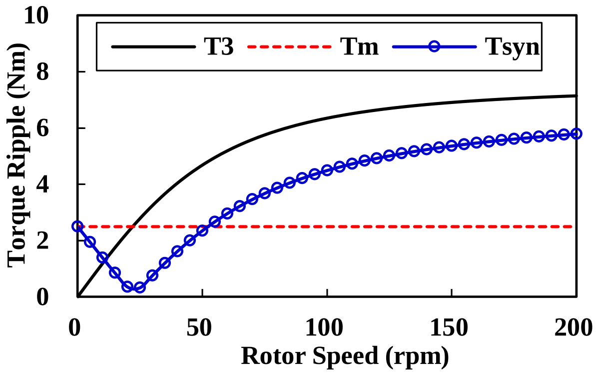

Fig. 6.12 Torque ripple characteristics of the proposed sensorless method at different speed.

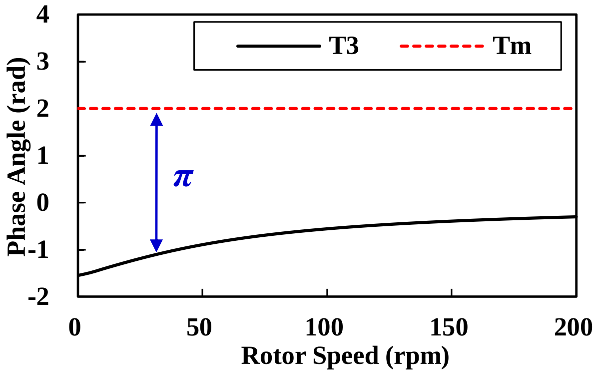

Fig. 6.13 Phase angles of the zero sequence induced torque ripple and the inherent torque ripple.

6.5.2 Loss Analysis

Imperfect current will lead to additional losses. The major power losses of the PMSM include mechanical loss, copper loss and iron loss. The mechanical loss can be regarded as the same. As for the copper loss, if the phase current contains harmonic components, the average copper loss can be quantified via (6.17) when skin effect is neglected

$$p_{loss-copper} = \frac{3\omega}{2\pi}\int_0^{2\pi/\omega} i^2 R dt \,. \tag{6.16}$$

Hence, the total loss can be compared in Table 6.2 at rated speed (170 rpm) via 2D FEA, of which the iron loss is calculated as [CHU13a]. The proposed method has comparable iron loss when compared to the no injection one. Higher copper loss will be induced by the proposed method. Hence, the total increased loss is 1.8%.

Table 6.2 Comparison of total loss of proposed method and no injection condition

	Copper loss (W)	Iron loss (W)	Total loss (W)	Percentage of increased total loss
No injection	50.7	63.6	114.3	0%
Proposed method	52.7	63.6	116.3	1.8%

6.5.3 Parameter Sensitivity Analysis

The frozen permeability method [CHU13a] for 2D FEA is used to obtain the on-load back EMF waveforms of the OW-PMSM. The spectrum analysis of the phase back EMF waveforms at different load conditions is shown in Fig. 6.14 (a) and (b). It can be seen that the fundamental and third harmonic back EMF components almost keep the same at different load conditions. But slight difference occurs for the phase angle of the 5th back EMF harmonic which induces tiny variation.

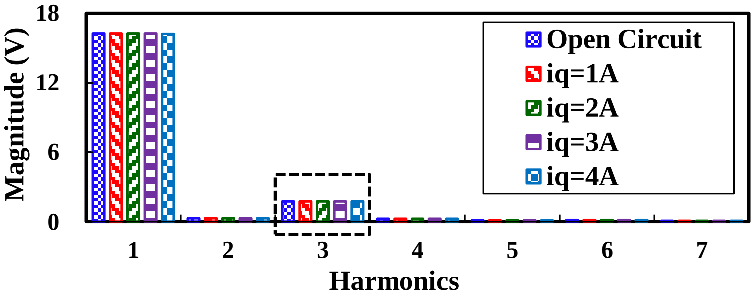

(a)

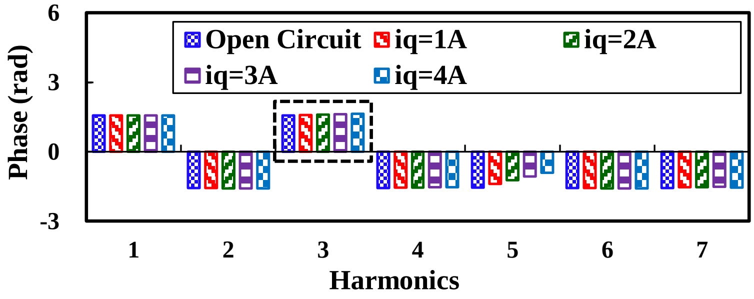

(b)

Fig. 6.14 On load back EMF analysis using frozen permeability based FEA. (a) Spectrum analysis for magnitude. (b) Spectrum analysis for phase.

According to the proposed sensorless method, the actual zero sequence back EMF is modelled as

$$\dot{E}_0 = R_s\dot{I}_0 + j\omega_0 L_0\dot{I}_0\,. \tag{6.17}$$

Meanwhile, if there exist deviations of the zero sequence parameters, the estimated zero sequence back EMF could be different from the actual one. Moreover, it can also be found that the estimation error is also relevant to ω_0 even the deviations are invariable. The estimated zero sequence back EMF can be modelled as

$$\hat{\dot{E}}_0 = (R_s + \Delta R_s)\dot{I}_0 + j\omega_0 (L_0 + \Delta L_0)\dot{I}_0 \tag{6.18}$$

where ΔR_S is the deviation of the phase resistance and ΔL_0 is the deviation of zero sequence inductance.

The deviations will influence both the amplitude and phase of the estimated zero sequence back EMF. However, only the phase is the concern which will affect the estimated rotor position. The estimation error of the estimated zero sequence back EMF is

$$\Delta\theta = \arctan\frac{R_s + \Delta R_s}{\omega_0 (L_0 + \Delta L_0)} - \arctan\frac{R_s}{\omega_0 L_0}\,. \tag{6.19}$$

Fig. 6.15 shows the estimation error against phase resistance and zero sequence inductance deviations. It can be seen that if the parameters are accurate, the estimation error is not sensitive to the operation speed. In the low speed range, the estimation error is more sensitive to phase resistance deviation. In the high speed range, the deviation of zero sequence inductance imposes more influence on the estimation error. Fig. 6.16 shows the estimation error at low speed (15 rpm) and high speed (80 rpm) conditions with both deviations of phase resistance and zero sequence inductance. Negative phase resistance deviation and positive zero sequence inductance deviation condition has more influence on the estimation error at low speed. Meanwhile, positive phase resistance deviation and negative zero sequence inductance deviation condition induces higher estimation error at high speed.

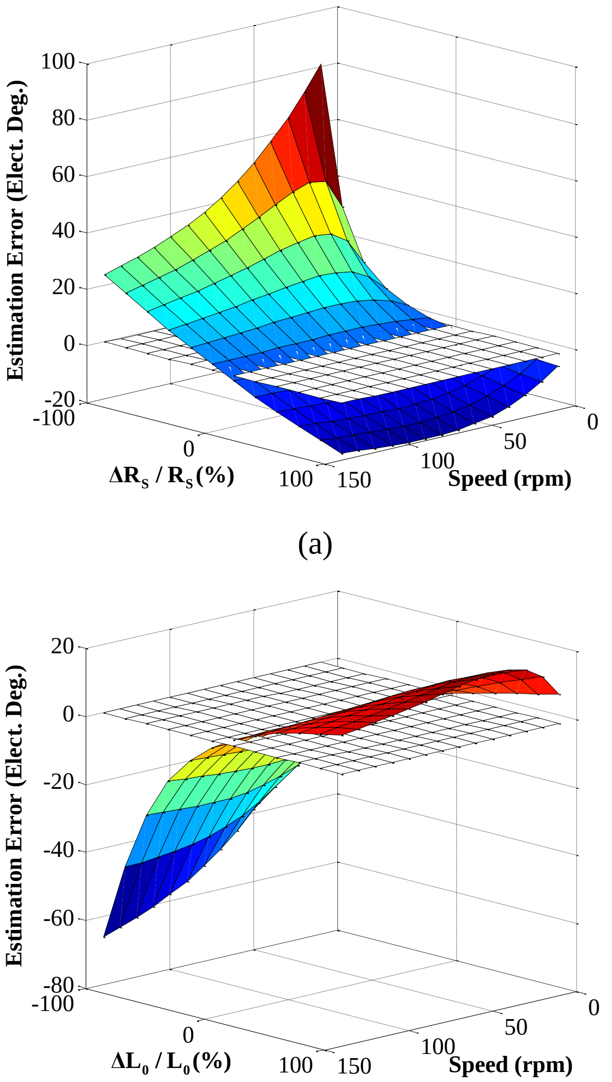

(a)

(b)

Fig. 6.15 Estimation errors against phase resistance and zero sequence inductance deviations. (a) Estimation errors against phase resistance deviation. (b) Estimation errors against zero sequence inductance deviation.

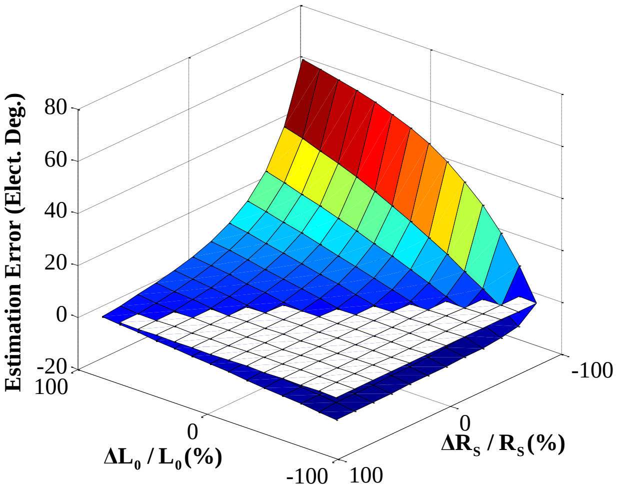

(a)

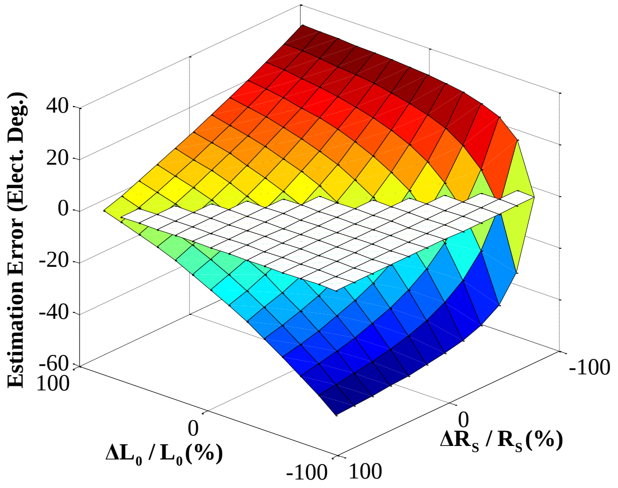

(b)

Fig. 6.16 Estimation errors at different speed conditions. (a) Low speed-15 rpm. (b) High speed-80 rpm.

6.6 Experimental Validation

The proposed algorithm is validated on a 3 kW outer rotor OW-PMSM drive based on dSPACE system shown in Fig. 6.12. The specification of the OW-PMSM is listed in Table 6.3. The PWM switching frequency is 5 kHz which is the same as the interrupt period and the dead-time is set to 2 μs. The DC bus voltage is 80 V. Fig. 6.17 shows the platform picture including the OW-PMSM, load PMSM and position sensor.

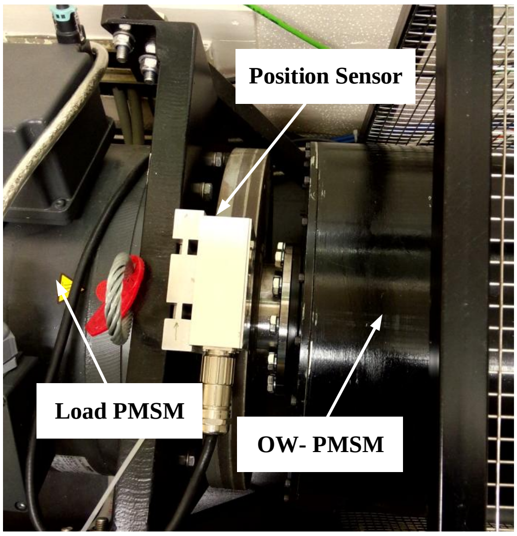

Fig. 6.17 Platform picture including the OW-PMSM, load PMSM and position sensor.

TABLE 6.3 SPECIFICATION OF TESTED OW-PMSM

Parameter	Value
Pole pairs	16
Resistance (Ω)	3.76
Rated RMS current (A)	2.83
Rated speed (rpm)	170
No-load PM flux linkage (Wb)	0.9
Encoder resolution	4096
Rated frequency (Hz)	45.33
d-axis inductance (mH)	17
q-axis inductance (mH)	17
System inertia (kg m^2)	2.5

Fig. 6.18 (a) shows the estimated rotor position signal, the encoder rotor position signal and the estimation error under no load condition. The maximum and minimum estimation error of rotor position are 6.1 ° and 1.7 °, respectively. Fig. 6.18 (b) shows the input original zero sequence current signal and its inphase and quadrature signals. The inphase signal is more sinusoidal than the input signal due to the filtering effect of the PLL as stated in Section 6.4.2. Similarly, Fig. 6.19 (a) shows the estimated rotor position signal, the encoder rotor position signal and the estimation error under rated load condition. The maximum and minimum estimation error of rotor position are 6.2 ° and -10.0 °, respectively. The ripple of the estimation error increases due the distortion of the signal. Fig. 6.19 (b) shows the input

original zero sequence current signal and its inphase and quadrature signals. It can be seen that the input signal is more distorted than the no load one.

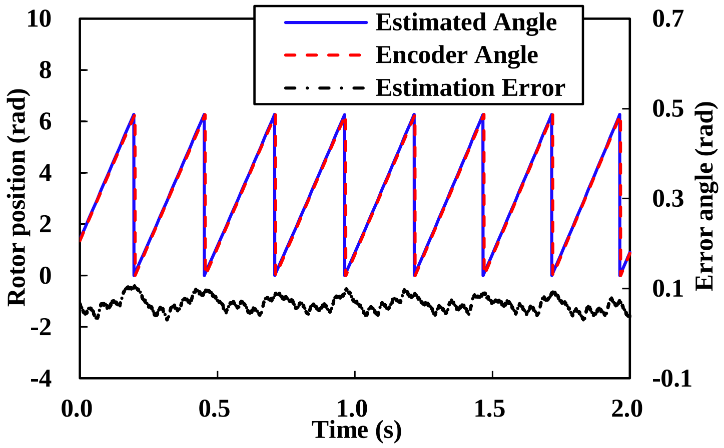

(a)

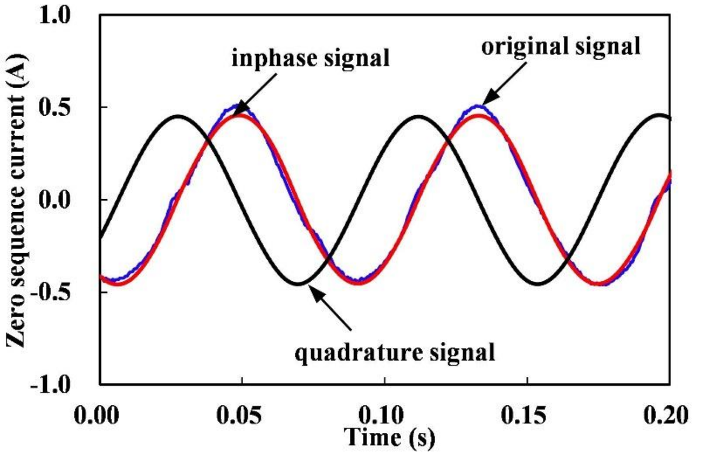

(b)

Fig. 6.18 Steady state estimation performance and PLL signals under no load condition. (a) Estimated rotor angle, encoder angle and estimation error. (b) Input zero sequence current signal and its in-phase and quadrature signals.

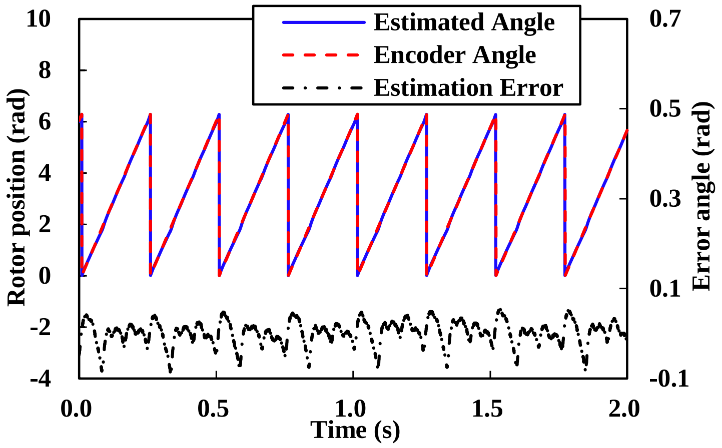

(a)

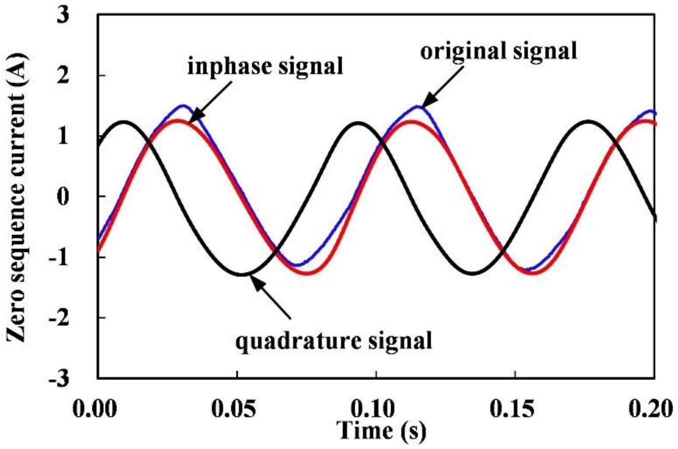

(b)

Fig. 6.19 Steady state estimation performance and PLL signals under rated load condition. (a) Estimated rotor angle, encoder angle and estimation error. (b) Input zero sequence current signal and its in-phase and quadrature signals.

Fig. 6.20 (a) shows the closed loop transient estimation performance including the estimated speed, encoder speed, speed reference, estimation speed error and estimation position error under rated load disturbance. Fig. 6.20 (b) shows the corresponding *d*-axis, *q*-axis and the phase A currents. The rated load disturbance is applied at 6 s and released at 20 s. Fig. 6.21 (a) shows the transient estimation performance including the estimated speed, encoder speed, speed reference, estimation speed error and estimation position error with step speed reference from 15 rpm to 40 rpm. The speed dependent ripples in the estimated and encoder speed signals are due to the installation eccentricity of the outer rotor OW-PMSM. Fig. 6.21 (b) shows the corresponding *d*-axis, *q*-axis and the phase A currents under the same condition. The increase of *q*-axis current in Fig. 6.21 (b) simultaneously with the speed is mainly due to the resistance coefficient of the drive system. Meanwhile, since the LPF is not applied to the estimated speed, the ripple of the estimation angle error is amplified by the speed calculation, namely, the differential block and the estimation ripple is obvious. The transient time is longer than conventional PMSMs having similar power rating since the OW-PMSM drive system has relative large inertia which is 2.5 kg $\cdot$m^2.

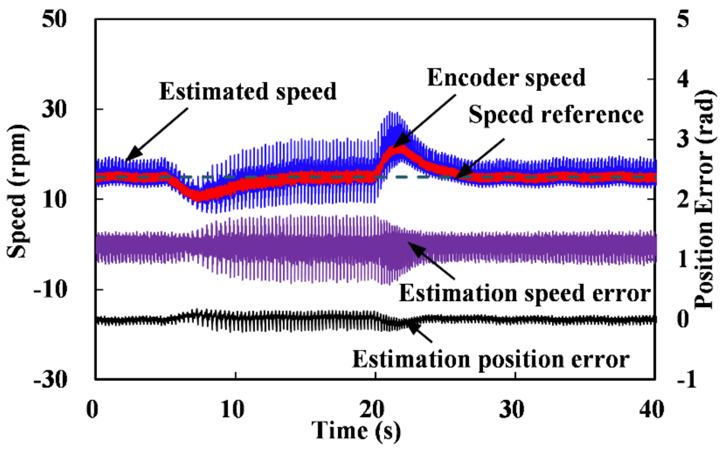

(a)

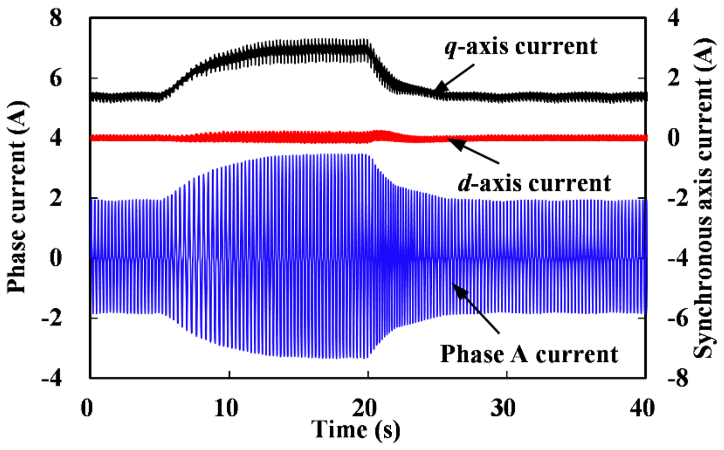

(b)

Fig. 6.20 Transient estimation performance and current signals under rated load disturbance (Rated load disturbance is applied at 6 s and released at 20 s). (a) Estimated speed, encoder speed, speed reference, estimation speed error and estimation position error. (b) *d*-axis, *q*-axis and phase A currents.

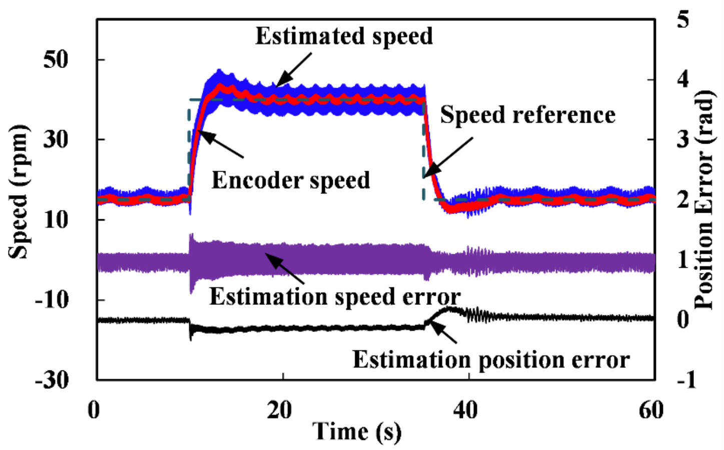

(a)

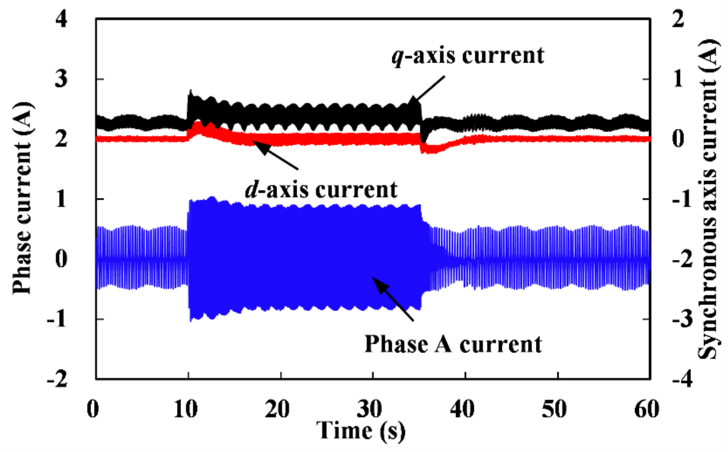

(b)

Fig. 6.21 Transient estimation performance and current signals with step speed reference from 15 rpm to 40 rpm at 10 s and from 40 rpm to 15 rpm at 35 s. (a) Estimated speed, encoder speed, speed reference, estimation speed error and estimation position error. (b) *d*-axis, *q*-axis and phase A currents.

In order to show high speed test, the DC link voltage is increased to 200 V. Fig. 6.22 shows the transient estimation performance and current signals with step speed reference from 80 rpm to 40 rpm at about 7 s. Meanwhile, the reversal speed test is shown in Fig. 6.23. The speed reference steps from -80 rpm to -40 rpm at about 7 s. The load torque condition for 80 rpm and -80 rpm is about 30% of the rated torque. The load torque condition for 40 rpm and -40 rpm is about 20% of the rated torque.

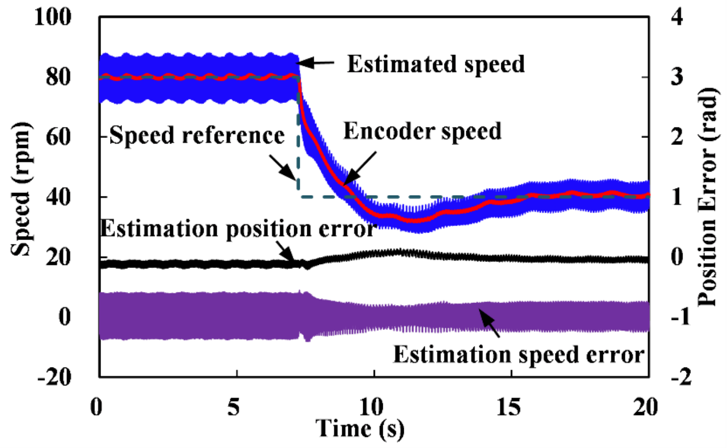

(a)

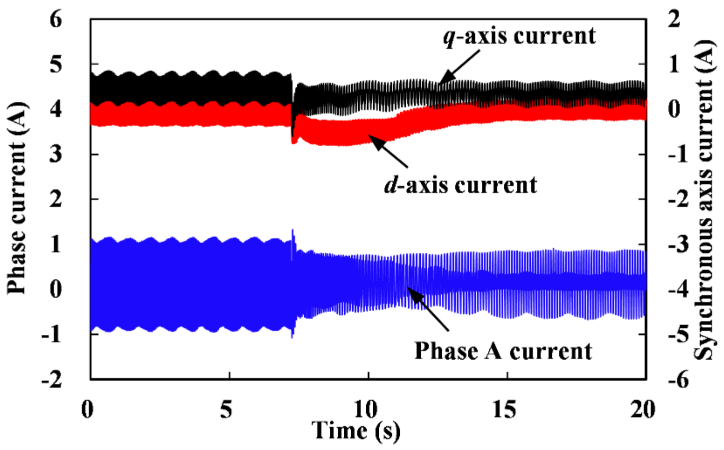

(b)

Fig. 6.22 Transient estimation performance and current signals with step speed reference from 80 rpm to 40 rpm at 7 s. (a) Estimated speed, encoder speed, speed reference, estimation speed error and estimation position error. (b) *d*-axis, *q*-axis and phase A currents.

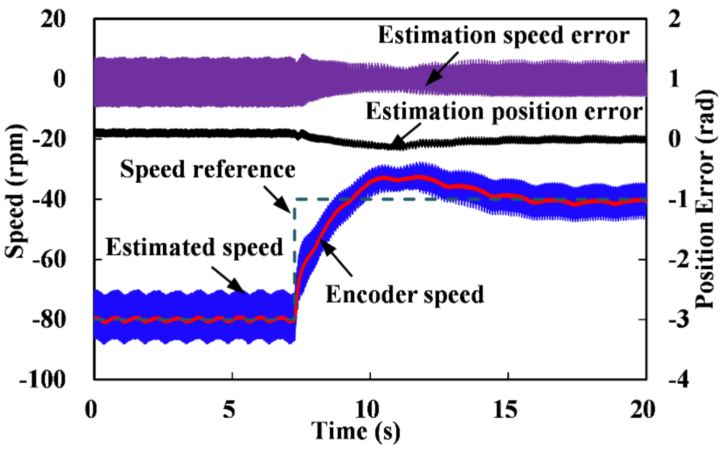

(a)

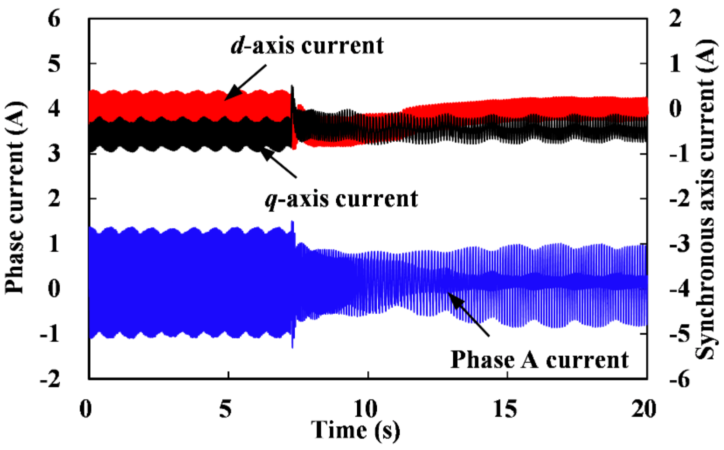

(b)

Fig. 6.23 Transient estimation performance and current signals with step speed reference from -80 rpm to -40 rpm at 7 s. (a) Estimated speed, encoder speed, speed reference, estimation speed error and estimation position error. (b) *d*-axis, *q*-axis and phase A currents.

In order to evaluate the stiffness capability of the proposed sensorless method, the ultimate speed response experiment is shown in Fig. 6.24 with rated load condition at 80 rpm. The transient response performance shown in Fig. 6.24 demonstrates the maximum speed loop stiffness of the proposed method for reliable operation when step speed reference signal (no ramp smoothening) is given. The zoomed regions I and II in Fig. 6.24 (a) are shown in Figs. 6.24 (c) and (d), respectively. The transient response time is around 250 ms.

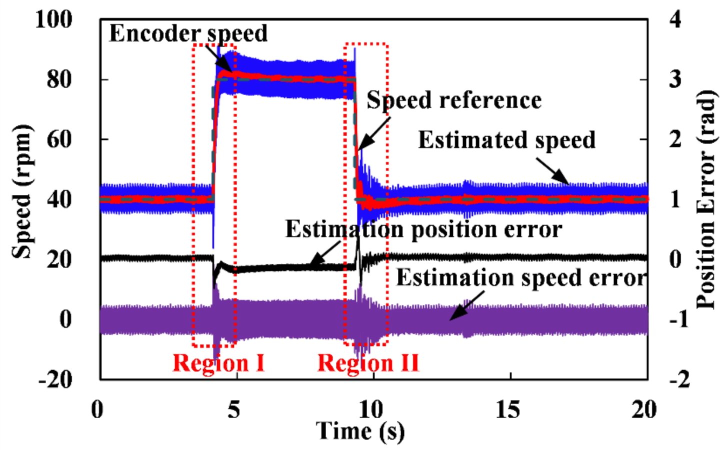

(a)

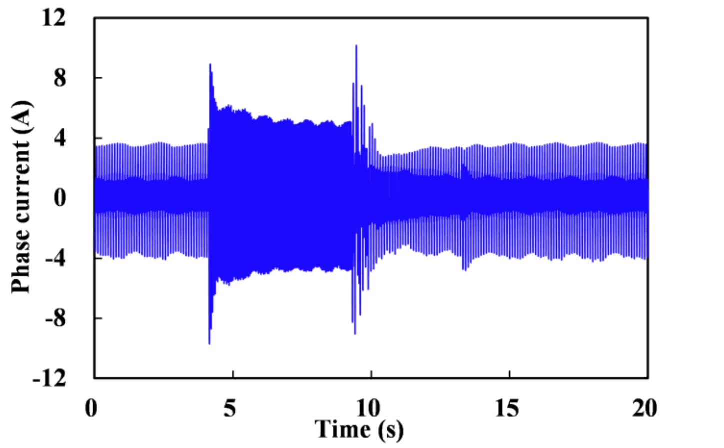

(b)

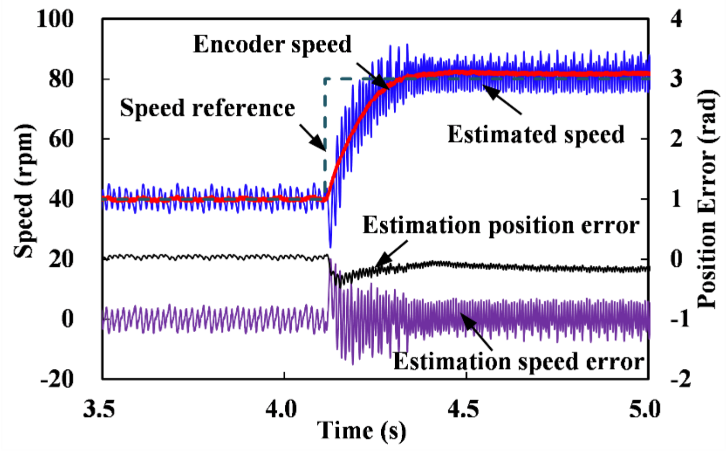

(c)

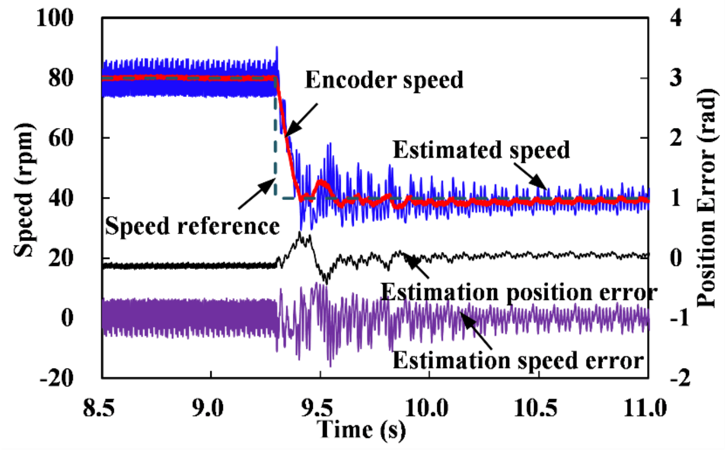

(d)

Fig. 6.24 Transient estimation performance and current signal with step speed reference from 40 rpm to 80 rpm at 4.2 s and from 80 rpm to 40 rpm at 9.3 s. (a) Estimated speed, encoder speed, speed reference, estimation speed error and estimation position error. (b) Phase A current. (c) Zoomed region I. (d) Zoomed region II.

6.7 Conclusion

A novel zero sequence model based sensorless method for OW-PMSM with common DC bus has been proposed in this chapter. The proposed method estimates the rotor position information from the reconstructed third harmonic back EMF by using the induced zero sequence current. No voltage transducer and three phase resistance network are required for the proposed sensorless method when compared to the conventional third harmonic based sensorless method. The proposed method shows acceptable torque ripple and comparable total loss characteristics when compared to no injection operation as confirmed by the results predicted by 2D FEA. Meanwhile, the zero sequence parameter sensitivity analysis for the proposed method has also been implemented. Due to the decoupling of coordinate axis, the proposed method possesses better robustness than conventional fundamental model based sensorless methods which are affected by *d*- and *q*-axis currents and voltages.

CHAPTER 7 NON PARAMETRIC ZERO SEQUENCE BASED SENSORLESS METHOD

The zero sequence current based sensorless method is proposed in Chapter 6. However, the zero sequence current could induce additional losses and torque ripple. In this chapter, an improved sensorless method having non-parametric nature is proposed. The zero sequence current is suppressed by the zero sequence current controller and the proposed method no longer requires any machine parameters.

This chapter is published in IEEE Transactions on Power Electronics.

7.1 Introduction

Permanent magnet synchronous machines (PMSMs) are widely used in industrial applications such as air condition compressors, injection molding machines and servo systems because of the favorable advantages including good efficiency, compact volume and higher torque density. Meanwhile, the PMSMs are also popularly applied in wind power generation, electrical vehicle (EV)/hybrid EV (HEV) and port machinery equipment as the power units [WAN16] [XIE16] [MWA16].

In order to further improve the PMSM drive systems, the open winding-PMSM (OW-PMSM) was then proposed and investigated [JAH80] [WEL04] [SAN13]. The OW-PMSM drive provides several benefits such as higher DC bus voltage utilization, multi-level modulation, potential fault tolerant capability and flexible current controllability that makes it a potential candidate for wind power and EV/HEV applications. From the perspective of DC sources of the inverters, the OW-PMSM drives can be categorized into two, viz., the common and the isolated DC bus topologies [BOD13] [BOD14]. The isolated DC bus topology has higher DC bus voltage utilization but also leads to high system cost and size. The common DC bus topology avoids the disadvantages but brings the circulating current issue [BOD15] [AN16] due to the existence of zero sequence path.

Besides the drive topologies, the sensorless (self-sensing) strategies [CHE03] [WAN14] [MOR02] [JAN95] [JAN04] [YAN12] are also drawing wide attention for the elimination of the position sensor which is usually required in the vector control drive. Hence, combining the sensorless strategy together with the OW-PMSM drive can be a good choice to utilize their synergies. Generally, the sensorless methods are divided into two types including the back EMF based methods [CHE03] [WAN14] [MOR02] and the rotor saliency (inductive and resistive saliency) based methods [JAN95] [JAN04] [YAN12]. The back EMF based methods introduce no additional harmonic current excitation, which are usually used for high speed application. However, the back EMF based methods have poor performance at low speed and are not feasible for zero speed condition. Hence, the saliency based methods using high frequency injection [JAN95] [JAN04] [YAN12] or PWM excitation [GAO09] are adopted for the operation at low speed range. Hence, these two methods can be integrated for the full speed range operation [WAN13a]. However, for specific products, the back EMF based methods are used independently such as the air condition compressor which is normally working at high speed range. The startup can be achieved via appropriate open loop strategy [WAN12a].

Particularly, the zero sequence based sensorless methods are actually either saliency [BRI05] [BRI06] [XU16] [XU16a] [LEI11] [CAR05] [CON06] or back EMF based [SHE04] [SHE06] [LIU14a] [TSO15] [ZHA16a], which are considered as an independent category from a different point of view. The saliency can also induce signal modulation in zero sequence, which can be used to estimate the rotor position. In [BRI05] the authors proposed a zero sequence carrier voltage signal based sensorless method and then the zero sequence current based method is studied in [BRI06] for a delta connected salient machine. In [XU16], the injection signal is imposed at the anticlockwise rotating estimated reference frame to improve the estimation performance, which is also based on the nature of saliency. Meanwhile, in [XU16a], the saturation information used for polarity identification is included and the modulated zero sequence signal in zero sequence containing both second saliency and polarity information is extracted. Therefore, the issue of ambiguous polarity detection in conventional saliency based methods is solved. Besides, the PWM voltage is used as the excitation signal in [LEI11] to modulate the rotor position information in zero sequence and hence no additional disturbance signal is introduced. A nonintegrating Rogowski coil is used in [CAR05] to extract the zero sequence current derivative from the test voltage vectors to track the flux position of the induction machine (IM). In [CON06], a low frequency signal demodulation strategy in zero sequence is studied to identify the air gap flux position for IM.

The zero sequence back EMF based sensorless method is also called third harmonic based method [SHE04]. The harmonic back EMF in zero sequence is utilized to estimate the rotor position information. In [SHE04], the sensorless method for brushless DC (BLDC) machine, which uses zero sequence back EMF from voltage transducer, is studied together with flux weakening algorithm. The phase locked loop (PLL) technique is introduced in [SHE06] to improve the estimation performance. The digitized enhanced estimator is proposed in [LIU14a] for the further improvement. Besides, an improved signal processing technique of measured zero sequence voltage which contains position information for sensorless commutation of the BLDC machine is proposed in [TSO15], which is called adaptable sensorless commutation. A zero sequence current based sensorless method for OW-PMSM is proposed in [ZHA16a].

In this chapter, a novel zero sequence back EMF based sensorless method together with circulating current suppression is proposed for the OW-PMSM drive. The proposed method extracts the rotor position information from the output signal of the zero sequence current controller (ZSC). The zero sequence steerable space vector pulse width modulation (SVPWM) (ZSS-SVPWM) strategy is designed for the ZSC. When compared to the conventional zero sequence back EMF based sensorless methods, the voltage transducer and three phase resistance network, viz., zero sequence voltage measurement is no longer necessary. The proposed method is non-parametric when compared with conventional fundamental back EMF based methods. Hence, the superiority of the proposed method also emerges under machine parameter uncertainty due to temperature or load variations. The disturbance voltage drops due to the resistance, inductance and cross coupling which are inevitable in conventional fundamental back EMF based methods can be avoided in the proposed method. Along with the essence of axis decoupling, stronger robustness is guaranteed in the proposed method. This chapter is organized as follows: In Section 7.2, the system configuration and OW-PMSM model considering zero sequence is introduced. Frozen permeability for 2 dimensional (2D) finite element analysis (2D-FEA) is used to investigate the influence on zero sequence back EMF of the prototype OW-PMSM from the armature current. In Section 7.3, the phase shift based zero sequence steerable SVPWM (ZSS-SVPWM) is presented. In Section 7.4, the principle of the proposed method is exhibited. The experimental validation is shown in Section 7.5.

7.2 Common DC Bus Based OW-PMSM Drive System Configuration and Modelling

7.2.1 OW-PMSM Drive System Configuration

Fig. 7.1 shows the integral OW-PMSM drive system diagram. The adopted OW drive topology is based on a dual 2-level voltage source inverter (VSI) structure with common DC bus. Each phase of the OW-PMSM is equivalently controlled by an H-bridge single phase inverter. Hence, the current in each phase can be controlled independently. Meanwhile, this control strategy is an improved sensorless field oriented control with easier implementation, which includes the proposed non-parametric sensorless method and the phase shift based ZSS-SVPWM strategy. The proposed non-parametric sensorless method enables a simple sensorless implementation without using machine parameters. The improved phase shift based ZSS-SVPWM is achieved via reconstructing voltage reference signals and adding additional zero sequence component in the conventional SVPWM module. The installed encoder is for the experimental comparison. The prototype OW-PMSM has outer rotor structure and large inertia coupled with the load, which is designed for wind power application.

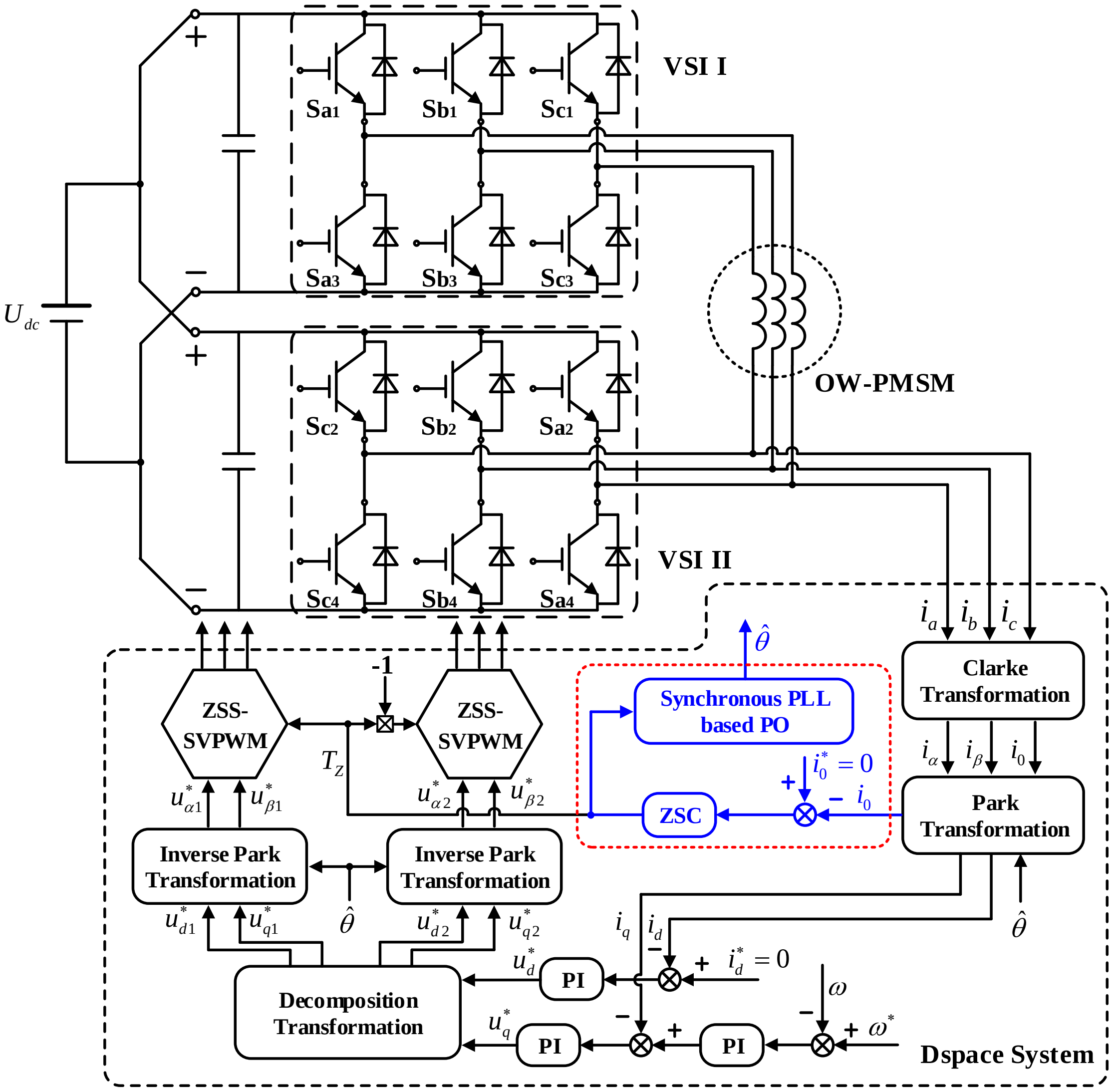

Fig. 7.1 OW-PMSM drive system diagram.

7.2.2 Model of OW-PMSM with Common DC Bus

The mathematical model for OW-PMSM with common DC bus is different from the conventional single inverter fed PMSM drive model since the existence of zero sequence path in this system. The delta connection PMSM usually has uncontrollable and short circuited zero sequence path. Meanwhile, the zero sequence circuit for Y connection PMSM is open circuited. The OW-PMSM drive with common DC bus is capable of steerable zero sequence output voltage. Hence, the zero sequence equation in the model for this system should be considered. The integral mathematical model expressed in the *d*-*q* synchronous coordinate system has been shown in (4.1)

Fundamental back EMFs are usually utilized to extract the rotor position information. Besides, the third harmonic back EMF is also used when the access of neutral point of Y connection PMSM is available. The third harmonic is the dominant harmonic back EMF in the PMSMs, which ensures enough signal noise ratio (SNR) for the estimation. When the third harmonic back EMF is considered to be the indicator of position signal, it is necessary to investigate the variation of third harmonic back EMF under different load conditions, especially for the phase of third harmonic back EMF.

However, it is only feasible to measure the open circuit back EMF waveform of the PMSM, while the on load one cannot be measured since the PWM harmonics, winding inductance and resistance voltage drops are superimposed. Hence, the frozen permeability method [CHU13a] for 2D-FEA is used to carry out this investigation. Fig. 2.1(a) shows the comparison between the measured open circuit phase back EMF waveform and the result from 2D-FEA at 10rpm. The measured fundamental phase back EMF has 4.4% lower amplitude when compared to the 2D-FEA result due to the end effect of the machine. The 2D-FEA result is consistent with the measured one, which confirms the effectiveness of FEA. Fig. 2.1 (b) shows the phase analysis of the open circuit and on load back EMF waveforms under different load currents. It can be seen that the third harmonic back EMF component of the OW-PMSM is hardly affected by the load current. Whereas, this is mainly due to the large air gap of the OW-PMSM which is a surface mounted PMSM and common for industry applications.

7.3 Phase Shift Based ZSS-SVPWM for OW-PMSM

In the conventional SVPWM strategy, the zero sequence components, namely, the vector $\boldsymbol{V_0}$ and $\boldsymbol{V_7}$ are essentially decided by the modulation strategy itself. Meanwhile, the zero sequence component exhibiting as quasi-triangle wave can improve the DC bus utilization ratio of the system. However, for OW system with common DC bus, the zero sequence path is no longer open circuit, which means that the zero sequence disturbance voltage will induce relevant harmonic currents for the system. These harmonic currents will increase the losses of the machine and drives. Moreover, the additional torque ripple which is produced by third harmonic current and zero sequence back EMF, is usually inevitable. From another aspect, the third harmonic back EMF contained in the OW-PMSM is the zero sequence disturbance source which should be compensated via the zero sequence voltage produced from inverter side. Hence, the indispensable PWM strategy for OW-PMSM drive system requires two aspects. One is the elimination of the zero sequence disturbance voltage produced by the PWM strategy. Another is the steerable zero sequence component which could be controlled to the matching voltage versus zero sequence back EMF from the machine side. The proposed method is based on the phase shift SVPWM strategy improved by adding steerable zero sequence component for each SVPWM module, viz., ZSS-SVPWM.

The associated techniques have been introduced in Chapter 2. When the reference voltage signals are generated, they are input into the individual ZSS-SVPWM module together with T_z which is the control signal from ZSC. This control signal T_z is superimposed on the internally generated zero sequence component. The control signal for the second set of VSI is multiplied by -1 due to the corresponding phase reversal. It can be seen that the zero sequence control signal imposes no influence on the sector selection which means the conventional selection process is available for the ZSS-SVPWM.

The phase shift process is used to eliminate the inner zero sequence disturbance voltage of the SVPWM strategy, while the steerable zero sequence component receives regulation signal from the ZSC to produce matching zero sequence voltage to the zero sequence back EMF. For each set of VSI, the produced zero sequence voltage still contains quasi-triangle wave, which is used to increase the DC bus utilization, and superimposed by the steerable zero sequence signal generated by the ZSC. However, due to the cancellation of third harmonic between two sets of the inverters, the equivalent disturbance component for the ZSC is merely the zero sequence back EMF.

7.4 Principle of Proposed Sensorless Method

7.4.1 Equivalent Zero Sequence Circuit Model

The conventional zero sequence back EMF based sensorless method is shown in Fig. 6.3. The voltage transducer is necessary and the neutral point of the machine should be accessible for this application. Meanwhile, the corresponding equivalent zero sequence is shown as Fig. 6.4. The resistance network is used to reconstruct a measurement point for the circuit. Since it is an open circuit for the conventional topology, the zero sequence back EMF can be measured between point *R* and *N* or point *O* and *N* in Fig. 6.4. However, the voltage between *O* and *N* contains zero sequence voltage produced by the adopted PWM strategy superimposed on the zero sequence back EMF signal, the voltage measurement between *R* and *N* is usually chosen. When the neutral point of the machine is not accessible, not only the voltage between reconstructed neutral point *R* and *O* is required, but also independent phase voltage measurement is necessary. It means that additional voltage transducer is usually utilized in this case.

The equivalent zero sequence circuit for OW-PMSM drive with common DC bus is no longer open circuited. The zero sequence back EMF exists as third harmonic voltage source. The position and speed information is contained in the third harmonic back EMF. Meanwhile, the output of the ZSC is the other voltage source in the circuit used for compensating the zero sequence back EMF to avoid zero sequence circulating current. Hence, the corresponding equivalent zero sequence circuit can be modelled as Fig. 6.5. It can be seen that the circuit is divided into two sides, namely, the inverter side and the machine side. The inverter side is a single controlled voltage source. The machine side includes zero sequence inductance, phase resistance and zero sequence back EMF.

7.4.2 Circulating Current Suppression

As illustrated in Section 7.4.1, the zero sequence differential equation can be expressed as

$$u_0 = (L_{s0} - 2M_{s0})\frac{di_0}{dt} + i_0 R_s + 3\omega\psi_{f0}\sin 3\theta \tag{7.1}$$

where $e_0 = 3\omega\psi_{f0}\sin 3\theta$, L_{s0} represents the average phase self-inductance and M_{s0} represents the average mutual-inductance between any two phases.

The Laplace transform of (7.1) can be given as

$$\frac{U_0(\mathrm{s})-\dfrac{9\psi_{f0}\omega^2}{s^2+9\omega^2}}{(L_{s0}-2M_{s0})s+R_s}=I_0(\mathrm{s}) \tag{7.2}$$

where U_0(s) and I_0(s) are the Laplace transform of u_0 and i_0, respectively.

The traditional PI controller

$$C(\mathrm{s})=k_p+\frac{k_i}{s} \tag{7.3}$$

is adopted as ZSC to suppress the zero sequence circulating current in this paper. Hence, a closed zero sequence current loop is formed.

Moreover, the inverters are simplified as a first order inertia system, viz.,

$$G_{inv}(\mathrm{s})=\frac{k_{PWM}}{\tau_s s+1} \tag{7.4}$$

where K_{PWM} is the amplification factor.

The sampling delay block is defined as

$$H_s(\mathrm{s})=\frac{1}{\tau_d s+1} \tag{7.5}$$

where τ_d is the sampling delay time constant.

Hence, the block diagram of the zero sequence current loop can be shown in Fig. 7.2.

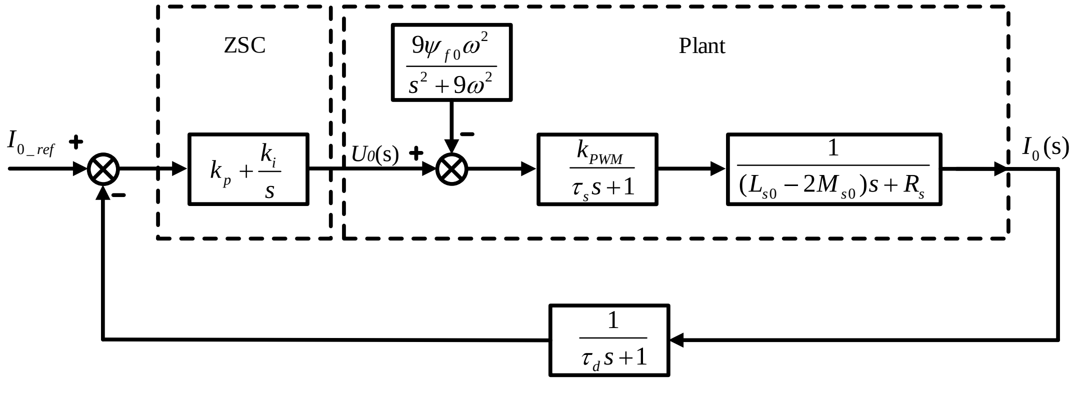

Fig. 7.2 Block diagram of the zero sequence current loop.

In order to analyze the stability of the control mode, root locus can be used for the analysis. Firstly, the open loop transfer function of zero sequence current loop can be given as

$$\begin{aligned} G_{op}(s) &= C(s)G_{inv}(s)H_s(s) \\ &= \frac{k(s+k_i/k_p)}{s(s+1/\tau_s)[s+R_s/(L_{s0}-2M_{s0})](s+1/\tau_d)} \end{aligned} \tag{7.6}$$

where the loop gain k satisfies

$$k = \frac{k_{PWM}k_p}{\tau_s\tau_d(L_{s0}-2M_{s0})}. \tag{7.7}$$

Meanwhile, the time constant of the zero sequence circuit is defined as $\tau_0=(L_{s0}-2M_{s0})/R_S$. The selection of k_p and k_i for ZSC usually satisfies

$$\tau_c = k_p/k_i = \lambda\tau_0. \tag{7.8}$$

When $\lambda=1$, pole-zero cancellation is achieved. However, if the parameters of the plant are not accessible, λ can be configured via experiment and is in a certain range around 1.

The phase resistance and zero sequence inductance of the tested OW-PMSM are 3.76Ω and 12mH, respectively. Hence, τ_0=3.2ms. Fig. 7.3 shows the root locus of the zero sequence current loop with different τ_c. It can be seen that the stability of the loop can be guaranteed via proper parameter selection to make all the roots on the left-hand plane.

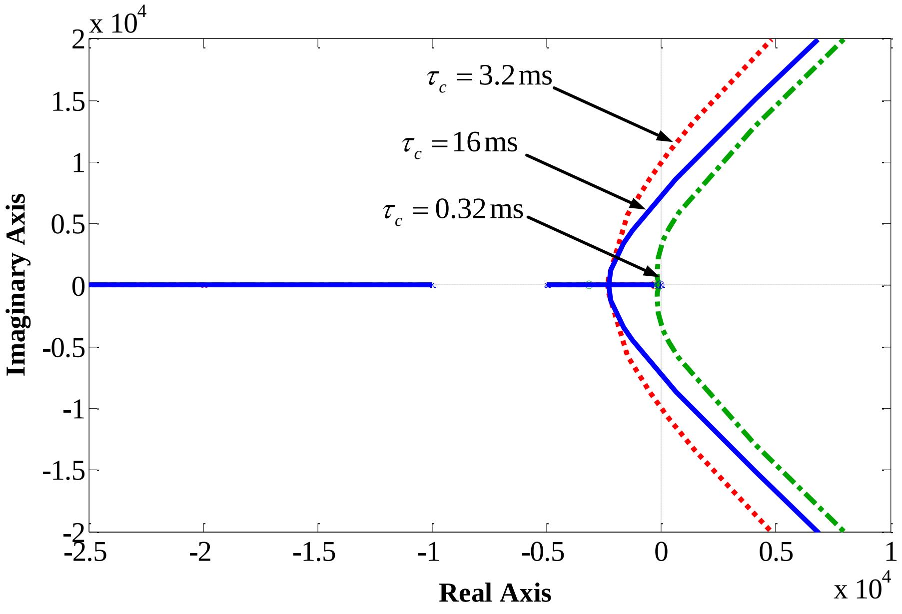

Fig. 7.3 Root locus of the zero sequence current loop.

In order to verify the suppression performance of the third harmonic component, the bandwidth analysis is conducted as follows.

Since the time constants τ_s and τ_d satisfy $\tau_s \ll \tau_0$ and $\tau_d \ll \tau_0$, the small time constants can be merged together as $\tau_p=\tau_s+\tau_d$. The open loop transfer function can be simplified as

$$G_{op}(s)=\frac{k'(\tau_c s+1)}{\tau_c s(\tau_p s+1)(\tau_0 s+1)} \tag{7.9}$$

where k' satisfies

$$k'=\frac{k_{PWM}k_p}{R_s}. \tag{7.10}$$

Choose $\tau_c=\tau_0$, the closed loop function can be expressed as

$$G_{cl}(s)=\frac{k'}{\tau_c\tau_p s^2+\tau_c s+k'}. \tag{7.11}$$

It can be seen that (7.12) is a 2-order system and the damping ratio is

$$\zeta=\frac{1}{2}\sqrt{\frac{\tau_0}{\tau_p k'}}. \tag{7.12}$$

According to engineering design, choose $\zeta=0.707$, the open loop cut-off frequency and the closed loop bandwidth can be expressed as

$$\omega_{op}=\frac{1}{\tau_p}\sqrt{\frac{\sqrt{2}-1}{2}} \tag{7.13}$$

$$\omega_{cl}=\frac{\sqrt{3}-1}{2\tau_p}. \tag{7.14}$$

The PWM switching frequency of the control system is chosen as 5kHz. Hence, the closed loop bandwidth is

$$\omega_{cl}=\frac{\sqrt{3}-1}{2\tau_p}=194\,\text{Hz}. \tag{7.15}$$

Meanwhile, the maximum operation speed of the OW-PMSM is n_m=80rpm and the corresponding operation frequency is

$$f_m = \frac{n_m p}{60} \approx 21.33\,\text{Hz}\,. \tag{7.16}$$

The maximum frequency of the suppressed third harmonic component is

$$f_{3rd} = 3 f_m = 64\,\text{Hz} \tag{7.17}$$

which is within the designed bandwidth.

7.4.3 Signal Process and Position Estimation

As indicated in (7.1), if the zero sequence current is suppressed completely and supposed as zero, the output zero sequence voltage u_0 produced by the dual inverters satisfies

$$u_0 = 3\omega\psi_{f0}\sin 3\theta = e_0\,. \tag{7.18}$$

It means that the regulation output signal of the ZSC is equivalent to zero sequence back EMF e_0. Hence, this signal can be consequently used for position estimation. It can be also noticed that no voltage measurement is required here to obtain the zero sequence back EMF information. Moreover, when compared to the conventional fundamental back EMF based methods using *d*- and *q*-axis equations as

$$\begin{bmatrix} u_d \\ u_q \end{bmatrix} = \underbrace{\begin{bmatrix} R_s + pL_d & -\omega L_q \\ \omega L_d & R_s + pL_q \end{bmatrix}\begin{bmatrix} i_d \\ i_q \end{bmatrix}}_{\text{disturbance voltage drops}} + \begin{bmatrix} 0 \\ \omega\psi_f \end{bmatrix} \tag{7.19}$$

where *p* is the differential operator, the output signal of ZSC is simply the zero sequence back EMF without any other disturbance voltage drops, such as resistance, inductance and rotating cross coupling voltage drops, which are included in the first term in the right hand side of (7.19). No matter what the signal process technique (model reference adaptive system, Kalman filter or sliding-mode observer) is, the deduction of the disturbance voltage drops is always firstly required for the fundamental back EMF based methods. Consequently, it makes these methods become sensitive to motor parameters accuracy and variations since the disturbance voltage drops are directly relevant to these motor parameters. Even sliding-mode observer owns more robust characteristic, the motor parameters are still demanded. However, the basic equation (7.18) used in the proposed method contains no motor parameters even the zero sequence parameters. It is much more concise than (7.19), which indicates the ease of signal process and reconstruction. In addition, the zero axis is independent from the *d*- and *q*-axes, hence the variation of load imposes no influence which should be considered in the conventional fundamental back EMF based methods.

Once the equivalent zero sequence back EMF signal is obtained, it can be used as the input signal of a synchronous PLL based position observer (PO). The proposed position estimation process is shown in Fig. 7.4.

The synchronous PLL based PO has a single phase PLL structure, in which the low pass filters (LPFs) are

$$G_{LPF}(\mathrm{s}) = \frac{\overline{e}_{d0}(\mathrm{s})}{e_{d0}(\mathrm{s})} = \frac{\overline{e}_{q0}(\mathrm{s})}{e_{q0}(\mathrm{s})} = \frac{\omega_f}{s+\omega_f} \tag{7.20}$$

where ω_f is the cut-off frequency.

The LPFs can be transformed into the stationary reference coordinate and behave as band pass filter (BPF) and LPF, respectively. The center frequency of the BPF is adaptive to the operation frequency. The frequency multiplication index *h* is used for the multiplication between fundamental and harmonic (third harmonic) back EMFs. Hence, the transfer functions are expressed as

$$G_d(\mathrm{s}) = \frac{e'_{\alpha 0}(\mathrm{s})}{e_{\alpha 0}(\mathrm{s})} = \frac{k_f \omega_0 s}{s^2 + k_f \omega_0 s + \omega_0^2} \tag{7.21}$$

$$G_q(\mathrm{s}) = \frac{e'_{\beta 0}(\mathrm{s})}{e_{\alpha 0}(\mathrm{s})} = \frac{k_f \omega_0^2}{s^2 + k_f \omega_0 s + \omega_0^2} \tag{7.22}$$

where $k=\omega_f/\omega_0$ and $\omega_0=h\omega=3\omega$.

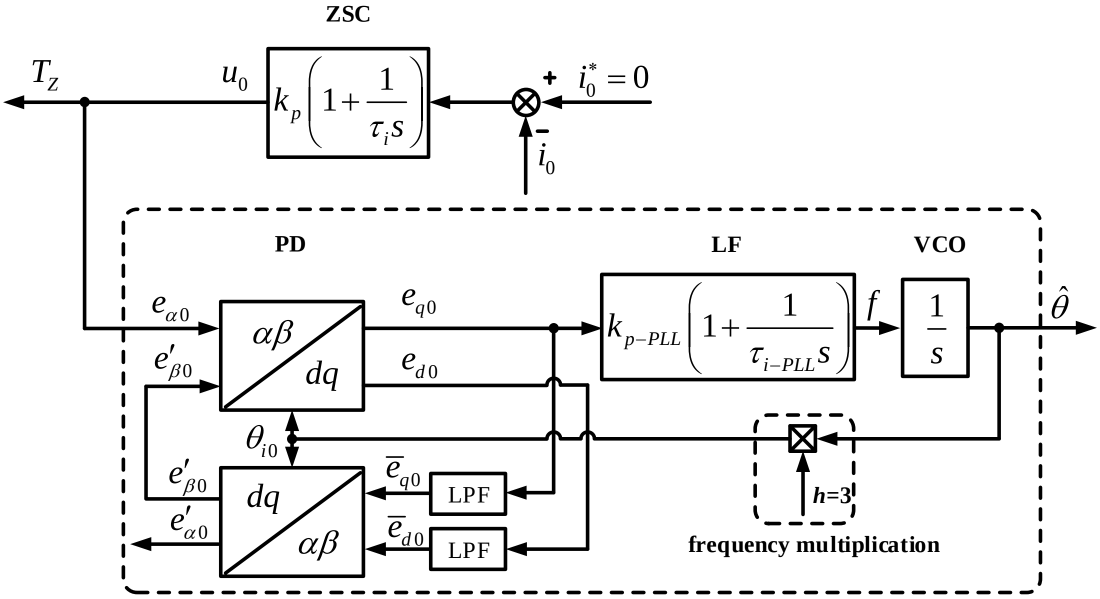

Fig. 7.4 Position estimation process using synchronous PLL based PO.

The proposed sensorless method can be understood as similar to the restart process [IUR11] for conventional back EMF based sensorless control of PMSM under free-running condition. For the sensorless restart process, the output voltage of the inverter is firstly generated to match the back EMF of the PMSM to suppress to phase currents to zero. Meanwhile, the generated voltage is equivalent to the back EMF which is consequently used for position estimation. The proposed method has the similar process by generating matching output voltage for back EMF, viz., zero sequence back EMF. However, the conventional restart process is temporary and the disturbance voltage drops are still needed to be considered at regular operation condition with different load currents and speed references. The proposed method can be deemed as persistent sensorless restart process which receives no influence from the operation conditions. The operation requirement for zero sequence remains unchanged, namely, zero current for zero sequence. An independent virtual coil in zero sequence having harmonic back EMF is controlled to zero current condition and this coil is decoupled from *d*- and *q*-axes. This virtual coil is not used to generate any torque for the drive system. From another perspective, the proposed method can be regarded as an independent virtual position senor integrated with the drive system. Stronger robustness could be expected for the proposed method.

7.5 Experimental Validation

The experimental validation is conducted on a 3kW outer rotor OW-PMSM platform. The algorithm is implemented based on dSPACE system. The specification of the OW-PMSM and control system are listed in Table 7.1. Fig. 4.6 shows the figure of the experiment platform. The load machine is a three phase PMSM working in generator mode and connected to the adjustable power resistance.

Fig. 7.5 shows the suppression performance for the circulating current at 15rpm including the phase A current and circulating current waveforms. This strategy is implemented with encoder feedback as the preliminary validation. The ZSC is enabled at 5s in Fig. 7.5 (a) and the circulating current is suppressed after the ZSC enabled. Figs. 7.5 (b) and (c) show the magnified regions marked as I and II in Fig. 7.5 (a), respectively. There exists dominant third harmonic current in the circulating current before the suppression.

TABLE 7.1 SPECIFICATION OF OW-PMSM AND CONTROL SYSTEM

Parameter	Value
Pole pairs	16
Resistance (Ω)	3.76
Rated RMS current (A)	2.83
Rated speed (rpm)	80
No-load PM flux linkage (Wb)	0.9
Encoder resolution	4096
Rated frequency (Hz)	45.33
d-axis inductance (mH)	17
q-axis inductance (mH)	17
DC bus voltage (V)	200
PWM switching frequency (kHz)	5
Dead-time (μs)	2

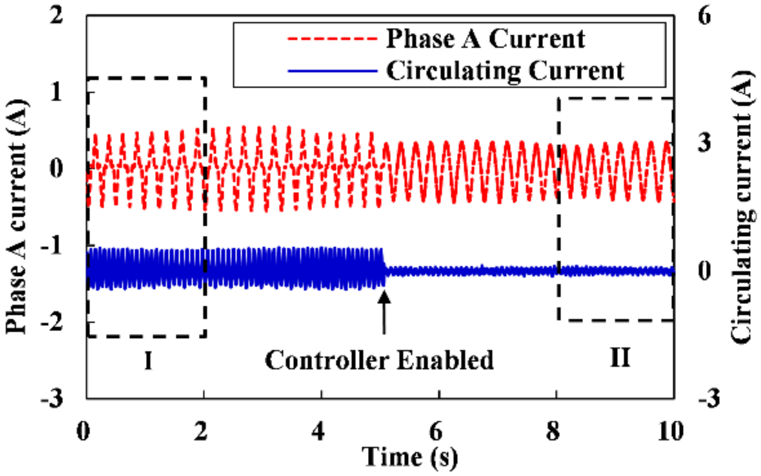

(a)

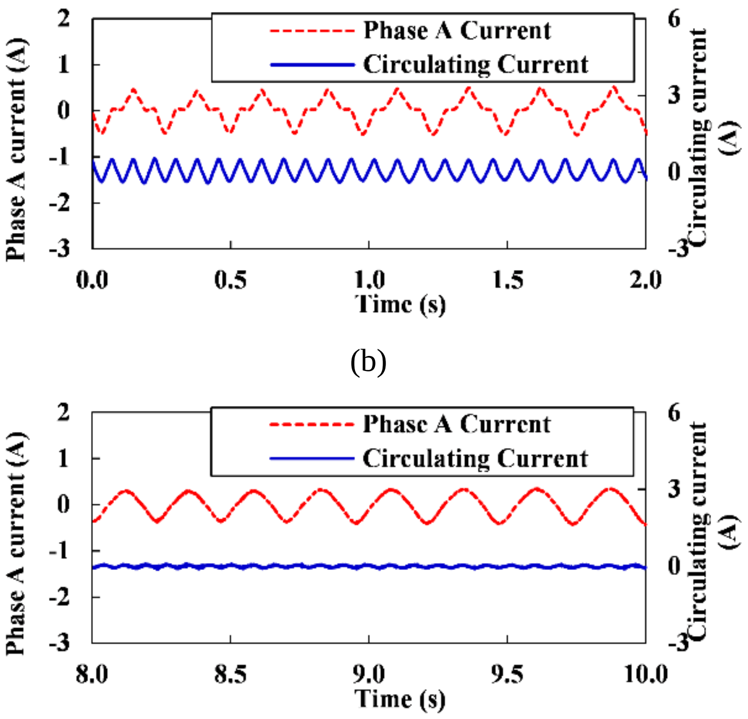

(b)

(c)

Fig. 7.5 Circulating current suppression performance before and after controller enabled. (a) Circulating current suppression performance with controller enabled at 5s. (b) Before the ZSC enabled-region I. (c) After the ZSC enabled-region II.

Fig. 7.6 shows the steady state estimation performance of the proposed sensorless method. Fig. 7.6 (a) shows the estimated angle, encoder angle and estimation error at 15rpm with no load condition. Fig. 7.6 (b) shows the counterpart at 15rpm with rated load. The on load condition induces larger estimation error than the no load condition. Meanwhile, the 15rpm is the minimum robust operation speed condition for the proposed method under step speed reference and load disturbances.

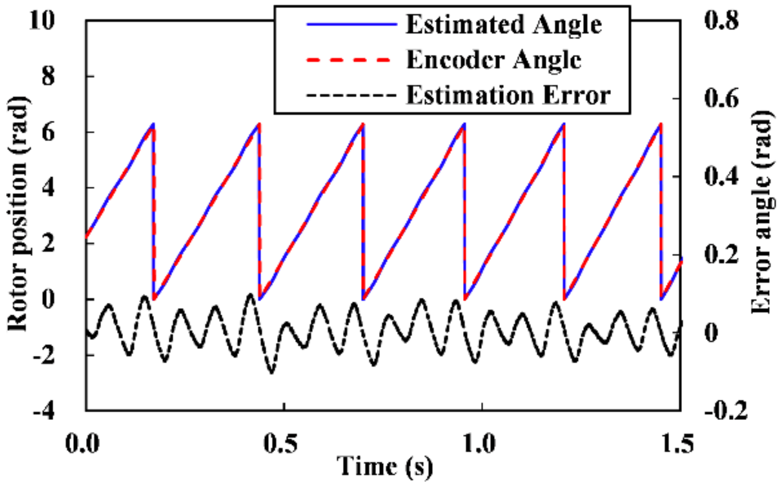

(a)

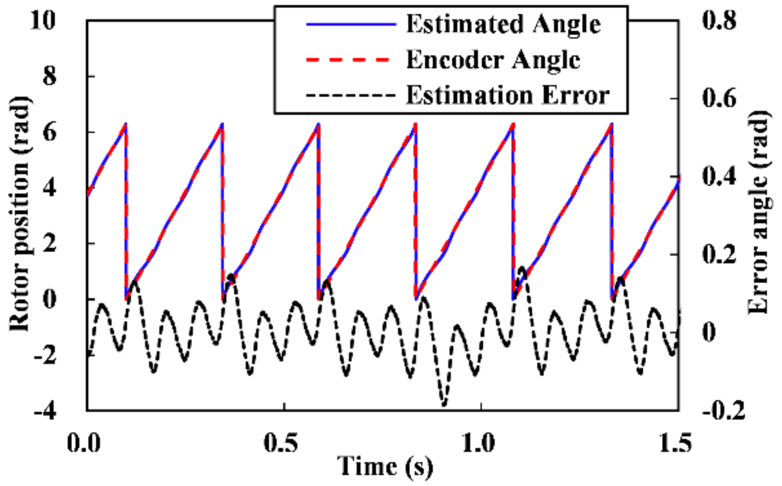

(b)

Fig. 7.6 Steady state estimation performance including estimated angle, encoder angle and estimation error at 15rpm with no load and rated load conditions. (a) No load condition. (b) Rated load condition.

Fig. 7.7 shows the transient state estimation performance and current signals under rated step load disturbance. The step load is imposed at 7s and released at 22s. Fig. 7.7 (a) shows the estimated speed, encoder speed, speed reference and estimation position error, respectively. Fig. 7.7 (b) shows the magnified region I in Fig. 7.7 (a), viz., steady state estimation process at 40rpm with no load condition. Fig. 7.7 (c) shows the magnified region II in Fig. 7.7 (a), viz., steady state estimation process at 40rpm with rated load condition. Fig. 7.7 (d) shows the simultaneous *d*-axis, *q*-axis and phase A currents, respectively.

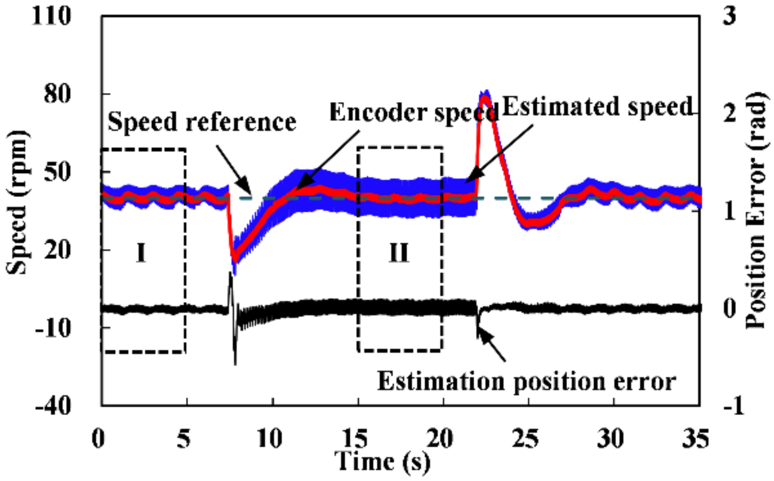
Speed reference
Encoder speed
Estimated speed
I
II
Estimation position error
Speed (rpm)
110
80
50
20
-10
-40
Position Error (rad)
3
2
1
0
-1
0
5
10
15
20
25
30
35
Time (s)

(a)

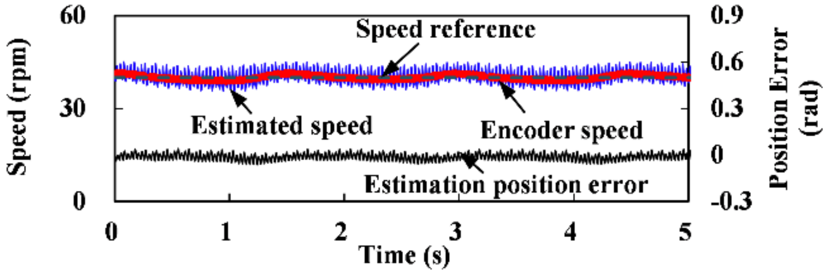
Speed reference
Estimated speed
Encoder speed
Estimation position error
Speed (rpm)
60
30
0
Position Error (rad)
0.9
0.6
0.3
0
-0.3
0
1
2
3
4
5
Time (s)

(b)

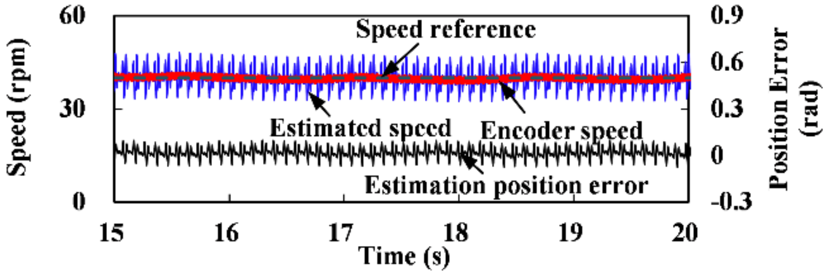
Speed reference
Estimated speed
Encoder speed
Estimation position error
Speed (rpm)
60
30
0
Position Error (rad)
0.9
0.6
0.3
0
-0.3
15
16
17
18
19
20
Time (s)

(c)

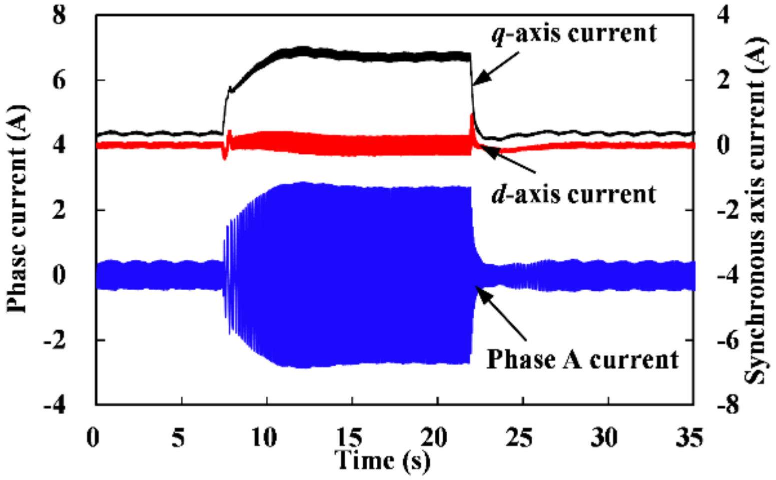
q-axis current
d-axis current
Phase A current
Phase current (A)
8
6
4
2
0
-2
-4
Synchronous axis current (A)
4
2
0
-2
-4
-6
-8
0
5
10
15
20
25
30
35
Time (s)

(d)

Fig. 7.7 Transient state estimation performance and current signals under rated step load disturbance. (a) Estimated speed, encoder speed, speed reference and estimation position error. (b) Magnified region I (40rpm-no load). (c) Magnified region II (40rpm-rated load). (d) *d*-axis, *q*-axis and phase A currents.

Fig. 7.8 shows the transient state estimation performance and current signals with step speed reference from 40rpm to 80rpm. The step speed reference is given at 10s and steps back at 25s. Fig. 7.8 (a) shows the corresponding estimated speed, encoder speed, speed reference and estimation position error, respectively. Fig. 7.8 (b) shows the magnified region III in Fig. 7.8 (a), viz., steady state estimation process at 80rpm with no load condition. Fig. 7.8 (c) shows the simultaneous *d*-axis, *q*-axis and phase A currents, respectively.

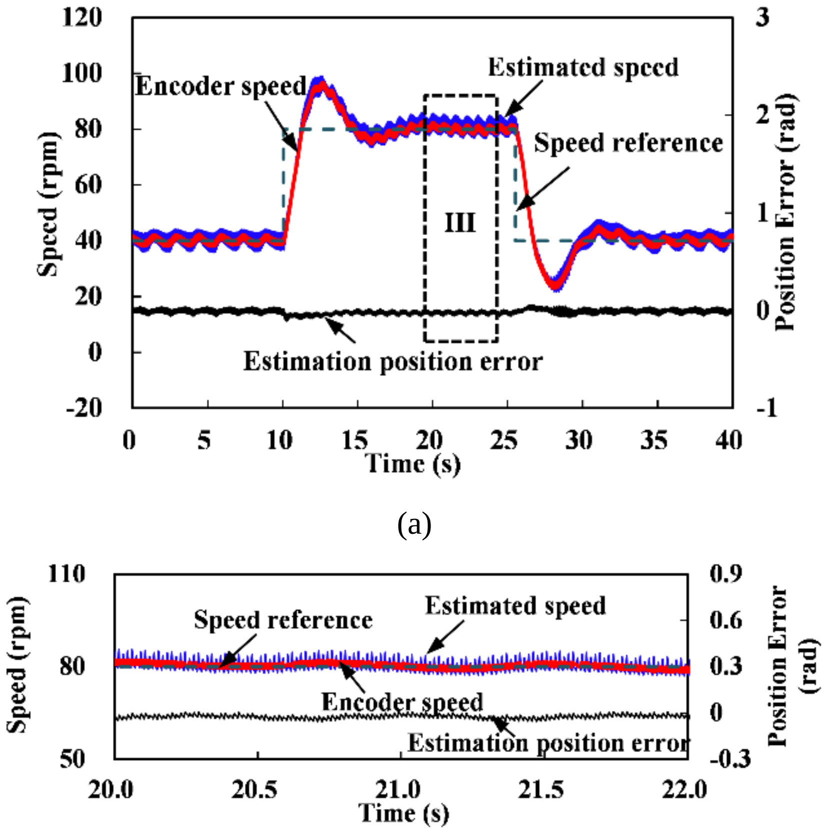

(a)

(b)

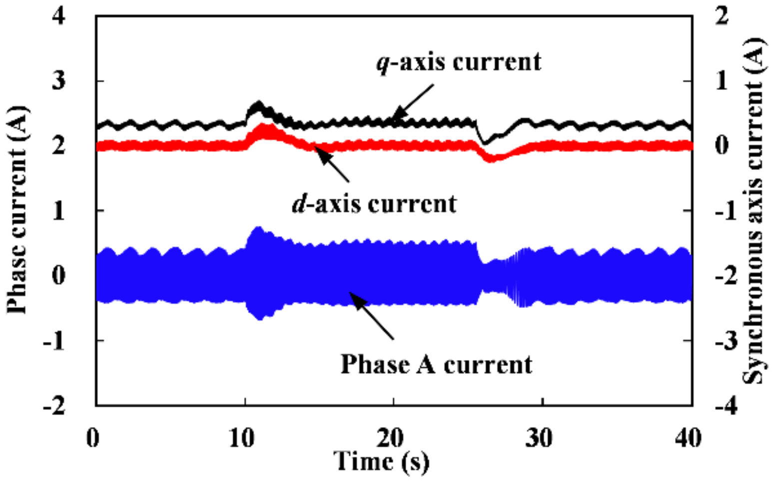

(c)

Fig. 7.8 Transient state estimation performance and current signals with step speed reference from 40rpm to 80rpm. (a) Estimated speed, encoder speed, speed reference and estimation position error. (b) Magnified region III (80rpm-no load). (c) *d*-axis, *q*-axis and phase A currents.

It can be seen that the higher speed operation induces lower estimation error and the loaded condition induces higher estimation error by comparing the steady state estimation error in region I, II and III in Fig. 7.7 (a) and Fig. 7.8 (a). It is also noteworthy that the transient performance has larger settling time when compared to the same power level drive system since the large inertia (2.5kg m^2) due to the special design for wind power prototype system. The low order current harmonic envelope is due to the assembly deviation of the shaft.

7.6 Conclusion

A novel zero sequence back EMF based sensorless method for OW-PMSM together with circulating current suppression has been proposed in this chapter. The proposed method has been achieved by extracting the rotor position information from the output signal of the ZSC working with the ZSS-SVPWM. The synchronous PLL has been adopted for the signal processing. The proposed method possesses several merits including the elimination of voltage measurement in conventional zero sequence back EMF based method, the non-parametric essence and higher robustness. The proposed non-parametric sensorless method has been validated through experiments on a 3kW OW-PMSM platform.

CHAPTER 8 ZERO SEQUENCE HIGH FREQUENCY VOLTAGE INJECTION BASED SENSORLESS METHOD

The back EMF based sensorless methods introduced in Chapters 6 and 7 can be effective for the machine speed above certain value. In this chapter, a novel zero sequence high frequency voltage injection based sensorless method is proposed, which is suitable for the zero and low speed operations that cannot be covered by the methods proposed in Chapters 6 and 7.

This chapter has been submitted to IEEE Journal of Emerging and Selected Topics in Power Electronics.

8.1 Introduction

Permanent magnet synchronous machines (PMSMs) are extensively used in all kinds of industrial applications including wind power generation, electrical vehicle (EV)/hybrid EV (HEV), home appliance, industrial robot, etc., of which, interior PMSM (IPMSM) becomes more and more attractive due to its better flux weakening and PM saving capabilities. Meanwhile, open winding topology possessing the merits of higher DC bus voltage utilization, potential fault tolerant capability, multi-level modulation and flexible current controllability enables OW-IPMSM to obtain both identities from OW and IPMSM and become worthy of attention. In addition to the machine topologies, the control methods are of importance to improve the whole performance of the driving system. Whereby, researchers put much effort into sensorless control which brings the benefits of lower system cost, compact volume, higher robustness and faster installation.

From the perspective of disturbance essence, the sensorless methods can be generally classified into signal injection based and non-signal injection based methods. According to the injection patterns, signal injection based methods mainly include pulsating high frequency (HF) injection [JAN04], rotating HF injection [JAN95] and stationary axis HF injection [LIU14]. The injection waves consist of sinusoidal [JAN04] [JAN95] [LIU14] and square waves [YOO11]. The pulse width modulation (PWM) based method can be regarded as a specific type of square wave injection. Meanwhile, the non-signal injection based methods principally include the fundamental and third harmonic back electro-motive force (EMF) based methods [BOL99] [HAM13] [WAN14d] [SHE04] [SHE06a] [LIU14a] [TSO15] [ZHA16a] [ZHA17a]. The fundamental back EMF based methods are approached by using

Kalman filter [BOL99], adaptive observer [HAM13], sliding mode observer (SMO) [WAN14d], etc. Although the fundamental back EMF based methods introduce no signal injection but require accurate machine parameters. Inaccurate parameters can result in large estimation error or even system failure. The third harmonic back EMF based methods having non-parametric essence for the position estimation can overcome the parameter dependence and offer higher robustness. However, the access of the neutral point of the machine, three phase resistance network and voltage transducer are unavoidable for conventional third harmonic back EMF based sensorless methods.

In general, many sensorless methods are designed based on zero sequence to obtain advantages of control performance over other methods. Meanwhile, it is investigated via both signal injection and non-signal injection approaches.

The non-signal injection approach is mainly based on zero sequence back EMF which is usually the third harmonic back EMF [SHE04] [SHE06a] [LIU14a] [TSO15] [ZHA16a] [ZHA17a]. A third harmonic back EMF based sensorless control strategy is proposed in [SHE04] together with flux weakening control algorithm. Then, the phase lock loop (PLL) is adopted in [SHE06a] to implement improved position estimation performance. Enhanced position estimator is proposed in [LIU14a] to further improve the dynamic performance with digital differentiator which was popularly used in grid power converter [XIN15]. Reference [TSO15] proposes a deployment strategy for adaptable sensorless commutation technique by using zero sequence voltage. However, the conventional zero sequence back EMF based sensorless methods require voltage transducer and proper measurement point, such as the access of neutral point and three phase resistance network. In order to avoid these, a zero sequence model based sensorless method is developed in [ZHA16a] for OW-PMSM, in which, the zero sequence circulating current is used for position estimation. Not only the merits of OW structure but also the eliminations of voltage transducer and three phase resistance network are achieved. Nonetheless, the zero sequence circuit model parameters are necessary in [ZHA16a], and hence, the non-parametric method is proposed in [ZHA17a] by using zero sequence current controller to achieve this target.

In addition to the non-signal injection based methods, the signal injection based methods utilizing zero sequence are also investigated broadly [LEI11] [XU16] [XU16a] [CAR05] [CON06] [BRI05]. In [LEI11], the inherently generated PWM vector in zero sequence is employed to modulate rotor position information in phase current differential and higher dynamic effect can be consequently obtained. An additional zero sequence path constructed by resistance and capacitance is required. Meanwhile, in [XU16], HF signal is injected in the anticlockwise rotating estimation frame and the rotor position information is extracted from the measured zero sequence HF voltage. Better estimation performance regarding to estimation harmonics is achieved via the proposed method. The proposed principle is therefore used for initial rotor position estimation including the polarity identification in [XU16a]. Besides, the zero sequence current differential is used in [CAR05] to estimate flux position of induction machine via test voltage vectors. Low frequency signal demodulation for zero sequence is investigated in [CON06] to estimate the air gap flux position of induction machine.

Specifically, sensorless methods for OW-PMSM are developed by utilizing the equivalent closed zero sequence circuit containing third harmonic back EMF [ZHA16a] [ZHA17a]. However, it is well known that back EMF based sensorless methods are restricted by the operation speed, namely, minimum operation speed always exists in these methods to ensure enough signal noise ratio (SNR), and hence, the signal injection based methods depending on machine saliency are developed to tackle this issue, which are for the conventional single three phase IPMSM. The specific signal injection based sensorless method for OW-IPMSM has not been reported yet. This papers investigates a signal injection based sensorless approach for OW-IPMSM, in which, the zero sequence HF voltage injection is adopted. Conventionally, the deliberate zero sequence signal injection cannot be implemented in single three phase system. Nonetheless, due to the existence of zero sequence path in OW-IPMSM, the zero sequence signal injection is now feasible for OW-IPMSM with common DC bus. When compared to the published signal injection based methods relying on zero sequence [LEI11] [XU16] [XU16a] [CAR05] [CON06] [BRI05], the proposed method can avoid measuring resistance network, voltage transducer [XU16] [XU16a] [CON06] and deliberately constructed zero sequence path containing resistance and capacitance [LEI11].

This chapter is organized as follows: In Section 8.2, the equivalent HF model of OW-IPMSM is built. The implementation of zero sequence HF voltage injection is presented in Section 8.3. The proposed zero sequence-HF voltage injection (ZS-HFVI) is introduced in Section 8.4. The experiment validation is presented in Section 8.5.

8.2 Equivalent HF Model of OW-IPMSM with Concentrated Winding

8.2.1 Inductance Characteristics of OW-IPMSM

The investigated OW-IPMSM has fractional slot and concentrated winding structure. The cross-section of the 12-slot/10-pole OW-IPMSM is shown in Fig. 8.1. Meanwhile, the phase self and mutual inductance curves are shown in Fig. 8.2. It can be seen that the phase self inductance contains noteworthy second harmonic and the mutual inductance contains much less. Namely, the saliency of the 12-slot/10-pole OW-IPMSM is principally formed by the variation of self inductance. Fig. 8.1 also shows the armature winding flux line of phase A, which is excited by DC current in phase A winding. The generated flux linkage is mainly self flux linkage while the mutual component is much less. The phenomenon leads to relatively lower mutual inductance for the concentrated winding machine, which also brings better capability for fault tolerance [ELR06].

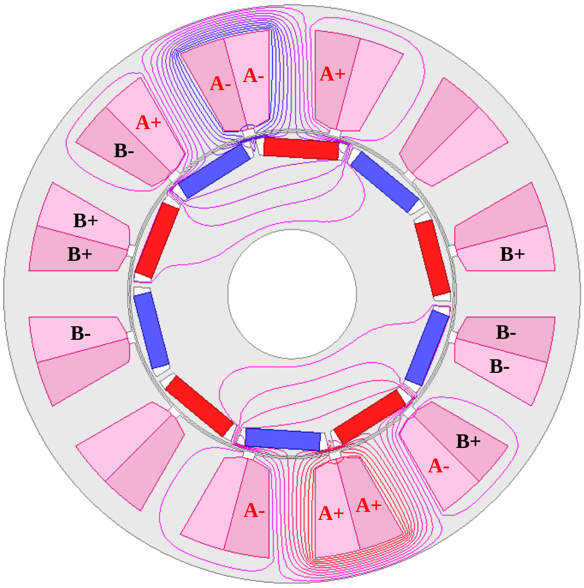

Fig. 8.1 Cross-section of the 12-slot/10-pole OW-IPMSM with phase A excitation current.

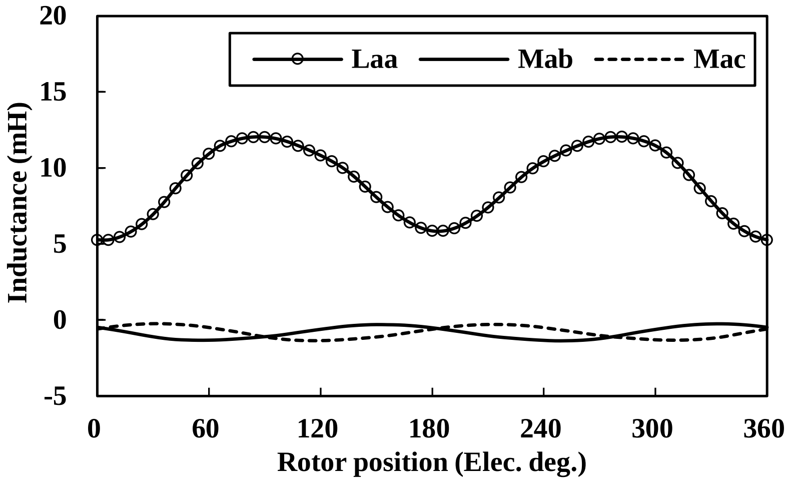

Fig. 8.2 Phase self and mutual inductance curves of the 12-slot/10-pole OW-IPMSM.

Table 8.1 Geometric Parameters of 12-Slot/10-Pole OW-IPMSM

Parameter	**Value**
Stator outer diameter	100mm
Split ratio	0.57
Magnet thickness	3.0mm
Slot opening width	2mm
Tooth-tip slot	10 °
Magnet permeability	1.05
Axial length	50mm
Airgap length	1.0mm
Pole arc/pitch ratio	0.75
Tooth-tip thickness	1mm
Lamination material	M300
Magnet remanence	1.2T
Slot number	12
Pole number	10
Tooth width	9.5mm
Yoke height	5.2mm
Turns per phase	160

8.2.2 Rotor Position Modulation in Equivalent HF Model

In the equivalent HF model of the OW-IPMSM, the winding resistance is neglected. Hence, the machine can be described as a 3×3 inductance matrix, viz.,

$$
\mathbf{L_{abc}} = \begin{bmatrix} L_{aa} & M_{ab} & M_{ac} \\ M_{ba} & L_{bb} & M_{bc} \\ M_{ca} & M_{cb} & L_{cc} \end{bmatrix}
= \begin{bmatrix} L_{s0} - L_{s2}\cos 2\theta & -M_{s0} - M_{s2}\cos 2(\theta + \frac{2\pi}{3}) & -M_{s0} - M_{s2}\cos 2(\theta - \frac{2\pi}{3}) \\ -M_{s0} - M_{s2}\cos 2(\theta + \frac{2\pi}{3}) & L_{s0} - L_{s2}\cos 2(\theta - \frac{2\pi}{3}) & -M_{s0} - M_{s2}\cos 2\theta \\ -M_{s0} - M_{s2}\cos 2(\theta - \frac{2\pi}{3}) & -M_{s0} - M_{s2}\cos 2\theta & L_{s0} - L_{s2}\cos 2(\theta + \frac{2\pi}{3}) \end{bmatrix}
\tag{8.1}
$$

where L_{s0} and M_{s0} represent the average inductance components of the self and mutual inductances, L_{s2} and M_{s2} represent the amplitudes of the second harmonics of the self and mutual inductances.

Therefore, the voltage equation with HF excitation is

$$
\mathbf{L_{abc}} \frac{d\mathbf{i_{abc}}}{dt} = \mathbf{u_{abc}} \tag{8.2}
$$

where $\mathbf{i_{abc}}=[i_{ah}, i_{bh}, i_{ch}]^T$ and $\mathbf{u_{abc}}=[u_{ah}, u_{bh}, u_{ch}]^T$.

Assume the HF voltage is injected into zero sequence, the terminal voltage can be represented as $\mathbf{u_{abc}}=[u_i, u_i, u_i]^T$ where $u_i=U_0\sin\omega_h t$ and ω_h represents the frequency of the injected signal. However, it is complicated to deduce $d\mathbf{i_{abc}}/dt$ from (8.2), and hence it can be re-written as

$$
\frac{d\mathbf{i_{abc}}}{dt} = \mathbf{C}\mathbf{L_{dq0}^{-1}}\mathbf{u_{dq0}}\,. \tag{8.3}
$$

where

$$
\mathbf{C} = \begin{bmatrix} \cos\theta & -\sin\theta & 1 \\ \cos(\theta - \frac{2\pi}{3}) & \sin(\theta - \frac{2\pi}{3}) & 1 \\ \cos(\theta + \frac{2\pi}{3}) & \sin(\theta + \frac{2\pi}{3}) & 1 \end{bmatrix} \tag{8.4}
$$

$$\mathbf{L}_{\mathbf{dq0}}^{\mathbf{-1}} = \frac{1}{\det\left|\mathbf{L}_{\mathbf{dq0}}\right|}\mathbf{L}_{\mathbf{dq0}}^{*} \tag{8.5}$$

$$\mathbf{L}_{\mathbf{dq0}}^{*} = \begin{bmatrix} L_0 L_q - 2L_\Delta^2 \sin^2 3\theta & -2L_\Delta^2 \sin 3\theta \cos 3\theta & -2L_q L_\Delta \cos 3\theta \\ -2L_\Delta^2 \sin 3\theta \cos 3\theta & L_0 L_d - 2L_\Delta^2 \cos^2 3\theta & 2L_d L_\Delta \sin 3\theta \\ -L_q L_\Delta \cos 3\theta & L_d L_\Delta \sin 3\theta & L_d L_q \end{bmatrix} \tag{8.6}$$

$$\det\left|\mathbf{L}_{\mathbf{dq0}}\right| = L_d L_q L_0 - L_\Delta^2 (L_d + L_q) - L_\Delta^2 (L_q - L_d)\cos 6\theta \tag{8.7}$$

$$\mathbf{u}_{\mathbf{dq0}} = [0, 0, u_i]^T \tag{8.8}$$

$$L_d = L_{s0} + M_{s0} - \frac{1}{2}L_{s2} - M_{s2} \tag{8.9}$$

$$L_q = L_{s0} + M_{s0} + \frac{1}{2}L_{s2} + M_{s2} \tag{8.10}$$

$$L_0 = L_{s0} - 2M_{s0} \tag{8.11}$$

$$L_\Delta = \frac{1}{2}(M_{s2} - L_{s2})\,. \tag{8.12}$$

Since $L_\Delta^2 (L_q - L_d) \ll L_d L_q L_0 - L_\Delta^2 (L_d + L_q)$, the sixth harmonic is relatively small and $\det\left|\mathbf{L}_{\mathbf{dq0}}\right|$ can be approximately regarded as constant.

In consequence, the three phase currents can be represented as

$$\mathbf{i}_{\mathbf{abc}} = \frac{U_0 \cos \omega_h t}{\omega_h \det\left|\mathbf{L}_{\mathbf{dq0}}\right|} \cdot \left\{ \begin{bmatrix} L_\Delta (L_d + L_q)\cos 2\theta + L_\Delta (L_q - L_d)\cos 4\theta \\ L_\Delta (L_d + L_q)\cos(2\theta + 2\pi/3) + L_\Delta (L_q - L_d)\cos(4\theta - 2\pi/3) \\ L_\Delta (L_d + L_q)\cos(2\theta - 2\pi/3) + L_\Delta (L_q - L_d)\cos(4\theta + 2\pi/3) \end{bmatrix} - L_d L_q \mathbf{I} \right\} \tag{8.13}$$

where **I**=[1, 1, 1]^T.

According to (8.13), it can be found that the three phase HF currents excited by zero sequence HF voltage contain rotor position information. The envelopes of the three phase HF currents are modulated by rotor position. However, the amplitudes of the three phase currents contains not only rotor position dependent components but also the same DC bias which is $L_d L_q$. The rotor position dependent components consist of second and fourth harmonics. Since

$L_\Delta(L_d+L_q) \gg L_\Delta(L_q-L_d)$, the second harmonic is the dominant component which can be used for rotor position estimation. Hence, (8.13) can be further simplified as

$$\mathbf{i_{abc}} = \frac{U_0 \cos\omega_h t}{\omega_h \det\left|\mathbf{L_{dq0}}\right|}\left\{\begin{bmatrix} L_\Delta(L_d+L_q)\cos 2\theta \\ L_\Delta(L_d+L_q)\cos(2\theta+2\pi/3) \\ L_\Delta(L_d+L_q)\cos(2\theta-2\pi/3) \end{bmatrix} - L_d L_q \mathbf{I}\right\}. \tag{8.14}$$

8.3 Implementation of Injection Pattern

8.3.1 ZSS-SVPWM

The ZSS-SVPWM has been used in Chapter 2. The difference for the ZSS-SVPWM used in this chapter is that the input signal is generated from zero sequence controller in Chapters 2 and 7, while in this chapter it is generated in an open loop way. The HF voltage reference is directly from the HF signal generator.

8.3.2 Zero Sequence Voltage Injection

According to the ZSS-SVPWM, the input signals include u_α, u_β and T_Z, in which, T_Z is used for the HF signal input. Hence, it satisfies

$$T_{Z1} = \frac{1}{2}U_0 \sin\omega_h t \tag{8.15}$$

$$T_{Z2} = -\frac{1}{2}U_0 \sin\omega_h t \tag{8.16}$$

where T_{z1} and T_{z2} are for the dual SVPWM modules, respectively.

Consequently, the injection signal in zero sequence is superimposed on the zero sequence quasi triangle waves of the two sets of inverters. The phase shift between the zero sequence quasi triangle waves of the two sets of inverters is $2\pi/3$ and the phase shift between the HF zero sequence voltage is π. Fig. 8.3 (a) shows the implementation of the injection pattern and Fig. 8.3 (b) shows the modulation signals of the two sets of inverters as well as the synthetic modulation signal. Although the phase modulation signal for each set contains third harmonic and HF signals, the third harmonic signals of the two sets of inverters are counteracted and the HF signal becomes double in the synthetic modulation signal. Meanwhile, it should also be noticed that the injected HF current will consequently induce additional power losses and noise.

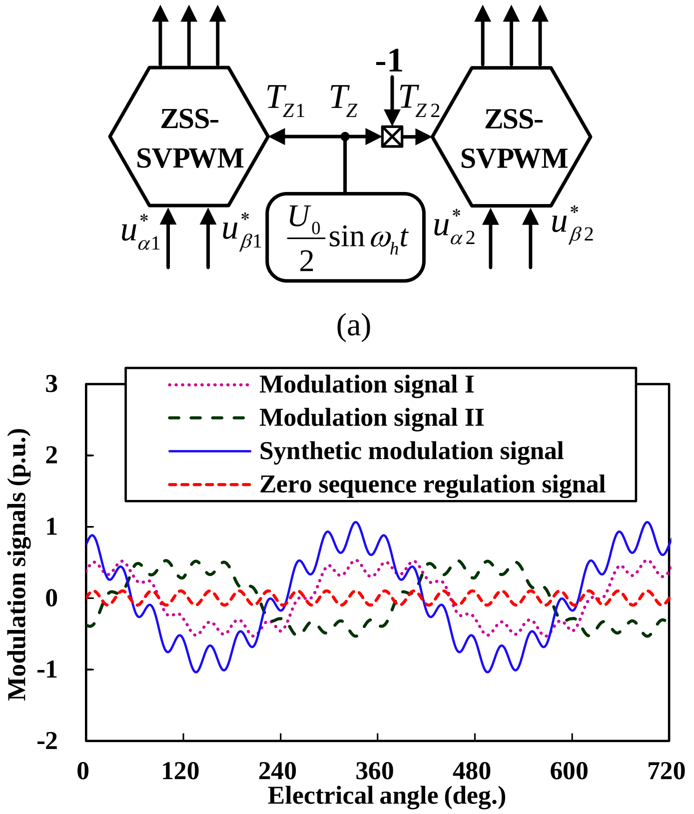

(a)

(b)

Fig. 8.3 Implementation of the zero sequence HF voltage injection. (a) Injection pattern. (b) Modulation signals.

8.4 ZS-HFVI Based Sensorless Control

8.4.1 Position Extraction

According to (8.13), the HF current signals are amplitude-modulated by the rotor position. The primary saliency, namely, the second harmonic is dominant, which can be used for position estimation. The first step is to demodulate the HF signals via amplitude demodulation process which is shown in Fig. 8.4. For each channel, it contains a multiplier, a low pass filter (LPF) and a high pass filter (HPF). The HPFs are used to extract HF currents from the fundamental currents, which can be expressed as (8.14). Multiply the signals after HPFs by cos$\omega_h t$ to obtain

$$\mathbf{i}_{\mathbf{abc}}^{\mathbf{HPF}} = \frac{U_0 \cos 2\omega_h t}{2\omega_h \det\left|\mathbf{L}_{\mathbf{dq0}}\right|}\left\{\begin{bmatrix} L_\Delta(L_d+L_q)\cos 2\theta \\ L_\Delta(L_d+L_q)\cos(2\theta+2\pi/3) \\ L_\Delta(L_d+L_q)\cos(2\theta-2\pi/3) \end{bmatrix} - L_d L_q \mathbf{I}\right\} + \frac{U_0}{2\omega_h \det\left|\mathbf{L}_{\mathbf{dq0}}\right|}\left\{\begin{bmatrix} L_\Delta(L_d+L_q)\cos 2\theta \\ L_\Delta(L_d+L_q)\cos(2\theta+2\pi/3) \\ L_\Delta(L_d+L_q)\cos(2\theta-2\pi/3) \end{bmatrix} - L_d L_q \mathbf{I}\right\}. \tag{8.17}$$

The first term, namely, the HF term, in (8.17) is filtered out by the subsequent LPF, and hence, the input signal for Clarke transformation is

$$\mathbf{i}_{\mathbf{abc}}^{\mathbf{LPF}} = \frac{U_0}{2\omega_h \det\left|\mathbf{L}_{\mathbf{dq0}}\right|}\left\{\begin{bmatrix} L_\Delta(L_d+L_q)\cos 2\theta \\ L_\Delta(L_d+L_q)\cos(2\theta+2\pi/3) \\ L_\Delta(L_d+L_q)\cos(2\theta-2\pi/3) \end{bmatrix} - L_d L_q \mathbf{I}\right\}. \tag{8.18}$$

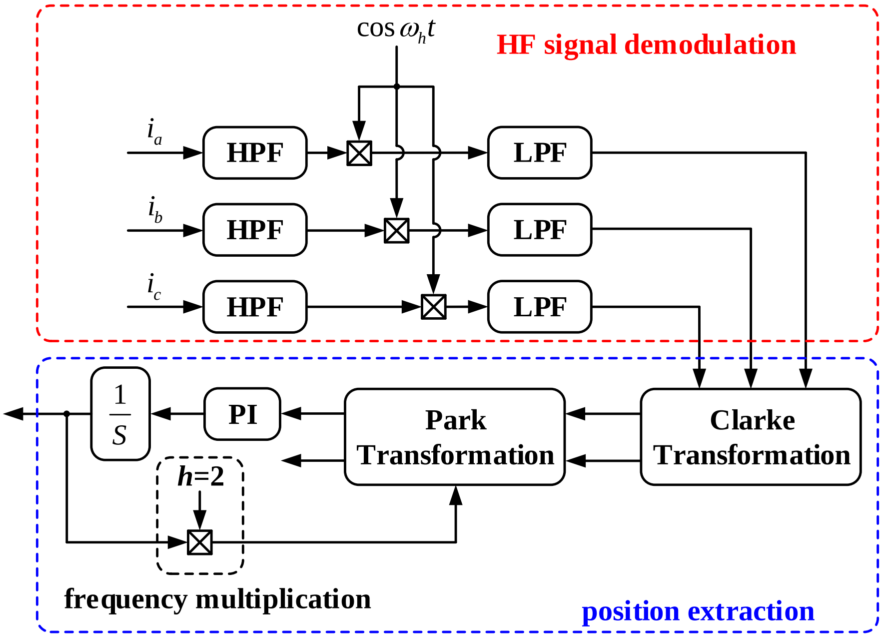

Fig. 8.4 Rotor position observer.

It can be seen that the subsequent signals in (8.18) include positive sequence and DC zero sequence signals. The position extraction adopted in Fig. 8.4 is based on synchronous PLL structure. Hence, the zero sequence imposes no influence on the extraction and the convergence position angle will adaptively be the dominant positive or negative sequence rotating component. In (8.13), the dominant rotating signal is the positive sequence which is the second harmonic and the fourth harmonic acting as negative sequence interference is much less significant. Moreover, the frequency multiplication factor *h*=2 is introduced in the angle feedback loop to enable the actual position convergence from the second harmonic. The Park and Clarke transformations used in Fig. 8.4 are

$$\mathbf{T}_{\mathbf{Clarke}} = \frac{2}{3}\begin{bmatrix} 1 & -\frac{1}{2} & -\frac{1}{2} \\ 0 & \frac{\sqrt{3}}{2} & -\frac{\sqrt{3}}{2} \\ \frac{1}{2} & \frac{1}{2} & \frac{1}{2} \end{bmatrix} \tag{8.19}$$

and

$$\mathbf{T}_{\mathbf{Park}} = \begin{bmatrix} \cos\theta & \sin\theta \\ -\sin\theta & \cos\theta \end{bmatrix}, \tag{8.20}$$

respectively.

Meanwhile, the measured Lissajous orbits of the three phase signals input into Clarke transformation are shown in Fig. 8.5. The processed signals are rotor position dependent and the dominant one is positive sequence. Fig. 8.5 (a) shows the Lissajous orbit with no load condition at 20rpm. Fig. 8.5 (b) shows the Lissajous orbit with rated load condition at the same speed. It can be seen that the loaded condition deteriorates the SNR of the effective signal. The degraded SNR can be induced by the distorted spatial magnetic permeance distribution caused by the armature reaction and saturation.

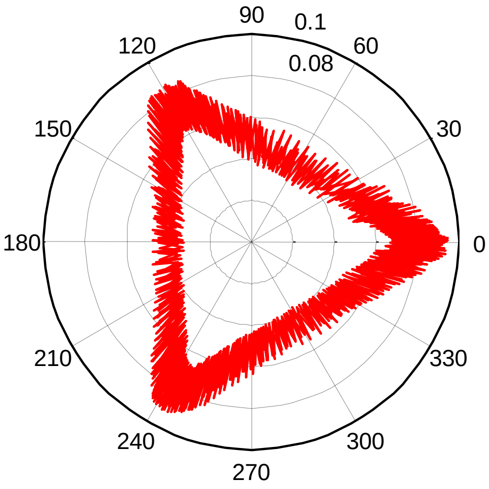

(a)

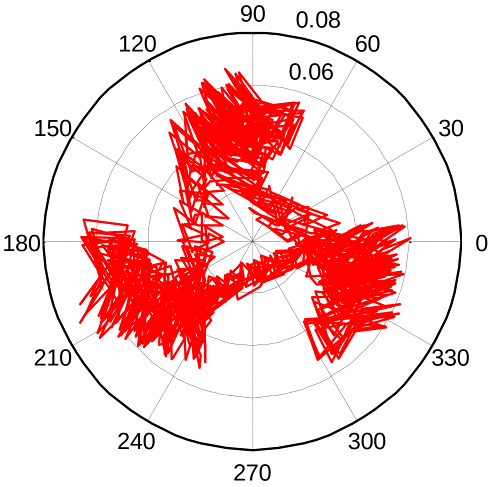

(b)

Fig. 8.5 Measured Lissajous orbits of the three phase signals input into Clarke transformation. (a) No load at 20rpm. (b) Rated load at 20rpm.

8.4.2 Systematic Control Strategy

The systematic control strategy is shown in Fig. 8.6, which is based on the proposed ZS-HFVI sensorless method together with the ZSS-SVPWM modules. The OW-IPMSM is driven by dual inverter structure with common DC bus. This topology is equivalent to H-bridge for each phase winding. The field oriented control is adopted to drive the OW-IPMSM and form the adjustable speed system.

8.5 Experimental Validation

The experimental validation is performed on the 12-slot/10-pole OW-IPMSM prototype. The specification of the OW-IPMSM and the control system are listed in Table 8.2. The experiment platform is shown in Fig. 8.7. The system is implemented on the dSPACE controller. A DC electric excitation machine is used as the load machine to provide adjustable load by using adjustable power resistance. The injection frequency is 500Hz and the amplitude of the injected signal is 20V.

TABLE 8.2 SPECIFICATION OF OW-IPMSM AND CONTROL SYSTEM

Parameter	Value
Resistance	0.62Ω
Rated RMS current	2.83A
Rated speed	400rpm
No-load PM flux linkage	0.084Wb
Rated frequency	33.33Hz
d-axis inductance	6mH
q-axis inductance	10.5mH
DC bus voltage	100V
PWM switching frequency	5kHz
Dead-time	$2\mu s$

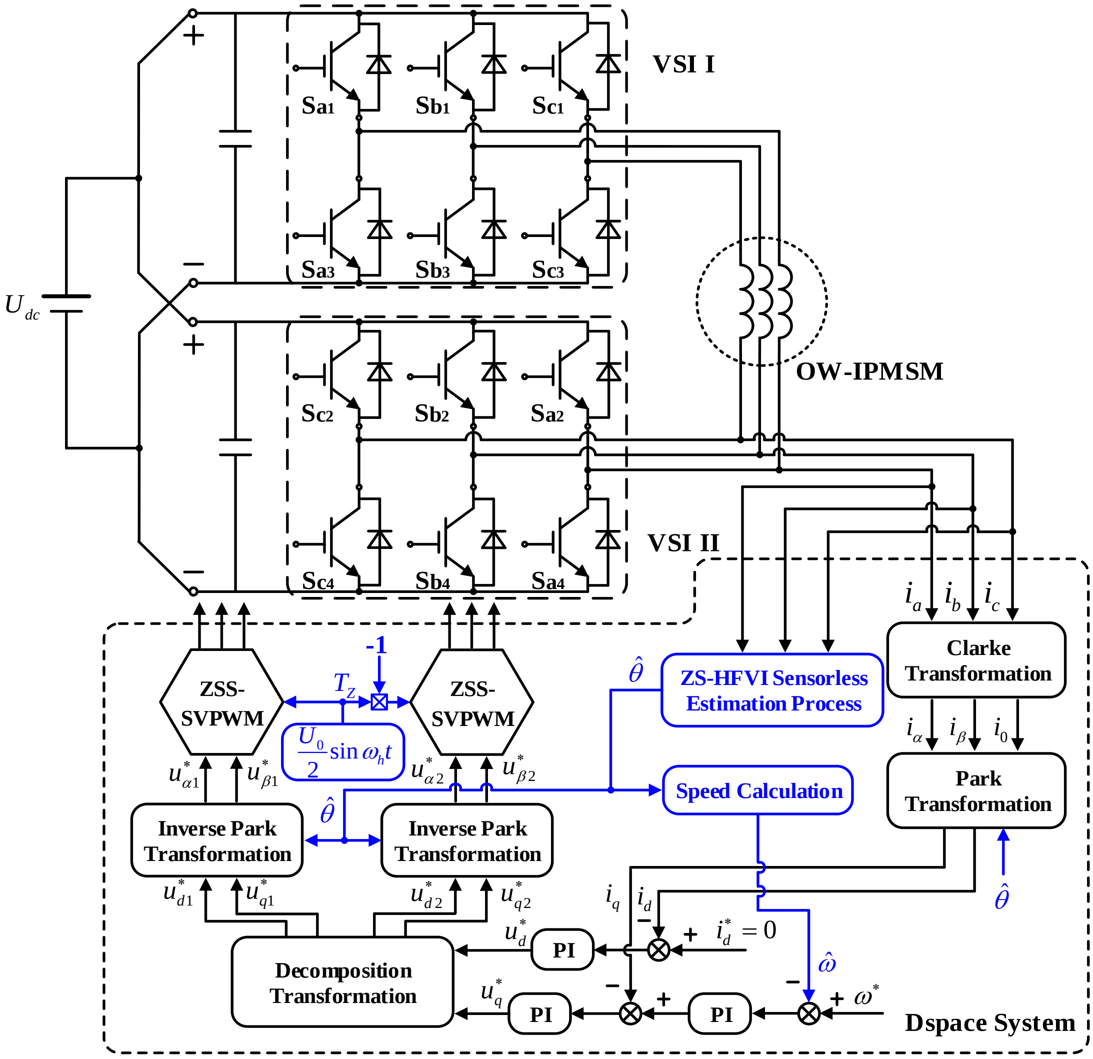

Fig. 8.6 System control strategy.

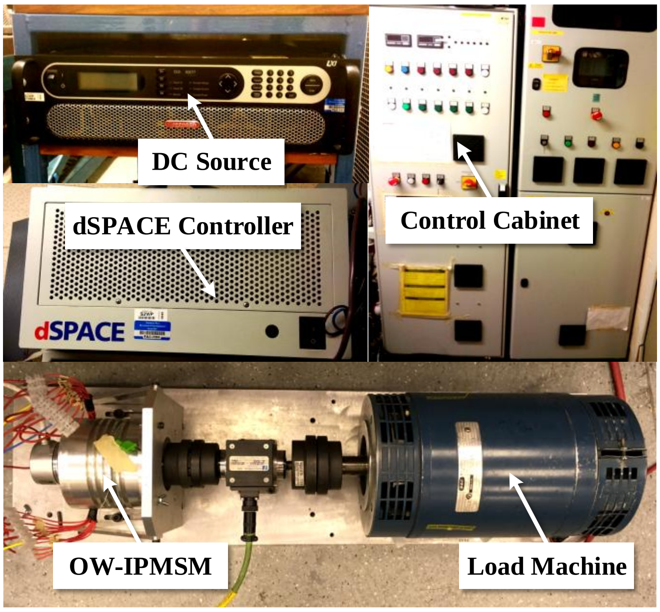

Fig. 8.7 Experiment platform.

Fig. 8.8 shows the startup performance with speed reference stepping from 0 to 50rpm. Fig. 8.8 (a) shows the estimated position, encoder position and estimated position error signals. Fig. 8.8 (b) shows the magnified region in Fig. 8.8 (a) between 4s and 5.5 s. The estimated position error has larger DC bias within the transient process, which is due to the limit of position estimator bandwidth. Fig. 8.8 (c) shows the magnified region in Fig. 8.8 (a) between 10s and 11.5s. The DC bias of the estimated position error in the steady state in Fig. 8.8 (c) attenuates when compared to the transient process in Fig. 8.8 (b), which can also be observed in Fig. 8.8 (a).

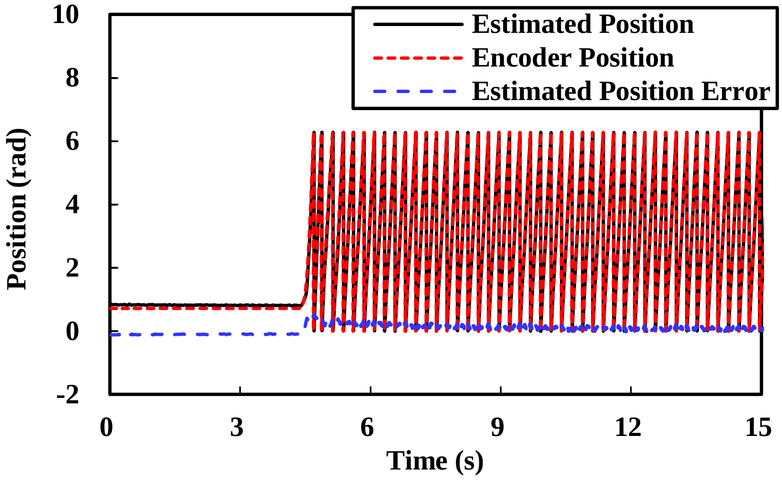

(a)

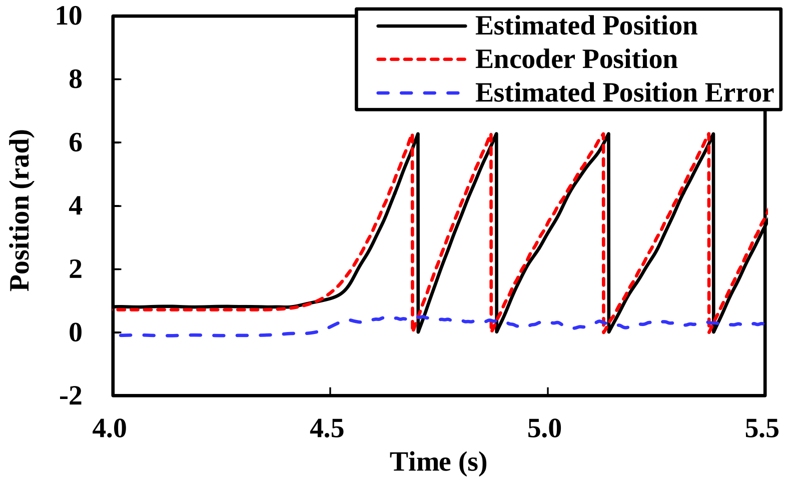

(b)

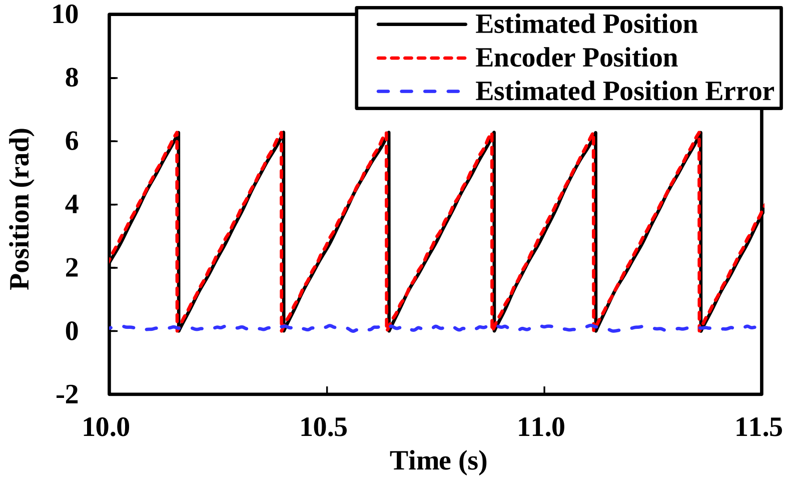

(c)

Fig. 8.8 Startup performance with speed reference stepping from 0 to 50rpm. (a) Estimated position, encoder position and estimated position error signals. (b) Magnified region for transient performance between 4s and 5.5s. (c) Steady state estimation performance between 10s and 11.5s.

Fig. 8.9 shows the step speed reversal test from 20rpm to -20 rpm at no load condition. Fig. 8.9 (a) shows the encoder speed, the estimated speed and the estimated speed error signals. Fig. 8.9 (b) shows the estimated positon, the encoder position and the estimated position error signals. Fig. 8.9 (c) shows the magnified region in Fig. 8.9 (b) from 0s to 2s, namely, the steady state estimation performance. Fig. 8.9 (d) shows the magnified region in Fig. 8.9 (b) from 4s to 6.5s, namely, the speed reversal transient performance. The sixth estimation error observed in Fig. 8.9 (c) is due to the negative sequence interference. The estimation error will be suppressed by decreasing the bandwidth of the synchronous PLL or increasing the operation frequency, such as Fig. 8.9 (c) at 50rpm. However, decreasing the bandwidth of the synchronous PLL will also decrease the dynamic performance of the position estimator. Hence, it is a design tradeoff between estimation error harmonic and dynamic performance.

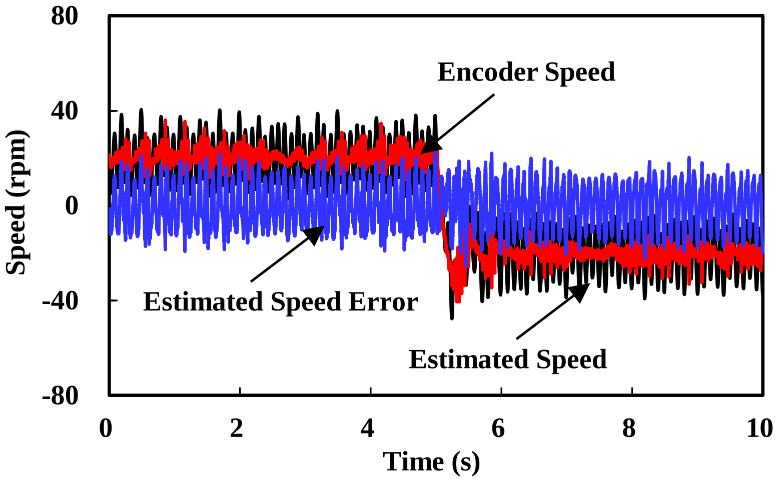

(a)

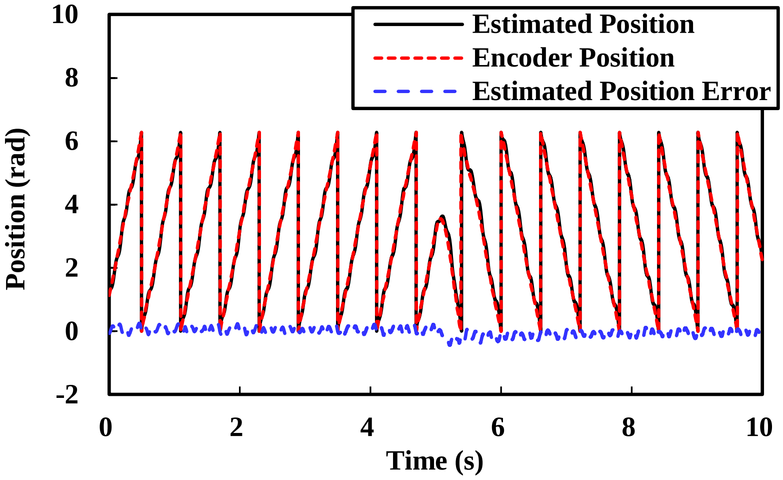

(b)

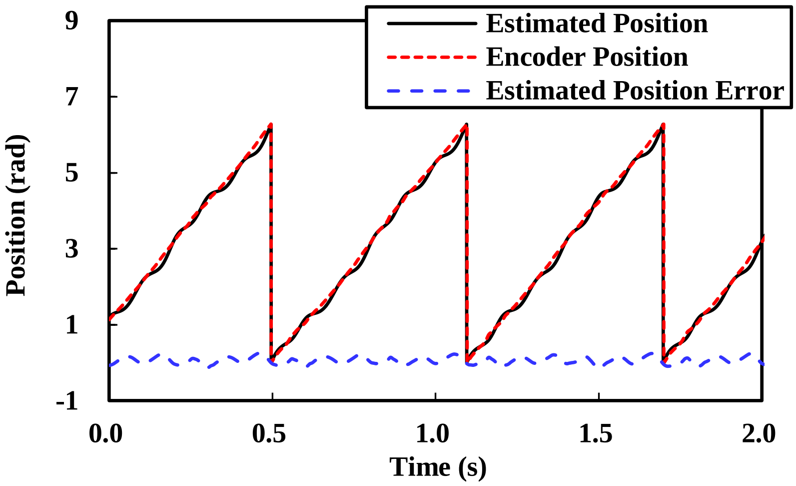

(c)

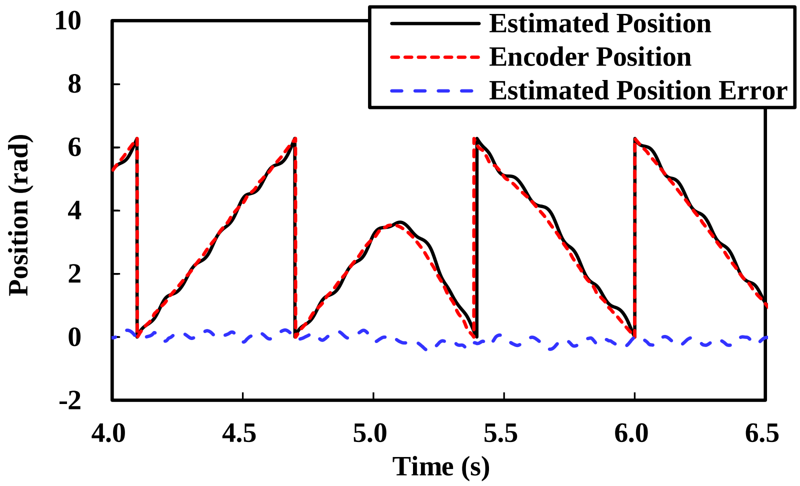

(d)

Fig. 8.9 Step speed reversal test from 20rpm to -20rpm at no load condition. (a) Encoder speed, estimated speed and the estimated speed error signals. (b) Estimated positon, encoder position and estimated position error signals. (c) Magnified steady state estimation performance between 0s and 2s. (d) Magnified speed reversal transient performance between 4s and 6.5s.

Fig. 8.10 shows the step speed reversal test from 20rpm to -20 rpm at rated load condition, which is the counterpart of Fig. 8.9. The estimation performance is deteriorated due to the distorted spatial magnetic permeance distribution caused by the armature reaction and saturation. Hence, more harmonics are introduced, which results in the higher ripple of estimation error curve.

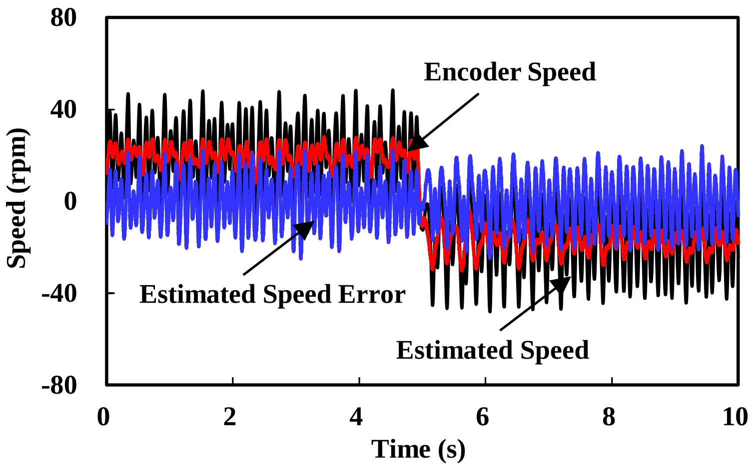

(a)

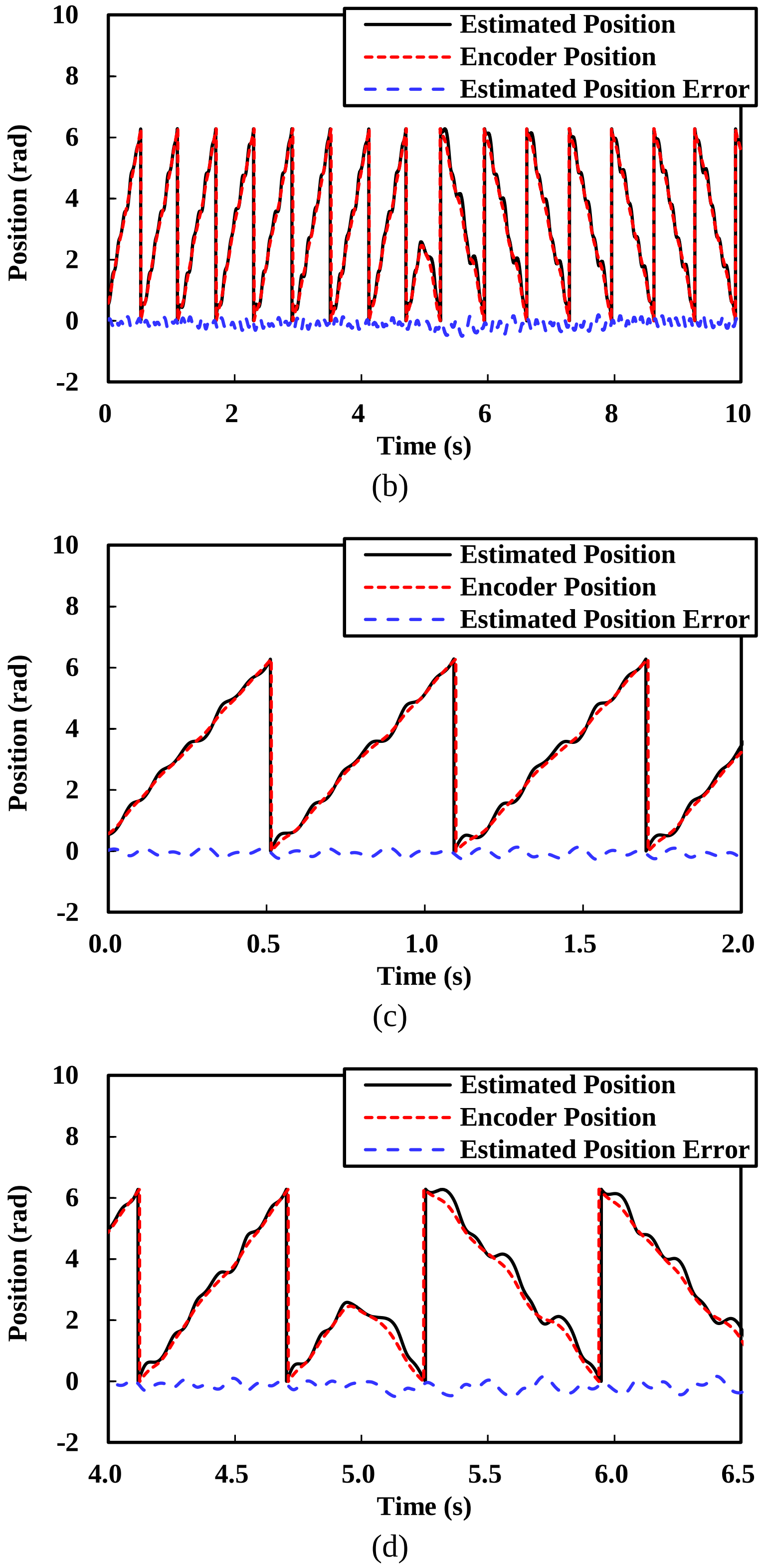

Fig. 8.10 Step speed reversal test from 20rpm to -20rpm at rated load condition. (a) Encoder speed, estimated speed and the estimated speed error signals. (b) Estimated positon, encoder position and estimated position error signals. (c) Magnified steady state estimation performance between 0s and 2s. (d) Magnified speed reversal transient performance between 4s and 6.5s.

8.6 Conclusion

A novel ZS-HFVI based sensorless method for OW-IPMSM has been developed in this chapter. The zero sequence signal injection has been achieved by using ZSS-SVPWM strategy. The rotor position has been demodulated from HF currents in each phase with concise signal processing. Eliminations of voltage transducer, three phase resistance network and additionally constructed zero sequence circuit have been achieved when compared to conventional signal injection based methods relying on zero sequence. This method has been experimentally verified on the prototype machine, which is suitable for zero and low speed operation when back EMF based methods are not feasible.

CHAPTER 9 GENERAL CONCLUSIONS AND FUTURE WORK

9.1 General Conclusions

In this thesis, the major research has been concentrated on the OW-PMSM drive with particular reference to zero sequence. The common DC bus OW-PMSM drive is the basic studied topology. This thesis aims at solving issues and proposing several improved techniques utilizing zero sequence component in the OW-PMSM drives. The conclusions of the thesis can be briefly list in Table 9.1.

Table 9.1 Conclusions of the thesis.

Chapter	Research Type	Achievements
Chapter 1	LR	✓ Conventional PMSM drives techniques have been reviewed. ✓ OW drive topologies have been reviewed.
Chapter 2	MA	✓ Systematic analysis and synthetic model for circulating current. ✓ Influences of the cross coupling voltages in zero sequence & the parasitic effects in inverter nonlinearity firstly identified.
Chapter 3	NM	✓ FA-PR controller based suppression method has been proposed. • Good dynamic performance & machine parameter dependent. ✓ ES algorithm based suppression method has been proposed. • Slower dynamic performance & better generality (non-model based).
Chapter 4	NM	✓ A torque enhancement method by using zero sequence current shaping has been proposed. ✓ Theoretical increased average torque: 18.06%; FE increased average torque: 17.62%; Experimental increased average torque: 17.52%.
Chapter 5	NM & MA	✓ A novel torque ripple reduction strategy based on zero sequence current injection has been proposed. ✓ Torque ripple mechanism has been analysed. ✓ Reducing the bandwidth requirement on the current controller from one six times of the maximum fundamental frequency to three times of that. ✓ Higher robustness.

Chapter 6	NM	✓ A novel zero sequence model based sensorless method has been proposed. ✓ Higher robustness. ✓ No voltage transducer and three phase resistance network are required ✓ Acceptable torque ripple and comparable total loss characteristics compared to no injection operation. ✓ Zero sequence parameter sensitivity analysis has been carried out. ✓ Medium & high speed operation.
Chapter 7	NM	✓ A novel zero sequence back EMF based sensorless method has been proposed. ✓ Non-parametric benefits. ✓ Zero sequence circulating current suppression. ✓ Incremental method for Chapter 6. ✓ Medium & high speed operation.
Chapter 8	NM	✓ A novel ZS-HFVI based sensorless method has been developed. ✓ Independent phase demodulation & potential fault tolerant capability ✓ Eliminations of voltage transducer, three phase resistance network and additionally constructed zero sequence circuit. ✓ Zero & low speed operation

where LR= Literature Review, MA=Mechanism Analysis, NM=New Method.

In order to integrate the chapters of the thesis and reveal the relationship between chapters regarding to zero sequence of OW-PMSM drives, the inter-connections of the chapters and research topics can be shown in Fig. 9.1.

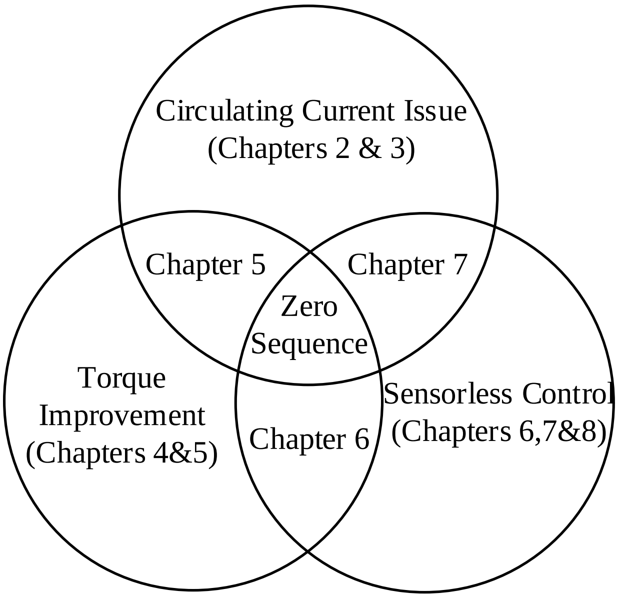

Fig. 9.1 Inter-connections of the chapters and research topics.

Firstly, the zero sequence circulating current phenomena are investigated in Chapter 2, of which, the zero sequence back EMF and cross coupling voltages from the machine side and the zero sequence modulated voltage and the inverter nonlinearity from the inverter side are identified as the zero sequence disturbances. The cross coupling voltages are firstly analysed and derived in this thesis. The parasitic effects of the inverter nonlinearity imposing influence on the zero sequence circulating current is also firstly investigated in this thesis. According to the analysis and models proposed in Chapter 2, two zero sequence circulating current suppression strategies are therefore proposed in Chapter 3. The first method is the FA-PR controller based one which is capable of suppressing zero sequence circulating current with quick response. In order to provide a steerable zero sequence component in the PWM strategy, a novel ZSS-SVPWM with phase shift is also proposed. However, the design of the control parameters relies on the associated machine parameters, which is essentially model-based method. Hence, in the second proposed method, a non-model based method is proposed by using the ES algorithm together with the adjustable SVPWM for OW-PMSM. The second method requires no information of the machine parameters, which is of high generality. But it should be noticed that the response time is longer than the first method.

- ✓ Deeper understanding of zero sequence circulating current phenomenon has been proposed.
- ✓ Suppression method 1 has high dynamic performance but is machine parameters dependent.

- ✓ Suppression method 2 is machine parameters independent but has lower dynamic performance.

In addition to tackling the zero sequence circulating current issue in the OW-PMSM drives, the zero sequence path can be also utilized to enhance the control performance. In Chapter 4 and Chapter 5, two torque optimization control algorithms are proposed, respectively. In Chapter 4, the zero sequence back EMF interacted with the deliberately injected zero sequence current is utilized to produce additional average torque component, namely, an average torque enhancement technique. Meanwhile, in Chapter 5, by correspondingly shaping the injected zero sequence current, the produced alternating torque component is used for compensating the inherent torque ripple of the OW-PMSM drive. A novel torque ripple reduction method is therefore proposed. The advantage is that the requirement on the bandwidth of the current controller is reduced to the half of the conventional methods. This will benefit the applications for high speed and low switching frequency (high power) systems which are lack of the controllability on relative high frequency current harmonics.

- ✓ Two aspects of torque improvement have been studied with new methods proposed.
- ✓ The zero sequence current injection has improved 17.52% of the average torque while the torque ripple will be introduced as well.
- ✓ Energy delivery concerned areas, such as the wind power generation, is the potential application for torque enhancement method.
- ✓ The shifted zero sequence current injection has reduced the dominant torque ripple and the bandwidth requirement on current controller has been reduced as well.
- ✓ High speed applications or high power converters with low switching frequency, which all result in limited bandwidth of current control, desire the advantage of the torque ripple reduction method much more.

Moreover, in Chapters 6 to 8, three sensorless methods relying zero sequence are proposed. In Chapter 6, the rotor position information is extracted from the zero sequence circulating current which is the third harmonic current. In order to further optimize the system with suppressed zero sequence circulating current, the non-parametric zero sequence based sensorless method is proposed in Chapter 7. The rotor information is extracted from the output of the zero sequence current controller in the proposed non-parametric sensorless. However, the sensorless methods proposed in Chapters 6 and 7 are back EMF based and have lowest operation speed limit. For the purpose of zero and low speed sensorless operation, in Chapter 8, a novel zero sequence high frequency voltage injection algorithm is proposed. The saliency information instead of the flux-linkage is utilized. Due to the equivalent independent phase injection, better fault tolerant capability can be achieved.

- ✓ Three sensorless methods relying on zero sequence for both zero/low and high speed operations have been proposed.
- ✓ Sensorless method 1 (Chapter 6) is of decoupling benefit while the zero sequence current is uncontrollable.
- ✓ Sensorless method 2 (Chapter 7) has tackled the issue of method 1 and introduced extra benefit of non-parametric effect on machine parameters.
- ✓ Sensorless method 2 is an extended method for method 1.
- ✓ Sensorless method 3 (Chapter 8) has covered the residual operation speed region for method 1 & 2.
- ✓ Sensorless method 3 has shown redundant position information output capability which is preferable for high reliable fault tolerant sensorless control.

In summary, the zero sequence of the OW-PMSM has been exploited in this thesis. The circulating current issue, the torque optimization techniques and sensorless methods have been investigated respectively. The associated advantages of the proposed techniques have been theoretically and experimentally validated.

9.2 Future Work

To further explore the utilization of the zero sequence in OW-PMSM, the followings could be carried out in the future:

1. In some of the proposed techniques, the zero sequence parameters including the zero sequence flux-linkage, cross-coupling inductances and equivalent resistance are necessary. The associated parameter identification algorithms could be interesting.

2. In analogy with the maximum torque per ampere control including direct calculation and adaptive perturbation based methods, the proposed torque optimization methods are direct calculation type and the corresponding adaptive methods requiring no machine parameters could be of interest.

3. Due to the decoupling effect of the zero sequence based sensorless methods proposed in this thesis, the higher robustness is obtained. Hence, the further fault tolerant sensorless methods could also be researched. The independent phase demodulation of the proposed sensorless methods are capable of redundant position signals.

4. The initial phase correction technique for the zero sequence based sensorless method should be also investigated to enable the robust operation.

5. Smooth transition among the zero sequence back EMF sensorless methods, high frequency based sensorless method and current regulation control might be investigated as well.

6. The identified zero sequence parameters could be the indicators for the motor temperature. Therefore, the corresponding temperature estimation techniques relying on zero sequence are also interesting.

The corresponding future research work is pointed out in the Fig. 9.2 which evolves from the research scope in Fig. 1.20.

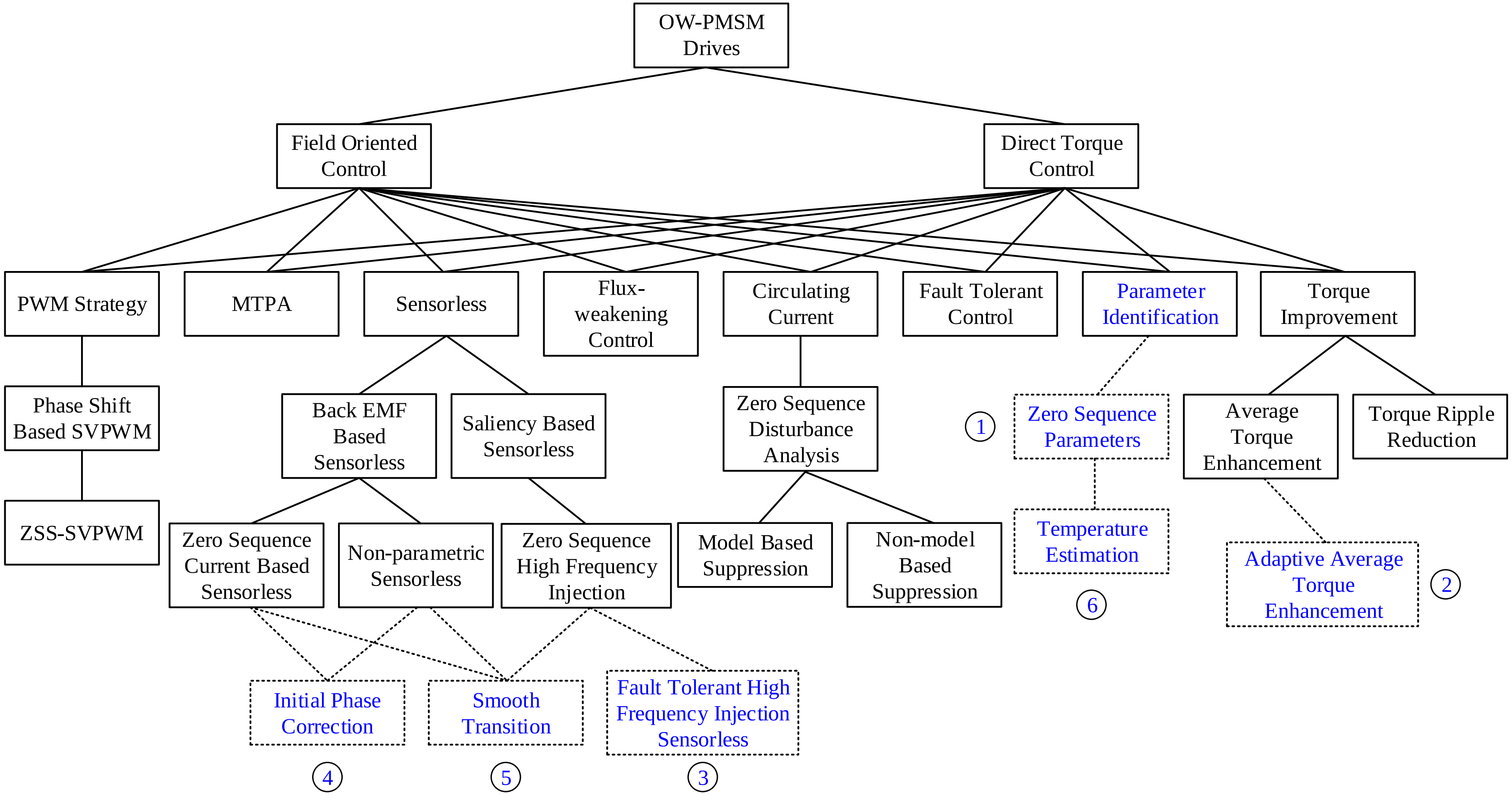

Fig. 9.2 Diagram of future research work.

REFERENCES

[AN16] Q. An, J. Liu, Z. Peng, L. Sun and L. Sun, “Dual-space vector control of open-end winding permanent magnet synchronous motor drive fed by dual inverter,” *IEEE Trans. Power. Electron.*, vol. 31, no. 12, pp. 8329-8342, Dec. 2016.

[ARI03] K.B. Ariyur and M. Krstic, *Real-Time Optimization by Extremum Seeking Feedback*. Hoboken, NJ: Wiley, 2003.

[BAY72] K. H. Bayer, H. Waldmann, and M. Weibelzahl, “Field-oriented closed-loop control of a synchronous machine with the new TRANSVECTOR control system,” *Siemens Rev.*, vol. 39, pp. 220-223, 1972.

[BIA08] N. Bianchi, S. Bolognani, J. Jang and S. K. Sul, “Advantages of inset pm machines for zero-speed sensorless position detection,” *IEEE Trans. Ind. Appl.*, vol. 44, no. 4, pp. 1190-1198, Jul./Aug. 2008.

[BLA72] F. Blaschke, “The principle of field orientation as applied to the new TRANSVECTOR closed loop control system for rotating field machines,” *Siemens Rev.*, vol. 34, pp. 217-220, 1972.

[BOD13] N. Bodo, E. Levi and M. Jones, “Investigation of carrier-based PWM techniques for a five-phase open-end winding drive topology,” *IEEE Trans. Ind. Electron.*, vol. 60, no. 5, pp. 2054-2065, May 2013.

[BOD14] N. Bodo, M. Jones and E. Levi, “A space vector PWM with common-mode voltage elimination for open-end winding five-phase drives with a single DC supply,” *IEEE Trans. Ind. Electron.*, vol. 61, no. 5, pp. 2197-2207,May 2014.

[BOD15] N. Bodo, M. Jones and E. Levi, “Zero-sequence current suppression strategy of open-winding pmsg system with common DC bus based on zero vector redistribution,” *IEEE Trans. Ind. Electron.*, vol. 62, no. 6, pp. 3399-3408, Jun. 2015.

[BOL99] S. Bolognani, R. Oboe and M. Zigliotto, “Sensorless full-digital PMSM drive with EKF estimation of speed and rotor position,” *IEEE Trans. Ind. Electron.*, vol. 46, no. 1, pp. 184-191, Feb. 1999.

[BRI05] F. Briz, M. W. Degner, P. García, and J. M. Guerrero, “Rotor position estimation of AC machines using the zero sequence carrier signal voltage,” *IEEE Trans. Ind. Appl.*, vol. 41, no. 6, pp. 1637–1646, Nov./Dec. 2005.

[BRI06] F. Briz, M. W. Degner, P. G. Fernández and A. B. Diez, “Rotor and flux position estimation in delta-connected AC machines using the zero-sequence carrier-signal current,” *IEEE Trans. Ind. Appl.*, vol. 42, no. 2, pp. 495-503, Mar/Apr. 2006.

[BRO88] H.W. v. d. Broeck, H.C. Skudelny and G.V. Stanke, “Analysis and realization of a pulsewidth modulator based on voltage space vectors,” *IEEE Trans. Ind. Appl.*, vol. 24, no. 1, pp. 142-150, Jan./Feb. 1988.

[CAR05] C. Caruana, G. M. Asher and J. C. Clare, “Sensorless flux position estimation at low and zero frequency by measuring zero-sequence current in delta-connected cage induction machines,” *IEEE Trans. Ind. Appl.*, vol. 41, no. 2, pp. 609-617, Mar./Apr. 2005.

[CHA96] C. C. Chan and K. T. Chau, “An advanced permanent magnet motor drive system for battery-powered electric vehicles,” *IEEE Trans. Vehic. Tech.*, vol. 45, no. 1, pp. 180-188, Feb. 1996.

[CHE03] Z. Chen, M. Tomita, S. Doki and S. Okuma, “An extended electromotive force model for sensorless control of interior permanent-magnet synchronous motors,” *IEEE Trans. Ind. Electron.*, vol. 50, no. 2, pp. 288-295, Apr. 2003.

[CHI09] S. Chi, Z. Zhang, and L. Xu, “Sliding-mode sensorless control of directdrive PM synchronous motors for washing machine applications,” *IEEE Trans. Ind. Appl.*, vol. 45, no. 2, pp. 582–590, Mar/Apr. 2009.

[CHO96] J. Choi and S. K. Sul, “Inverter output voltage synthesis using novel dead time compensation,” *IEEE Trans. Power. Electron.*, vol. 11, no. 2, pp. 221-227, Mar. 1996.

[CHU13] W. Q. Chu and Z. Q. Zhu, “Investigation of torque ripples in permanent magnet synchronous machines with skewing,” *IEEE Trans. Magn.*, vol. 49, no. 3, pp. 1211-1220, Mar. 2013.

[CHU13a] W. Q. Chu and Z. Q. Zhu, “Average torque separation in permanent magnet synchronous machines using frozen permeability," *IEEE Trans. Magn.*, vol. 49, no. 3, pp. 1202-1210, Mar. 2013.

[CON06] A. Consoli, G. Scarcella, G. Bottiglieri, G. Scelba, A. Testa and D. A. Triolo, "Low-frequency signal-demodulation-based sensorless technique for induction motor drives at low speed," *IEEE Trans. Ind. Electron*., vol. 53, no. 1, pp. 207-215, Feb. 2006.

[COR98] M. J. Corley and R. D. Lorenz, "Rotor position and velocity estimation for a salient-pole permanent magnet synchronous machine at standstill and high speeds," *IEEE Trans. Ind. Appl.*, vol. 34, no. 4, pp. 784-789, Jul/Aug. 1998.

[DEP88] M. Depenbrock, "Direct self-control (DSC) of inverter-fed induction machine," *IEEE Trans. Power Electron*., vol. 3, no. 4, pp. 420-429, Oct. 1988.

[DUR14] M. J. Duran, F. Salas and M. R. Arahal, "Bifurcation analysis of five-phase induction motor drives with third harmonic injection," *IEEE Trans. Ind. Electron*., vol. 55, no. 5, 2006-2014, May 2014.

[ELR06] A. M. El-Refaie and T. M. Jahns, "Scalability of surface PM machines with concentrated windings designed to achieve wide speed ranges of constant-power operation," *IEEE Trans. Energy Convers*., vol. 21, no. 2, pp. 362-369, Jun. 2006.

[ELR10] A. M. EL-Refaie, "Fractional-slot concentrated-windings synchronous permanent magnet machines: opportunities and challenges," *IEEE Trans. Ind. Electron*., vol. 57, no. 1, pp. 107-121, Jan. 2010.

[ELR14] A. M. EL-Refaie, J. P. Alexander, S. Galioto, P. B. Reddy, K. Huh, P. D. Bock and X. Shen, "Advanced high-power-density interior permanent magnet motor for traction applications," *IEEE Trans. Ind. Appl.*, vol. 50, no. 5, pp. 3235-3248, Sep./Oct. 2014.

[FRE96] C. French and P. Acarnley, "Direct torque control of permanent magnet drives," *IEEE Trans. Ind. Appl.*, vol. 32, no. 5, pp. 1080-1088, Sep./Oct. 1996.

[GAO09] Q. Gao, G. M. Asher, M. Sumner and L. Empringham, "Position estimation of a matrix-converter-fed AC pm machine from zero to high speed using PWM excitation," *IEEE Trans. Ind. Electron*., vol. 56, no. 6, pp. 2030-2038, Jun.

2009.

[GAR07] P. García, F. Briz, M. W. Degner and D. D. Reigosa, “Accuracy, bandwidth, and stability limits of carrier-signal-injection-based sensorless control methods,” *IEEE Trans. Ind. Appl.*, vol. 43, no. 4, pp. 990-1000, Jul./Aug. 2007.

[GON10] L. M. Gong and Z. Q. Zhu, “Modeling and compensation of inverter nonlinearity effects in carrier signal injection-based sensorless control methods from positive sequence carrier current distortion”, in *Proc. IEEE Energy Convers. Congr. Expo. (ECCE),* 2010, pp. 3434-3441.

[GUO15] H. Guo, J. Xu and Y. Chen, “Robust control of fault-tolerant permanent-magnet synchronous motor for aerospace application with guaranteed fault switch process,” *IEEE Trans. Ind. Electron*., vol. 62, no. 12, 7309-7321, Dec. 2015.

[HAM13] M. A. Hamida, J. D. Leon, A. Glumineau and R. Boisliveau, “An adaptive interconnected observer for sensorless control of PM synchronous motors with online parameter identification,” *IEEE Trans. Ind. Electron*., vol. 60, no. 2, pp. 739-748, Feb. 2013.

[HAQ10] M. E. Haque, M. Negnevitsky and K. M. Muttaqi, “A novel control strategy for a variable-speed wind turbine with a permanent-magnet synchronous generator,” *IEEE Trans. Ind. Appl.*, vol. 46, no. 1, pp. 331-339, Jan./Feb. 2010.

[HEN10] J. R. Hendershort, Jr. and T. J. E. Miller, *Design of Brushless Permanent-Magnet Machines*. Venice, FL: Motor Design Books, 2010, pp. 693-694.

[HEN94] J. R. Hendershot Jr. and T. J. E. Miller, *Design of Brushless Permanent Magnet Motors*. Oxford, U.K.: Magna Physics, 1994.

[HOL03] D. Grahame Holmes and T. A. Lipo, *Pulse Width Modulation for Power Converters: Principles And Practice*. Hoboken, NJ: John Wiley, 2003.

[HWA14] J. Hwang and H. Wei, “The current harmonics elimination control strategy for six-leg three-phase permanent magnet synchronous motor drives,” *IEEE Trans. Power. Electron.,* vol. 29, no. 6, pp. 3032-3040, Sep. 2014.

[ISH06] D. Ishak, Z. Q. Zhu and D. Howe, “Comparison of PM brushless motors, having either all teeth or alternate teeth wound,” *IEEE Trans. Enger. Conv.*, vol. 21, no. 1, pp. 95-103, Mar. 2006.

[ISL09] R. Islam, I. Husain, A. Fardoun and K. McLaughlin, “Permanent-magnet synchronous motor magnet designs with skewing for torque ripple and cogging torque reduction,” *IEEE Trans. Ind. Appl.*, vol. 45, no. 1, pp. 152-160, Jan./Feb. 2009.

[IUR11] H. Iura, K. Ide, T. Hanamoto and Z. Chen, “An estimation method of rotational direction and speed for free-running AC machines without speed and voltage sensor,” *IEEE Trans. Ind. Appl.*, vol. 47, no. 1, pp. 153-160, Jan/Feb. 2011.

[JAH80] T. M. Jahns, “Improved reliability in solid-state AC drives by means of multiple independent phase drive units,” *IEEE Trans. Ind. Appl.*, vol. IA-16, no. 3, pp. 321-331, May/Jun.1980.

[JAH87] T. M. Jahns, “Flux-weakening regime operation of an interior permanent-magnet synchronous motor drive,” *IEEE Trans. Ind. Appl.*, vol. IA-23, no. 4, pp. 681-689, Jul./Aug. 1987.

[JAH96] T. M. Jahns and W. L. Soong, “Pulsating torque minimization techniques for permanent magnet AC motor drives-a review,” *IEEE Trans. Ind. Electron.*, vol. 43, no. 2, pp. 321-330, Apr. 1996.

[JAN04] J. Jang, J. Ha, M. Ohto, K. Ide and S. K. Sul, “Analysis of permanent-magnet machine for sensorless control based on high-frequency signal injection,” *IEEE Trans. Ind. Appl.*, vol. 40, no. 6, pp. 1595-1604, Nov./Dec. 2004.

[JAN11] S. Jang, H. Park, J. Choi, K. Ko and S. Lee, “Magnet pole shape design of permanent magnet machine for minimization of torque ripple based on electromagnetic field theory,” *IEEE Trans. Magn.*, vol. 47, no. 10, pp. 3586-3589, Oct. 2011.

[JAN95] P. L. Jansen and R. D. Lorenz, “Transducerless position and velocity estimation in induction and salient AC machines,” *IEEE Trans. Ind. Appl.*, vol. 31, no. 2, pp. 240-247, Mar./Apr. 1995.

[JIA10] H. Jia, M. Cheng, W. Hua, W. Zhao and W. Li, “Torque ripple suppression in flux-switching PM motor by harmonic current injection based on voltage space-vector modulation,” *IEEE Trans. Magn.*, vol. 46, no. 6, pp. 1527-1530, Jun. 2010.

[JUN13] S. Jung, J. Hong and K. Nam, “Current minimizing torque control of the IPMSM using Ferrari’s method,” *IEEE Trans. Power Electron*., vol. 28, no. 12, pp. 5603-5617, Dec. 2013.

[KAL14] J. Kalaiselvi and S. Srinivas, "Passive common mode filter for reducing shaft voltage, ground current, bearing current in dual two level inverter fed open end winding induction motor," in *Proc. Int. Conf. Opt. of Elect. Electron. Equip.*, 2014, pp. 595-600.

[KAN06] R. S. Kanchan, P. N. Tekwani, and K. Gopakumar, “Three-level inverter scheme with common mode voltage elimination and DC link capacitor voltage balancing for an open-end winding induction motor drive,” *IEEE Trans. Power Electron.,* vol. 21, no. 6, pp. 1676-1683, Nov. 2006.

[KHA12] A. S. Abdel-Khalik, M. I. Masoud, S. Ahmed and A. M. Massoud, “Effect of current harmonic injection on constant rotor volume multiphase induction machine stators: a comparative study,” *IEEE Trans. Ind. Appl.*, vol. 48, no. 6, pp. 2002-2013, Nov./Dec. 2012.

[KIM04] J. Kim, J. Jung and K. Nam, "Dual-inverter control strategy for high-speed operation of EV induction motors," *IEEE Trans. Ind. Electron.,* vol. 51, no. 2, pp. 312-320, Apr. 2004.

[KIM13] S. Kim, Y. Yoon, S. K. Sul and K. Ide, “Maximum torque per ampere (MTPA) control of an IPM machine based on signal injection considering inductance saturation,” *IEEE Trans. Power Electron*., vol. 28, no. 1, pp. 488-497, Jan 2013.

[KIM13] S. Jung, J. Hong and K. Nam, “Maximum torque per ampere (MTPA) control of an IPM machine based on signal injection considering inductance saturation,” *IEEE Trans. Power Electron*., vol. 28, no. 1, pp. 488-497, Jan. 2013.

[KWA07] M. Kwak and S. K. Sul, “Flux weakening control of an open winding machine with isolated dual inverters,” in *Proc. IEEE Annu. Meeting Ind. Appl. Conf.,* 2007, pp. 251-255.

[LEI11] R. Leidhold, “Position sensorless control of pm synchronous motors based on zero-sequence carrier injection,” *IEEE Trans. Ind. Electron*., vol. 58, no. 12, pp. 5371-5379, Dec. 2011.

[LI03] Y. Li, J. Zou and Y. Lu, “Optimum design of magnet shape in permanent-magnet synchronous motors,” *IEEE Trans. Magn.*, vol. 39, no. 6, pp. 3523-3526, Nov. 2003.

[LI09] S. Li and Z. Liu, “Adaptive speed control for permanent-magnet synchronous motor system with variations of load inertia,” *IEEE Trans. Ind. Electron*., vol. 56, no. 8, pp. 3050-3059, Aug. 2009.

[LIN03] M. Linke, R. Kennel, and J. Holtz, “Sensorless speed and position control of synchronous machines using alternating carrier injection,” in *Proc. IEEE IEMDC*, 2003, vol. 3, pp. 1211–1217.

[LIU12] H. Liu and S. Li, “Speed control for PMSM servo system using predictive functional control and extended state observer,” *IEEE Trans. Ind. Electron*., vol. 59, no. 2, pp. 1171-1183, Feb. 2012.

[LIU13] Z. Liu, J. Zhang, S. Zhou, X. Li and Kan Liu, “Coevolutionary particle swarm optimization using AIS and its application in multiparameter estimation of PMSM,” *IEEE Trans. Cyber*., vol. 43, no. 6, pp. 1921-1935, Dec. 2013.

[LIU14] J. M. Liu and Z. Q. Zhu, “Novel sensorless control strategy with injection of high-frequency pulsating carrier signal into stationary reference frame,” *IEEE Trans. Ind. Appl.*, vol. 50, no. 4, pp. 2574-2583, Jul./Aug. 2014.

[LIU14a] J. M. Liu and Z. Q. Zhu, “Improved sensorless control of permanent-magnet synchronous machine based on third-harmonic back EMF,” *IEEE Trans. Ind. Appl.*, vol. 50, no. 3, pp. 1861-1870, May/Jun. 2014.

[LYR02] R. O. C. Lyra and T. A. Lipo, “Torque density improvement in a six-phase induction motor with third harmonic current injection,” *IEEE Trans. Ind. Appl.*, vol. 38, no. 5, pp. 1351-1360, Sep./Oct. 2002.

[MAT05] P. Mattavelli, L. Tubiana and M. Zigliotto, “Torque-ripple reduction in PM synchronous motor drives using repetitive current control,” *IEEE Trans. Power. Electron.*, vol. 20, no. 6, pp. 1423-1431, Nov. 2005.

[MON07] G. Mondal, K. Gopakumar, P. N. Tekwani and E. Levi, "A reduced-switch-count five-level inverter with common-mode voltage elimination for an open-end winding induction motor drive," *IEEE Trans. Ind. Electron.*, vol. 54, no. 4, pp. 2344-2351, Aug. 2007.

[MOR02] S. Morimoto, K. Kawamoto, M. Sanada and Y. Takeda, “Sensorless control strategy for salient-pole pmsm based on extended EMF in rotating reference frame,” *IEEE Trans. Ind. Appl.*, vol. 38, no. 4, pp. 1054-1061, Jul./Aug. 2002.

[MOR16] A. Mora, Á. Orellana, J. Juliet and R. Cárdenas, “Model predictive torque control for torque ripple compensation in variable-speed PMSMs,” *IEEE Trans. Ind. Electron.*, vol. 63, no. 7, pp. 4584-4592, Jul. 2016.

[MOR90] S. Morimoto, Y. Takeda, T. Hirasa and K. Taniguchi, “Expansion of operating limits for permanent magnet motor by current vector control considering inverter capacity,” *IEEE Trans. Ind. Appl.*, vol. 26, no. 5, pp. 866-871, Sep./Oct. 1990.

[MWA16] F. Mwasilu and J. W. Jung, “Enhanced fault-tolerant control of interior PMSMs based on an adaptive EKF for EV traction applications,” *IEEE Trans. Power Electron.*, vol. 31, no. 8, pp. 5746-5758, Aug. 2016.

[NGU17] N. K. Nguyen, F. Meinguet, E. Semail and X. Kestelyn, “Fault-tolerant operation of an open-end winding five-phase pmsm drive with short-circuit inverter fault,” *IEEE Trans. Ind. Electron.*, in press.

[NIA14] H. Nian and Y. Zhou, “Investigation on open winding PMSG system with the integration of full controlled and uncontrolled converter,” *IEEE Trans. Ind. Appl.*, vol. 51, no. 1, pp. 429-439, Jan./Feb. 2014.

[NIA15] H. Nian and Y. Zhou, “Investigation of open-winding PMSG system with the integration of fully controlled and uncontrolled converter,” *IEEE Trans. Ind. Appl.*, vol. 51, no. 1, pp. 429-439, Jan./Feb. 2015.

[NOG03] T. Noguchi and S. Kohno, “Mechanical-sensorless permanent-magnet motor drive using relative phase information of harmonic currents caused by frequency-modulated three-phase PWM carriers,” *IEEE Trans. Ind. Appl.*, vol. 39, no. 4, pp. 1085-1092, Jul./Aug. 2003.

[OLE05] V. Oleschuk, A. Sizov, B. K. Bose, and A. M. Stankovic, “Phase-shift based synchronous modulation of dual inverters for an open-end winding motor drive with elimination of zero-sequence currents,” in *Proc. Int. Conf. Power Electron.*

Drives Syst., 2005, vol. 1, pp. 325-330.

[PAN12] D. Pan and T. A. Lipo, "Series compensated open-winding PM generator wind generation system," in *Int. Power Electron. and Motion Contr. Conf.*, 2012, pp. LS7c.1-1-LS7c.1-8.

[PAR05] L. Parsa and H. A. Toliyat, "Five-phase permanent-magnet motor drives," *IEEE Trans. Ind. Appl.*, vol. 41, no. 1, pp. 30-37, Jan./Feb. 2005.

[PAR12] Y. Park and S. K. Sul, "A novel method utilizing trapezoidal voltage to compensate for inverter nonlinearity," *IEEE Trans. Power. Electron.*, vol. 27, no. 12, pp. 4837-4846, Dec. 2012.

[PET00] V. Petrovic, R. Ortega, A. M. Stankovic and G. Tadmor, "Design and implementation of an adaptive controller for torque ripple minimization in PM synchronous motors," *IEEE Trans. Power. Electron.*, vol. 15, no. 5, pp. 871-880, Sep. 2000.

[PRA15] S. Pramanick, N. A. Azeez, R. S. Kaarthik, K. Gopakumar and C. Cecati, "Low-order harmonic suppression for open-end winding IM with dodecagonal space vector using a single dc-link supply," *IEEE Trans. Ind. Electron*., vol. 62, no. 9, pp. 5340-5347, Sep. 2015.

[PRE13] M. Preindl and S. Bolognani, "Model predictive direct speed control with finite control set of PMSM drive systems," *IEEE Trans. Power Electron*., vol. 28, no. 2, pp. 1007-1015, Feb. 2013.

[PRI15] B. Prieto, M. M. Iturralde, L. Fontán and I. Elosegui, "Fault-tolerant permanent magnet synchronous machine – phase, pole and slot number selection criterion based on inductance calculation," *IET Electr. Power Appl.*, vol. 9, no. 2, pp. 138-149, 2015.

[QI09] G. Qi, J. T. Chen, Z. Q. Zhu, D. Howe, L. B. Zhou and C. L. Gu, "Influence of skew and cross-coupling on flux-weakening performance of permanent-magnet brushless AC machines," *IEEE Trans. Magn*., vol. 45, no.5, pp. 2110-2117, May 2009.

[RAH98] M. A. Rahman and M. A. Hoque, "On-line adaptive artificial neural network based vector control of permanent magnet synchronous motors," *IEEE Trans.*

Enger. Conv., vol. 13, no. 4, pp. 311-318, Dec. 1998.

[REI01] J. Reinert, A. Brockmeyer and R. W. A. A. D. Doncker, “Calculation of losses in ferro- and ferrimagnetic materials based on the modified steinmetz equation,” *IEEE Trans. Ind. Appl.*, vol. 37, no. 4, pp. 1055-1061, Jul./Aug. 2001.

[REN15] Y. Ren and Z. Q. Zhu, “Reduction of both harmonic current and torque ripple for dual three-phase permanent-magnet synchronous machine using modified switching-table-based direct torque control,” *IEEE Trans. Ind. Electron.*, vol. 62, no. 11, pp. 6671-6683, Nov. 2015.

[SAN13] A. P. Sandulescu, F. Meinguet, X. Kestelyn, E. Semail and A. Bruyere, “Flux-weakening operation of open-end winding drive integrating a cost-effective high-power charger,” *IET Electr. Syst. Transp.*, vol. 3, no. 1, pp. 10-21, Mar. 2013.

[SAN14] P. Sandulescu, F. Meinguet, X. Kestelyn, E. Semail and A. Bruyere, “Control strategies for open-end winding drives operating in the flux-weakening region,” *IEEE Trans. Power. Electron.*, vol. 29, no. 9, pp. 4829-4842, Sep. 2014.

[SCU14] F. Scuiller, “Magnet shape optimization to reduce pulsating torque for a five-phase permanent-magnet low-speed machine,” *IEEE Trans. Magn.*, vol. 50, no. 4, ID: 8100709, Apr. 2014.

[SER15] Alessandro Serpi, Giuseppe Fois, Federico Deiana and Gianluca Gatto, “Performance improvement of brushless DC machine by zero-sequence current injection,” in *Annu. Conf. of IEEE Ind. Electron. Soci*, pp. 3804-3809, 2015,.

[SHA10] M. A. Shamsi-Nejad, B. Nahid-Mobarakeh, S. Pierfederici and F. Meibody-Tabar, "Series architecture for fault tolerant PM drives: Operating modes with one or two DC voltage source(s)," in *Proc. IEEE Int. Conf. Ind. Tech.*, 2010, pp. 1525-1530.

[SHE04] J. X. Shen, Z. Q. Zhu and D. Howe, “Sensorless flux-weakening control of permanent-magnet brushless machines using third harmonic back EMF,” *IEEE Trans. Ind. Appl.*, vol. 40, no. 6, pp. 1085-1092, Nov./Dec. 2004.

[SHE06] J.X. Shen, Z.Q. Zhu and D. Howe, “Practical issues in sensorless control of PM brushless machines using third-harmonic back-EMF,” in *Proc. Int. Power Elect.*

Motio. Contr. Conf., 2006, vol. 2. pp. 1-5.

[SHE06a] J. X. Shen and S. Iwasaki, “Sensorless control of ultrahigh-speed PM brushless motor using PLL and third harmonic back EMF,” *IEEE Trans. Ind. Electron*., vol. 53, no. 2, pp. 421-428, Apr. 2006.

[SHI01] E. G. Shivakumar, K. Gopakumar, S. K. Sinha, A. Pittet and V. T. Ranganathan, "Space vector PWM control of dual inverter fed open-end winding induction motor drive," in *Proc. IEEE Annu. Appl. Powe. Electron. Conf. Expos.*, 2001, pp. 399-405.

[SHI08] K. Mu-Shin and S. Seung-Ki, "Control of an open-winding machine in a grid-connected distributed generation system," *IEEE Trans. Ind. Appl.*, vol. 44, no. 4, pp. 1259-1267, Jul./Aug.. 2008.

[SIA16] M. Siami, D. A. Khaburi and J. Rodríguez, “Torque ripple reduction of predictive torque control for PMSM drives with parameter mismatch,” *IEEE Trans. Power. Electron.*, DOI: 10.1109 / TPEL. 2016. 2630274, early access.

[SLE94] G. R. Slemon, “On the design of high-performance surface-mounted PM motors,” *IEEE Trans. Ind. Appl.*, vol. 30, no. 1, pp. 134-140, Jan./Feb. 1994.

[SOM02] V. T. Somasekhar, K. Gopakumar, A. Pittet, and V. T. Ranganathan, “PWM inverter switching strategy for a dual two-level inverter fed open end winding induction motor drive with a switched neutral,” *Proc. Inst. Elect. Eng.*, vol. 149, no. 2, pp. 152–160, Mar. 2002.

[SOM02a] V. Somasekhar, K. Gopakumar, E. Shivakumar, and S. Sinha, "A space vector modulation scheme for a dual two level inverter fed open-end winding induction motor drive for the elimination of zero sequence currents," *EPE Journal*, vol. 12, pp. 26-36, 2002.

[SOM04] V. T. Somasekhar, K. Gopakumar, and M. R. Baiju, "Dual two-level inverter scheme for an open-end winding induction motor drive with a single DC power supply and improved DC bus utilisation," in *IEE Proc. Electric Power Appl.,* 2004, pp. 230-238.

[SOM08] V. T. Somasekhar, S. Srinivas and K. K. Kumar, “Effect of Zero-Vector Placement in a Dual-Inverter Fed Open-End Winding Induction-Motor Drive

With a Decoupled Space-Vector PWM Strategy," *IEEE Trans. Ind. Electron.*, vol. 55, no. 6, pp. 2497-2505, Jun. 2008.

[SOM13] A. Somani, R. K. Gupta, K. K. Mohapatra and Ned Mohan, "On the causes of circulating currents in PWM drives with open-end winding AC machines," *IEEE Trans. Ind. Electron.*, vol. 60, no. 9, pp. 3670-3678, Sep. 2013.

[SON96] J. H. Song, J. M. Kim, and S. K. Sul, "A new robust SPMSM control to parameter variations in flux weakening region," *Proc. IEEE*, vol. 2, no. 8, pp. 1193-1198, Aug. 1996.

[SPR98] L. Springob and J. Holtz, "High-bandwidth current control for torque-ripple compensation in PM synchronous machines," *IEEE Trans. Ind. Electron*., vol. 45, no. 5, pp. 713-721, Oct. 1998.

[STA06] C. S. Staines, C. Caruana, G. M. Asher and M. Sumner, "Sensorless control of induction machines at zero and low frequency using zero sequence currents," *IEEE Trans. Ind. Electron*., vol. 53, no. 1, pp. 195-206, Apr. 2006.

[TAK86] I. Takahashi and T. Noguchi, "A new quick-response and high-efficiency control strategy of an induction motor," *IEEE Trans. Ind. Appl.*, vol. IA-22, no. 5, pp. 820-827, Sep./Oct. 1986.

[TSO15] S. Tsotoulidis and A. N. Safacas, "Deployment of an adaptable sensorless commutation technique on BLDC motor drives exploiting zero sequence voltage," *IEEE Trans. Ind. Electron*., vol. 62, no. 2, pp. 877-886, Feb. 2015.

[WAL07] O. Wallmark, L. Harnefors and O. Carlson, "Control algorithms for a fault-tolerant PMSM drive," *IEEE Trans. Ind. Electron*., vol. 54, no. 4, pp. 1973-1980, Aug. 2007.

[WAN12] J. Wang, R. Qu and L. Zhou, "Dual-rotor multiphase permanent magnet machine with harmonic injection to enhance torque density," *IEEE Trans. Appl. Super*., vol. 22, no. 3, Article No. 5202204, Jun. 2012.

[WAN12a] Z. Wang, K. Lu and F. Blaajerg, "A simple startup strategy based on current regulation for back-EMF-based sensorless control of PMSM," *IEEE Trans. Power Electron.*, vol. 27, no. 8, pp. 3817-3825, Aug. 2012.

[WAN13] Y. Wang, D. Panda, T.A. Lipo and D. Pan, "Open-winding power conversion systems fed by half-controlled converters," *IEEE Trans. Power. Electron.,* vol. 28, no. 5, pp. 2427-2436, May 2013.

[WAN13a] G. Wang, R. Yang and D. Xu, "DSP-based control of sensorless IPMSM drives for wide-speed-range operation," *IEEE Trans. Ind. Electron*., vol. 60, no. 2, pp. 720-727, Feb. 2013.

[WAN14] G. Wang, L. Qu, H. Zhan, J. Xu, L. Ding, G. Zhang and D. Xu, "Self-commissioning of permanent magnet synchronous machine drives at standstill considering inverter nonlinearities," *IEEE Trans. Power Electron*., vol. 29, no. 12, pp. 6615-6627, Dec. 2014.

[WAN14a] K. Wang, Z.Q. Zhu and G. Ombach, "Torque enhancement of surface-mounted permanent magnet machine using third-order harmonic," *IEEE Trans. Magn.,* vol. 50, no. 3, Article No. 8100210, Mar. 2014.

[WAN14b] K. Wang, Z. Q. Zhu; G. Ombach and W. Chlebosz, "Average torque improvement of interior permanent-magnet machine using third harmonic in rotor shape," *IEEE Trans. Ind. Electron*., vol. 61, no. 9, pp. 5047-5057, Sep. 2014.

[WAN14c] K. Wang, Z.Q. Zhu and G. Ombach, "Torque improvement of five-phase surface-mounted permanent magnet machine using third-order harmonic," *IEEE Trans. Enger. Conv.*, vol. 29, no. 3, 735-747, Sep. 2014.

[WAN14d] G. Wang, H. Zhan, G. Zhang, X. Gui and D. Xu, "Adaptive compensation method of position estimation harmonic error for EMF-based observer in sensorless IPMSM drives," *IEEE Trans. Power. Electron.,* vol. 29, no. 6, pp. 3055-3064, Jun. 2014.

[WAN15] K. Wang, Z. Q. Zhu, Y. Ren and G. Ombach, "Torque improvement of dual three-phase permanent-magnet machine with third-harmonic current injection," *IEEE Trans. Ind. Electron*., vol. 62, no. 11, 6833-6844, Nov. 2015.

[WAN16] F. Wang, Y. Wang, Q. Gao, C. Wang and Y. Liu, "A control strategy for suppressing circulating currents in parallel-connected PMSM drives with individual DC links," *IEEE Trans. Power Electron.*, vol. 31, no. 2, pp. 1680-1691, Feb. 2016.

[WEBa] http://www.yaskawa.com.sg/product/ac-inverter-drives/a1000---high-performance-vector-control

[WEBb] https://www.toyota.co.uk/new-cars/prius/index.json

[WEBc] https://www.siemens.com/press/en/feature/2013/energy/2013-03-akita-port.php

[WEL03] B. A. Welchko and J. M. Nagashima, "The influence of topology selection on the design of EV/HEV propulsion systems," *IEEE Power Electron. Lett.*, vol. 1, no. 2, pp. 36-40, Jun. 2003.

[WEL04] B. A. Welchko, T. A. Lipo, T. M. Jahns and S. E. Schulz, “Fault tolerant three-phase AC motor drive topologies: a comparison of features, cost, and limitations,” *IEEE Trans. Power Electron.*, vol. 19, no. 4, pp. 1108-1116, Jul. 2004.

[WU15] D. Wu and Z. Q. Zhu, “Design tradeoff between cogging torque and torque ripple in fractional slot surface-mounted permanent magnet machines,” *IEEE Trans. Magn.*, vol. 51, no. 11, ID: 8108704, Nov. 2015.

[XIE16] G. Xie, K. Lu, S. K. Dwivedi, J. R. Rosholm and F. Blaabjerg, “Minimum-voltage vector injection method for sensorless control of PMSM for low-speed operations,” *IEEE Trans. Power Electron.*, vol. 31, no. 2, pp. 1785-1794, Feb. 2016.

[XIN15] Z. Xin, X. Wang, P. C. Loh and F. Blaabjerg, “Realization of digital differentiator using generalized integrator for power converters,” *IEEE Trans. Power. Electron. Lett.*, vol. 30, no. 12, pp. 6520-6523, Dec. 2015.

[XU16] P. L. Xu and Z. Q. Zhu, “Novel carrier signal injection method using zero-sequence voltage for sensorless control of PMSM drives,” *IEEE Trans. Ind. Electron.*, vol. 63, no. 4, pp. 2053-2061, Apr. 2016.

[XU16a] P. L. Xu, Z. Q. Zhu and D. Wu, “Carrier signal injection based sensorless control of permanent magnet synchronous machines without the need of magnetic polarity identification,” *IEEE Trans. Ind. Appl.*, vol. PP, no. 99, 2016.

[YAN10] W. Yang, T. A. Lipo, and P. Di, “Half-controlled-converter-fed open-winding permanent magnet synchronous generator for wind applications,” in *Proc. Int. Power Electron. Motion Contr. Conf.*, 2010, pp.123-126.

[YAN12] S. C. Yang and R. D. Lorenz, "Surface permanent magnet synchronous machine position estimation at low speed using eddy-current-reflected asymmetric resistance," *IEEE Trans. Power. Electron.*, vol. 27, no. 5, pp. 2595-2604, May 2012.

[YAN12b] S. C. Yang and R. D. Lorenz, "Comparison of resistance-based and inductance-based self-sensing controls for surface permanent-magnet machines using high-frequency signal injection," *IEEE Trans. Ind. Appl.*, vol. 48, no. 3, pp. 977-986, May/Jun. 2012.

[YOO11] Y. Yoon, S. K. Sul, S. Morimoto and K. Ide, "High-bandwidth sensorless algorithm for AC machines based on square-wave-type voltage injection," *IEEE Trans. Ind. Appl.*, vol. 47, no. 3, pp. 1361-1370, May/Jun. 2011.

[ZHA16] H. Zhan, Z.Q. Zhu and M. Odavic, "Analysis and suppression of zero sequence circulating current in open winding PMSM drives with common DC bus", in *Proc. IEEE Energy Convers. Congr. Expo. (ECCE),* 2016.

[ZHA16a] H. Zhan, Z.Q. Zhu, M. Odavic and Y. Li, "A novel zero sequence model based sensorless method for open-winding PMSM with common DC bus," *IEEE Trans. Ind. Electron.*, vol. 63, no. 11, 6777-6789, Nov. 2016.

[ZHA17] H. Zhan, Z. Q. Zhu and M. Odavic, "Analysis and suppression of zero sequence circulating current in open winding permanent magnet synchronous machine drives with common DC bus," *IEEE Trans. Ind. Appl.*, DOI: 10.1109/TIA.2017.2679678, 2017.

[ZHA17a] H. Zhan, Z. Q. Zhu and M. Odavic, "Nonparametric sensorless drive method for open-winding PMSM based on zero-sequence back EMF with circulating current suppression," *IEEE Trans. Power Electron.*, vol. 32, no. 5, pp. 3808-3817, May 2017.

[ZHAO17] N. Zhao, G. Wang, D. Xu, L. Zhu, G. Zhang and J. Huo, "Inverter power control based on DC-link voltage regulation for IPMSM drives without electrolytic capacitors," *IEEE Trans. Power Electron.*, early access, DOI: 10.1109/TPEL.2017.2670623, 2017.

[ZHE16] Z. Zheng, D. Sun and J. Zhu, "Torque ripple suppression of open-winding PMSMs by current injection considering magnetic saturation," in *Proc. IEEE*

Vehi. Powe. and Prop. Conf., 2016, pp. 1-5.

[ZHO02] K. Zhou and D. Wang, “Relationship between space-vector modulation and three-phase carrier-based PWM: a comprehensive analysis [three-phase inverters],” *IEEE Trans. Ind. Electron*., vol. 49, no. 1, pp. 186-196, Feb. 2002.

[ZHO14] K. Zhou and D. Wang, “Average torque improvement of interior permanent-magnet machine using third harmonic in rotor shape,” *IEEE Trans. Ind. Electron*., vol. 61, no. 9, pp. 5047-5057, Sep. 2014.

[ZHO15] Y. Zhou and H. Nian, “Zero-Sequence current suppression strategy of open-winding PMSG system with common DC bus based on zero vector redistribution,” *IEEE Trans. Ind. Electron.*, vol. 62, no. 6, pp. 3399-3408, Jun. 2015.

[ZHO16] Y. Zhou and H. Nian, “ Current zero-crossing duration reduction of a semicontrolled open-winding PMSG system based on third harmonic current injection,” *IEEE Trans. Ind. Electron.*, vol. 63, no. 2, pp. 750-760, Feb. 2016.

[ZHO97] L. Zhong, M. F. Rahman, W. Y. Hu and K. W. Lim, “Analysis of direct torque control in permanent magnet synchronous motor drives,” *IEEE Trans. Power Electron*., vol. 12, no. 3, pp. 528-536, May 1997.

[ZHU09] L. Zhu, S. Z. Jiang, Z. Q. Zhu and C. C. Chan, “Analytical methods for minimizing cogging torque in permanent-magnet machines,” *IEEE Trans. Magn.*, vol. 45, no. 4, pp. 2023-2031, Apr. 2009.

[ZHU11] Z.Q. Zhu, “Switched flux permanent magnet machines - Innovation continues” in *Proc.* ICEMS, Aug. 2011, pp. 1-10.

[ZHU12] N. Zhu, J. Kang, D. Xu, B. Wu and Y. Xiao, “An integrated AC choke design for common-mode current suppression in neutral-connected power converter systems,” *IEEE Trans. Power. Electron.*, vol. 27, no. 3, pp. 1228-1236, Mar. 2012.

APPENDIX A ROBUST INITIAL PHASE CORRECTION STRATEGY FOR ZERO SEQUENCE BACK EMF BASED SENSORLESS CONTROL

In this section, a robust initial phase correction strategy, which avoids the false correction, for zero sequence back EMF based sensorless drive switched from I/*f* control is proposed. The transitory HF signal causing negligible audible noise is injected to obtain transitory second saliency reflected position angle and the corresponding phase difference to the estimation of the zero sequence back EMF based sensorless is consequently used to determine the actual estimation state of the zero sequence back EMF based sensorless. Hence, the robust correction can be further achieved according to the identified estimation state.

This appendix was published in IEMDC 2017.

A.1 Conventional Method and Existing Issue

A.1.1 I/*f* Startup Process

The I/*f* startup process usually includes two procedures, viz., the initial position locating and the current closed loop regulation based on the virtual position generated from a ramp function generator. The initial position can be located by injecting DC current to force the rotor *d*-axis to align with the predetermined position in which phase A axis is the usual case. However, this DC injection method is simple but not capable of typical application with large inertia such as fan drives. The pre-positioning process will keep in damped oscillation during a long duration which is not acceptable. Hence, the initial position identification by using HF and pulse voltage injections is considered for these applications. Besides, the current closed loop regulation based on virtual position usually adopts maximum phase current output reference to adapt to different load levels. The synchronization of the rotor is guaranteed via ramp function with reasonable gradient k_c shown in Fig. A.1, instead of step variation. The relationship can be obtained as

$$\theta_e = k_c t \tag{A.1}$$

where t indicates the time from startup command.

The phase difference between the *d*-axis and the space current vector is self-stabilized based on different load levels. The larger the load is imposed, the smaller the phase difference will be. The overload condition might lead to the collapse of the I/*f* control. The typical I/*f* startup process with DC injection is shown in Fig. A.1.

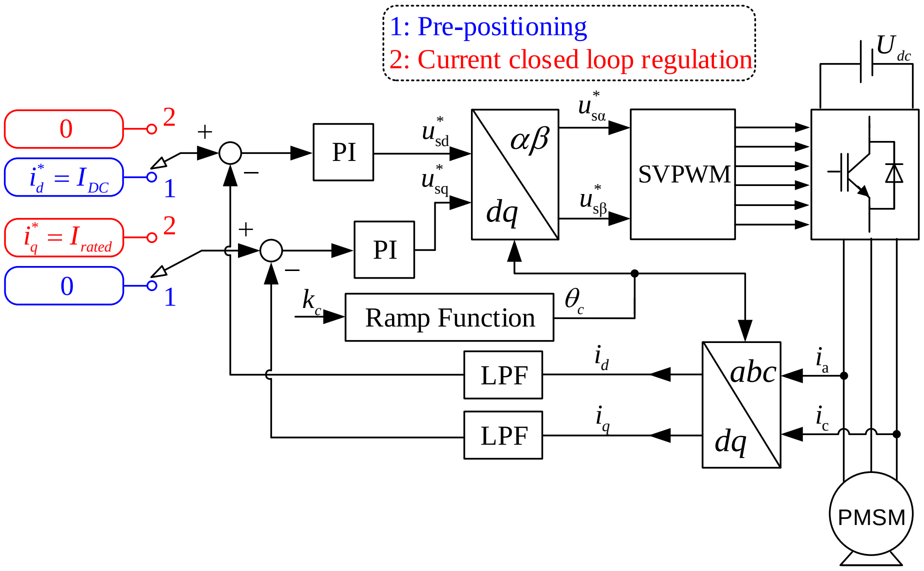

Fig. A.1 Typical I/*f* startup process with DC injection.

The first stage is the pre-positioning for initial startup. The DC current is injected into the virtual *d*-axis and the rotor will be forced to the virtual initial position which will consequently be the real *d*-axis. Only the dual current controllers for current loop are used at this stage. After that, the current references are switched to rotating mode, namely, the current closed loop regulation. The *d*-axis current reference is given as zero and the *q*-axis current reference is given as the rated or higher than the rated current. The virtual position signal generated by the ramp function is simultaneously increasing. The rotor will finally follow the rotating current vector synchronously. The low pass filters (LPF) used in Fig. A1 are first order infinite impulse response filters. The transfer function can be expressed as

$$G_{LPF}(\mathrm{s}) = \frac{\omega_{f1}}{s + \omega_{f1}} \tag{A.2}$$

where ω_{f1} is the cut-off frequency of the LPFs.

A.1.2 Zero Sequence Back EMF Based Sensorless Method

The zero sequence back EMF [1] which is usually the third harmonic contains the rotor position information. Hence, it can be used to estimate the rotor position. The zero sequence back EMF is measured via a three phase resistance network and a voltage transducer, which is shown in Fig. A.2. Meanwhile, the neural point of the PMSM is usually required. The measured third harmonic is taken as the input signal of a phase locked loop (PLL) or observer to extract the phase information. Fig. A.2 shows a zero sequence back EMF based sensorless method using phase locked loop where θ_z is the estimation position angle.

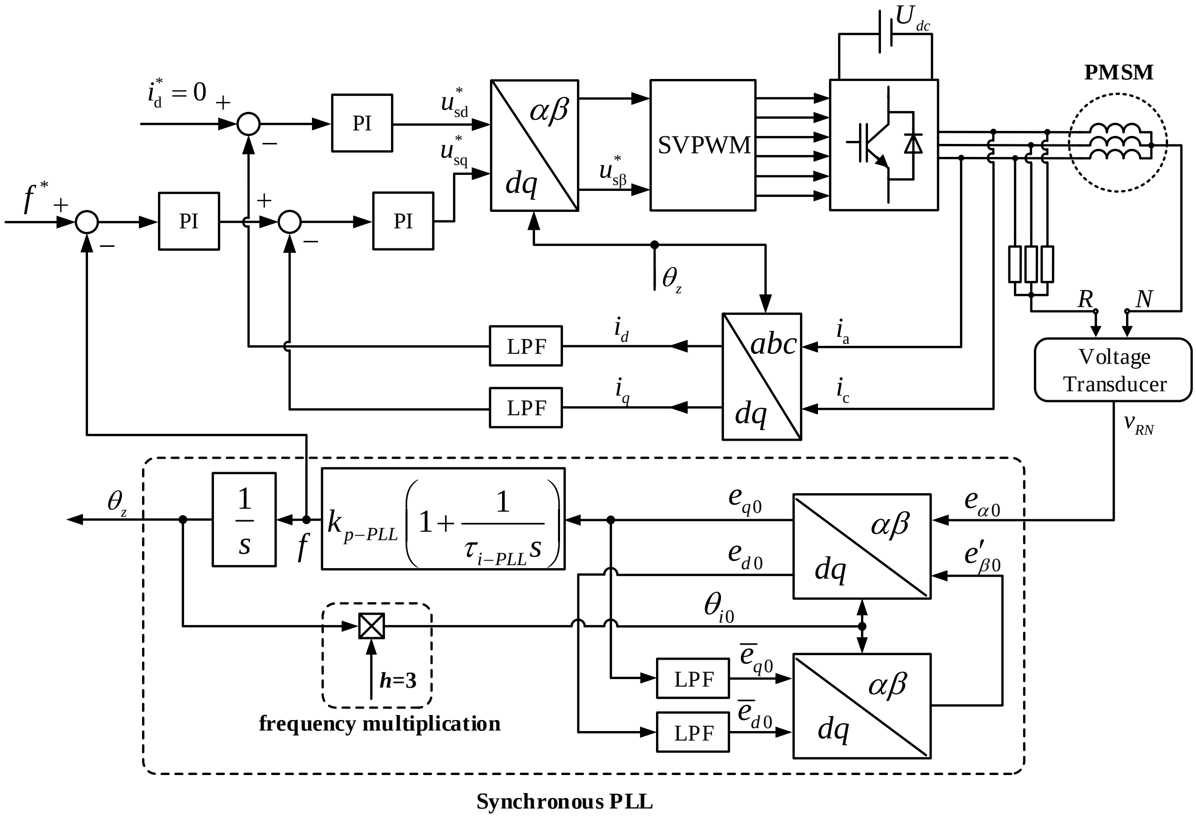

Fig. A.2 Zero sequence back EMF based sensorless control.

In the adopted synchronous PLL, the LPFs are transformed into the stationary reference coordinate. Hence, they will perform as the band pass filter (BPF) and LPF, respectively. The center frequency of the BPF is adaptive to the operation frequency. The frequency multiplication h=3 is designed for the multiplication between the fundamental and the third harmonic back EMF. The transfer functions can be written as

$$G_d(\mathrm{s}) = \frac{k_f \omega_0 s}{s^2 + k_f \omega_0 s + \omega_0^2} \tag{A.3}$$

$$G_q(\mathrm{s}) = \frac{k_f \omega_0^2}{s^2 + k_f \omega_0 s + \omega_0^2} \tag{A.4}$$

where $k_f = \omega_f / \omega_0$, ω_f is the cut-off frequency of the LPFs, $\omega_0 = h\omega = 3\omega$ and ω is the electrical angular speed.

A.1.3 Switching Process and Associated Issue

When the back EMF signal is strong enough above certain speed, the I/*f* control can be switched to zero sequence back EMF based sensorless mode enabling the speed closed loop control. Since the zero sequence back EMF is usually the third harmonic, the estimation position angle can start from three possible phase points as shown in Fig. A.3. The estimation angle θ_z from zero sequence back EMF based sensorless method belongs to the set $\{\theta_{z1}=\theta, \theta_{z2}=\theta-2\pi/3, \theta_{z3}=\theta-4\pi/3\}$. Only θ_{z1} reflects the real position angle. Meanwhile, the position angle transition is usually based on the nearest principle, namely, one of the three possible estimation position angles from zero sequence back EMF based sensorless method, which is nearest to the currently used position angle, is chosen as the correct estimation. The currently used position angle in the framework in this paper is the virtual angle generated by the ramp function generator.

However, the switching process might cause the collapse of the control, viz., false phase correction. The I/*f* control is only current closed loop and the amplitude of the phase current keeps constant under different load conditions. The self-stabilization is guaranteed by distributing matching *q*-axis for the load and residual current in *d*-axis to achieve the constant amplitude of the phase current. Hence, phase difference between the virtual position angle and the actual *d*-axis occurs. The lighter the load is imposed, the larger phase difference will appear. The phase difference depends on the specific machine parameters. Fig. A.3 shows the process and it can be seen that the θ_{z2} might be selected as the correct estimation at no load condition for the specific condition.

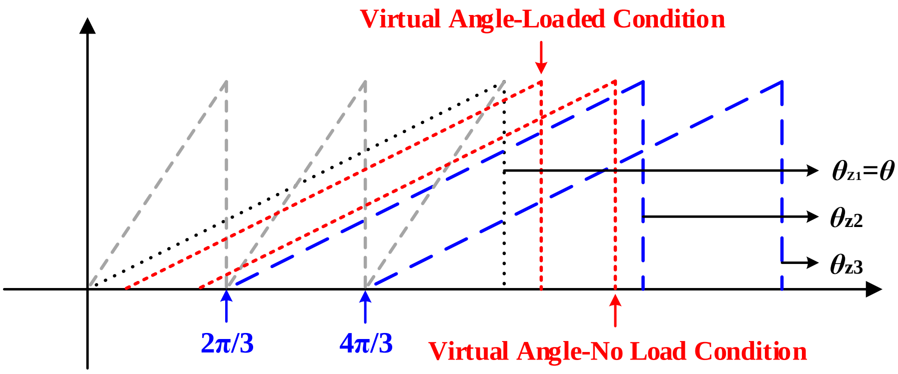

Fig. A.3 False phase correction illustration.

Fig. A.4 shows experimental results for I/*f* control under no load and load conditions at 200rpm. The encoder angle is only used as reference for the actual *d*-axis to evaluate the phase difference under different loads. The no load condition has 0.55π rad phase difference which can lead to the false phase correction and the load condition can enable the correct switching. Hence, the conventional switching strategy is not robust enough to ensure successful transition.

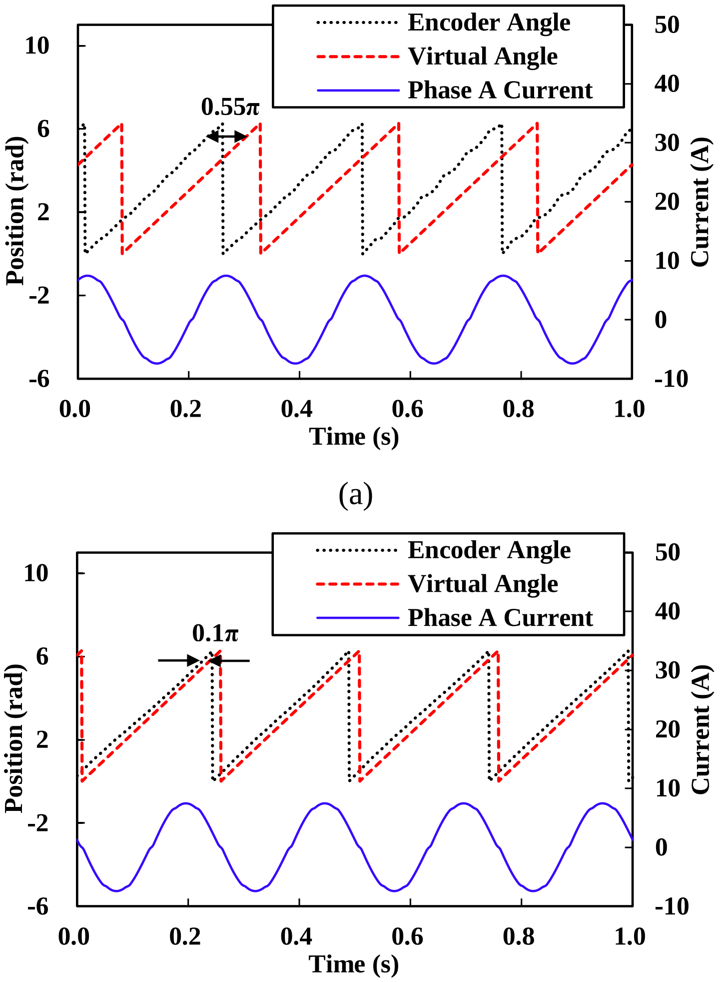

(a)

(b)

Fig. A.4 Phase differences under no load and loaded conditions at 200rpm. (a) No load condition. (b) Loaded condition.

A.2 Proposed Initial Phase Correction Strategy

According to the analysis in Section A.1.3, the conventional phase correction strategy may collapse due to the large phase difference between the space current vector and the *d*-axis. The robust correction method requires the information of phase difference between the real position angle and the estimation position angle from zero sequence back EMF based sensorless method. The proposed initial phase correction strategy is achieved by injecting transitory HF signal into the stator winding to track the secondary saliency information. Then the estimation position angle from HF injection, which can be in-phase or π rad shifted to the real position angle, is used in tandem with the estimation position angle from zero sequence back EMF based sensorless method to deduce the required phase correction values which can be 0, 2/3π or 4/3π.

In order to succinctly describe the proposed strategy, the phase difference between the estimation position angle from HF injection, viz. θ_h, and the estimation position angle from zero sequence back EMF based sensorless method θ_z is defined as $\Delta\theta_{hz}= \theta_h- \theta_z$. It is unknown that the estimated θ_h is in-phase or π rad shifted to the real position angle θ. Hence, it belongs to the set $\{\theta_{h1}=\theta, \theta_{h2}=\theta-\pi\}$. Similarly, θ_z belongs to the set $\{\theta_{z1}=\theta, \theta_{z2}=\theta-2\pi/3, \theta_{z3}=\theta-4\pi/3\}$ which is illustrated in Section A.1.3. Therefore, it can be easily obtained that the mapping between θ_z and $\Delta\theta_{hz}$ is shown in Fig. A.5. The relationship is not a multivalued function and hence the estimation condition of the θ_z can be uniquely determined via $\Delta\theta_{hz}$. Namely, once $\Delta\theta_{hz}$ is calculated, θ_z is consequently determined. And then, the actual positon θ is the proper phase shifted θ_z which can be 0, 2π/3 or 4π/3 rad.

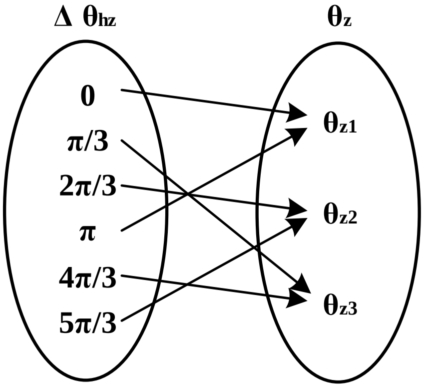

Fig. A.5 Mapping between θ_z and $\Delta\theta_{hz}$.

The transitory HF signal is injected before the switching process enabled and stopped after $\Delta\theta_{hz}$ is obtained, which is a short duration. The estimations of θ_z and θ_h are conducted simultaneously. It is not necessary to use voltage pulse or similar disturbance signal to identify the polarity of θ_h since either the right or wrong convergence value can ensure the correct condition selection.

However, the estimations of zero sequence back EMF based sensorless and the HF injection method might have certain estimation errors. The practical strategy should have error tolerance which is defined as $\Delta\tau$. The selection of the estimation state of θ_z is shown in Fig. A.6 where the indicator numbers 1, 2 and 3 represent θ_{z1}, θ_{z2} and θ_{z3}, respectively.

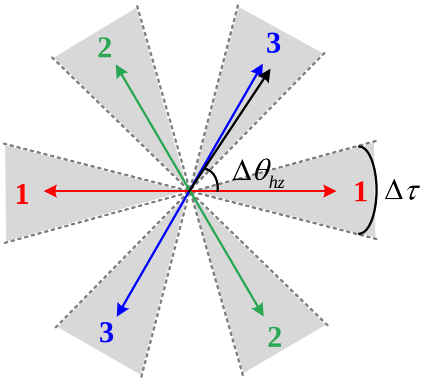

Fig. A.6 Selection of estimation state of θ_z with error tolerance.

Meanwhile, the HF injection method can be either pulsating or rotating injection. The adopted method is pulsating injection in *d*-axis, which is shown in Fig. A.7 together with the proposed initial phase correction strategy. The injected HF voltage signal in estimated *d*-axis is $u_h \cos\omega_h t$. The corrected estimation angle is defined as $\hat{\theta}$.

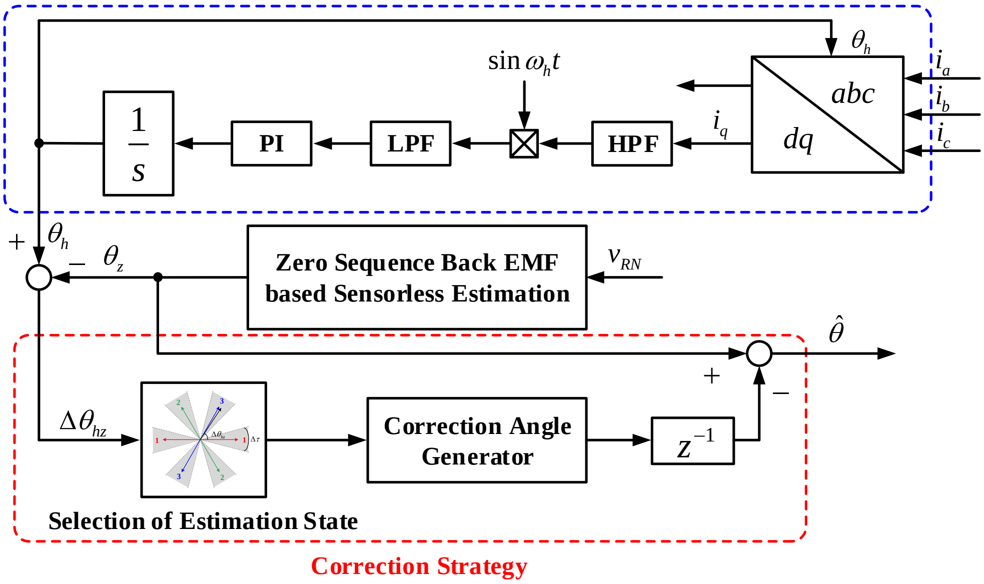

Fig. A.7 Proposed initial phase correction strategy with HF injection estimation.

A.3 Experimental Validation

The proposed strategy is validated on a 12 slots/10 poles fractional slot PMSM drive based on dSPACE system. The PWM switching frequency is 10kHz which is the same as the interrupt period and the dead-time is set to 1 μs. The DC bus voltage is 40 V. Table I shows the specification of the 12 slots/10 poles fractional slot PMSM and Fig. A.8 shows the associated cross section. Meanwhile, the test platform of the PMSM with load machine is shown in Fig. A.8.

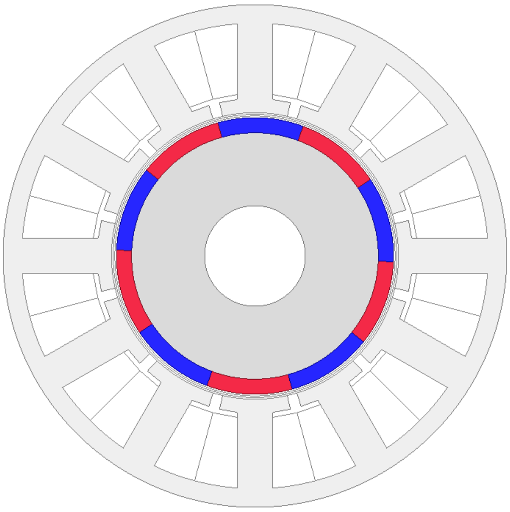

Fig. A.8 Cross section of the 12 slots/10 poles fractional slot PMSM.

Table A.1 Specification of Two prototype PMSM

Parameter	**Value**
Pole number	10
Slot number	12
Stack length	50 mm
Airgap length	1 mm
Slot opening	2 mm
Stator bore radius	28.5 mm
Stator outer radius	N/A
Magnet thickness	3 mm
Magnet remanence	1.2 T
Magnet conductivity	$6.67\times10^{5}\ (\Omega\mathrm{m})^{-1}$
Series turns per phase	132
Tooth tip width	12.92 mm
Pole-pitch	17.91 mm
Rated torque	3.85Nm
Rated current	7A
Rated speed	400rpm
Rated frequency	33.33Hz

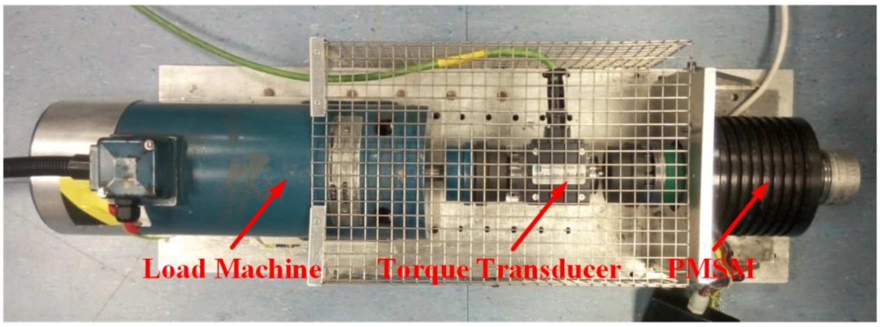

Fig. A.9 Test platform of the 12 slots/10 poles fractional slot PMSM.

Fig. A.9 (a) to Fig. A.9 (f) show all the possible estimation state combinations. The encoder angle is only for reference. Fig. A.9 (a) to Fig. A.9 (c) show the correct estimated θ_h with the three possible initial phase estimations of zero sequence back EMF based sensorless. When the correction is enabled, the indicator number is immediately calculated within one interrupt period. The correction is conducted in the next interrupt period. θ_z is calibrated to be in phase with the encoder angle. Similarly, Fig. A.9 (d) to Fig. A.9 (f) show the π rad shifted θ_h with the three possible initial phase estimations of zero sequence back EMF based sensorless. The robust correction is therefore obtained via the proposed strategy.

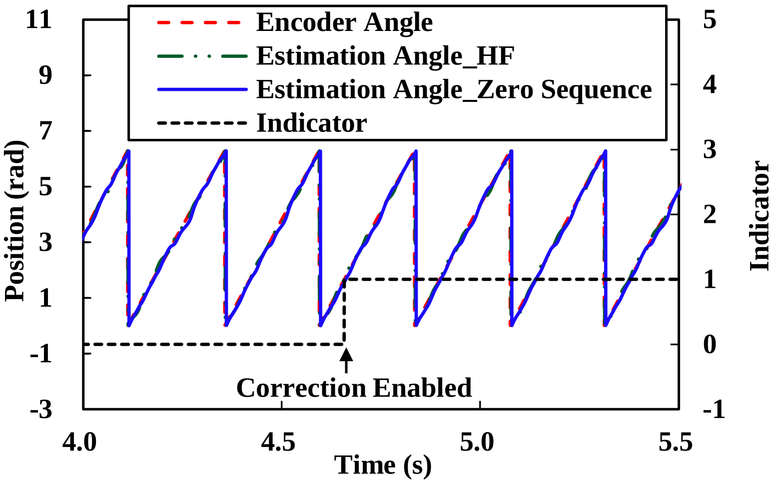

(a)

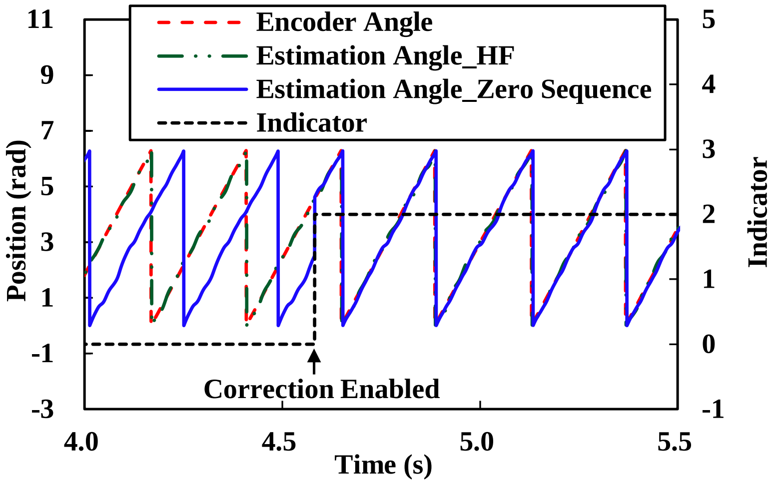
Encoder Angle
Estimation Angle_HF
Estimation Angle_Zero Sequence
Indicator
Position (rad)
11
9
7
5
3
1
-1
-3
Indicator
5
4
3
2
1
0
-1
Correction Enabled
4.0
4.5
5.0
5.5
Time (s)

(b)

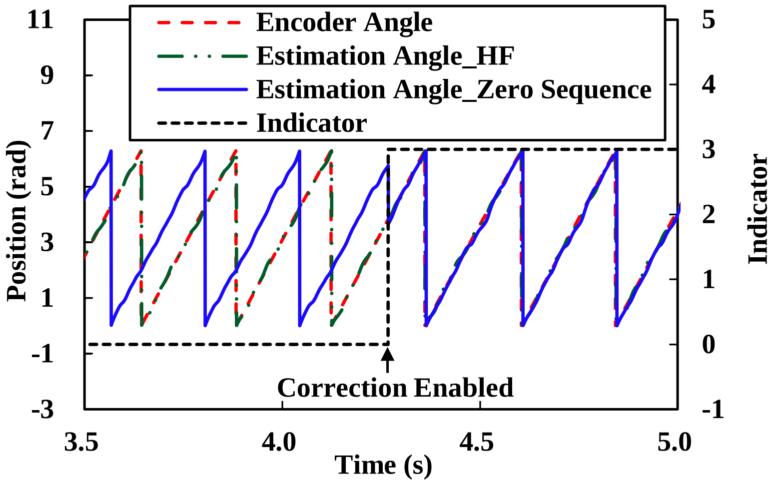
Encoder Angle
Estimation Angle_HF
Estimation Angle_Zero Sequence
Indicator
Position (rad)
11
9
7
5
3
1
-1
-3
Indicator
5
4
3
2
1
0
-1
Correction Enabled
3.5
4.0
4.5
5.0
Time (s)

(c)

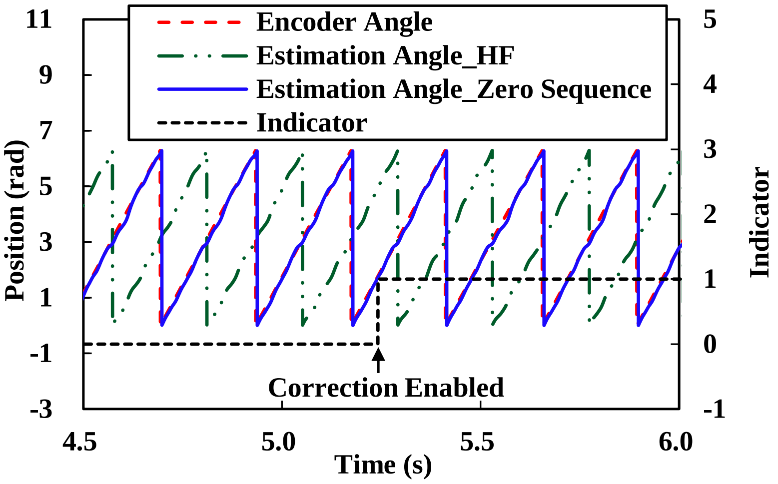
Encoder Angle
Estimation Angle_HF
Estimation Angle_Zero Sequence
Indicator
Position (rad)
11
9
7
5
3
1
-1
-3
Indicator
5
4
3
2
1
0
-1
Correction Enabled
4.5
5.0
5.5
6.0
Time (s)

(d)

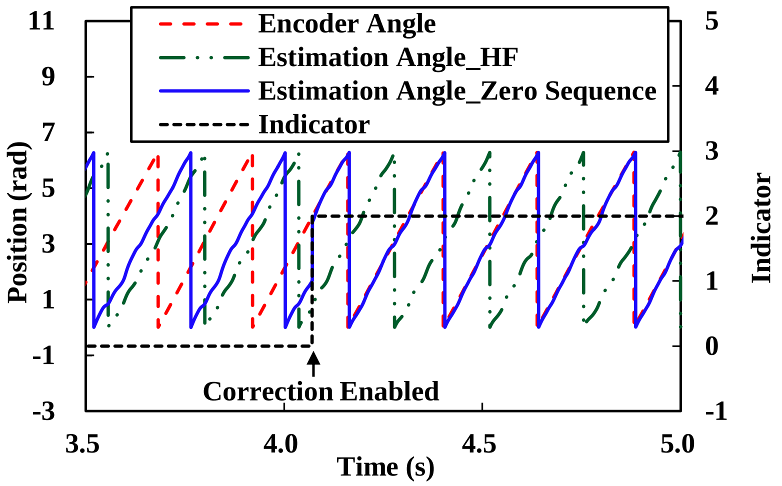

(e)

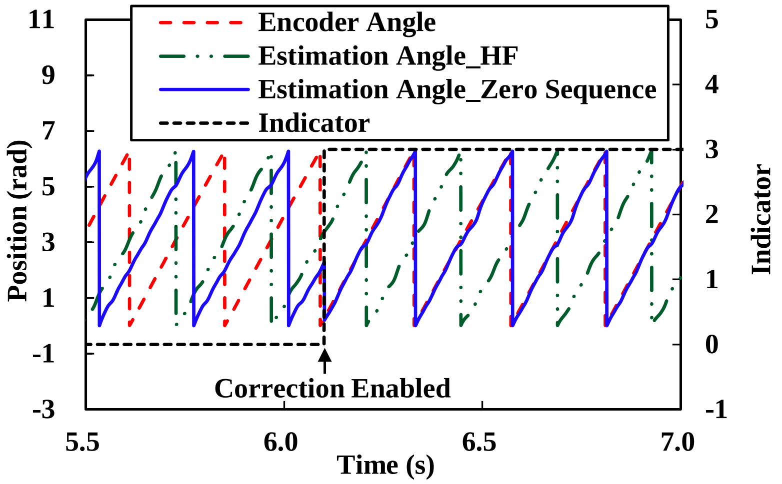

(f)

Fig. A.9 Correction performance with all possible combinations. (a) $\theta_{h1}+\theta_{z1}$. (b) $\theta_{h1}+\theta_{z2}$. (c) $\theta_{h1}+\theta_{z3}$. (d) $\theta_{h2}+\theta_{z1}$. (e) $\theta_{h2}+\theta_{z2}$. (f) $\theta_{h2}+\theta_{z3}$.

A.4 Conclusion

A novel robust initial phase correction strategy has been proposed in this appendix. The adopted I/*f* control and zero sequence back EMF based sensorless methods as well as the false correction issue including the experimental validation have been illustrated. The robust correction performance of the proposed strategy using phase difference between estimations from transitory HF injection and zero sequence back EMF has been validated under all possible combinations.

A.5 Reference

[1] J. M. Liu and Z. Q. Zhu, “Improved sensorless control of permanent-magnet synchronous machine based on third-harmonic back EMF,” *IEEE Trans. Ind. Appl.*, vol. 50, no. 3, pp. 1861-1870, May/Jun. 2014.

APPENDIX B PUBLICATIONS DURING PHD STUDY

Journal Papers:

[2] **H. Zhan**, Z. Q. Zhu, M. Odavic and Y. Li, “A novel zero-sequence model-based sensorless method for open-winding PMSM with common DC bus,” *IEEE Trans. Ind. Electron.*, vol. 63, no. 11, pp. 6777-6789, Nov. 2016.

[3] **H. Zhan**, Z. Q. Zhu and M. Odavic, “Nonparametric sensorless drive method for open-winding PMSM based on zero-sequence back EMF with circulating current suppression,” *IEEE Trans. Power Electron.*, vol. 32, no. 5, pp. 3808-3817, May 2017.

[4] **H. Zhan**, Z. Q. Zhu and M. Odavic, “Analysis and Suppression of Zero Sequence Circulating Current in Open Winding Permanent Magnet Synchronous Machine Drives with Common DC Bus,” *IEEE Trans. Ind. Appl.*, early access, DOI: 10.1109/TIA. 2017.2679678, 2017.

[5] D. J. Evans, Z.Q. Zhu, **H. Zhan**, Z.Z. Wu and X. Ge, “Flux-weakening control performance of partitioned stator-switched flux PM machines,” *IEEE Trans. Ind. Appl.*, vol. 52, no. 3, pp. 2350-2359, May/Jun. 2016.

[6] H. Yang, Z.Q. Zhu, H. Lin; P. Xu, **H. Zhan**, S. Fang and Y. Huang, “Design synthesis of switched flux hybrid-permanent magnet memory machines,” *IEEE Trans. Enger. Conv.*, vol. 32, no. 1, pp. 65-79, Mar. 2017.

[7] Z. Wu, Z. Q. Zhu and **H. Zhan**, “Comparative analysis of partitioned stator flux reversal PM machine and magnetically geared machine operating in stator-PM and rotor-PM modes,” *IEEE Trans. Enger. Conv.*, early access, DOI: 10.1109/TEC.2017.2693028, 2017.

[8] H. Hua, Z.Q. Zhu and **H. Zhan**, “Novel consequent-pole hybrid excited machine with separated excitation stator,” *IEEE Trans. Ind. Electron.*, vol. 63, no. 8, pp. 4718-4728, Aug. 2016.

[9] Z. Wu, Z. Q. Zhu and **H. Zhan**, “Comparative analysis of partitioned stator flux reversal PM machines having fractional-slot non-overlapping and integer-slot overlapping windings,” *IEEE Trans. Enger. Conv.*, vol. 31, no. 2, pp. 776-788, Jun. 2017.

[10] C. C. Awah, Z. Q. Zhu, Z. Z. Wu, **H. Zhan**, J. T. Shi, D. Wu and X. Ge, “Comparison of partitioned stator switched flux permanent magnet machines having single- or double-layer windings,” *IEEE Trans. Magn.*, vol. 52, no. 1, ASN: 9500310, Jan. 2016.

[11] H. Yang, Z. Q. Zhu, H. Lin, **H. Zhan**, H. Hua, E. Zhuang, S. Fang and Y. Huang, "Hybrid-excited switched-flux hybrid magnet memory machines," *IEEE Trans. Magn.*, vol. 52, no. 6, ASN: 8202215, Jun. 2016.

[12] Y. Oner, Z. Q. Zhu, L. J. Wu, X. Ge, **H. Zhan** and J. T. Chen, "Analytical on-load subdomain field model of permanent-magnet vernier machines," *IEEE Trans. Ind. Electron.*, vol. 63, no. 7, pp. 4105-4117, Jul. 2016.

[13] X. Y. Ma, G. J. Li, G. W. Jewell, Z. Q. Zhu and **H. Zhan**, "Performance comparison of doubly salient reluctance machine topologies supplied by sinewave currents," *IEEE Trans. Ind. Electron.*, vol. 63, no. 7, pp. 4086-4096, Jul. 2016.

[14] G. Li, Z. Q. Zhu, M. P. Foster, D. A. Stone and **H. Zhan**, "Modular permanent-magnet machines with alternate teeth having tooth tips," *IEEE Trans. Ind. Electron.*, vol. 62, no. 10, pp. 6120-6130, Oct. 2015.

Journal Papers under Review

[1] **H. Zhan**, Z. Q. Zhu and M. Odavic, "Adaptive space vector PWM strategy for open-winding PMSM drive with circulating current suppression capability," *IEEE Trans. Ind. Electron.*, under review.

[2] **H. Zhan**, Z. Q. Zhu, Z. Y. Wu and M. Odavic, "Torque enhancement strategy for open winding PMSM using zero sequence current shaping technique," *IEEE Trans. Power Electron.*, under review.

[3] **H. Zhan**, Z. Q. Zhu, Y. Liu, Z. Y. Wu and M. Odavic, "Torque ripple mitigation strategy for open-winding PMSM with reduced bandwidth requirement on current controller," *IEEE Trans. Ind. Electron.*, under review.

[4] **H. Zhan**, Z. Q. Zhu, M. Odavic and Z. Y. Wu, "A novel zero sequence high frequency voltage injection based sensorless method for open winding-IPMSM," *IEEE Jour. of Emerg. and Selet. Topics in Power Elect.*, under review.

Submitted Patents:

[1] **H. Zhan**, Z. Q. Zhu and Z.Y. Wu, "A zero sequence high frequency voltage injection based sensorless method for open winding interior permanent magnet synchronous machine," 14 Jul. 2016.

[2] Z. Q. Zhu, **H. Zhan**, A. S. Thomas and M. Odavic, "Torque enhanced permanent magnet synchronous machine open-winding drives with third harmonic current injection," 12 Oct. 2015.

Conference Papers:

[1] **H. Zhan** and Z. Q. Zhu, "Nonintrusive online rotor permanent magnet temperature tracking for permanent magnet synchronous machine based on third harmonic voltage," in *Proc. IEEE Energy Convers. Congr. Expo.*, pp. 1-8, Sep. 2016, Milwaukee, WI, USA.

[2] **H. Zhan**, Z. Q. Zhu and M. Odavic, "Analysis and suppression of zero sequence circulating current in open winding PMSM drives with common DC bus," in *Proc. IEEE Energy Convers. Congr. Expo.*, pp. 1-8, Sep. 2016, Milwaukee, WI, USA.

[3] **H. Zhan**, Z. Q. Zhu and Z.Z. Wu, "Active voltage regulation of partitioned stator switched flux permanent magnet generator supplying isolated passive load," in *Proc. IEEE Energy Convers. Congr. Expo.*, pp. 1-8, Sep. 2016, Milwaukee, WI, USA.

[4] **H. Zhan**, Z.Q. Zhu, M. Odavic, Z. Wu and A. S. Thomas, "Performance evaluation of adjustable space-vector PWM strategy for open-winding PMSM drives," in *Proc. IEEE Inter. Electric Mach. & Drives Conf.*, May 2017, Miami, FL, USA. (Accepted)

[5] **H. Zhan**, Z.Q. Zhu, M. Odavic, Z. Wu and A. S. Thomas, "Robust initial phase correction strategy for zero sequence back EMF based sensorless drive under transition from current regulation control," in *Proc. IEEE Inter. Electric Mach. & Drives Conf.*, May 2017, Miami, FL, USA. (Accepted)

[6] Z.Q. Zhu, **H. Zhan** and Z.Z. Wu, "Electromagnetic performance of partitioned stator switched flux permanent magnet synchronous generator," in *Proc. IEEE Inter. Electric Mach. & Drives Conf.*, May 2017, Miami, FL, USA. (Accepted)

[7] D. J. Evans, Z.Q. Zhu, **H. Zhan**, Z.Z. Wu and X. Ge, "Flux-weakening control performance of partitioned stator switched flux PM machines," in *Proc. IEEE Inter. Electric Mach. & Drives Conf.*, pp. 391-397, May 2015, Coeur d'Alene, ID, USA.

[8] D. J. Evans, Z.Q. Zhu, Z.Z. Wu, **H. Zhan** and X. Ge, "Comparative analysis of parasitic losses in partitioned stator switched flux PM machines with double- and single-layer windings," in *Proc. IEEE Inter. Electric Mach. & Drives Conf.*, pp. 167-173, May 2015, Coeur d'Alene, ID, USA.